HUNGARIAN UNIVERSITY OF AGRICULTURE AND LIFE SCIENCES

Efficiency improvement of solar air collectors used in drying processes

PhD Dissertation

by

Machi Maytham Hasan Mahdi

Gödöllő

2025

Doctoral school

Denomination: Doctoral School of Mechanical Engineering

Science: Mechanical Engineering

Leader: Prof. Dr. Gábor Kalácska, DSc
Institute of Technology
Hungarian University of Agriculture and Life Science, Gödöllő, Hungary

Supervisor: Prof. Dr. István Farkas, DSc
Institute of Technology
Hungarian University of Agriculture and Life Science, Gödöllő, Hungary

Co-Supervisor: Dr. János Buzás, PhD
Institute of Technology
Hungarian University of Agriculture and Life Science, Gödöllő, Hungary

…………………………………   …………………………………
Affirmation of supervisors   Affirmation of head of school

CONTENTS

Contents

NOMENCLATURE AND ABBREVIATION

A	Area (m²)
B	Channel depth (m)
Cd	Discharge coefficient
C_p	Specific heat of air (J kg⁻¹ °C⁻¹)
D_h	Hydraulic diameter (m)
D_R	Drying rate
d.b.	Dry basis
$F_{f,av}$	Heat removal factor relating to the mean fluid temperature
F_R	Heat removal factor
H	Height of the fin (m)
h	Heat transfer coefficient (W m⁻² K⁻¹)
h_{le}	Latent heat of vaporization (kJ kg⁻¹)
h_r	Radiative heat transfer coefficient (W m⁻² K⁻¹)
h_w	Heat transfer coefficient due to wind (W m⁻² K⁻¹)
I	Instantaneous solar radiation on inclined surface (W m⁻²)
k	thermal conductivity (W m⁻¹K⁻¹)
K	Factor used in matrices
L	Length of the collector (m)
m	Mass (kg)
$\dot{m}$	Mass flow rate (kg s⁻¹)
MR	Moisture ratio
m_p	Moisture content (%) w.b.
N	Number of fins
Nu	Nusselt number
P	Pressure (Pa)
Pr	Prandtl number
Q	Heat rate (W)
Re	Reynolds number
S	Flux absorbed in the absorber plate (W m⁻²)
t	Time (s)
T	Temperature (°C)
Ub	Bottom heat loss coefficient (W m⁻² K⁻¹)
Ut	Top heat loss coefficient (W m⁻² K⁻¹)
V_w	Wind velocity (m s⁻¹)
W	Width of the collector (m)
w.b.	Wet basis
xb	Back cover insulation thickness (m)

Greek symbols

α	Absorptance of the collector absorber plate
β	Ratio between the orifice diameter to that of the duct
Δ	Change
ε	Emissivity
η_C	Collector thermal efficiency

η_D	Drying efficiency
$\lambda_{1,2}$	Factor used in matrices
μ	Dynamic viscosity (kg m^{-1}s^{-1})
ρ	Density (kg m^{-3})
σ	Stefan-Boltzmann constant (W m^{-2}K^{-4})
τ	Transmissivity of the glass cover
ϕ	Factor use in matrices
ψ	Factor use in matrices

Subscripts

1	Glass cover, first pass
2	Absorber plate, second pass
3	Back surface
a	Ambient, air
ch	Chanel
D	Drying
dr	Drying chamber
f	Fluid
fin	Fin
g	Glass
h	Horizontal surface
i	Inlet/initial
o	Outlet
or	Orifice
p	Absorber plate, projection
s	Sky
u	Useful

Abbreviations

Bl	Black matt
CFD	Computational fluid dynamics
DPSAC	Double pass solar air collector
EPS	Expanded polystyrene sheets
FDPSAC	Finned double pass solar air collector
FESAC	Front entrance solar air collector
FPSAC	Flat plate solar air collector
MFR	Mass flow rate
PV	Photovoltaic
SAC	Solar air collector
Se	Selective coating
SESAC	Side entrance solar air collector
SPSAC	Single pass solar air collector
TPSAC	Triple pass solar air collectors
XPS	Extruded polystyrene sheets

1. INTRODUCTION, OBJECTIVES

This chapter presents the background and importance of the research work, along with the primary objectives of the study.

1.1. Introduction

As the global population continues to grow and industrial activities expand, energy consumption is rising steadily. This increasing demand, combined with the environmental impact of greenhouse gas emissions, estimated at 21.3 billion tons of CO_2 annually from fossil fuel combustion, is accelerating the global transition toward renewable and alternative energy sources (Ray et al., 2025).

Renewable energy sources, including solar, wind, and hydropower, play a crucial role in meeting global energy demand and are essential for the future of the energy industry. Their adoption helps reduce greenhouse gas emissions, mitigate global warming, and support environmental sustainability (Obaideen et al., 2023). Among all types of renewable sources, the importance of solar energy is evident due to its abundance and influence. It is considered the primary source that supplies the earth with energy, where the sun emits about 5600 ZJ of yearly global insolation (Moriarty and Honnery, 2018).

Solar energy is the most massive renewable energy source, representing the primary source of energy to the earth. Solar energy can be utilized by using several technologies that work as a converter through converting the solar radiation to usable electricity or heat using photovoltaic (PV) and thermal systems. Photovoltaic cells produce electricity directly, while solar thermal systems produce heat for buildings, industrial processes, or domestic hot water. Solar thermal energy is an abundant and cost-effective renewable energy source that has received significant attention. Solar thermal energy systems harness the sun's radiant and transport it to a fluid, such as oil, water, and air through a device known as a solar collector. These collectors efficiently transport and utilize harvested heat in various applications, including domestic water, space heating, and drying (Machi et al., 2022, 2024).

Highlighting the importance of sustainable energy solutions, the flat-plate solar air collector (SAC) emerges as a vital tool in air heating, solidifying its position as a prevalent solar collector across various applications. SACs typically consist of a wooden or metal box insulated with appropriate materials, a flat transparent cover that allows sunlight to pass through, and heat-absorbing surfaces that capture solar energy. The performance of a SAC hinges on its ability to transfer as much heat as possible from absorbed solar radiation to the operating fluid (Debnath et al., 2018; Salih et al., 2019). Nevertheless, conventional SACs typically experience difficulties due to the constrained efficiency in the heat exchange process from the absorbing surface to the air in circulation. This caused an elevated absorber plate temperature, increased heat losses, and ultimately reduced overall thermal efficiency. This inherent limitation of SACs arises attributable toward the significantly low specific heat of air, which is roughly a quarter of water's capacity. This discrepancy plays a direct role in affecting their thermal efficiency (Mund et al., 2021; Razak et al., 2016).

Enhancing the thermal energy transfer in SACs is imperative for augmenting their thermal performance and overall efficiency. Researchers are actively exploring ways to improve SAC

performance, often focusing on innovative design modifications of the absorber surface. Additionally, using different flow channel configurations (single, double, or triple pass) can be beneficial depending on the application. Balancing these improvements with the potential drawbacks is key to optimizing SAC thermal efficiency and advancing sustainable energy solution.

1.2. Objectives

A comprehensive review of experimental and theoretical studies has identified various factors influencing the performance of SACs. However, there remains a significant lack of experimental investigations to evaluate SACs performance, particularly regarding the effects of entrance flue conditions, channel height, selective coatings, and different absorber configurations on SAC efficiency. Notably, the effect of entrance flue conditions has not been introduced in the literature. Previous research has primarily examined these aspects either mathematically or through indoor experiments, which do not accurately reflect the impact of various weather conditions such as wind speed, humidity, and ambient temperature changes. This research aims to address these gaps through detailed experimental analysis conducted outdoors under real weather conditions.

For this purpose, four collectors were constructed, and several experiments were conducted using both single (SPSAC) and double (DPSAC) pass solar air collectors. Additionally, novel V-angled fins with different lengths and orientations were introduced and examined. Therefore, this study is dedicated to enhancing the performance of SACs through rigorous experimentation.

The primary objectives of this research are:

- To examines the effect of entrance flue conditions on the performance of single pass solar air collectors.
- To study experimentally the performance of double pass solar air collectors using different absorber configurations.
- To investigate and compare the effect of using selective coating on the performance of solar air collectors.
- To examine numerically and experimentally the effect of channel height on the performance of solar air collector.
- To study experimentally the influence of different fins configuration on drying process.

By addressing these objectives, this study aims to enhance the understanding of SAC performance and contribute to the development of more efficient and sustainable solar air heating systems.

2. LITERATURE REVIEW

This chapter offers an extensive examination of the different types of SACs utilized across various applications. It covers the foundational concepts and classifications of SACs and evaluates their performance. The main aim is to conduct a thorough comparative analysis of the designs studied, emphasizing their unique characteristics and features.

2.1. Solar air collector fundamentals

Flat plate solar air collector (FPSAC) collects and transforms solar energy into thermal energy, which is ideal for low-temperature uses such as heating and drying process (Hedau and Singal, 2023). A FPSAC typically features a channel with a glass top surface that allows sunlight to penetrate and hit the black-painted metal surface that absorbs heat. The metal surface, serving as the channel's bottom, is surrounded by insulation on the sides and below the absorber to minimize heat losses. As air moves through the channel, it captures heat from the metal surface, making the FPSAC useful for thermal applications.

The energy flow of a SAC begins with the absorption of incoming solar radiation through a transparent cover, which then reaches the absorber plate. The absorber plate converts this solar radiation into thermal energy. The generated heat is transferred to the air flowing through the collector, either by direct contact or convection. This heated air is then circulated, potentially with the aid of a fan or blower. During this process, some heat is inevitably lost due to convection and radiation from the absorber plate, as well as conduction through the collector's casing. Insulation and specific design features aim to minimize these losses. Finally, the heated air is delivered to the intended application, such as space heating or drying processes. Fig. 2.1 illustrates a graphical representation of a typical solar air collector with energy flow representation.
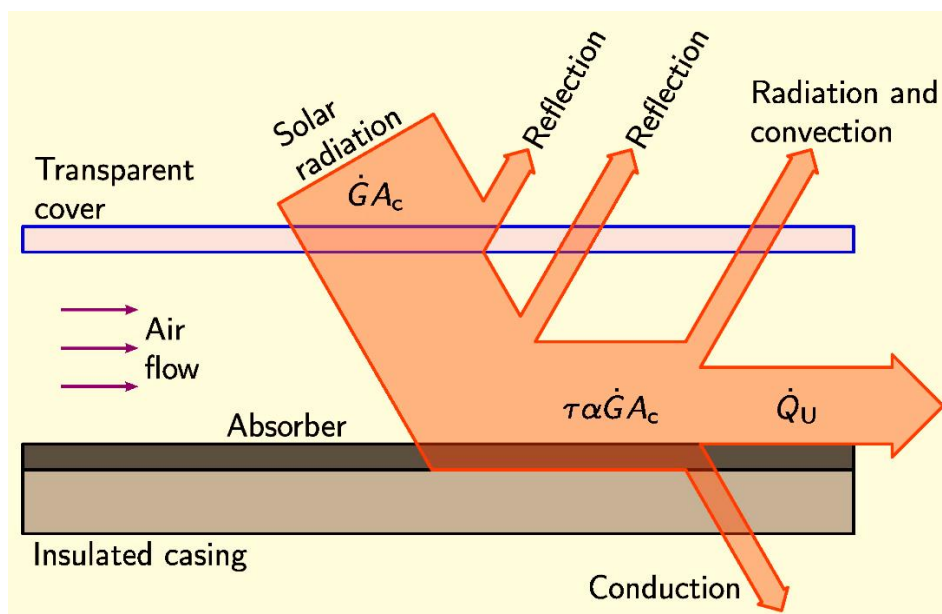

Fig. 2.1. Graphical representation of a typical SAC with energy flow (Araújo, 2020)

The classification of SACs has been widely debated in the literature, with researchers noting the inherent challenges in establishing a systematic classification (Tyagi et al., 2012). SACs

can be categorized based on various criteria, including their application, mode of operation (active, hybrid, or passive), absorber configuration, and flow passes. According to (Oztop et al., 2013), SACs can be classified based on the type of collector cover, absorber materials, shape of the absorbing surface, absorber flow pattern, flow configurations, hybrid collectors, and their specific applications. The primary challenge in these classifications has been to enhance heat transfer within the solar air collectors. A detailed classification is provided in Fig. 2.2, where each main category is further divided into subcategories.
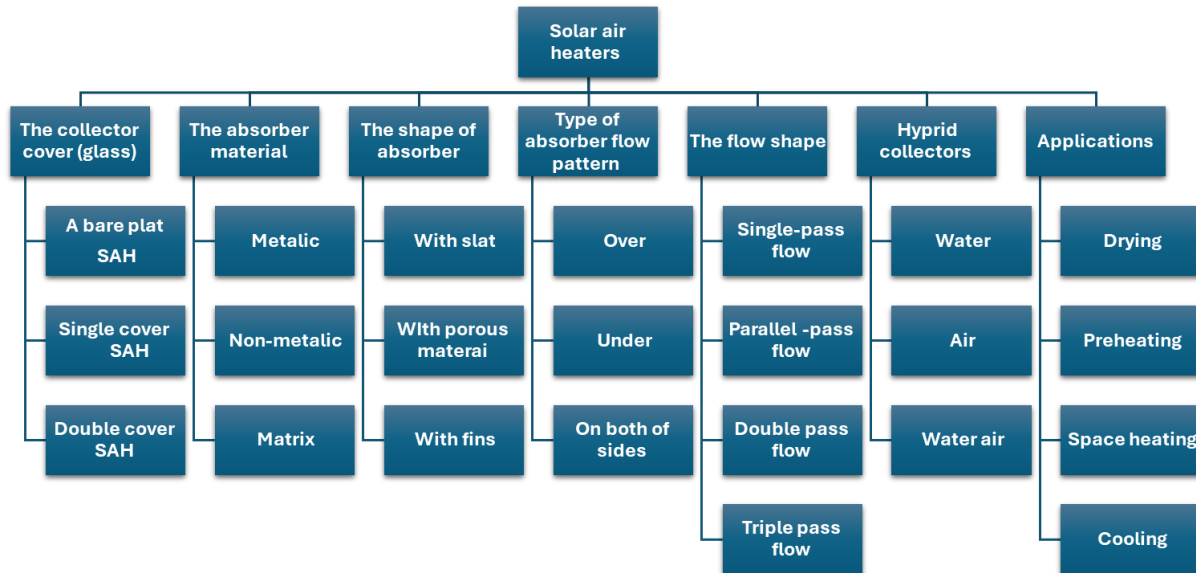
Fig. 2.2. Detailed classification of SACs (Oztop et al., 2013)

2.2. Enhancing methods for performance of collectors

The performance of SACs can be enhanced in several ways, as it influenced by various parameters, including the intensity of solar radiation, convection between the absorber surface and air, and heat losses from the absorber plate. Researchers have addressed one or more of these factors and have made corresponding design modifications to improve overall efficiency (Arunkumar et al., 2020). Some of these modifications include optimizing airflow patterns, enhancing duct geometry, increasing the number of glazing covers, improving absorber plate geometry, and incorporating turbulators and fins to enhance heat transfer. These modifications can be summarized in Fig. 2.3 as reported by (Hegde et al., 2023). For the purposes of this thesis, the focus will be on the flow passes number, absorber configuration and selectivity, and the intended application of the solar air collectors.
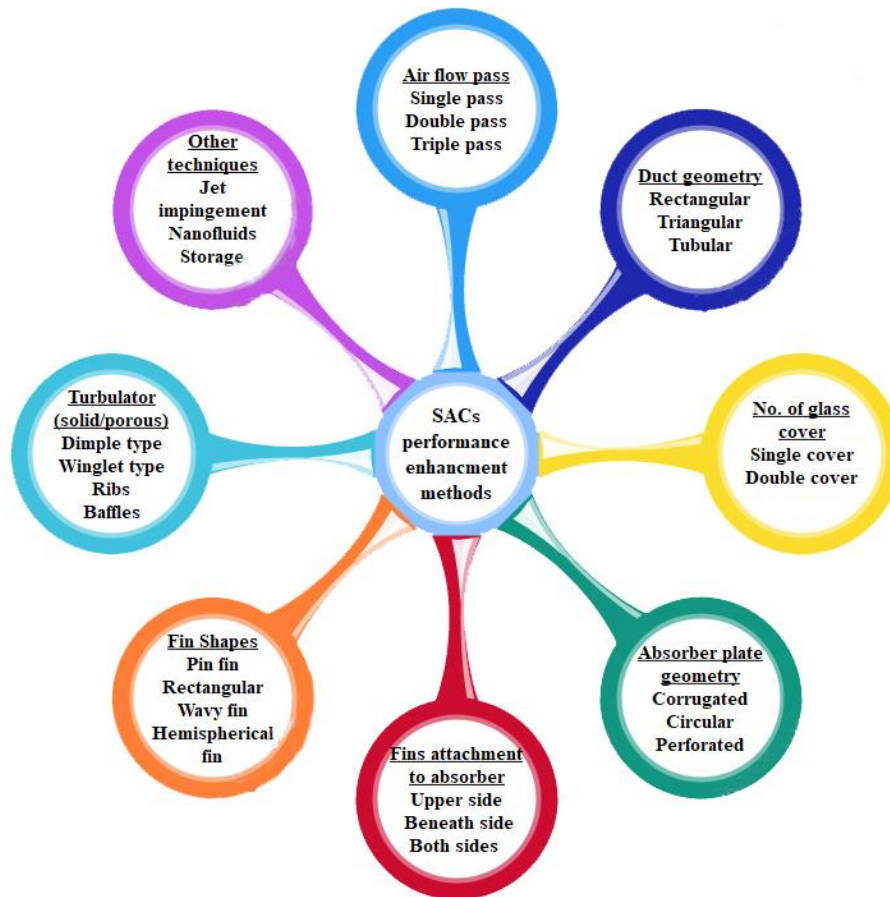
Fig. 2.3. Enhancement methods in SACs (Hegde et al., 2023)

2.2.1. Effect of airflow pass

The design of SACs can vary and may include multiple air channels. There are single pass solar air collectors (SPSAC), double pass solar air collectors (DPSAC), and triple pass solar air collectors (TPSAC). Each type has an increasing number of air channels, which enhances heat transfer efficiency. The choice of air pass configuration is typically determined by the intended application, ensuring optimal performance for specific uses. These collectors may incorporate different absorber configurations, such as smooth plates, fins, ribs, or artificially roughened surfaces. Numerous studies, both mathematical and experimental, have highlighted the significance of absorber configuration in enhancing heat transfer rates within the collector. These configurations will be discussed in the subsequent subsections.

2.2.1.1. Single pass collectors

This type of SAC is the most prevalent and straightforward. It features a single passage for air to directly enter and exit the channel. The air channel can be located either between the collector's glass cover and the absorber plate, or between the rear of the absorber and the insulation layers. The absorber plate can feature a smooth, grooved, or finned surface. Various researchers have experimented with these different configurations to enhance the thermal performance of the collector. Further detailed configurations of this kind of SAC will be reported in other subsections. Fig. 2.4. demonstrates a schematic view of ordinary SPSAC.
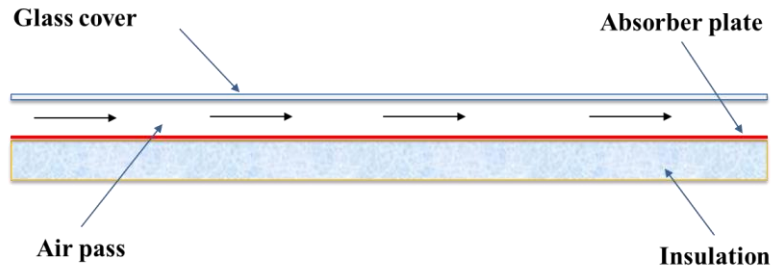
Fig. 2.4. Schematic view of SPSAC

2.2.1.2. Double pass collectors

Conventional SACs can be enhanced by increasing the number of air passes and separating the air streams. Studies indicate that replacing single air passes with double or multiple air passes can lower radiation and convective emissions to the environment, thereby minimizing thermal losses (Goel et al. 2021). In a double-pass configuration, air movement can follow a parallel path, flowing both over and beneath the absorber (see Fig. 2.5). The other possible air movement is the counter flow, in which the air moves over the absorber plate to extract heat and then is redirected beneath the absorber to collect as much energy as possible. The other configuration is the recycled DPSAC, in which a portion of the outlet air is mixed with fresh inlet air to improve the heat transfer process (Alam and Kim 2017). Numerous studies on DPSACs with various absorber configurations have been reported and will be discussed in further detail in the subsequent subsections.
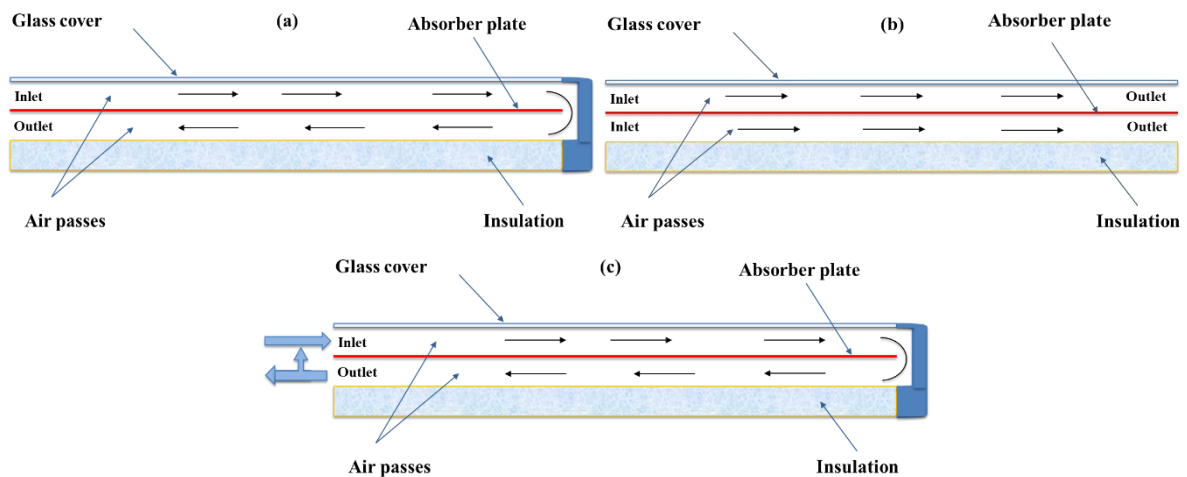
Fig. 2.5. Schematic view of DPSACs: a) counter flow, b) parallel flow c) recycled

2.2.1.3. Multi pass collectors

In these collectors, more than two passes are employed to enhance the heat collection efficiency. However, compared to other types of SACs, there is a limited amount of research available on this configuration in the literature. Fig. 2.6 illustrates schematics view of TPSAC. Yassien et al. (2020) evaluated the efficiency of two types of TPSACs. The first system had a single glass cover, while the second included a net of tubes below the absorber surface and a double glass cover. The second system achieved 80.2% efficiency, surpassing the first system's 73.4%. The modifications significantly enhanced heat transfer rates. The second system is ideal

for applications requiring larger temperature differences, while the first system suits smaller ones. Khanlari et al. (2020) conducted an experimental study involving the design and testing of v-groove triple-pass and quadruple-pass SACs, specifically aimed at drying municipal sewage sludge. They employed both conventional and solar absorber drying chambers in their experiments. The study found that the quadruple-pass heater, when combined with the solar absorber chamber, achieved a maximum efficiency of 91.1%, significantly outperforming the triple-pass design and other configurations tested. Omotosho and Hackney (2024) developed a mathematical model and performed experimental tests on a low-cost SAC using upcycled aluminium cans. They found that the ten-pass configuration delivered the highest heat gain, outperforming single-pass and five-pass designs in terms of temperature and efficiency. Esam et al. (2024) analysed the thermal performance of a combined parallel and triple-pass v-corrugated SAC using CFD and experimental methods. They found that the combined-SAC system yielded the highest air temperature rise, with an average thermal efficiency of 81.7% at 0.019 kg/s and maximum exergy efficiency of 49.5%.
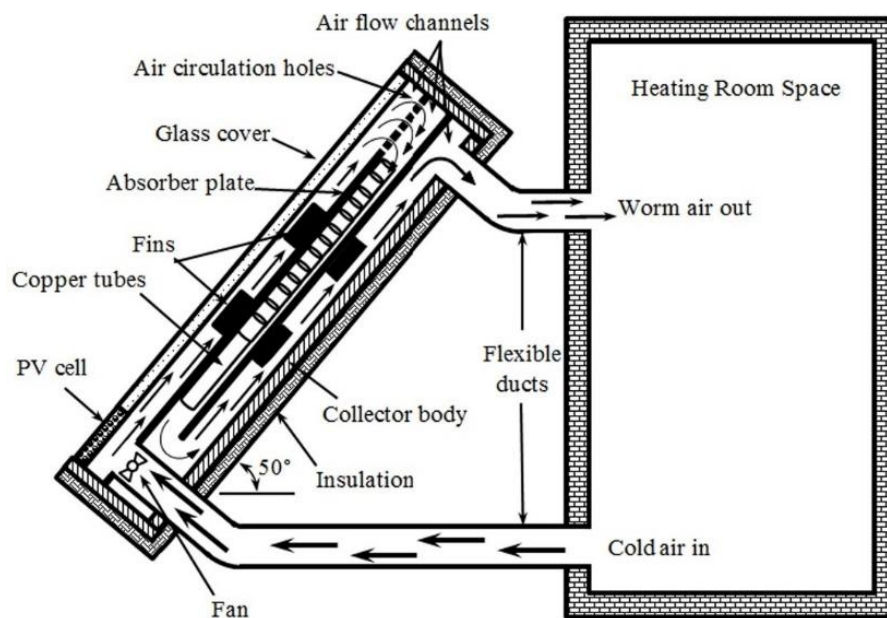
Fig. 2.6. Illustrate schematics view of triple pass SAC (Yassien et al., 2020)

2.2.2. Effect of absorber configuration

As mentioned earlier, SACs with smooth surfaces often suffer lower performance because of the limited transfer of heat across the fluid and the absorbing surface. When air flows over a heated absorber, a thin layer forms between them, slowing heat transfer. This effect, known as a laminar boundary layer, can be reduced by causing the airflow to become turbulent. For that, various enhancement methods like grooves, baffles, pins, and fins are employed to enhance heat transfer, although they can increase friction and pumping needs (Hamad et al., 2023; Machi et al., 2022, 2024; Vengadesan et al., 2024). The effect of various absorber configuration on the collector performance will be discussed below.

2.2.2.1. Smooth absorber

In their research, Yang et al. (2012) analysed six SPACs with an iron absorbing surface, customizing five key parameters that influence performance. They identified that minimizing heat transfer resistance in the air passage significantly enhances thermal efficiency. Optimizing the height of the stationary air layer and improving the optical properties of the transparent cover was highly effective. However, modifications to the back plate's thermal resistance and reducing the absorber plate's emittance had minimal effects. Chabane et al. (2013) conducted an experimental analysis on the thermal efficiency of a SPSAC using a smooth plate absorber under varying mass flow rates. Findings indicated that the optimal thermal efficiency was achieved at a mass flow rate of 0.0202 kg/s, reaching efficiencies up to 63.6%. The results demonstrated that increasing the mass flow rate improves thermal efficiency, with significant gains observed between flow rates of 0.0108 kg/s and 0.0184 kg/s, where the efficiency ranged from 39.7% to 50.4%. The research underscores the crucial role of mass flow rate in enhancing the performance of SACs. Mahboub et al. (2016) evaluated a new SAC design featuring a curved flow channel and convex absorber plate. Tested in Biskara, Algeria, the prototype showed thermal efficiencies of 49.2%, 66.3%, and 82.9% at mass flow of 0.0172, 0.029, and 0.0472 kg/sm², respectively. This improvement is due to enhanced heat transfer from secondary flow vortices without a significant increase in pressure drop. This design offers better performance than traditional flat plate heaters without additional manufacturing costs.

Raj et al. (2019) assessed the performance of DPSACs by examining fluid properties, channel depth, and flow rates. The study highlighted solar radiation and ambient temperature as the main factors affecting energy and exergy efficiency, with relative humidity having minimal impact. Results showed thermal efficiencies ranging from 20% to 41% and exergy efficiencies between 5.6% and 18% at MFRs of 0.02 kg/s and 0.03 kg/s, respectively. Additionally, the air temperature was consistently higher in the lower channel, and the collector's performance was significantly influenced by channel depth, ambient conditions, and MFR variations.

2.2.2.2. Corrugated absorber

El-Sebaii et al. (2011) conducted a study to evaluate the performance of DPSACs featuring both smooth and V-corrugated surfaces. The research demonstrated that the V-corrugated DPSAC outperformed the smooth version by 11–14%, with the highest thermo-hydraulic efficiencies observed at 0.02 kg/s MFR. Moreover, the maximum outlet temperature achieved for the V-corrugated DPSAC was 64.5 °C. Additionally, V-corrugated DPSAC had higher output power at 474 W and lower overall heat losses at 546 W compared to the smooth DPSAC. Karim et al. (2014) developed a computational model for a corrugated DPSAC using MATLAB, which showed a maximum deviation of 7% compared to experimental data. The study identified solar radiation, MFR, and inlet air temperature, along with collector length, as key factors influencing efficiency. Moreover, the MFR and inlet temperature were found to be the most impactful. The research suggested that DPSAC systems provide superior efficiency compared to SPSAC systems. Kabeel et al. (2016b) experimentally evaluated the thermal performance of flat, finned, and v-corrugated plate SACs. Their findings indicated that corrugated plate SAC exhibited superior performance, demonstrating a 14.5% higher efficiency than the flat plate and a 10.5% increase over the finned plate. Hedayatizadeh et

al. (2016) optimized the exergy efficiency of a double-pass/glazed v-corrugated SAC. Through thermal modelling and exergy analysis, they minimized exergy losses and found that the highest exergy efficiency of 6.2% was achievable. The temperature difference between the sun and the plate was the main source of exergy loss, making up 63.5% of total losses. Sahel and Benzeguir (2017) studied a SAC with corrugated surfaces and baffles, varying the heating surface ratio (HCSR) up to 0.5 and Reynolds numbers from 8000 to 20000. Findings indicated that heat transfer and friction factors increased with Reynolds numbers. The highest thermal performance, a factor of 2.7, was achieved at HCSR=0.5, where corrugated surfaces and baffles increased turbulence, leading to greater pressure losses.

Sudhakar and Cheralathan (2020) conducted an experiment on a DPSAC with pin-fins and a corrugated absorber plate designed for drying agricultural products. The results emphasized airflow's role in efficiency, showing a 17.4% rise in thermal efficiency at a flow rate of 0.035 kg/s compared to standard models. Additionally, the average outlet temperature increased by 12%, with a peak temperature difference of 14.8 °C. The system achieved a maximum efficiency of 52%, greatly exceeding traditional designs. Farhan et al. (2021) examined a V-corrugated SAC with twisted tape inserts (TTI), finding significant enhancements in thermal and thermo-hydraulic efficiencies. The optimal configuration, featuring a twisted tape ratio (Y) of 1 and five channels (N), achieved thermal efficiencies of 74.4% and thermo-hydraulic efficiencies of 17% at a Reynolds number of 12,000. This setup also recorded a 17% increase in accumulated useful heat gain over a similar collector without TTI.

Alomar et al. (2022) examined enhancements in SACs by testing two models. Model-1, a V-corrugated absorber with perforated jets, consistently outperformed the standard V-corrugated Model-2, showing efficiency improvements of 11.5% to 13.2% across different MFRs. The optimal thermal performance was observed at a flow rate of 0.037 kg/s, with Model-1 achieving 82.3% efficiency compared to 69.1% for Model-2. A subsequent study, (Abd et al., 2022) introduced a dual-plate version of Model-2, featuring both an absorbing and a jet plates, and evaluated it to Model-1 with specialized jets. Model-1 demonstrated substantial efficiency gains over Model-2, ranging from 9% to 11.5%. The peak efficiency reached 84.5% for Model-1, significantly higher than Model-2's 73%. These findings emphasize the value of design changes in enhancing heater performance and recommend further research on optimizing port placement.

Kumar et al. (2022) studied a SAC with a shot-blasted v-corrugated surface, noting a 15% higher energy efficiency and a 34% greater exergy efficiency than conventional SACs at 0.02 kg/s airflow. Increases in energy efficiency were 2.4%, 3.1%, and 5.8% at MFRs of 0.01, 0.015, and 0.02 kg/s, respectively. Exergy efficiency improvements were 0.21, 0.36, and 0.70. The modified SAC also reduced CO_2 emissions by 10.3, 18, and 28.7 tons annually at these rates, with enviro-economic improvements of 23.4%, 15.1%, and 18.2% over the conventional model. Abed et al. (2023) assessed SACs with smooth and v-corrugated absorbers using CFD analysis. The v-corrugated absorber achieved 46.7% thermal efficiency, outperforming the smooth collector with 33.01% thermal efficiency. The v-corrugated collector reached an outlet temperature of 61 °C, while the smooth type was 53 °C. Increasing the corrugation height and

decreasing pitch improved heat transfer and efficiency, showing that v-corrugated surfaces enhance solar collector performance.

Hussein et al. (2023) examined the thermal efficiency of DPSAC by replacing traditional flat plate absorbers with tubular ones oriented either perpendicular or parallel to the airflow. The parallel-oriented tubular absorber reached effective efficiency exceeding 80.5% at 0.03 kg/s, outperforming the flat plate and perpendicular models by 4.2% and 9.8%, respectively. The useful heat peaked 292 W at the same MFR. The study highlighted that higher mass flow rates lead to increased energy gains and that absorber orientation significantly impacts thermal efficiency.

Qamar et al., (2023) optimized a SAC using corrugated absorber plates with baffles and insulation materials like polystyrene sheets, achieving 63% energy efficiency with reduced thermal losses, and found it cost-effective for agricultural drying applications. The SAC could save 30 Pakistani Rupee/kWh when used as a preheater for a spray dryer.

2.2.2.3. Artificial roughened absorber

SAC designers attempt to maximize heat transfer from the plate to the air. One strategy to achieve this is by incorporating artificial roughness along the collector plate. This disrupts the smooth flow of air, preventing the formation of a stagnant layer that would otherwise hinder heat transfer. This approach promotes better mixing of the air stream, ensuring more particles encounter the hot plate, leading to efficient heat transfer Jain et al., (2019).

In his study, Simarpreet Singh (2017) assessed a SAC with a metallic, arched absorbing surface, using turbulators in triangular and dimpled rib designs on the absorber plate. Tests covered a Reynolds number range from 3800 to 14000. Utilizing ANSYS 16.2 for analysis, the results showed that these design enhancements in the SAC increased thermal and hydraulic efficiency. This improvement was linked to increased turbulence and vortex generation, reducing the laminar air layer near the absorber. Furthermore, this increased turbulence boosted the Nusselt number at higher Reynolds numbers, with only a slight rise in the friction factor.

Hans et al. (2010) achieved the most significant enhancements, with Nusselt numbers and friction factors increasing up to six and five times in SACs featuring multiple V-rib (W-shaped) configurations, underlining the importance of optimal roughness parameters. Collectively, these studies underscore the critical role of precise rib configurations and gap placements in maximizing the thermal and thermohydraulic performance SACs. Karwa and Srivastava (2012) assessed the thermal performance of a SAC with a V-down ribbed absorber plate for space heating in a closed-loop mode. Using a validated mathematical model, they found that the roughened plate improved thermal efficiency by 6% to 26% compared to smooth ducts, especially at lower flow rates. The ribbed design increased heat transfer efficiency by inducing turbulence near the surface. They recommended a relative roughness height of 0.07 for optimal performance in space heating applications. Later, Karwa and Chitoshiya (2013) experimentally evaluated a SAC with a 60° v-down discrete rib roughness absorbing surface in an open-loop mode. They found that this design improved thermal efficiency by 12.5-20%, particularly at lower flow rates, due to an increased heat transfer coefficient, which lowered the operating temperature and reduced heat loss.

In their research, Ravi and Saini (2016) evaluated a DPSAC with V-shaped and staggered ribs, focusing on relative staggered rib sizes from 1 to 2.5. The research showed significant thermal efficiency gains, with the roughened geometry enhancing heat transfer and increasing friction compared to smooth ducts. The roughened DPSAC reached a peak Nusselt number of 440.47 at a Reynolds number of 20,000 and a friction factor three times higher than that of smooth ducts. Expanding on this, Ravi and Saini (2018) explored variations in rib pitch, sizes, and roughness, demonstrating that optimal roughness increased the Nusselt number up to 4.52 times and the friction factor up to 8.53 times compared to standard models. Key roughness parameters were a rib size ratio of 3.5, a rib pitch ratio of 0.6, and a roughness width ratio of 7, markedly enhancing DPSAC performance.

Sharma et al. (2017) conducted an experimental study on a DPSAC with V-shaped ribs, showing maximum Nusselt numbers and friction factors compared to smooth plates. Key parameters included a relative roughness pitch of 10, relative roughness height of 0.044, and an angle of attack of 60°. The developed correlations predict heat transfer and pressure drop, demonstrating the V-shaped ribs' effectiveness in enhancing DPSAC performance.

The majority of research on employing V-shape ribs as roughened surfaces has focused on SPSAC. Alam et al. (2014b) enhanced SPSAC heat transfer with V-shaped perforated blocks, achieving 33% higher Nusselt numbers and 32% lower friction factors than solid blocks. Maximum Nusselt numbers occurred at a blockage ratio of 0.8. Nusselt numbers increased with open area ratios up to 20% but decreased at 5% due to expanding jet diameters. Alam et al. (2014a) further validated these findings, achieving maximum heat transfer and developing precise correlations for Nusselt numbers and friction factors, with deviations of 5.03% and 4.99%, respectively, demonstrating the effectiveness of V-shaped perforated blocks in enhancing SPSAC performance.

Kumar et al. (2017) studied heat transfer in SACs using multi-V-down perforated baffles. They found that adjusting baffle width, while keeping other parameters constant, significantly influenced thermal performance. Optimal heat transfer occurred at a relative baffle width ratio of 5.0, yielding the highest Nusselt number and friction factor ratios, demonstrating the effectiveness of baffle adjustments in enhancing SAC performance. Sharma and Kalamkar (2017) investigated SACs with truncated ribs in four configurations using experiments and simulations. They found that Nusselt and Reynolds numbers increased together. Elevated temperatures developed between the ribs due to boundary layer disturbances and recirculation zones. The friction factor also rose with increasing Reynolds number.

Likewise, Jain and Lanjewar (2019) investigated the effect of V-ribs with symmetrical gaps and staggered configurations on an SPSAC absorber plate, focusing on the influence of the P/e ratio on performance. They discovered that Nusselt numbers and friction factors significantly improved with 2.30 and 3.13 compared to a smooth SPSAC, highlighting the peak in thermohydraulic performance. Furthermore, Deo et al. (2016) experimentally studied a SPSAC roughed by multi-gap V-down ribs combined with staggered ribs. They result revealed that optimal enhancement attained by a relative roughness pitch of 12, a roughness height of 0.044, and 60° angle of attack. Their study showed that using broken V-down and staggered ribs

improved the thermohydraulic performance parameter by 2.45 times. This emphasizes the effectiveness of creating gaps in rib roughness at specific geometrical conditions.

Jin et al. (2017) demonstrating that multiple V-shaped rib significantly outperform inline configurations in SACs, attributed to the enhanced generation of subsidiary vortices and flow redevelopment. They attained a peak thermohydraulic performance factor of 2.43 in SACs using staggered multiple V-shaped ribs, emphasizing the critical role of rib geometry in optimizing thermal efficiency. Moreover, Jin et al. (2019) numerically explored heat transfer enhancement in SACs with multiple V-shaped ribs, achieving a peak thermohydraulic performance factor of 2.35. Optimal rib count, influenced by channel height and rib dimensions, significantly impacted efficiency. Their numerical model, validated against experimental data, aligns with their study Jin et al. (2015), which highlighting the effects of V-shaped ribs on fluid flow and heat transfer. The highest thermal performance parameter observed was 1.93.

Kumar et al. (2016) experimented with SACs using broken multiple V-type baffles to study the influence of baffle relative width on thermal performance. They found that a relative width of 5.0 maximized heat transfer efficiency, with broken V-type baffles outperforming smoother designs due to enhanced heat transfer and reduced friction, making them optimal for SAC applications. Zhang and Zhu, (2022) also noted that varied channel configurations in these SACs enhance heat transfer. However, they cautioned that increasing the number of channels can raise airflow resistance and power consumption, necessitating careful design and optimization of these channels for efficiency. Singh et al. (2022a) experimentally investigated the performance of a parallel flow DPSAC with perforated and continuous multi-V ribs. They found that perforated ribs significantly improved heat transfer and reduced friction compared to continuous ribs, with a maximum Nusselt number of 481.14 at Reynolds of 18000. The perforated ribs enhanced thermal performance, achieving a thermo-hydraulic performance parameter 2.97. Kumar et al. (2024) used CFD Fluent to optimize thermal performance in a SPSAC with V-ribs and ring turbulators. The best performance was achieved with a W_D/W_{VR} (duct width to V-rib width) ratio of 5.0, resulting in a thermohydraulic performance factor of 2.58 at Re = 16,000 and a Nusselt number of 289 at Re = 20,000, significantly enhancing heat transfer efficiency.

Patel and Lanjewar (2018, 2019) and Singh et al. (2019) conducted studies on SACs with various V-shaped roughness geometries, demonstrating that optimized configurations significantly enhance heat transfer and friction factors, with the highest performance achieved at specific rib pitch-to-height ratios and Reynolds numbers. Correlations developed for heat transfer and friction factors were validated experimentally, providing reliable predictions for SAC performance under different conditions.

Gabhane and Patil (2017) studied a SAC with a double-flow design using C-shaped ribs to induce surface roughness. They achieved a maximum Nusselt number of 415 at a relative roughness pitch (P/e) of 24 and a roughness angle of 90°, with a Reynolds number of 15,000. The friction factor was 0.031, and the thermohydraulic performance parameter was 3.48, significantly improving heat transfer efficiency over traditional single-flow setups. Hedau and Singal (2023) conducted a numerical analysis of a DPSAC with semi-circular tubes and

perforated baffles. They found a maximum Nusselt number of 274.29 at a Reynolds number of 19,000 and the highest friction factor of 0.6290 at Reynolds 3000. Increasing the tube amplitude ratio (a/H) from 0.2 to 0.5 raised the Nusselt number from 65.64 to 242.72, while the friction factor peaked at 0.2155. The study suggests that geometric modifications can balance heat transfer enhancement and increased friction.

Likewise, Singh and Kumar (2023) experimentally studied a SAC with frustum-shaped roughness elements. The study tested various configurations, finding that the highest thermal efficiency of 79% was achieved at a relative roughness pitch of 12 and 0.0486 kg/s MFR. The roughened plates significantly improved heat transfer compared to smooth ones, although increased roughness also raised the friction factor, potentially increasing energy requirements. The research emphasizes the need to optimize roughness geometry for a balance between thermal efficiency and pressure drop. Similarly, Kumar and Murmu (2023) performed a comprehensive study on SAC improved with roughening through the use of spherical balls set at an incline, examining their performance in terms of thermal, thermohydraulic, and exergetic efficiencies. Their findings indicated a marked improvement in thermal efficiency for the absorbers with enhanced surfaces, with peak exergetic efficiency occurring under precise conditions of temperature elevation.

Chhaparwal et al. (2024) explored the impact of circular detached ribs on the performance of a SAC duct. They utilized both computational simulations and experimental methods to examine different rib configurations. Their findings indicate that optimizing these configurations significantly enhances the collector's efficiency by improving heat transfer and airflow dynamics, offering a notable improvement over traditional design.

Sharma and Debbarma (2024) improved reverse flow SACs using perforated absorbers and delta-wing turbulators. Inline delta-wing configurations notably enhanced heat transfer, with a 6.6-fold increase in the Nusselt number and a 9.4-fold rise in the friction factor at a 75° attack angle. Overall thermohydraulic performance improved 3.06 times compared to smooth ducts. Pachori et al. (2024) conducted a comprehensive analytical and CFD investigation of a decentralized SAC with V-shaped ribs. They found that the V-ribbed absorber increased thermal efficiency by 40% compared to a smooth duct, achieving optimal performance at specific configurations of relative roughness and angle. The study also introduced a novel sustainability index and improvement potential, highlighting significant enhancements in both efficiency and sustainability.

Kumar et al. (2023) and Kumar and Layek (2018, 2019) investigated SACs with twisted rib turbulators using experimental and numerical methods. They found that a configuration with a relative roughness pitch (P/e) of 8, rib orientation angle (α) of 60°, and twist ratio (y/e) of 3 significantly improved performance. This design enhanced thermal and exergetic efficiencies up to 1.81 times and heat transfer up to 2.58 times compared to smooth plate heaters, effectively improving heat transfer and reducing frictional losses. Thakur et al. (2017) applied 2D computational fluid dynamics to enhance SACs using novel hyperbolic rib structures. Their findings revealed that ribs measuring 1 mm in height and spaced 10 mm apart at a *Re* of 6000 significantly improved thermohydraulic efficiency over conventional rib designs. Patel et al. (2021) optimized groove parameters in SACs with reverse NACA 0040 profile ribs, enhancing

thermo-hydraulic performance. Their configuration achieved a maximum performance parameter of 2.65 at a *Re* of 6000, significantly outperforming traditional designs.

Panda and Kumar, (2024) evaluated the performance of SACs with staggered dimpled absorber plates at different pitch ratios. They found that the collector with a 1.25 pitch ratio achieved the highest efficiency, with thermal and daily efficiencies 34.5% and 35.5% higher than smooth plate collectors. The dimpled design significantly improved heat transfer and reduced heat loss. Kumar et al. (2022) studied the effects of perforated delta-shaped winglets on a solar air heater's performance. They found that using winglets with a 0 mm spacer length enhanced the Nusselt number and friction factor to 5.17 and 4.52 times, respectively, of those observed with a smooth plate. This configuration significantly improved the heat transfer efficiency of the system.

Yadav et al. have explored various rib shapes to enhance the heat transfer efficiency of SACs over several years. Their investigations have included different configurations such circular transverse wire rib roughness (Yadav and Bhagoria, 2013), equilateral triangular sectioned rib roughness (Yadav and Bhagoria, 2014a), semi- circular sectioned transverse rib roughness (Yadav and Bhagoria, 2014b), square-sectioned transverse ribs (Singh Yadav and Bhagoria, 2015), opposite apex triangular cross-sectioned rib (Yadav and Sharma, 2022). Each of these studies consistently found that these rib configurations led to significant improvements in the thermal efficiency of SACs.

Mund et al. (2024) experimentally evaluated an impinging jet solar air heater (IJSAH) with stepped transverse ribs, focusing on two rib sizes (R1 at 2 × 4 cm and R2 at 4 × 6 cm) across pitches of 2, 4, and 8 cm, and jet diameters of 3, 6, and 9 mm. They found that the R1 rib with a 4 cm pitch and 3 mm jet diameter achieved the highest Nu of 128.78, a 31.22% improvement over the smooth IJSAH. Additionally, the R1 configuration with a 4 cm pitch and 6 mm jet diameter demonstrated the best thermohydraulic performance parameter (THPP) at 1.75, which was 19.49% higher than that of the smooth IJSAH. These results indicate that the R1 rib at a 4 cm pitch is optimal for enhancing heat transfer efficiency.

Thapa et al. (2024) conducted an analytical study on a jet impingement solar thermal collector (JISTC) featuring discrete multi-arc shaped ribs (DMASRs) to enhance thermal, effective, and exergetic efficiencies. They optimized key parameters including rib distance-to-length ratio (D_d/L_v = 0.27-0.86), and arc angle (35°-65°). The study found a 2.77-fold improvement in exergetic efficiency over smooth plates at an optimal configuration of D_d/L_v = 0.67, P_{rib}/H = 1.7, and α_a = 60°. These results emphasize the role of DMASRs in maximizing heat transfer efficiency by inducing turbulence and minimizing pressure losses.

Srivastav et al. (2024) experimentally analysed a submerged impingement jet solar air heater (SAHSIJ) to evaluate heat transfer and frictional characteristics. Their study examined several geometric parameters, including jet spacing ratio (S_j/D_h) (0.108 to 0.433), jet diameter ratio (d/D_h) (0.043 to 0.076), jet angle (α) (75° to 90°), stream-wise pitch ratio (X/D_h) (0.43 to 1.73), and span-wise pitch ratio (Y/D_h) (0.43 to 1.08). They observed that the Nu reached a peak enhancement at S_j/D_h of 0.217 and α of 85°, with a *Re* of 18,000. The maximum thermo-hydraulic performance parameter (THPP) was 3.19, indicating a significant improvement over conventional SACs.

Mahfoud et al. (2024) performed an experimental and computational analysis on innovative chicane shapes in SACs, specifically CT_{Prism} (Trapezoidal prism), CR_{Rec} (Rectangular with upper part), and CR (Rectangular without upper part) designs. They investigated the arrangement impacts of inline and staggered configurations under *Re* ranging from 600 to 4500. Findings revealed that CT_{Prism} in staggered arrangement produced a notable enhancement in heat transfer (up to 68%) and turbulent intensity (95%) compared to smooth ducts. The maximum thermo-hydraulic performance parameter (THPP) reached 2.39 for CT_{Prism} at lower *Re* values, showing its superiority in both thermal and flow efficiency relative to traditional designs.

2.2.2.4. Absorber with porous material

Sopian et al. (2009) developed a theoretical model and conducted experimental validation for a dual-pass solar collector incorporating porous material in the lower pass. Their results indicated that the porous material enhanced the outlet temperature, thereby improving system efficiency. The study concluded that the typical efficiency of these collectors ranges between 60-70%. Ramani et al. (2010) investigated DPSACs with and without porous additions through theoretical and outdoor experiments. Incorporating porous material improved efficiency by 20–25% over non-porous DPSACs and 30–35% over SPSACs, due to increased heat transfer surface area. The double-pass design also reduced heat loss, making it suitable for high-efficiency applications such as food drying. In their research, Dhiman and Singh (2015) proposed analytical models to predict the efficiency of DPSAC having packed bed, demonstrating that recycle flow enhances efficiency. Subsequently, Singh and Dhiman (2016) investigated energy and exergy efficiencies, finding that optimal mass flow rates and recycle ratios improve performance. Further, Singh and Dhiman (2018) evaluated the combined effect of recycle flow and fractional mass flow rate, concluding that lower recycle ratios and equal mass flow rate fractions yield higher thermo-hydraulic efficiency.

Chouksey and Sharma (2016) analysed a SAC with blackened wire screen matrices using a C++ finite difference model. The model predicted temperature distributions and performance metrics, with deviations from experimental results ranging from 7.1% to -9.8% for air temperatures and 7.2% to -9.6% for thermal efficiency. Factors such as absorber geometry, bed depth, and mass flow rate impacted thermal efficiency, with deeper beds showing less effective heat transfer. Moreover, Salih et al. (2021) compared finned DPSACs with and without a porous medium. The porous medium significantly improved performance, achieving peak efficiencies of 87% under natural convection and 81% under forced convection, compared to 82% and 67% without the porous medium. This underscores the porous medium's impact on heat transfer, making it ideal for high-temperature applications like drying.

Ahmadkhani et al. (2021) analysed DPSAC with various flow configurations and recycling patterns. They found that adding a matrix to the second channel increases thermal efficiency, reaching up to 79%, but also raises the pressure drop, reducing thermohydraulic efficiency at higher flow rates. Upward recycling without a matrix offers similar thermal efficiency with lower costs due to reduced fan power requirements. Farzan and Zaim (2023) studied a DPSAC with perforated absorbers and steel wool as porous material. The porous DPSAC achieved higher exhaust temperatures of 58 °C and 53 °C at 0.012 kg/s and 0.024 kg/s MFR,

respectively, compared to 54 °C and 48 °C for the non-porous model. It also showed thermal efficiency improvements of 11.8% and 15.3%, with daily efficiencies of 49.1% and 66.1%. Alomar et al. (2023) demonstrated that incorporating a porous material above the absorbing surface in a SAC increased efficiency by 7%, with the highest efficiency reaching 67%. This modification holds the potential to markedly boost the performance of SACs, underscoring the substantial prospects for enhancing their performance.

Promvonge et al. (2022) studied a SAC with trapezoidal louvered winglets and wavy grooves. They find that specific configurations, particularly at a 20° angle, significantly outperformed conventional designs. This research provides key insights for optimizing SAC systems. Promvonge et al. (2019) evaluated combined V-rib and chamfered-V-groove vortex generators (VGs) in SAC channels. The combined VG increased the Nusselt number by 11%, with a 13% gain using baffle-groove configurations. The study highlights the potential for improved SAC performance with these VGs. In the same manner several experimental and theoretical studies conducted by (Kumar, and Singh, 2020; Promvonge et al., 2021; Qader et al., 2019; Saravanakumar et al., 2019) using fins, ribs and vortex generator to improve the efficiency of SAC. They observed that using such absorber configuration enhance the rate of heat transfer and improve the collector performance.

Alnakeeb et al. (2024) analysed the efficiency of a SAC with a corrugated plate and vortex generators using a 3D numerical model. Testing various vortex shapes and angles, they found that rectangular vortex generators at a 30° angle achieved the highest thermal-hydraulic performance of 0.91 at Re 7000, significantly enhancing heat transfer and overall performance. Abushanab et al. (2023) explored the performance of a SAC integrated with an aluminium sponge porous medium. Their findings indicated that this addition significantly enhanced the system's efficiency, with the modified collector showing a notable 45.6% increase in daily exergetic efficiency at an airflow rate of 0.049 kg/s compared to the standard model.

2.2.2.5. Fins equipped absorber

Many researchers have explored the use of various categories of ribs and baffles with the aim of enhancing heat transfer rates inside the collectors. They achieve this by expanding the area for heat exchange and fostering turbulent flow conditions (Chabane and Aouissi, 2024; Kumar et al., 2023).

Akpinar et al. (2010) investigated a SAC with three obstacle configurations and no obstacles, evaluating heat loss, gain, and efficiency. They found that efficiency is greatly influenced by solar intensity, absorber plate design, and airflow, improving with higher airflow rates and temperature gradients. El-khawajah et al. (2011) studied a DPSAC with 2, 4, and 6 fins and wire mesh. Efficiency increased with more fins and higher mass flow rates, reaching 85.9% with six fins at 0.042 kg/s, demonstrating the impact of fin configuration on temperature and efficiency.

Ozgen et al. (2009) explored three absorbing surface arrangements in parallel flow DPSAC. They discovered that incorporating aluminium cans in the collector will increase the heat transfer area, producing turbulence, hence increasing convection heat coefficient. A staggered cans arrangement attained maximum thermal efficiency at 0.05 kg/s MFR exceeding 70%. In

their study, Abdullah et al. (2018) evaluated a counterflow DPSAC with aluminium cans as fins in different configurations and compared it to a SPSAC. The flat DPSAC configuration improved the Nusselt number by 22% over the SPSAC. Aligned and staggered fins enhanced Nu by 58–68% at 0.05 kg/s MFR. The staggered configuration with air guidance achieved up to 68% daily efficiency, surpassing both the flat DPSAC and the SPSAC. Likewise, Al-Damook et al. (2019) studied DPSACs using recycled aluminium cans as turbulators and analysed three designs via COMSOL Multiphysics: cocurrent, countercurrent, and U-shape. Outdoor tests compared three U-shaped models: without cans, with in-line cans, and with staggered cans. The staggered cans model was the most efficient at 60.2%, outperforming the in-line (53.1%) and plain models (49.4%), making the U-shape model overall more energy-efficient by 5.4% to 6.5%. (Kabeel et al. 2018a) conducted experiments on a SPSAC modified with longitudinal fins and an enhanced entrance. They tested fin heights of 3, 5, and 8 cm with guide blades for better air distribution. The modified SPSAC with 8 cm fins achieved 57% daily efficiency at 0.04 kg/s MFR, significantly outperforming the standard collector's 32% efficiency at the same flow rate. In another study, Kabeel et al. (2018b) investigated the thermal performance of a modified SAC with a glazed entrance and internal baffles. They found that the collector with 800 baffles achieved a maximum efficiency of 83.8% at 0.04 kg/s, significantly outperforming conventional designs. Chand et al. (2022) empirically studied a SAC performance with louvered fins attached to the absorbing surface at different spacings. They found a substantial improvement in thermal performance, with the best results achieved at a 2 cm fin spacing. The addition of louvered fins enhanced the collector's thermal efficiency. Later, Chand et al. (2024) experimentally evaluated the exergetic performance of a louvered finned SAC under various conditions. They found that the finned collector with 2 cm fin spacing, and 0.007 kg/s mass flow rate achieved a maximum exergy efficiency of 3.31%, significantly outperforming the smooth SAC. Saravanan et al. (2021) executed a series of experimental investigations to evaluate a SAC performance that integrates a unique absorber plate with staggered, C-shaped fins attached to its upper surface. They explored different flow metrics and geometrical parameters, including Reynolds number and pitch-to-gap ratios. The study identified optimal pitch/gap ratios for peak thermal performance and established corresponding empirical relationships.

Obaid et al. (2022) studied SAC performance with various designs and turbulators. They reported that delta turbulators improved airflow and reduced thermal boundary layers, enhancing thermal performance and cost-effectiveness. Higher mass flow rates increased efficiency. The rectangular plate collector performed best, while the triangular turbulator showed varying efficiencies at different tilt angles. Bezbaruah et al. (2020) conducted an analytical study using ANSYS to investigate SAC designs. They focused on a unique design with a finned absorber plate that promotes helical airflow. The study found that this helical flow pattern enhances heat transfer by creating vortices and localized eddies. However, it also increases frictional resistance, leading to a pressure drop. Similarly, Alok et al. (2021) carried out computational research to investigate the impact of varying airflow rates and solar intensities on a SAC with circular fins aligned along its length. The study highlighted the accuracy of a Surface-to-Surface (S2S) model in estimating output air temperature, suggesting it as a practical alternative to experimental methods for performance prediction. Antony et al.

(2020) optimized a flat plate SAC using cylindrical stepped turbulators. Their study showed that stepped fins outperformed regular ones due to increased surface area and turbulence, enhancing heat transfer and reducing flow.

Kumar and Chand (2017) researched enhancing SAC efficiency with herringbone corrugated obstacles beneath the absorber. Using a theoretical framework and MATLAB simulations, they found that increased solar power improves thermal performance across all mass flow rates and fin pitches. Salih et al. (2019) investigated a trapezoidal DPSAC in winter, comparing natural and forced convection. The results showed rectangular aluminium fins on the absorber enhanced heat exchange. Natural convection achieved 73.5% efficiency and a 45.5 °C temperature difference, while forced convection achieved 65% efficiency and a 17 °C difference. The study concluded that natural convection is better for high-temperature applications like drying, while forced convection suits household heating. Chabane et al. (2020) experimentally studied rectangular baffles' impact on heat transfer and pressure drop in a SPSAC. Testing various configurations, they found 18 baffles achieved the highest thermal efficiency at 70%, followed by 14 and 10 baffles at 65%, six at 58%, and three at 50%. Placing six baffles in the centre balanced high efficiency with manageable pressure drop. Karwa (2024) experimentally improved SAC efficiency using a plate with longitudinal inclined fins forming triangular passages. Aluminium fins with a 26.5 mm width enhanced efficiency by 25.8% compared to conventional designs, significantly increasing heat transfer without extra pumping power. Chang et al. (2024) used CFD Fluent to optimize SACs with longitudinal and transverse baffles. The results showed transverse baffles increased air velocity and reduced vortex zones, achieving 2.3% to 6.9% higher efficiency than longitudinal baffles. Four baffles achieved 54.32% efficiency at 0.026 kg/s, with six baffles optimal for higher rates (60% to 64.3%). Satyender Singh (2020) enhanced a finned SAC's thermal efficiency through experimental and numerical methods, finding that a hybrid staggered fin configuration improved thermohydraulic performance by 3.5% to 3.8%. The DPSAC achieved 79% efficiency, 13% higher than the SPSAC.

Alrashidi et al. (2024) experimentally analysed a SAC with V-shaped straight interrupted fins, focusing on energy and exergy performance. The findings indicated that tilting the SAC at 20° improved solar absorption and airflow, achieving peak energy efficiency of 38.2%, exergy efficiency of 26.4%, and a sustainability index of 1.36, significantly outperforming the horizontal setup. Yusaidi et al. (2024) explored the thermal efficiency of a DPSAC featuring fins shape like a staggered diamond. Their experiments showed a peak efficiency of 59.3%, while simulations indicated 62% efficiency at 0.0261 kg/s and 1000 W/m² solar irradiance. The fins improved efficiency by enhancing turbulence and heat transfer.

Taha and Farhan (2021) explored the performance enhancement of a SAC equipped with herringbone metal foam fins. They demonstrated that SACs with a corrugation angle of 30 degrees achieved the highest thermal efficiency, attaining a maximum of 87.7% at an airflow rate of 0.04 m³/s, significantly surpassing the efficiency of standard, smooth SAC designs.

Priyam and Chand (2016) investigated the performance of a wavy finned SAC, discovering that it significantly outperformed traditional designs by achieving a thermal efficiency of 83.8% at an airflow rate equal to 0.04 kg/s. Their results underscore the benefits of

incorporating wavy fins into solar air heaters. Hosseini et al. (2018) conducted numerical analyses on SACs with varying fin shapes, specifically rectangular, triangular, and elliptical. They found that the optimal angles for the highest mass flow rates were 45°-60° for triangular and elliptical fins and 50°-75° for rectangular fins. They demonstrated that SACs with rectangular fins exhibited higher performance compared to those with other fin shapes. Rajendran et al. (2023) studied the efficiency of a SAC with inclined and winglet baffles compared to a traditional flat plate SAC. Their findings showed that the modified SAC substantially outperformed the conventional design, achieving a peak efficiency of 85.1% at an airflow rate of 0.03 kg/s, which is significantly higher than that of the flat plate SAC.

Bensaci et al. (2020) investigated the effect of baffle positioning in SACs on thermal and hydraulic performance using numerical and experimental approaches. They evaluated four baffle configurations and discovered that placing baffles in the first half of the air channel led to the highest thermo-hydraulic performance factor, significantly outperforming the other configurations tested. Nonetheless, adopting these modifications interferes with the boundary air layer adjacent to the absorber. While this leads to a heightened the coefficient of transferred heat, it simultaneously escalates drop of the pressure throughout the test segment (Suresh Bhuvad et al., 2023; Yang et al., 2014). Researchers are currently striving to determine the optimal design of blockages that can effectively minimize pressure drop while simultaneously enhancing thermal efficiency

2.2.3. Effect of reducing thermal losses

In SACs, thermal losses predominantly occur through the top surface of the collector, primarily due to the glazing. This thermal inefficiency significantly impacts the overall performance of SACs. As illustrated in Fig. 2.7, several techniques can be employed to mitigate these losses. These strategies include the application of selective coatings on the absorber plate, the implementation of two-pass or multi-pass systems, the utilization of honeycomb structures, the incorporation of multiple glazing layers, and the use of alternative mediums or evacuated spaces. Each of these methods aims to enhance the thermal efficiency of SACs by effectively reducing heat losses through the top surface (Garg, 1987; Hegde et al., 2023; Singh et al., 2022b). Mohamad (1997) investigated a SAC with a counter-flow design featuring two glass covers. This setup preheats air by forcing it over the front cover before it reaches the absorber, reducing heat loss and maximizing heat extraction. The use of a porous absorber further enhanced efficiency, achieving over 75%, significantly higher than conventional designs. El-Sebaii and Al-Snani (2010) assessed mathematically the impact of selective coatings on SAC efficiency. They found that using nickel-tin coatings significantly improved thermal performance, achieving notably higher efficiency compared to traditional coatings. This suggests that selective coatings can greatly enhance solar heater effectiveness. Khanlari et al. (2022) conducted a comprehensive study on a vertical SAC featuring nano-enhanced absorber coating and perforated baffles. Their investigation demonstrated that the heater with the nano-embedded black paint achieved a thermal efficiency ranging from 58.1% to 76.2% and an exergy efficiency increase of 9.2% to 10.5% over the uncoated system, highlighting the significant performance enhancements provided by the nano-coating.
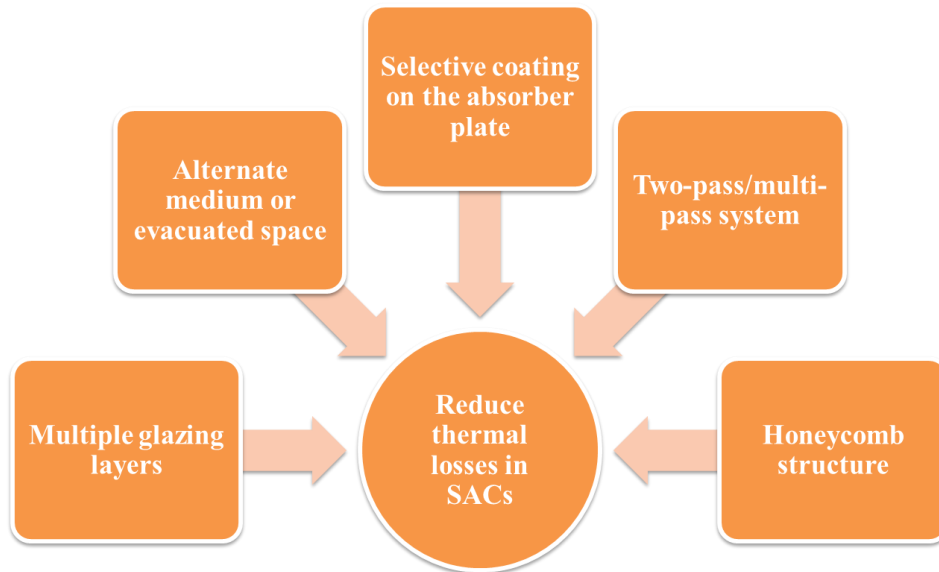
Fig. 2.7. Methods to reduce thermal losses in SACs

Mohammed et al. (2024) evaluated the efficiency of SACs with various absorber plate designs in a solar dryer setup. Model-4, featuring horizontal fins with a 15% Si coating on the solar air heater, showed the best performance. This model enhanced drying efficiency by 65% over the base model, significantly reducing drying time and increasing outlet air temperature. The Si coating on the solar air heater improved energy absorbing and reduced thermal losses, leading to enhanced overall dryer performance. Abdelkader et al. (2020) evaluated a SAC enhanced with a novel coating of carbon nanotubes and cupric oxide nanoparticles. This study aimed to improve the collector energy capture and efficiency. They found that the new coating increased the energy efficiency by about 24.4% and improved exergy efficiency, especially at higher airflow rates, indicating better thermal energy conversion than conventional coatings.

2.2.4. Effect of using thermal energy storage

The variability in solar radiation intensity has prompted researchers to explore methods for maintaining consistent heating throughout the day, leading to the investigation of heat storage systems. Various materials have been examined by researchers for their effectiveness as heat storage media. These media can be composed of either sensible or latent thermal energy storage materials (STES, LTES).

Saxena et al. (2013) studied SAC performance improvement by incorporating granular carbon as a heat-absorbing medium. Testing various configurations under natural and forced convection, and with auxiliary power using a halogen tube, they found that the new setups performed better than conventional heaters, even at night or in poor weather conditions. Saxena et al. (2015) investigated a new SAC design incorporating a blend of desert sand with granular carbon. They found that the thermal efficiencies varied between 18% and 20.7% for natural convection, and between 52.2% and 80% for forced convection. Likewise, Sivarathinamoorthy and Sureshkannan (2021) used granular carbon in the performance of DPSAC, they reported that the collector with STES maintain higher outlet temperature than the standard collector at a MFR of 0.008 kg/s. Ismail et al. (2022) investigate lava rocks as STES incorporated to

DPSAC for drying purposes. They reported that the outlet temperature increased by 17.5% compared to traditional collector.

Kabeel et al. (2016a) conducted an experimental study on the performance of smooth and v-corrugated plate SACs, with and without phase change materials PCM as LTES. Their results demonstrated that the v-corrugated heater with PCM achieved a daily efficiency 12% greater than without PCM and surpassed the smooth collector by 15% and 21.3% with and without PCM, respectively, at an airflow rate of 0.062 kg/s. (Saxena et al., 2020a; 2020b) demonstrated that SAC incorporating a blend of granular carbon powder with paraffin wax exhibited superior performance compared to those without thermal storage and those with only paraffin wax. They reported a thermal efficiency of 79.1% for the SAC with the paraffin wax and granular carbon mixture, whereas the SAC with only paraffin wax achieved 57.41% and the SAC without thermal storage attained approximately 50%. Arfaoui et al. (2017) investigated the efficiency of a SAC with LTES using PCM encapsulated in spherical capsules. They found that the system achieved a daily energy efficiency of 47%, maintaining a constant outlet temperature of approximately 27 °C during night-time.

In their study, Ghiami (2018) investigated SAC performance with latent storage using three absorber plate designs: non-baffled, sequenced-array baffled, and staggered-array baffled. The sequenced-array baffled plate had the highest energy efficiency at 26.7% with a MFR of 0.017 kg/s, outperforming the other designs. The staggered-array baffled plate achieved a peak exergy efficiency of 20.4%. The study highlighted the impact of baffle configurations and MFRS on improving SAC efficiency. Sudhakar and Cheralathan (2019) compared SACs with and without PCM using three absorber plates: traditional flat, flat with PCM, and inclined with PCM. The results showed outlet temperatures ranged from 45 °C to 55 °C, suitable for solar drying. Efficiency was 31% for the conventional plate, 39% for the flat plate with PCM, and 43% for the inclined plate with PCM, the highest efficiency. Assadeg et al. (2021) analysed a DPSAC having fins and PCM using MATLAB. They tested four configurations: fins and PCM, PCM alone, fins alone, and flat without PCM or fins. The fins and PCM setup performed best, achieving 73% thermal efficiency at 0.15 kg/s airflow and 2.5% to 4.2% exergy efficiency at 1 kW/m² solar irradiance.

Several studies conducted on latent heat storage materials including numerical (Satyender Singh and Negi, 2020) and empirical (Chen et al., 2020; Kabeel et al., 2017; Singh et al., 2021; Zhang et al., 2021), reported that using TES enhanced the performance of SAC increasing efficiency.

2.3. Applications of solar air collectors

The broad use of SACs is due to their low fabrication costs, high efficiency, and minimal operational and installation expenses. These factors make them suitable for a variety of applications. Some applications of SACs presented in Fig. 2.8 (Kumar et al. 2021). For the purpose of this thesis, the primary focus will be on the drying applications in a specific type of solar dryer.
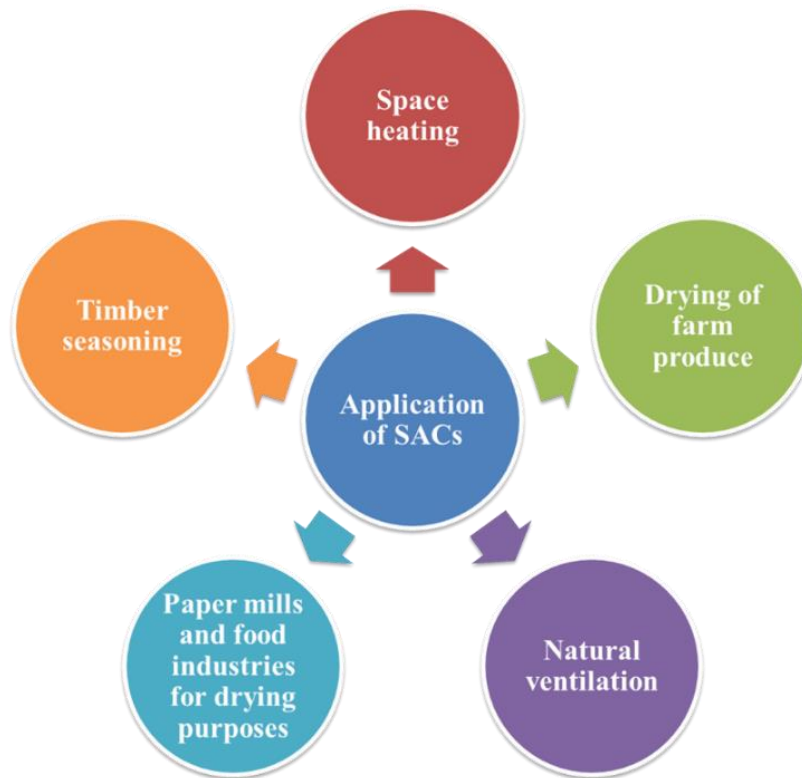
Fig. 2.8. Some applications of SACs (Hegde et al., 2023)

2.3.1. Products drying

The expansion of solar energy in agriculture is driven by rising fuel prices and environmental awareness. A key application of solar energy is drying, which removes moisture from products to extend storage life and reduce post-harvest losses. Historical evidence shows solar drying has been practiced in the Middle East since 12,000 BCE, initially using natural methods like sunlight, heat, wind, and smoke, primarily for food. Over time, especially post-industrial revolution, drying technologies evolved from natural methods to fossil-fuel-based, energy-intensive systems such as hot air drying. These systems, which rely on direct or indirect combustion of fuels like coal, diesel, and natural gas, provide controlled drying conditions but contribute to high energy consumption, waste heat, and greenhouse gas emissions. Consequently, research has increasingly focused on reducing drying temperatures and transitioning toward renewable-based drying technologies (Acar et al., 2020).

The rising global population has increased food demand, leading to shortages. Reducing food losses at all stages of production is essential to address this issue. In developing countries, losses of 10-40% are common due to poor storage and transportation. Drying is a key solution, preserving food by removing moisture and extending shelf life. While traditional sun drying has issues like contamination and spoilage, improving these techniques can significantly reduce food losses and help meet demand (Murthy, 2009; Esper and Mühlbauer, 1998).

2.3.1.1. Principle of dryers

The primary function of dryers is to reduce the moisture content of products, thereby stabilizing them and extending their shelf life. This process occurs in three stages, as shown in Fig. 2.9.

Initially, during the initial period, the product reaches thermal equilibrium within the drying chamber. It then undergoes the constant rate period, where external moisture is removed steadily, influenced primarily by drying conditions such as air temperature, velocity, and relative humidity. When the critical moisture content is achieved, the process transitions to the falling rate period. At this stage, drying relies on diffusion instead of external conditions, with the product's internal characteristics, such as size and structure, becoming crucial factors (Belessiotis and Delyannis, 2011; Can, 2000; Lamidi et al., 2019).
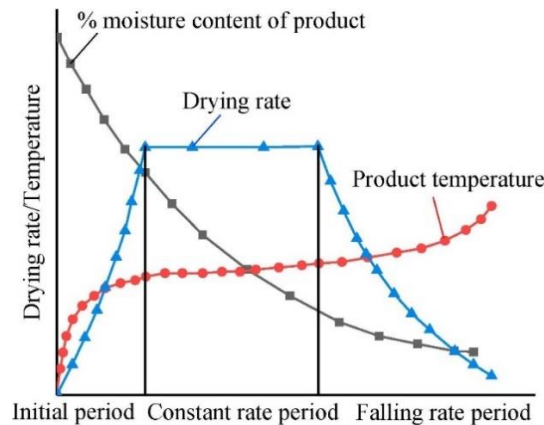

Fig. 2.9. Product drying curve (Lamidi et al., 2019)

2.3.1.2. Parameters influencing the solar drying process

Several parameters critically affect the efficiency of solar dryers. These include the type of material, its loading and pre-treatment, the temperature within the dryer, the drying air velocity, and the relative humidity. The product type is crucial, as heat-sensitive materials should not be dried at high temperatures to preserve taste and colour. Moreover, the volume of material also significantly impacts drying characteristics; larger volumes require more air, and if the dryer cannot provide sufficient airflow and drying time, product quality may suffer (Kapadiya and Desai, 2014).

In addition to the above, pre-treatment of samples plays a vital role. Pre-treating samples before drying enhances the drying rate and reduces drying time, leading to lower energy consumption and higher product quality (Hedayatizadeh and Chaji, 2016). Another critical parameter is the temperature within the dryer. Temperature affects both the drying rate and the final properties of a sample. Higher temperatures are necessary for materials with high initial moisture content to shorten drying duration. However, for low moisture content, temperature has minimal effect as only a small amount of heat is required (Lingayat et al., 2017). Airflow rate is also critical. Higher airflow rates reduce heat loss but may not allow sufficient time for moisture evaporation, decreasing efficiency. Conversely, inadequate airflow raises dryer temperature and slows moisture extraction. Relative humidity significantly impacts solar dryer performance. High humidity requires more energy as saturated air cannot absorb moisture, leading to a slow drying rate. Conversely, dry air absorbs moisture more efficiently, resulting in shorter drying times (El Hage et al., 2018).

2.3.1.3. Types of solar dryers

Solar dryers are designed in various sizes and configurations to suit different applications and farmers' needs. They are classified by working temperature into high and low-temperature dryers, by air movement system, air flow direction, type of material to be dried, insulating material used, and the extent of solar energy utilization (Chauhan and Rathod, 2020; P. Kumar and Singh, 2020; Suherman et al., 2024; Toshniwal and Karale, 2013). Furthermore, solar dryers can be classified according to their heating techniques or operational configurations. The main types include direct, indirect, mixed-mode, greenhouse, hybrid, and those equipped with energy storage systems (Fig. 2.10) (El-mesery et al., 2022).
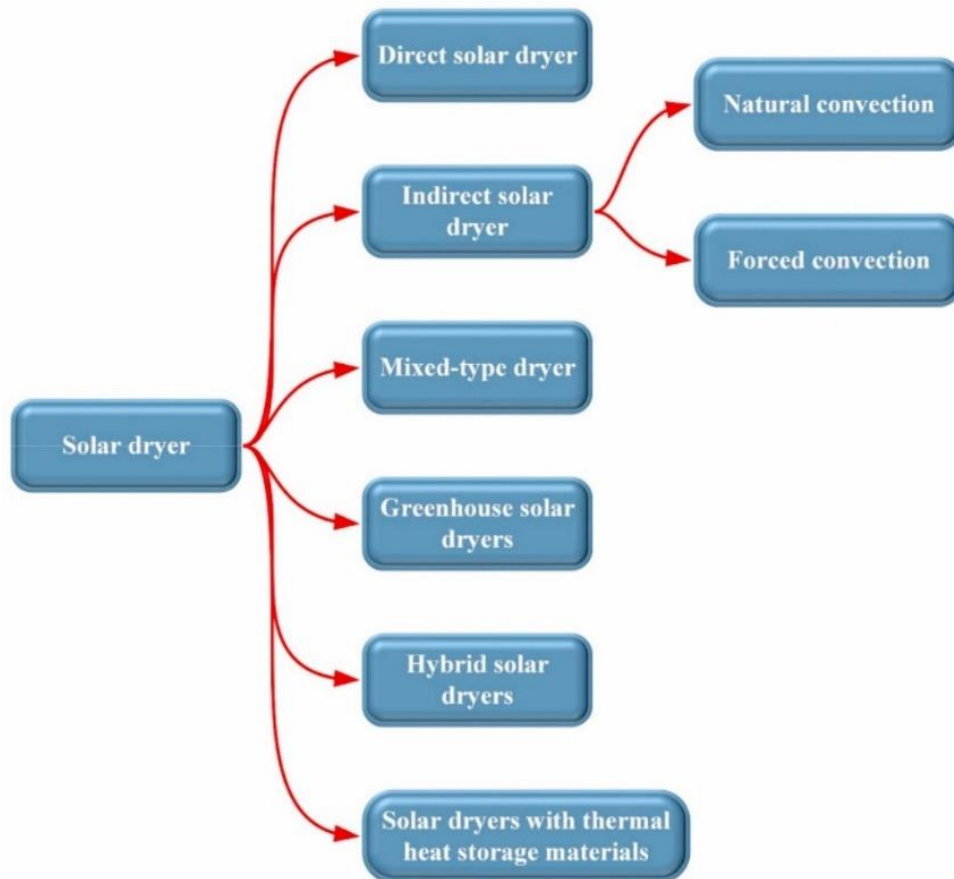

Fig. 2.10. Classification of solar dryers (El-mesery et al. 2022)

Indirect solar drying represents an advanced technology that enhances the efficiency of solar radiation utilization compared to traditional direct exposure methods. It provides faster drying and offers better control over dryer temperature and solid loading. This method uses a solar collector to heat ambient air, which is then directed into a drying chamber containing the products (Akamphon et al., 2018). The heated air removes moisture from the products and exits through a chimney. Indirect solar dryers can be categorized into active and passive systems; active dryers use fans powered by electricity to circulate air, while passive dryers rely on natural convection (Lingayat et al., 2020; Mohana et al., 2020). As previously noted, solar dryers come in various types and modes. However, to meet the objectives of this thesis, we will focus exclusively on indirect solar dryers operating in forced convection mode.

Romano et al. (2009) analysed the energy and environmental parameters of a modular solar cabinet dryer for apple and carrot slices and cubes. They found that drying efficiency was highly dependent on weather conditions, with apples requiring 3300.1 kJ/kg and carrots 7428.2 kJ/kg to remove moisture. The dryer effectively reduced moisture without significantly altering sensory properties. Gupta et al. (2012) investigated the drying efficiency of tomatoes using an indirect solar dryer in both natural and forced convection modes. The apparatus, featuring a SAC and a three-tray drying chamber, operated at average temperatures of 45 °C for natural convection and 40 °C for forced convection. The respective MFR were 0.00653 kg/s and 0.014 kg/s. The drying chamber achieved an overall efficiency of 17%, while the collector's efficiency was 30%. Vijayan et al. (2016) designed an indirect active solar dryer incorporating sensible heat storage, effectively reducing the moisture content of bitter gourd from 92% to 9% in 7 hours, compared to 10 hours with open sun drying. The system, which utilized pebble-based thermal storage, demonstrated solar collector and drying efficiencies of 22% and 19%, respectively, and was recommended for its consistency and higher product quality.

Khadraoui et al. (2017) developed and tested an indirect solar dryer incorporating PCM to store heat for night-time use. The system exhibited a daily energy efficiency of 33.9% and successfully kept the chamber of drying temperature ranged from 4 to 16 °C above the inlet temperature during the night. Abubakar et al. (2018) found that integrating thermal energy storage in solar dryers improved drying efficiency by 13% compared to systems without thermal storage.

2.4. Summary of literature review

Solar energy stands out as the most promising and sustainable energy source. Among its various applications, SACs have gained popularity due to their potential for providing effective thermal energy solutions. This chapter identifies and analyses the core components and functional mechanisms of SACs, focusing on their structure, classifications, enhancement techniques, and applications.

A comprehensive assessment of scientific research on SACs is presented, reviewing recent advancements in SAC technologies. Several studies have concentrated on enhancing design and material selection to increase efficiency. Key development areas include optimizing absorber plate design and airflow management. Innovations such as turbulators and modified absorber surfaces have shown potential for improving heat transfer by disrupting the boundary layer near the absorber surface. However, these modifications pose the challenge of balancing effective heat transfer with minimal pressure loss.

Among the reviewed studies, and to the best of our knowledge, no study has examined V-angled fins in both continuous and discrete arrangements and various orientations within DPSACs or SPSACs. The study investigates how using V-angled perforated fins can increase the surface area for heat transfer and create more turbulent airflow, which together can improve the overall heat transfer efficiency in DPSACs. Additionally, this research experimentally investigates the influence of different fin configurations on the drying process, assessing their role in optimizing heat transfer and moisture removal. While theoretical considerations suggest

promising outcomes, empirical data is necessary to quantify the precise influence of these fins on the overall thermal performance of DPSACs.

The role of air entry conditions in SACs is crucial but has not been thoroughly investigated. The way air is introduced into the collector significantly influences its thermal efficiency and overall heat production. This work examines the effects of entrance flue conditions on SAC performance.

The current literature reveals a limited number of studies on the impact of air pass depth on the performance of SACs. This research addresses this gap through both numerical simulations and outdoor experimental approaches to examine its effect on SAC performance.

Furthermore, the effect of selective coatings on outlet and absorber plate temperatures under real outdoor conditions has not been extensively investigated. Selective coatings are essential for enhancing thermal efficiency by reducing radiative heat losses and increasing solar absorption. These coatings may behave differently under various outdoor conditions, impacting critical performance parameters. This dissertation presents a comparative analysis of SACs with and without selective coatings under real-world conditions to provide a more precise assessment of their practical benefits. By systematically analysing these differences, we aim to offer a clearer understanding of the coatings' effectiveness and practical implications for SAC performance.

Through these investigations, it is advanced the development of more effective and efficient SACs, improving both the theoretical understanding and practical implementation of SAC technologies, particularly in drying applications.

3. MATERIALS AND METHODS

This chapter presents a detailed account of the materials, techniques, and equipment employed in the experimental procedures, as well as the scientific methods adopted to fulfil the thesis objectives. It includes a thorough explanation of the experimental design, data acquisition processes, and the graphical analyses conducted.

3.1. Study location

The experimental research for this dissertation was conducted at the Solar Energy Laboratory of the Hungarian University of Agriculture and Life Sciences (MATE) in Gödöllő, Hungary. The experimental setup is located at 47° 35′ 39″ N latitude and 19° 21′ 59″ E longitude, as shown in Fig. 3.1. Hungary experiences a substantial amount of sunshine annually, with the total annual global horizontal solar radiation amounting to 1280 kWh/m², indicating good potential for solar energy utilization (Atsu et al., 2021). The experiments took place on sunny, mostly clear days during the periods from May to September in 2022, 2023, and 2024. Summers in Gödöllő are warm to relative hot, providing optimal conditions for solar energy research, while the spring and autumn months are mild with moderate rainfall. Overall, the weather during these months is favourable for outdoor experiments.
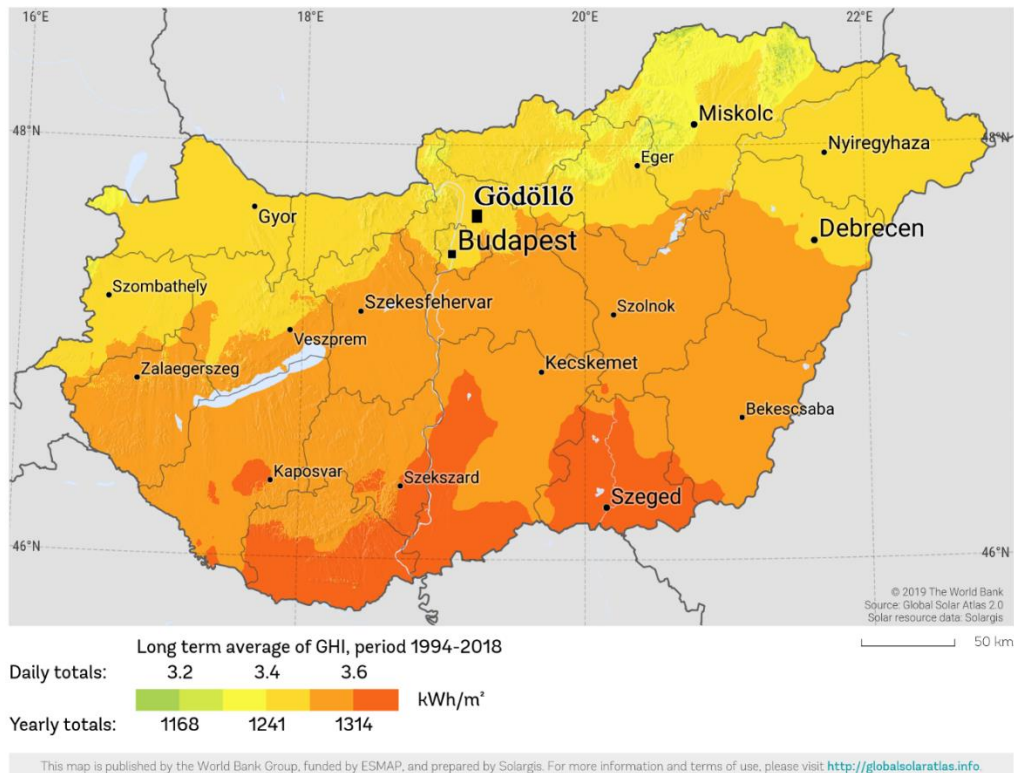

Fig. 3.1. Location of the solar energy laboratory at MATE

A general rule for optimizing solar energy capture throughout the year is to set the tilt angle of a solar collector equal to the latitude of the installation site, with a slight variation of ±10-15°. This adjustment allows for fine-tuning the system to account for seasonal variations in solar radiation. The collector should always face the equator due south in the northern hemisphere

and due north in the southern hemisphere to maximize solar exposure (Soteris Kalogirou, 2009). For that, the tested rigs are maintained at a 45° tilt angle, facing due south.

3.2. Description of the tested rigs

To achieve the objectives of this thesis, four SACs were constructed using locally available materials. Each collector was uniquely modified to meet specific research goals, which will be detailed in the following sections. Generally, SAC consists of a wooden frame insulated with appropriate materials, a transparent cover that allows sunlight to pass through, and a heat-absorbing surface that captures solar energy. Additionally, two drying chambers were fabricated. The details of the design and manufacturing processes for both the SACs and drying chambers will be outlined in the subsequent sections.

3.2.1. *Fabrication of single-pass collectors*

Two SPSACs with forced convection were constructed using namely wood, copper, and plastic. Each collector had a wooden frame measuring 125 cm length, 50 cm width, 13 cm height, and 2 cm in thickness. On the rear side of each collector, two wooden covers with a thickness of 4 mm were fixed on squared wood strips with a thickness of 2 cm. Expand polystyrene sheets (EPS) with thicknesses of 2 cm and 3 cm were inserted between the wooden covers and the absorber, respectively, to construct the insulated bottom side of the collectors. Fig. 3.2 showing the construction materials of the SACs. Each collector utilized a smooth copper plate measuring 121 cm length, 46 cm width, and 1.2 mm thickness as an absorber coated with black matt paint (see Fig. 3.3). Moreover, a transparent plastic sheet with superior light transmittance qualities was utilized to encase the top surface of the collectors, ensuring that solar radiation could effectively reach the absorbing surface (see Fig. 3.4). The spacing between the absorber and the transparent cover was set at 55 mm, defining the air passage of the collector. Fig. 3.5 illustrates the fabrication process of the tested rigs.
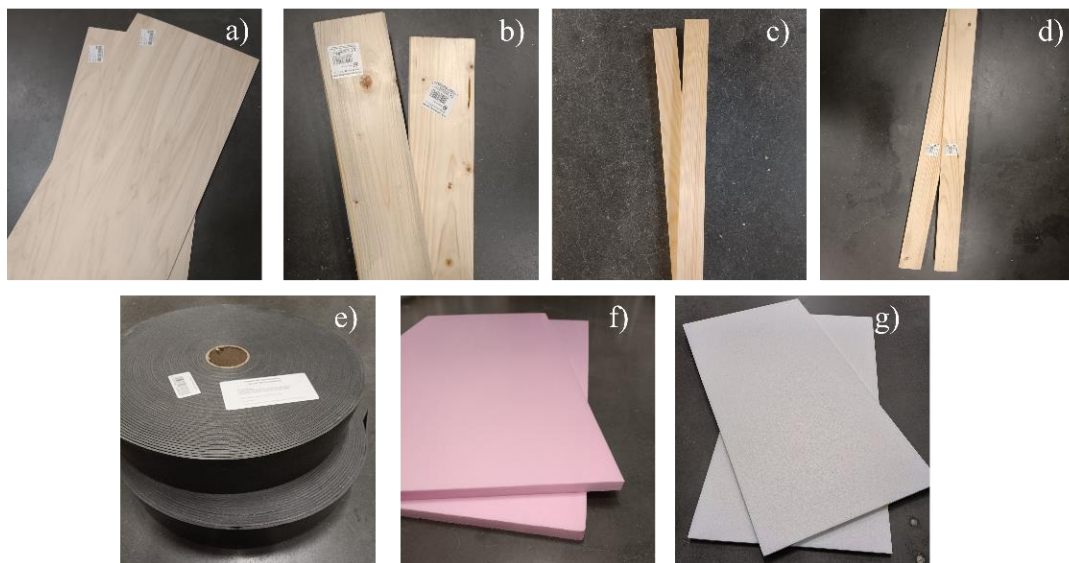

Fig. 3.2. SACs construction materials: a) wood covers, b) sidewalls, c) buffers and support, d) entrance side walls, e) adhesive insulation, f) XPS polystyrene sheet, g) EPS polystyrene sheets

Fig. 3.3. Copper absorber plate   Fig. 3.4. Transparent plastic cover

Fig. 3.5. Fabrication process of SPSAC

3.2.2. *Fabrication of double pass collectors*

The DPSACs were fabricated using the same materials as outlined in the previous section for the single-pass collectors. The key distinction between the two designs lies in the addition of a second air passage in the double-pass configuration.

Two DPSACs were fabricated, each had an outer wooden frame, which also served as the collector's walls, measuring 125 cm in length, 50 cm in width, 13 cm in height, and 2 cm in thickness. Initially, both collectors were equipped with smooth copper absorber plates (121 cm × 46 cm × 1.2 mm) coated with black matte for optimal heat absorption. Later, different absorber configurations were used to meet specific objectives, which will be detailed in the

following sections. A transparent plastic sheet was used to cover the collectors, allowing maximum solar radiation to reach the absorber. The first airflow path included a 5.5 cm air passage between the absorber plate and the transparent cover. Beneath the absorber plate, a second air passage of 35 mm was established. Six wooden buffers were strategically positioned to guide the airflow, enhancing distribution in the lower air passage. The detailed design and configuration of the two double-pass collectors are depicted in Fig. 3.6.

Fig. 3.6. Fabrication process of DPSAC

3.2.3. Drying chamber

The drying chambers are constructed from extruded polystyrene insulation (XPS) sheets, known for their excellent thermal insulation properties and ease of fabrication. Two identical rectangular chambers were built, each with a wall thickness of 0.05 m. The internal dimensions of both chambers are 52 cm in depth, 47 cm in width, and 1.0 m in height. Inside, each chamber contains three drying trays, measuring 51 cm by 46 cm and made of plastic netting, securely mounted to facilitate the drying process. All components are assembled using high-quality adhesive materials to ensure durability and structural stability.

The trays are designed to slide, allowing for easy removal during the loading and unloading of products. The chamber's sides are opaque, except for the front, which features a transparent cover. The roof is inclined, creating a tent-like structure to enhance airflow within the chamber. Air enters through an inlet on the front, located below the door, and exits through an outlet on the roof.

The drying chamber is connected to SAC via a 100 mm piping system, which is insulated with polyfoam material. Fig. 3.7 provides an illustration of the drying chamber's fabrication process.
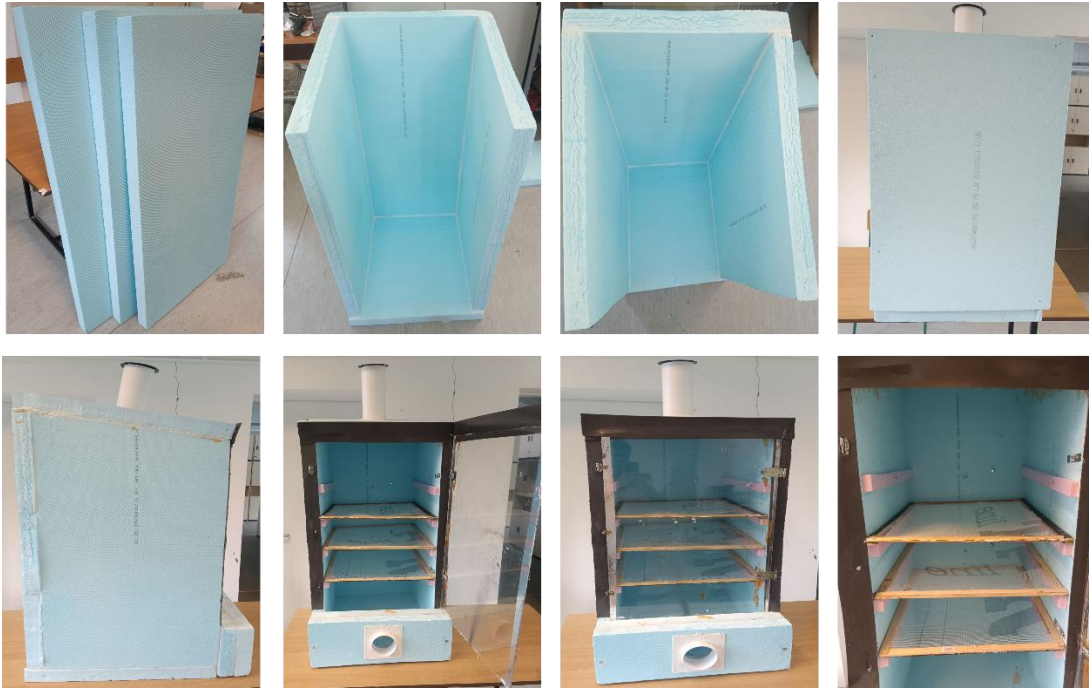
Fig. 3.7. Fabrication of the drying chamber

3.3. Measurement instruments

Accurate and reliable measurement instruments are essential for assessing the performance of the solar air collectors in this study. A range of high-precision tools were employed to monitor key parameters such as temperature, solar radiation, relative humidity, and air mass flow rate. These instruments were selected based on their ability to provide precise and consistent data, ensuring the validity of the experimental results. The following subsections describe the specific measurement instruments used and the processes followed to capture each parameter.

3.3.1. Temperature

Temperature measurement is a critical component in evaluating the performance of SACs. T-type thermocouples were utilised with a class 1 tolerance rating for their high accuracy and reliability, the thermocouple placement and measurement process are listed as follows:

- **Absorber plate measurements:** The DPSACs and SPSACs were equipped with 6 and 10 thermocouples, respectively. These thermocouples were strategically positioned across the absorber plate to accurately capture the temperature distribution and profile.

- **Outlet temperature measurements**: At the outlet, four thermocouples were placed in the circular duct, located at the centre of an equal cross-sectional area, 15 cm away from the exit port. This setup aims to minimize temperature variations, targeting a difference of less than 0.5 °C.

- **Inlet temperature measurements**: Similarly, for the inlet temperatures, four thermocouples were affixed in each collector, placed 15 cm away from the inlet port to accurately capture the temperature of the incoming air.

- **Ambient temperature measurements:** To measure the ambient temperatures, two thermocouples were employed, with their readings averaged for improved accuracy.

- **Drying chamber temperature measurement:** The temperature inside the drying chamber was measured using five thermocouples. One thermocouple was placed on each tray, with additional sensors positioned at the inlet and the outlet to monitor the air temperature entering and exiting the chamber.

All thermocouples underwent precise welding and calibration procedures to ensure accurate and consistent data acquisition. Data acquisition and recording were carried out using Advantech ADAM-4000 series data acquisition modules, which are detailed in the subsections below.

3.3.2. Solar radiation

Solar radiation measurements were conducted employing a precisely calibrated pyranometer manufactured by Kipp & Zonen, specifically the CM11 model, known for its high precision. The recorded solar radiation data were efficiently captured and logged using an Advantech ADAM-4017 analogue input module.

3.3.3. Airflow measurement

The determination of airflow rate was accomplished through the utilization of an orifice plate meter, grounded in the principles of Bernoulli. The airflow rate was deduced based on the pressure difference across the orifice plate, measured using a SENSIRON SDP-816 analogue differential pressure sensor. The data captured by these sensors were systematically recorded and processed using the Advantech ADAM-4017 analog input module.

3.3.4. Humidity measurement

Air humidity was measured using 11 Honeywell HIH-4000-004 relative humidity sensors. The sensors were positioned as follows:

- One sensor to measure ambient relative humidity.
- One sensor at the inlet and another at the outlet of each dryer.
- One sensor placed above each tray in each dryer.

3.3.5. Data logging system

The data logging system utilized high-accuracy Advantech ADAM-4000 series data acquisition modules, each with 8 input channels. Different models were employed and assembled in a box, as illustrated in Fig. 3.8, which shows the data logging system used during the experiment. The specific models are detailed below:

3.3.5.1. Temperature data modules
To ensure precise recording of temperature data from the SACs, the following ADAM modules were used:

- Three ADAM-4018+, 8-ch thermocouple input modules
- One ADAM-4019+, 8-ch universal analogue input module

3.3.5.2. Analogue voltage modules

Two ADAM-4017, 8-ch analogue input modules, providing a total of 16 channels, were used to record data from the differential pressure sensors, solar radiation sensors, and humidity sensors in the drying chambers.

3.3.5.3. RS-232 to RS-422/485 converter/repeater

The ADAM-4520 module was used to convert data transmitted via RS-485 from the ADAM data acquisition modules into RS-232 format, enabling efficient data transfer over a short distance to the PC.

The accuracy, range, and graphical representation of all sensors and data acquisition modules are presented in Table 3.1.
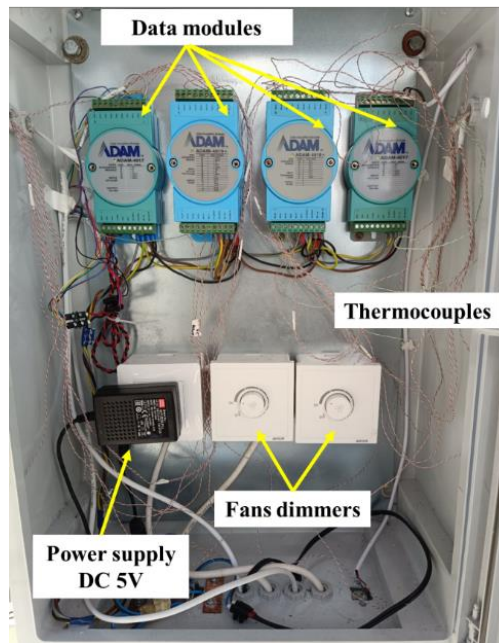
Fig. 3.8. Photograph of the data logging system

Table 3.1. Specifications and accuracy of measurement instruments

No	Instrument	Model	Range	Accuracy	Function
1	Temperature Thermocouples	T-type	-250 to 250 °C	±0.5 °C	
2	Relative Humidity Sensor	Honeywell HIH-4000-004	0 to 100%	±3.5%	

3	Differential pressure sensor	SENSIRION SDP-816	-500 to 500 Pa	±3%	
4	Solar Radiation Pyranometer	Kipp & Zonen CM11	0 to 1400 W/m²	<0.6%	
5	Data Logger (Temperature)	Advantech ADAM 4018+	-100 to 400 °C	±0.1%	
6	Data Logger (Temperature)	Advantech ADAM 4019+	-100 to 400 °C	±0.1%	
7	Data Logger (Pressure, Humidity, Radiation)	Advantech ADAM-4017	0 to 10 V	±0.1%	
8	RS-232 to RS-422/485 converter/repeater	Advantech ADAM-4520	Transmission speed up to 115.2 Kbps	–	

3.4. Theoretical analysis of the collectors

The theoretical approach to the thermal analysis of a SAC can be presented with making necessary assumptions which important for simplifying the model. The assumptions can be presented as fellow (Ong, 1995):

- Steady-state and one-dimensional heat transfer.
- The heat transferred to the air is uniform along the length of the collector.
- Ambient wind speed assumed to be constant.

- The airflow is uniformly distributed throughout the collector, and the air temperature changes in a linear manner along the collection.
- The edge losses are negligible, as it well isolated.

3.4.1. Single pass collector analysis

The heat transfer coefficient and the thermal resistance network are illustrated in Fig. 3.9. The heat balance equations are determined at various points: T_1 represents the temperature of the glass cover, T_{f1}, is the mean air temperature, and T_2 denotes the temperature of the absorber plate. The equations are as follows:

$$T_1: I \; \alpha_g + h_{r21}(T_2 - T_1) + h_1(T_{f1} - T_1) = U_t(T_1 - T_a), \tag{3.1}$$

$$T_{f1}: h_2(T_2 - T_{f1}) = h_1(T_{f1} - T_1) + Q_{u1}, \tag{3.2}$$

$$T_2: I \; \alpha_p \tau_g = h_2(T_2 - T_{f1}) + h_{r21}(T_2 - T_1) + U_b(T_2 - T_a). \tag{3.3}$$
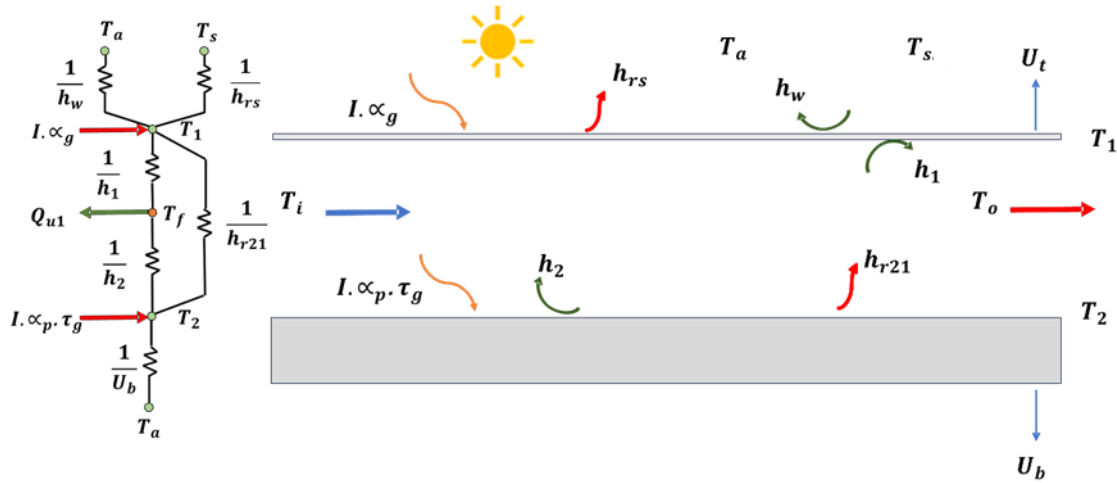

Fig. 3.9. Schematic representation of the thermal network in SPSAC

The temperature distribution along the airflow direction is represented as follows: At a distance y from the inlet, the air temperature is assumed to be T_f. Assuming uniform temperature distribution across the section, the mean air temperature is calculated to be $(T_f + (dT_f/dy)\,\Delta y)$ at $(y+\Delta y)$ (see Fig. 3.10). The heat balance equation for this element is detailed in Eq. 3.4 as described by (Ong, 1995).
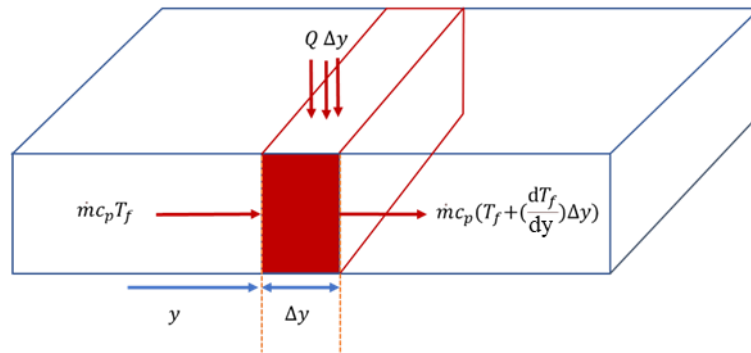

Fig. 3.10. Energy balance of an element in the flow path

$$\dot{m}c_p T_f + QW\Delta y = \dot{m}c_p(T_f + (\frac{dT_f}{dy})\Delta y). \tag{3.4}$$

After simplification through division by Δy, and assuming that the useful heat is uniformly distributed along the length L of the collector channel, integrating the previously described equation results in the mean air temperature at the outlet, as expressed in Eq. 3.5.

$$T_{fo} - T_{fi} = \frac{QWL}{\dot{m}c_p},$$ (3.5)

In the case of collectors shorter than 10 meters, both theoretical and experimental studies, such as those conducted by Fudholi et al. (2013) and Ong (1995) assumed a scenario with a uniformly distributed wall temperature and a linear variation in airflow temperature along the collector. The mean air temperature is given as the arithmetic mean, as indicated in Eq. 3.6:

$$T_f = (T_{fo} + T_{fi})/2.$$ (3.6)

The useful heat gained can be written in terms of the mean air and inlet temperatures as Eq. (3.7):

$$Q_u = 2\,\dot{m}c_p/WL(T_f - T_{fi}).$$ (3.7)

After substituting Eq. (3.7) in Eq. (3.2) and doing some arrangement to the Eq. (3.1) − Eq. (3.3) with considering $\lambda = \frac{2\,\dot{m}c_p}{WL}$, $S_1 = I.\alpha_g$, and $S_2 = I.\alpha_p.\tau_g$ we will get the flowing:

$$(h_1 + h_{r21} + U_t)T_1 - h_1T_{f1} - h_{r21}T_2 = S_1 + U_tT_a,$$ (3.8)

$$h_1T_1 - (h_1 + h_2 + \lambda)T_{f1} + h_2T_2 = -\lambda T_{f1i},$$ (3.9)

$$-h_{r21}T_1 - h_2T_{f1} + (h_2 + h_{r21} + U_b)T_2 = S_2 + U_bT_a.$$ (3.10)

The system of equations can be represented in matrix form as [A] [T] = [B], where the matrix [A] contains the coefficients, and [T] represents the vector of unknown temperatures: T_1, T_{fi}, and T_2. For find the mean temperature vector, the matrix inversion method is used, resulting in $[T] = [A]^{-1} [B]$. The specific system of equations for the heat transfer problem is shown below:

$$\begin{bmatrix} (h_1 + h_{r21} + U_t) & -h_1 & -h_{r21} \\ h_1 & -(h_1 + h_2 + \lambda) & h_2 \\ -h_{r21} & -h_2 & (h_2 + h_{r21} + U_b) \end{bmatrix} \begin{bmatrix} T_1 \\ T_{f1} \\ T_2 \end{bmatrix} = \begin{bmatrix} S_1 + U_tT_a \\ -\lambda T_{f1i} \\ S_2 + U_bT_a \end{bmatrix}.$$ (3.11)

The calculations for the radiative and convective heat transfer coefficients will be explained at the end of this section, following the thermal analysis of the DPSAC, as both processes use the same correlations.

3.4.2. Double pass collector analysis

This section focuses on the analysis of the DPSAC, in line with the thesis objectives. The analysis is divided into two subsections: the first examines the smooth double-pass collector, while the second explores the performance of the finned double-pass collector.

3.4.2.1. Smooth double pass collector analysis

This subsection analyses the thermal and fluid dynamics of the smooth DPSAC. The current configuration lacks surface modifications, such as fins, allowing for performance assessment based solely on airflow and heat transfer through a simple channel design. In this context, the temperatures of the glazing cover, air in the first pass, absorbing plate, air in the second pass, and insulation are denoted as T_1, T_{f1}, T_2, T_{f2}, and T_3, respectively. Heat balance equations for each temperature point with assumptions critical for model simplification are derived as

documented by (Fudholi et al., 2011; Naphon, 2005; Ong, 1995). Energy balance equations for DPSAC without fins, as outlined by the thermal network in Fig. 3.11, are introduced as follows:
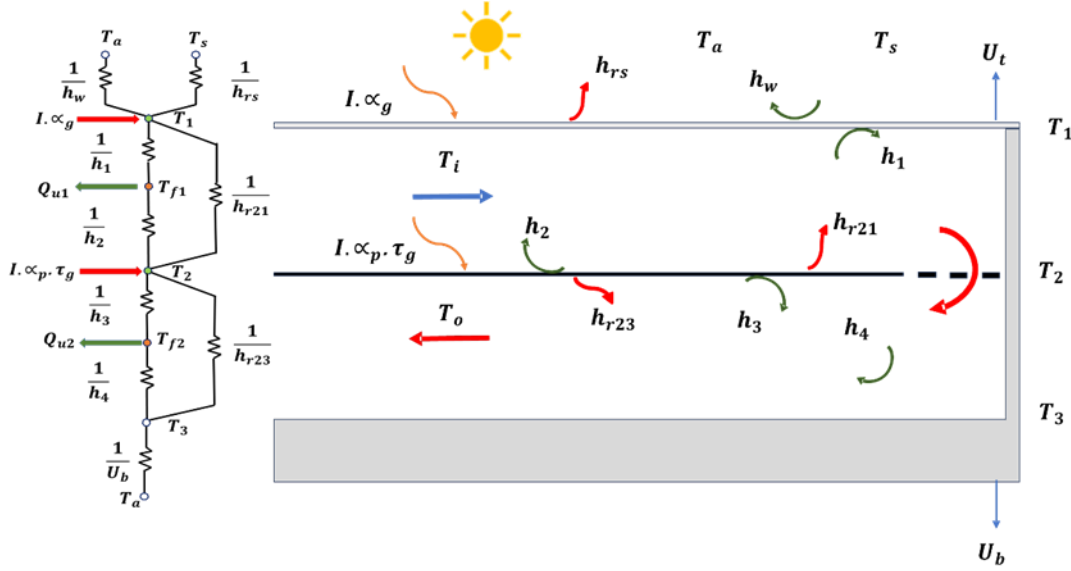

Fig. 3.11. Schematic representation of the thermal network in smooth DPSAC

Glass cover energy balance at T_1:

$$I \; \alpha_g + h_{r21}(T_2 - T_1) + h_1(T_{f1} - T_1) = U_t(T_1 - T_a). \tag{3.12}$$

For the flowing air at the first pass at T_{f1} is:

$$h_2(T_2 - T_{f1}) = h_1(T_{f1} - T_1) + Q_{u1}. \tag{3.13}$$

For the absorber plate at T_2:

$$I \; \alpha_p \tau_g = h_2(T_2 - T_{f1}) + h_3(T_2 - T_{f2}) + h_{r21}(T_2 - T_1) + h_{r23}(T_2 - T_3). \tag{3.14}$$

For the flowing air at the second pass at T_{f2}:

$$h_3(T_2 - T_{f2}) = h_4(T_{f2} - T_3) + Q_{u2}. \tag{3.15}$$

For the bottom insulation surface at T_3:

$$h_4(T_{f2} - T_3) + h_{r23}(T_2 - T_3) = U_b(T_3 - T_a). \tag{3.16}$$

In the equations Q_{u1}, Q_{u2} represent the useful heat from the first and second passes, respectively. These variables reach their final form after simplification and integration, as previously mentioned in the analysis of the SPSAC:

$$Q_{u1} = 2 \, \dot{m} c_p (T_{f1} - T_{f1i}))/WL, \tag{3.17}$$

$$Q_{u2} = 2 \, \dot{m} c_p (T_{f2} - T_{f2i})/WL, \tag{3.18}$$

$$T_{f1} = (T_{f1o} + T_{f1i})/2, \tag{3.19}$$

$$T_{f2} = (T_{f2o} + T_{f1o})/2. \tag{3.20}$$

After performing the necessary simplifications and substitutions, as outlined in the previous section on the SPSAC, where $\lambda_1 = \frac{2 \, \dot{m} c_p}{W_1 L_1}$, $\lambda_2 = \frac{2 \, \dot{m} c_p}{W_2 L_2}$, $S_1 = I.\alpha_g$, and $S_2 = I.\alpha_p.\tau_g$ a system of five heat transfer equations is derived:

$$(h_1 + h_{r21} + U_t)T_1 - h_1 T_{f1} - h_{r21}T_2 = S_1 + U_t T_a, \tag{3.21}$$

$$h_1 T_1 - (h_1 + h_2 + \lambda_1)T_{f1} + h_2 T_2 = -\lambda_1 T_{f1i}, \tag{3.22}$$

$$-h_{r21}T_1 - h_2 T_{f1} + (h_2 + h_3 + h_{r21} + h_{r23})T_2 - h_3 T_{f2} - h_{r23}T_3 = S_2, \tag{3.23}$$

$$2\lambda_2 T_{f1} + h_3 T_2 - (h_3 + h_4 + \lambda_2)T_{f2} + h_4 T_3 = \lambda_2 T_{f1i}, \tag{3.24}$$

$$-h_{r23}T_2 - h_4 T_{f2} + (h_{r23} + U_b + h_4)T_3 = U_b T_a. \tag{3.25}$$

The above equations for the DPSAC can be expressed in the following 5×5 matrix form, where [A] is the matrix of coefficients, and [T] represents the vector of unknown temperatures: T_1, T_{f1}, T_2, T_{f2}, and T_3. The mean temperature vector is found using matrix inversion of $[T] = [A]^{-1}[B]$.

$$\begin{bmatrix} (h_1 + h_{r21} + U_t) & -h_1 & -h_{r21} & 0 & 0 \\ h_1 & -(h_1 + h_2 + \lambda_1) & h_2 & 0 & 0 \\ -h_{r21} & -h_2 & (h_2 + h_3 + h_{r21} + h_{r23}) & -h_3 & -h_{r23} \\ 0 & 2\lambda_2 & h_3 & -(h_3 + h_4 + \lambda_2) & h_4 \\ 0 & 0 & -h_{r23} & -h_4 & (h_{r23} + U_b + h_4) \end{bmatrix}$$

$$\times \begin{bmatrix} T_1 \\ T_{f1} \\ T_2 \\ T_{f2} \\ T_3 \end{bmatrix} = \begin{bmatrix} S_1 + U_t T_a \\ -\lambda_1 T_{f1i} \\ S_2 \\ \lambda_2 T_{f1i} \\ U_b T_a \end{bmatrix} \tag{3.26}$$

3.4.2.2. Finned double pass collector analysis

Fig. 3.12 presents the thermal network outlines the energy balance equations for a DPSAC utilizing fins, showcasing how the presence of fins modifies the system to improve heat transfer and energy efficiency. The equations are presented as follows:
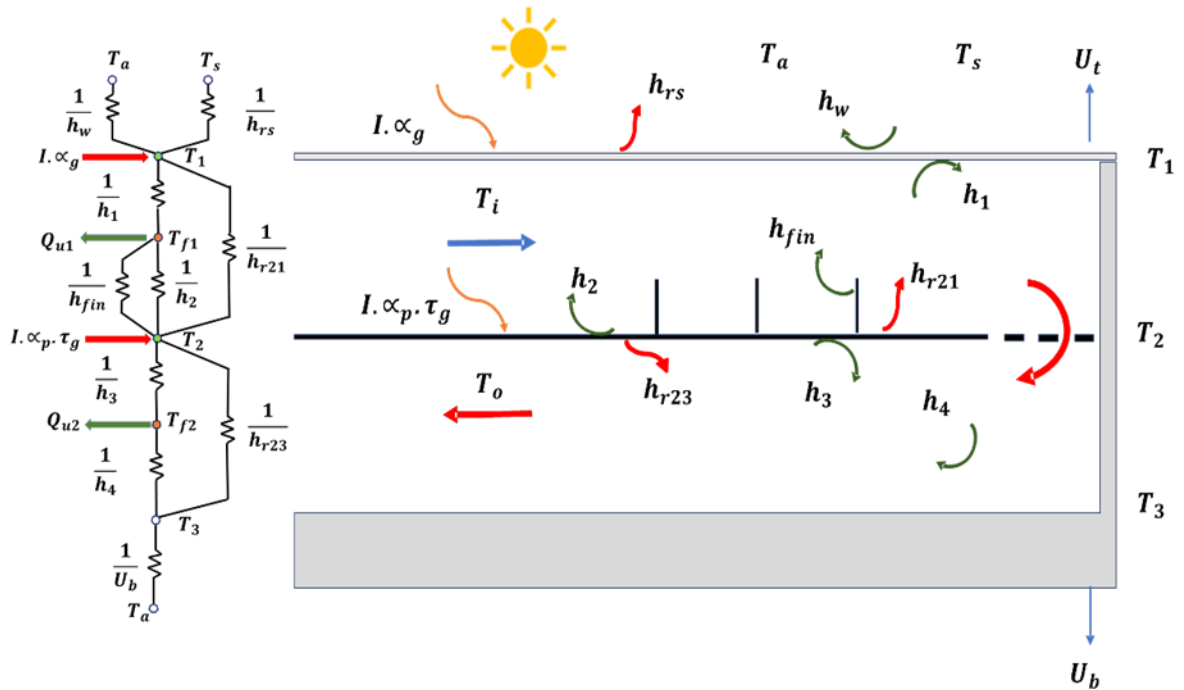

Fig. 3.12. Schematic representation of the thermal network in finned DPSAC

Glass cover energy balance at T_1:

$$I\ \alpha_g + h_{r21}(T_2 - T_1) + h_1(T_{f1} - T_1) = U_t(T_1 - T_a). \tag{3.27}$$

For the flowing air at the first pass at T_{f1} is:

$$h_2(T_2 - T_{f1}) = h_1(T_{f1} - T_1) + Q_{u1} + \frac{N}{A_{fin}} Q_n. \tag{3.28}$$

For the absorber plate at T_2:

$$I\ \alpha_p \tau_g = h_2(T_2 - T_{f1}) + h_3(T_2 - T_{f2}) + h_{r21}(T_2 - T_1) + h_{r23}(T_2 - T_3) + \frac{N}{A_{fin}} Q_n. \tag{3.29}$$

For the flowing air at the second pass at T_{f2}:

$$h_3(T_2 - T_{f2}) = h_4(T_{f2} - T_3) + Q_{u2}. \tag{3.30}$$

For the bottom insulation surface at T_3:

$$h_4(T_{f2} - T_3) + h_{r23}(T_2 - T_3) = U_b(T_3 - T_a). \tag{3.31}$$

As seen from the equation, the only difference is the inclusion of the fin effect in the upper pass. This effect is reflected in the equations for T_{f1} and T_2. The term Q_n represents the heat transfer rate from the fin:

$$Q_n = (2k_p A_{fin} l h_{fin})^{\frac{1}{2}}(T_2 - T_{f1})\tanh KH. \tag{3.32}$$

In this context, h_{fin} stands for the heat transfer coefficient, k_p denotes thermal conductivity of absorber plate, A_{fin} signifies fin area, H is the fin height and l indicates fin length. The value of K is determined through the following equation (Fudholi et al., 2011):

$$K = \left(\frac{2l h_{fin}}{k_p A_{fin}}\right)^{1/2}. \tag{3.33}$$

For simplifying the equation let $\psi = \tanh KH\ and\ \phi = (2k_p A_{fin} l h_{fin})^{1/2}$ then the heat transfer rate from the fin will be:

$$Q_n = \phi\psi(T_2 - T_{f1}). \tag{3.34}$$

Similarly, five equations can be derived and represented in matrix form. This matrix can then be solved to determine the unknown temperatures: T_1, T_{f1}, T_2, T_{f2}, and T_3.

$$(h_1 + h_{r21} + U_t)T_1 - h_1 T_{f1} - h_{r21}T_2 = S_1 + U_t T_a, \tag{3.35}$$

$$h_1 T_1 - \left(h_1 + h_2 + \lambda_1 + \frac{N}{A_{fin}}\phi\psi\right)T_{f1} + (h_2 + \frac{N}{A_{fin}}\phi\psi)T_2 = -\lambda_1 T_{f1i}, \tag{3.36}$$

$$-h_{r21}T_1 - (h_2 + \frac{N}{A_{fin}}\phi\psi)T_{f1} + \left(h_2 + h_3 + h_{r21} + h_{r23} + \frac{N}{A_{fin}}\phi\psi\right)T_2 - h_3 T_{f2} - h_{r23}T_3 = S_2 \tag{3.37}$$

$$2\lambda_2 T_{f1} + h_3 T_2 - (h_3 + h_4 + \lambda_2)T_{f2} + h_4 T_3 = \lambda_2 T_{f1i} \tag{3.38}$$

$$-h_{r23}T_2 - h_4 T_{f2} + (h_{r23} + U_b + h_4)T_3 = U_b T_a \tag{3.39}$$

$$\begin{bmatrix} (h_1 + h_{r21} + U_t) & -h_1 & -h_{r21} & 0 & 0 \\ h_1 & -\left(h_1 + h_2 + \lambda_1 + \dfrac{N}{A_{fin}}\phi\psi\right) & h_2 + \dfrac{N}{A_{fin}}\phi\psi & 0 & 0 \\ -h_{r21} & -(h_2 + \dfrac{N}{A_{fin}}\phi\psi) & (h_2 + h_3 + h_{r21} + h_{r23} + \dfrac{N}{A_{fin}}\phi\psi) & -h_3 & -h_{r23} \\ 0 & 2\lambda_2 & h_3 & -(h_3 + h_4 + \lambda_2) & h_4 \\ 0 & 0 & -h_{r23} & -h_4 & (h_{r23} + U_b + h_4) \end{bmatrix}$$

$$\times \begin{bmatrix} T_1 \\ T_{f1} \\ T_2 \\ T_{f2} \\ T_3 \end{bmatrix} = \begin{bmatrix} S_1 + U_t T_a \\ -\lambda_1 T_{f1i} \\ S_2 \\ \lambda_2 T_{f2i} \\ U_b T_a \end{bmatrix} \tag{3.40}$$

3.4.2.3. Heat transfer coefficient of the collectors

Ong (1995) outline the methodology for calculating the heat transfer coefficients due to radiation, identified as $h_{r1\text{-}s}$, h_{r21}, and h_{r23}, as follows:

For the top plastic cover to sky $h_{r1\text{-}s}$:

$$h_{r1-s} = \frac{\sigma \varepsilon_1 (T_1 + T_s)(T_1^2 + T_s^2)(T_1 - T_s)}{(T_1 - T_a)}. \tag{3.41}$$

From the absorbing plate to plastic cover h_{r21}:

$$h_{r21} = \frac{\sigma (T_1^2 + T_2^2)(T_1 + T_2)}{\left(\frac{1}{\varepsilon_1} + \frac{1}{\varepsilon_1} - 1\right)}. \tag{3.42}$$

For the absorber plate to bottom insulation surface h_{r23}:

$$h_{r23} = \frac{\sigma (T_2^2 + T_3^2)(T_2 + 3)}{\left(\frac{1}{\varepsilon_2} + \frac{1}{\varepsilon_3} - 1\right)} \tag{3.43}$$

where σ denotes the Stefan-Boltzmann constant, and ε_1, ε_2, and ε_3 are the emissivity of the plastic cover, absorber plate, and bottom insulation, respectively. Sky temperature T_s, linked to ambient temperature T_a, is determined by Eq. 3.44. Convective heat transfers due to wind, h_w is dependent on wind speed V_w, is calculated by Eq. 3.45. The overall top heat loss coefficient U_t is the sum of h_w and $h_{r1\text{-}s}$.as Eq.3.46. Heat loss from the back cover, U_b, through conduction is also considered as shown in Eq. 3.47 (Assadeg et al., 2021; Ong, 1995):

$$T_s = 0.0552\, T_a^{1.5}. \tag{3.44}$$

$$h_w = 2.8 + 3.3\, V_w. \tag{3.45}$$

$$U_t = h_w + h_{r1-s}. \tag{3.46}$$

$$U_b = \frac{1}{i = \sum_1^n (x_{bi}/k_{bi}) + 1/h_w}. \tag{3.47}$$

All convective heat transfer coefficients within the collector flow channels are determined according to the equation provided by (Assadeg et al., 2021; Ong, 1995):

$$h_1 = h_2 = h_3 = h_4 = h_{fin} = N_u \frac{k}{D_h}. \tag{3.48}$$

In this context, Nu indicates the Nusselt Number, k is the air thermal conductivity, while D_h is the hydraulic diameter of the ducts, and. For laminar flow region with Reynolds (Re < 2300), the transition flow region where (2300 < Re < 6000), and the turbulent flow region with (R_e >

6000), formulas for Nusselt and Reynolds numbers follow the guidelines provided in references (Naphon, 2005; Ong, 1995).

The Reynolds number for the airflow through the test section is calculated using the following correlation:

$$Re = \frac{\dot{m}D_h}{A_{ch}\,\mu}, \tag{3.49}$$

where the hydraulic diameter of the ducts D_h estimated as following:

$$D_h = \frac{4WB}{2(W+B)}. \tag{3.50}$$

For the laminar flow where the Reynolds number $Re < 2300$:

$$N_u = 5.4 + \frac{0.00190\left[RePr\left(\frac{D_h}{L}\right)\right]^{1.71}}{1+0.00563\left[RePr\left(\frac{D_h}{L}\right)\right]^{1.71}}. \tag{3.51}$$

For the transition flow where $2300 < Re < 6000$ the equation will be:

$$N_u = 0.116\left(Re^{\frac{2}{3}} - 125\right)Pr^{\frac{1}{3}}\left[1 + \left(\frac{D_h}{L}\right)^{\frac{2}{3}}\right]\left(\frac{\mu}{\mu_w}\right)^{0.14}. \tag{3.52}$$

For turbulence flow where $Re > 6000$ then the correlation will be:

$$N_u = 0.018\,Re^{0.8}Pr^{0.4}. \tag{3.53}$$

The specific heat, density, thermal conductivity and viscosity of air are estimated using the following equations, which account for the mean air temperature along the collector (Ong, 1995):

$$C_p = 1.0057 + 0.000066(T - 27) \tag{3.54}$$

$$\rho = 1.1774 - 0.00359(T - 27) \tag{3.55}$$

$$k = 0.02624 + 0.0000758(T - 27) \tag{3.56}$$

$$\mu = [1.983 + 0.00184(T - 27)] \times 10^{-5} \tag{3.57}$$

3.5. Experimental setup and procedure

This section presents the detailed experimental procedures employed to achieve the research objectives. The methodology, including setup, calibration, and data collection, will be thoroughly discussed. While the specific steps may vary depending on the objective, the data collection and performance assessment methods remain consistent across all experiments. These common techniques will also be explained in detail to ensure the validity and reproducibility of the results.

3.5.1. Effect of entrance flue design

The experiments were designed to assess the performance of two SPSAC: the front entrance solar air collector (FESAC) and the side entrance solar air collector (SESAC) under outdoor test conditions. The first collector has a rectangular air inlet measuring 11 cm by 5.5 cm, placed on the upper long side. The air outlet is directly opposite on the lower side, allowing efficient airflow through the collector. In contrast, the second collector has a divergent section at the inlet, 35 cm long and 46 cm wide at the base, designed to evenly distribute air over the absorber plate. The air outlet is directly opposite the inlet, ensuring consistent airflow. This design

enhances air distribution and improves heat transfer efficiency. Fig. 3.13 shows the structure layout of the collectors.

Both collectors were installed and tested simultaneously to isolate and examine the effect of their respective air entry designs on thermal performance. Prior to testing, accurate measures were taken to ensure the correct assembly of the collectors, particularly focusing on secure connections to the airflow ducts and minimizing the potential for air leakage. All measurement devices, including thermocouples and pressure sensors, were carefully calibrated and verified at steady-state conditions, confirming the consistency and accuracy of readings between both collectors.

The experiments were conducted over a series of clear days in August 2023. To evaluate the performance at different operating conditions, three distinct airflow rates were selected for testing: 0.01118 kg/s (case A), 0.01231 kg/s (case B), and 0.01469 kg/s (case C). These flow rates were controlled and monitored using a variable-speed fan connected to each collector, ensuring accurate and stable airflow throughout the test period. Fig. 3.14 and Fig. 3.15 provide a schematic and a visual representation of the test rigs, respectively

The following data were collected through the experiments every minute from 10:30 to 15:30 and graphed at five-minute intervals:

- The ambient temperature average of two sensors.
- The inlet temperature average of four sensors.
- The absorber plate temperature average of 10 sensors.
- The outlet temperature average of four sensors.
- The orifice plate pressure drops ΔP_{or}.
- The pressure drops ΔP across the collector channel.
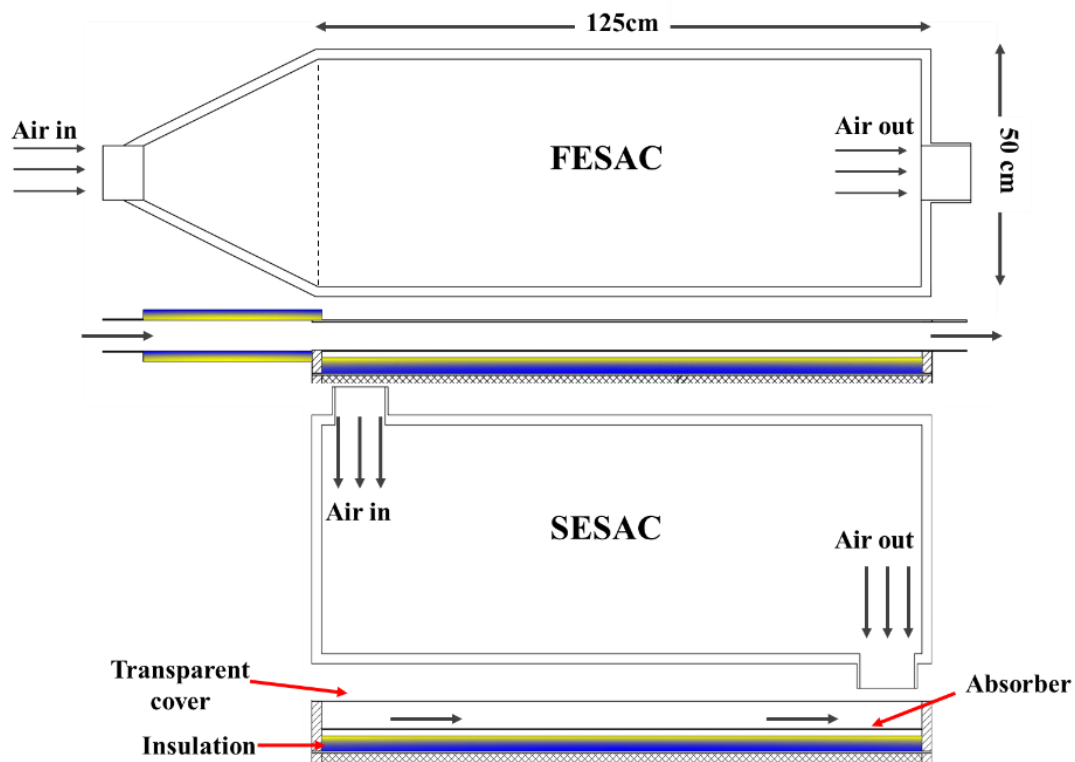- The solar radiation intensity.

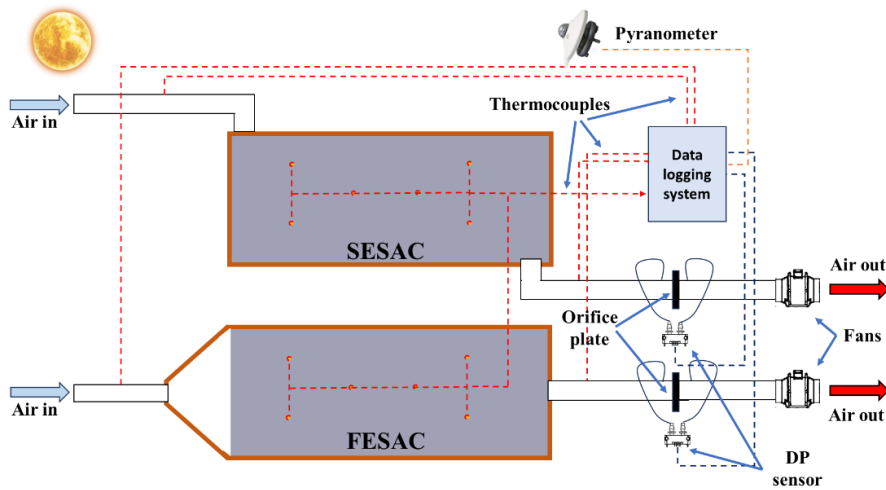Fig. 3.13. The structure layout of the collectors

Fig. 3.14. Schematic diagram of the experimental setup with sensors and data logging system
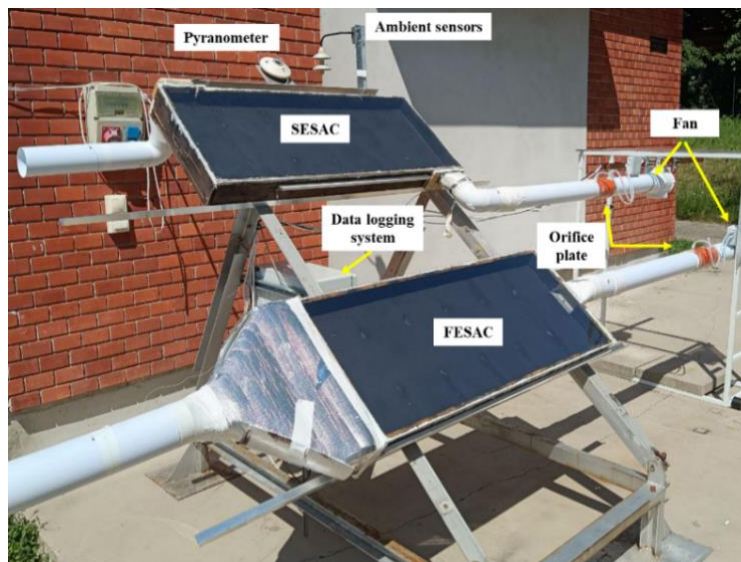

Fig. 3.15. Photograph of the tested rigs

3.5.2. Effect of V-angled fins design

3.5.2.1. Continuous perforated V-angled fins

Following the objectives of the thesis, this experiment focused on the influence of continuous V-angled perforated fins on the thermal performance of DPSACs. The materials and dimensions of the tested collectors are detailed in the rigs fabrication section, with the design configurations illustrated in Fig. 3.16. In this setup, the proposed fins were integrated into one of the collectors. Each fin, with a 90° angle between its 2.5 cm sides, was positioned at a 45° angle relative to the absorber plate to create an optimal angle of attack for the airflow. Along the 45 cm length of each fin, 78 systematically distributed holes (39 of 8 mm and 39 of 6 mm in diameter) were incorporated, ensuring that no holes of the same size were directly opposite each other. The fins were spaced 100 mm apart, with a total of nine fins installed across the absorber plate. To ensure efficient thermal contact, the fins were securely fastened using bolts and high-quality thermal silicone adhesive. The shape and design of the fins are depicted in Fig. 3.17.
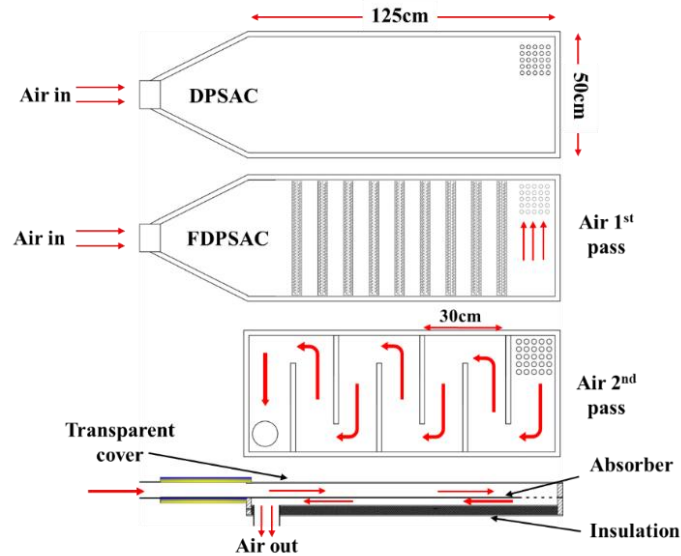
Fig. 3.16. Schematic view of the tested collectors

To assess the performance of the continuous V-angled fins, experiments were carried out using two collectors: one smooth (DPSAC) and the other equipped with V-angled fins (FDPSAC). Both collectors were tested side by side under outdoor conditions to isolate the effects of the finned configuration on thermal performance. Fig. 3.18 presents a schematic view of the experimental setup with sensors and the data logging system, while Fig. 3.19 provides a graphical representation of the setup. Careful attention was given to ensure both collectors were properly assembled, securely fastened, and sealed to minimize the risk of air leakage. Additionally, all temperature and pressure sensors were calibrated and checked at steady state, yielding nearly identical readings for both collectors. The tests were conducted on mostly clear days between August 15th and August 22nd, 2023.

Three distinct airflow rates were selected for testing: 0.00864 kg/s (case I), 0.01143 kg/s (case II), and 0.01317 kg/s (case III). Data were collected every minute between 10:30 AM and 3:30 PM and graphed at five-minute intervals. The following parameters were recorded:

- The ambient temperature average of two sensors.
- The inlet temperature average of four sensors.
- The absorber plate temperature average of six sensors.
- The outlet temperature average of four sensors.
- The orifice plate pressure drops ΔP_{or}.
- The pressure drops ΔP across the collector channel.
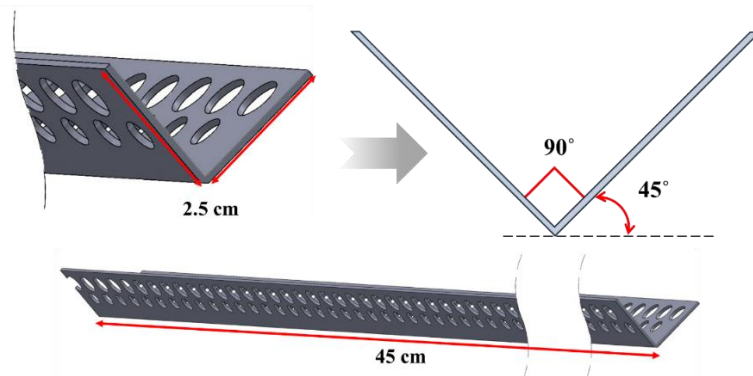- The solar radiation intensity.

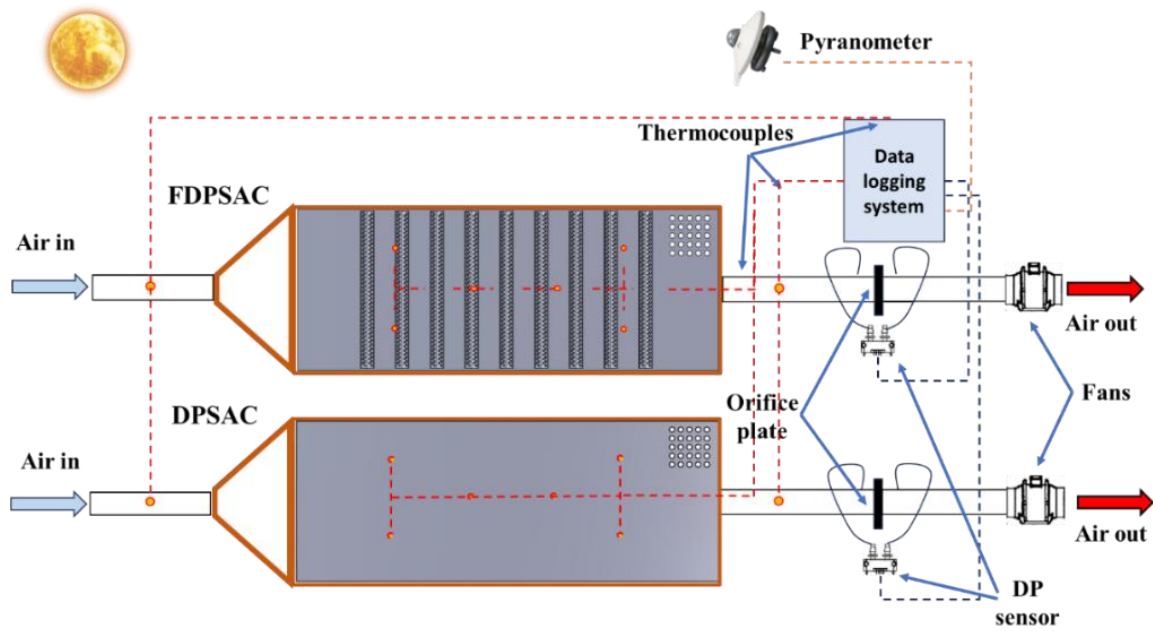Fig. 3.17. Continuous V-angled perforated fins

51

Fig. 3.18. Schematic diagram of the experimental setup with sensors and data logging system
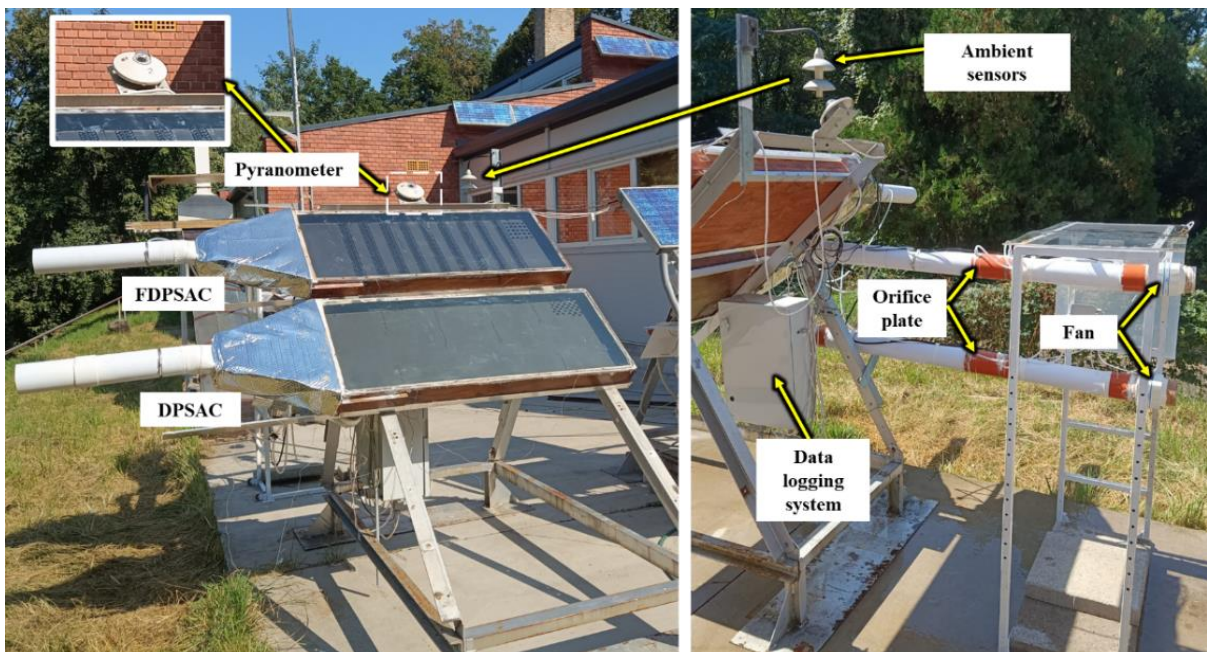

Fig. 3.19. Photograph of the tested rigs

3.5.2.2. Discrete perforated V-angled fins

As with the continuous perforated V-angled fins, this study evaluated the influence of discrete perforated V-angled fins on the thermal performance of SACs using the same collectors and experimental methodology (see Fig. 3.20). The discrete fins, with 6 cm sides and a 90° angle between them, were positioned at a 45° angle relative to the absorber surface to ensure optimal airflow. Each side of the fin featured six 4 mm diameter holes, systematically distributed along its length, with no holes directly opposing one another, as shown in Fig. 3.21. The fins were arranged in a staggered pattern, with 23 fins spaced 100 mm apart. Bolts and high-thermal adhesive were used to secure the fins for maximum heat transfer.
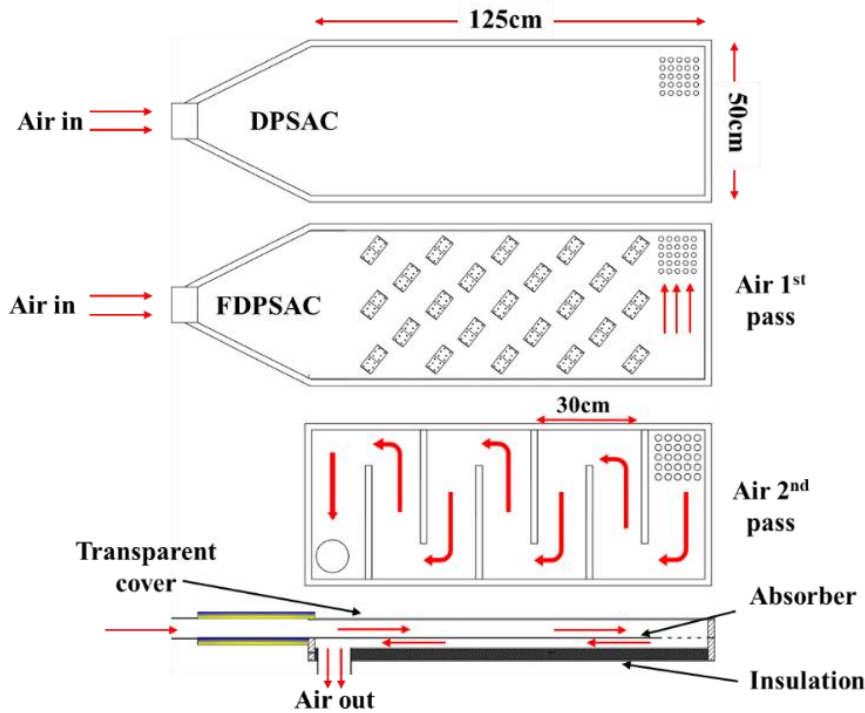
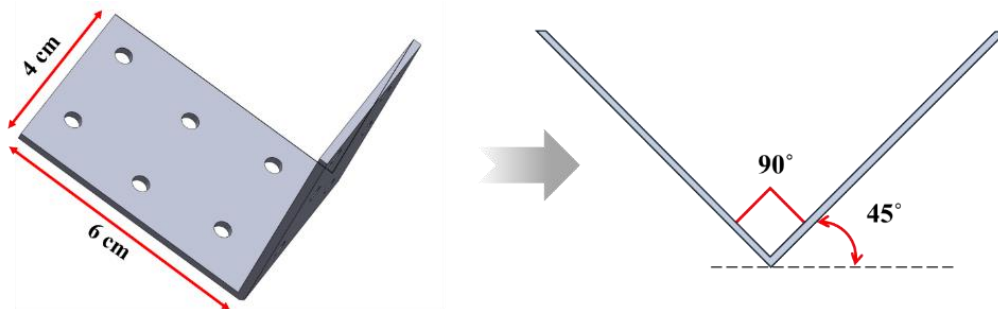Fig. 3.20. Schematic view of the tested collectors

Fig. 3.21. Schematic view of the fin

Three absorber configurations were introduced, each distinct in fin direction but using the same fin shape and number. *Type I* has fins oriented parallel to the airflow direction, *Type II* has fins inclined at a 45° angle to the airflow direction, and *Type III* has fins oriented perpendicular to the airflow direction, as shown in Fig. 3.22. These configurations, along with a smooth DPSAC, were tested side by side under outdoor conditions to assess their impact on thermal efficiency and airflow performance. Each collector was tested at three distinct MFRs: 0.00932 kg/s, 0.01143 kg/s, and 0.01311 kg/s, on separate days between September 1-15, 2023.

After completing the trials for each configuration and flow rate, the fin orientation on the finned collector was modified while the smooth collector remained unchanged. Data collection focused on several parameters, including:

- The ambient temperature average of two sensors.
- The inlet temperature average of four sensors.
- The absorber plate temperature average of six sensors.
- The outlet temperature average of four sensors.
- The orifice plate pressure drops ΔP_{or}.
- The pressure drops ΔP across the collector channel.
- The solar radiation intensity.

Observations were recorded every minute and visualized in five-minute intervals from 10:30 AM to 3:30 PM each test day. Fig. 3.23 presents a schematic view of the experimental setup with sensors and the data logging system, while Fig. 3.24 presents a photograph of the tested rigs.
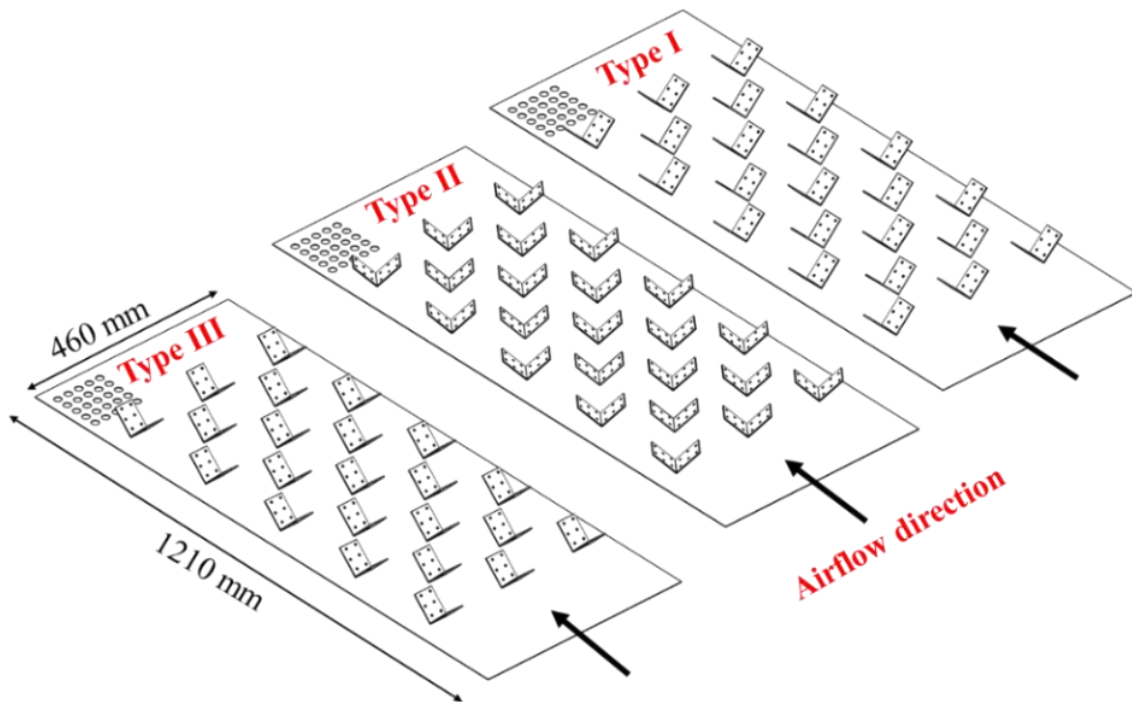

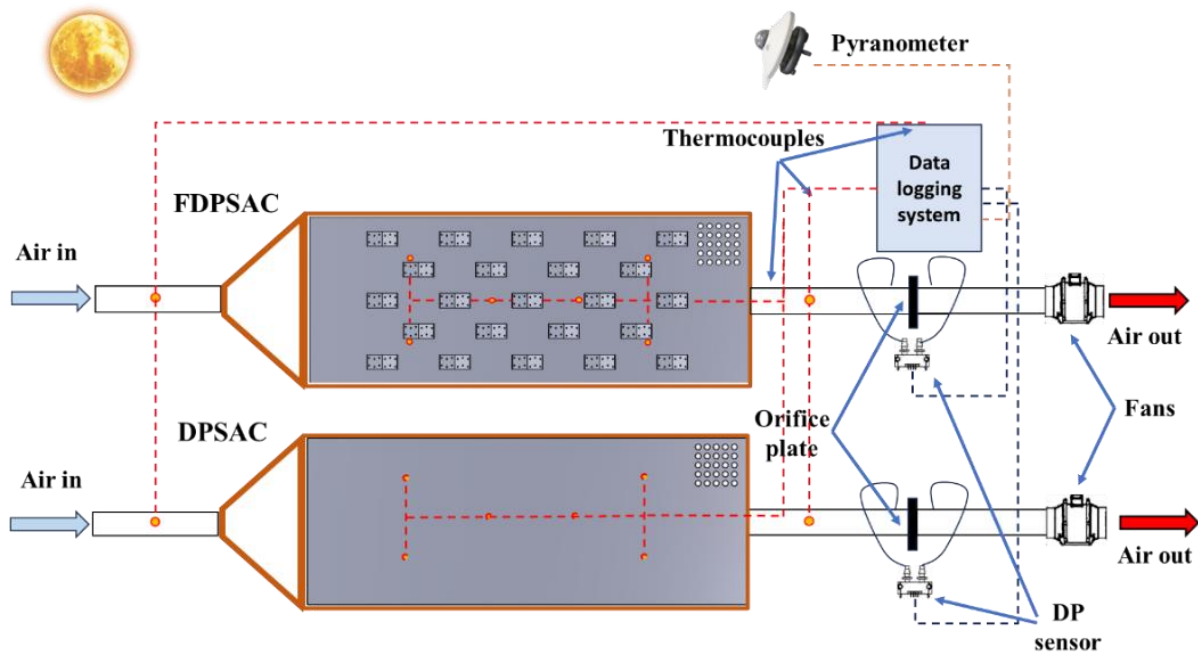Fig. 3.22. Shows the fins configuration on the absorber

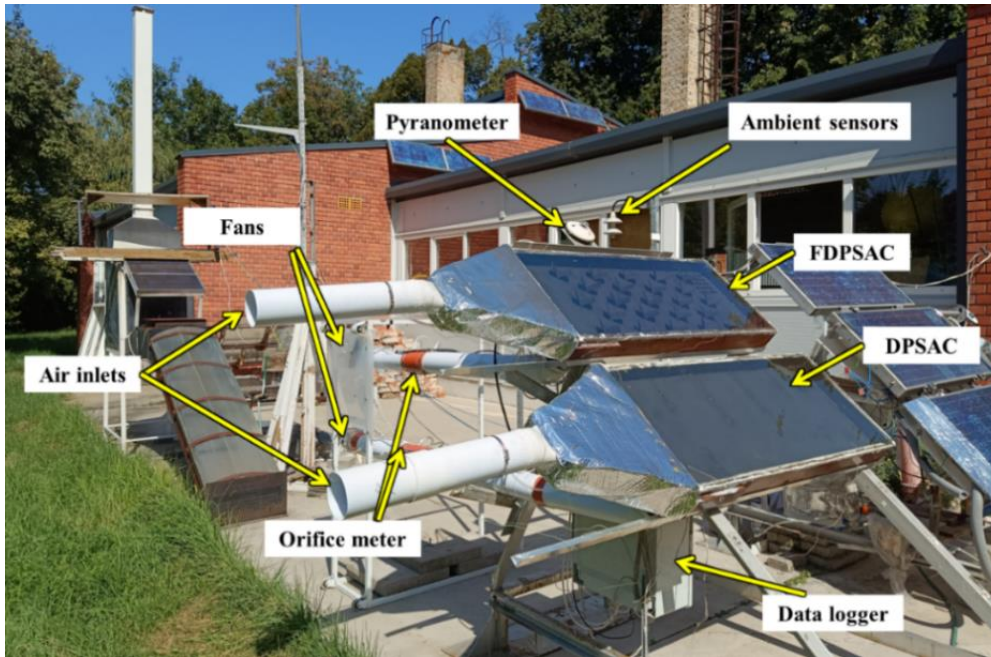Fig. 3.23. Schematic diagram of the experimental setup

Fig. 3.24. Photograph of the tested rigs

3.5.3. Impact of selective coatings

In this experiments, two smooth DPSACs were tested to evaluate the effect of different coatings on thermal performance. One collector was painted with regular black matte, while the other was coated with the solar selective coating SOLKOTE HI/SORB-II, following the manufacturer's guidelines.

Surface preparation involved sanding the absorber plate with 120 disk sandpaper to remove the old black paint, followed by 240 disk sandpaper to roughen the surface. The absorber was then degreased with acetone to ensure proper adhesion. The selective coating was applied using an air atomization spray in five layers, with 5-minute curing intervals between each layer. After application, the collector was left to cure at room temperature for two weeks. Fig. 3.25 illustrates the process of applying the solar selective coating to the absorber plate.

First, the DPSACs were tested side by side under outdoor conditions to isolate the effect of the selective coating. Careful attention was given to ensure both collectors were properly assembled, securely fastened, and sealed to minimize the risk of air leakage. Additionally, all temperature and pressure sensors were calibrated and checked at steady state, yielding nearly identical readings for both collectors.

After testing the DPSACs, the same collectors were converted into single-pass solar air collectors, allowing them to serve as dual-purpose devices. This conversion enabled the comparison of the selective coatings' effects on both double-pass and single-pass configurations. Fig. 3.26 photographic representation of the DPSAC and SPSAC experiments with the applied selective coating on the absorber plates. To assess the impact of selective coatings, both single-pass and double-pass configurations were tested across different mass flow rates.

The experiments were conducted over several days between June and August 2024, with various MFRs applied. For SPSAC, the MFRs were 0.00946 kg/s, 0.01388 kg/s, 0.02158 kg/s, and 0.02629 kg/s. The DPSACs were evaluated with MFR of 0.00877 kg/s, 0.01059 kg/s, 0.01425 kg/s, and 0.01632 kg/s. The data were collected every minute between 10:30 AM and 3:30 PM and graphed at five-minute intervals. The following parameters were recorded:

- The ambient temperature average of two sensors.
- The inlet temperature average of four sensors.
- The absorber plate temperature average of six sensors.
- The outlet temperature average of four sensors.
- The orifice plate pressure drops ΔP_{or}.
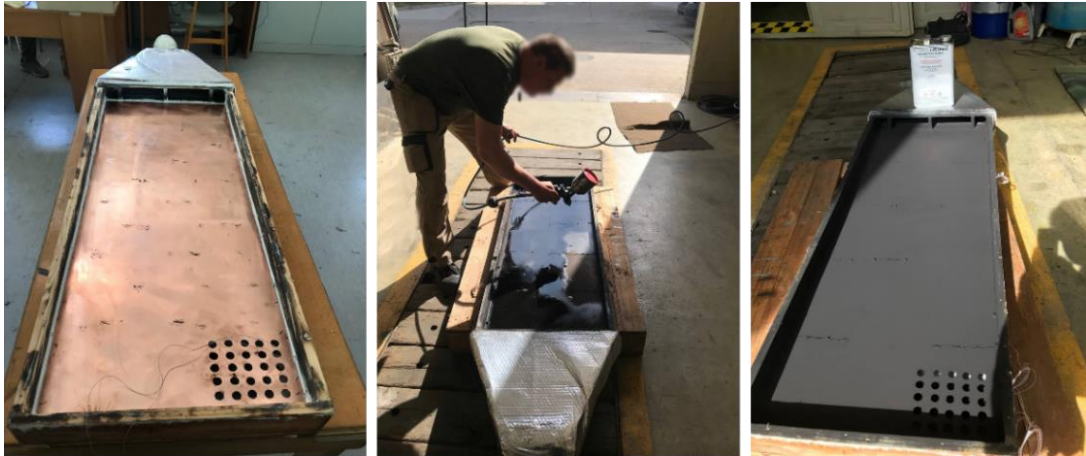- The solar radiation intensity.

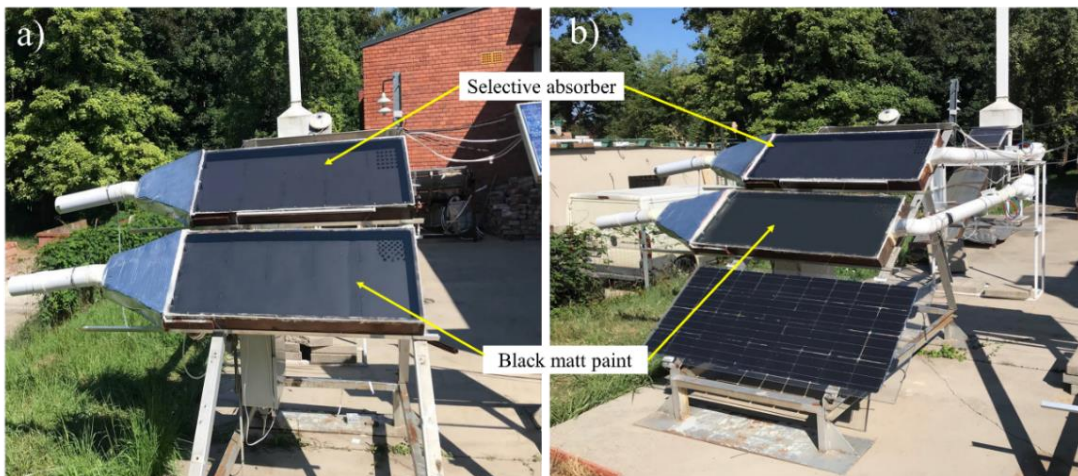Fig. 3.25. Solar selective coating application on the absorber plate

Fig. 3.26. Photograph of the collector with selective absorber: a) DPSAC, b) SPSAC

3.5.4. Influence of channel depth

The influence of channel depth (B) on the performance of SACs was investigated using both experimental and mathematical approaches. In the experimental setup, the SPSAC-5.5 cm, a reference collector with a fixed channel depth of 5.5 cm, was tested alongside SPSAC-7.5 cm and SPSAC-3.5 cm, which were configured at modified depths, as shown in Fig. 3.27. The study initially focused on single-pass operation, with SPSAC-7.5 cm set to a depth of 7.5 cm, while SPSAC-5.5 cm remained fixed at 5.5 cm. Tests were then repeated with SPSAC-3.5 cm, corresponding to a reduced depth of 3.5 cm. All experiments were conducted at a constant mass flow rate and repeated over several days to ensure reliable data. The SPSAC-7.5 cm was tested with mass flow rates of 0.00901 kg/s and 0.01527 kg/s, while the SPSAC-3.5 cm was tested at 0.00892 kg/s and 0.01813 kg/s.

For the double-pass mode, the effect of changing only the upper channel depth was examined using mathematical modelling. The model was validated against experimental data collected at a mass flow rate of 0.0103 kg/s, which showed good agreement between the modelled and experimental results. Following validation, the performance of DPSAC at various channel depths was analysed through simulations.
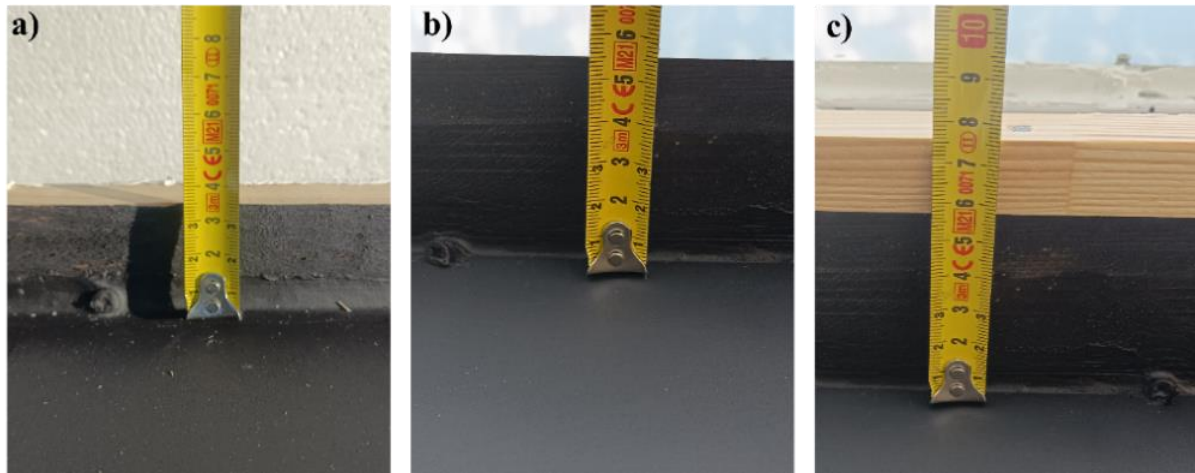

Fig. 3.27. SACs with varying channel depths: a) 3.5 cm, b) 5.5 cm, c) 7.5 cm

Experiments were conducted in August 2024, with data collected every minute between 10:30 AM and 3:30 PM, then averaged at five-minute intervals for analysis. Fig. 3.28 provides a photographic view of the tested SACs and Fig. 3.29 illustrates a schematic of the experimental setup.

The following parameters were recorded:
- The ambient temperature average of two sensors.
- The inlet temperature average of four sensors.
- The absorber plate temperature average of six sensors.
- The outlet temperature average of four sensors.
- The orifice plate pressure drops ΔP_{or}.
- The solar radiation intensity.

The mathematical modelling methodology, as outlined by (Bangura et al., 2022; Fudholi et al., 2013; Ong, 1995), is executed using MATLAB R2023a, with its systematic approach illustrated in Fig. 3.30. This modelling approach builds upon the theoretical framework discussed in Section 3.4, which provides the thermal analysis of the collectors. The process begins with inputting the relevant solar collector parameters, followed by estimating the initial average temperatures for the air channels, glass cover, absorber plate, and back insulation plate. After these preliminary steps, the algorithm computes the sky temperature and the convective heat transfer coefficient due to wind. In the next phase, the heat transfer coefficients (HTCs), U_t and U_b, are evaluated. The following step involves constructing the matrices [A], [T], and [C], with matrix [A] inverted to generate a new temperature matrix [T']. The newly calculated temperatures are compared with the initial estimates, and if the discrepancy between any corresponding values exceeds 0.01 °C, the process is repeated. This iterative cycle continues until all values converge, typically achieved within four to six iterations. Once convergence is reached, the algorithm replaces the initial temperature estimates with the newly computed

values and proceeds to calculate the outlet air temperature and the collector efficiency. Table 3.2 present the parameter used in the simulation process.
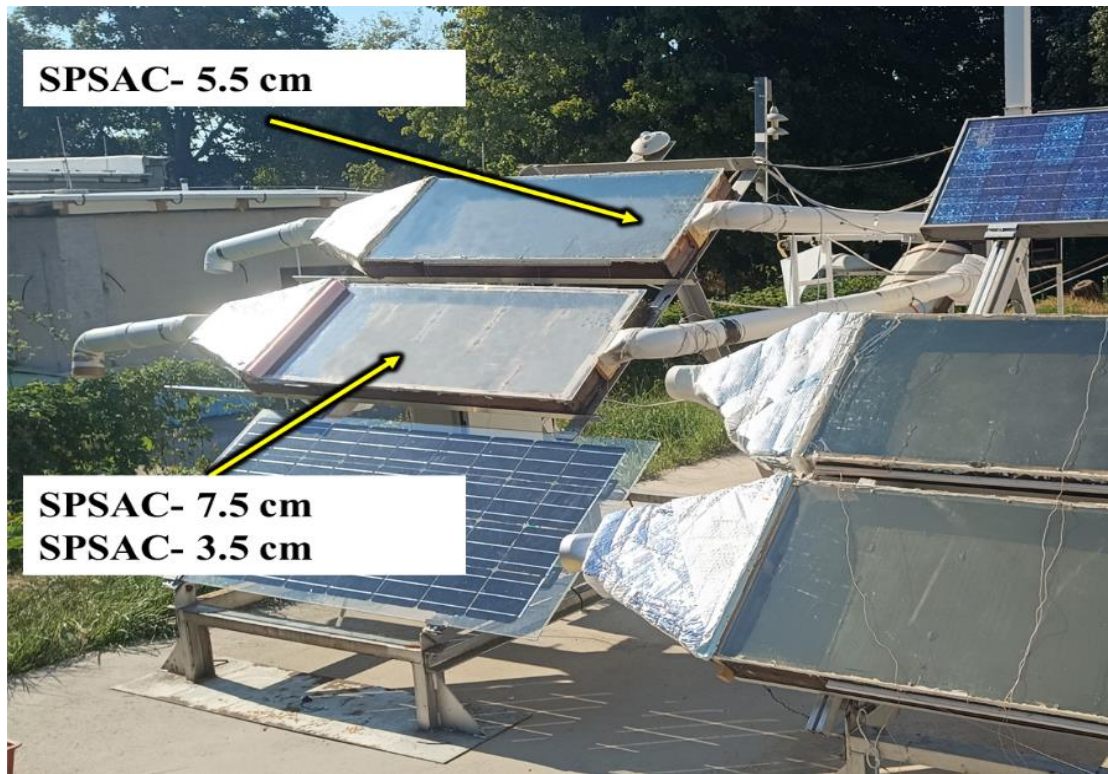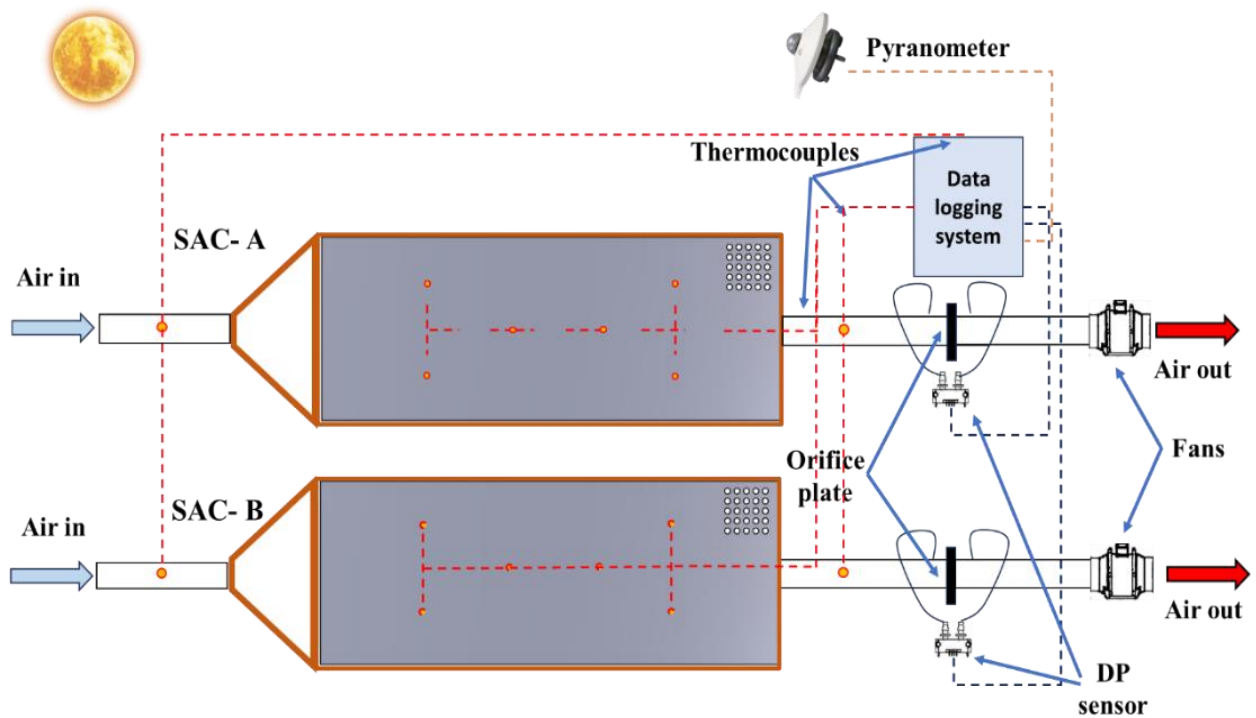

Fig. 3.28. Photograph of the tested rigs

Fig. 3.29. Schematic view of the proposed setup
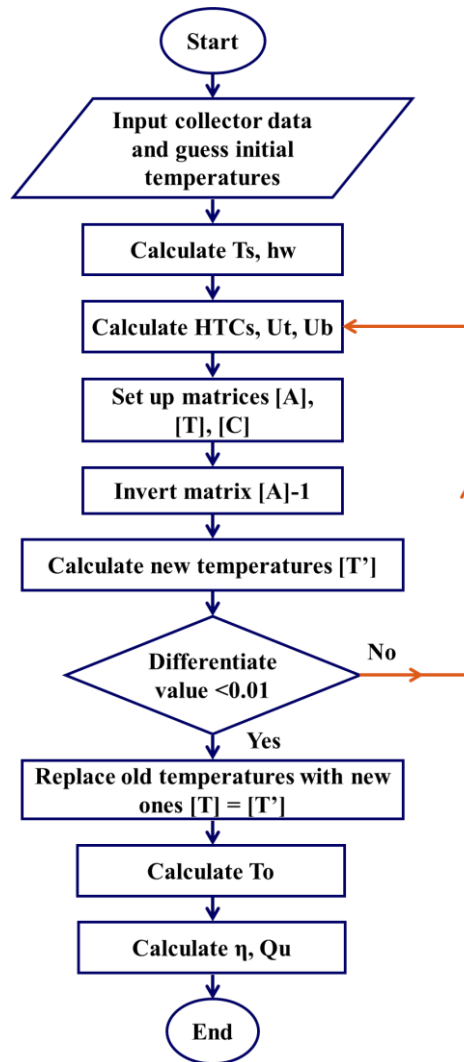
Fig. 3.30. Mathematical modelling process flow chart

Table 3.2. Parameter used in the simulation

Relevant Parameters	Numerical Value
Absorptivity of plastic cover	α_g=0.1
Absorptivity of absorber	α_p=0.94
Emissivity of the plastic cover	ϵ_g=0.8
Emissivity of the black absorber	ϵ_p=0.9
Emissivity of the back side insulation	ϵ_b=0.9
Transmissivity of plastic cover	τ_g=0.9
Density of air	Eq. 3.55
Viscosity of air	Eq. 3.57
Thermal conductivity of air	Eq. 3.56
Specific heat of air	Eq. 3.54
Wind speed	1 m/s

3.5.5. *Effect of different fin configurations on drying performance*

To assess the performance enhancement of the proposed collector modifications, the drying process was selected as a direct indicator of thermal efficiency improvements. The experiments were designed to evaluate the impact of various fin orientations within the DPSAC, each

59

previously detailed, on the drying efficiency. Specifically, the configurations included V-angled perforated fins in discrete and continuous forms. The discrete configurations included *Type I* (fins aligned parallel to the airflow), *Type II* (fins inclined at a 45° angle to the airflow), and *Type III* (fins oriented perpendicular to the airflow). The continuous configuration, *Type IV*, featured a V-angle fins oriented in perpendicular to the airflow. Each configuration was tested alongside a smooth absorber plate collector to assess relative performance, as illustrated in Fig. 3.31, which provides a photographic view of the drying system.

The drying process involved dehydrating 1200 grams of apple slices in each chamber. Each chamber contained three trays, with each tray holding 400 ± 1 grams of apple slices. The apple slices were cut to a uniform thickness of approximately 4 mm. The drying process began with the initial measurement of the apple slices' weight on each tray, followed by hourly weight measurements to monitor the progress of the drying process. The final weight of the apple slices was recorded at the conclusion of the experiment.

The experiments were conducted over several days at a fixed mass flow rate of 0.0103 kg/s. The drying process lasted five hours, starting at 10:30 and ending at 15:30. Fig. 3.32 provides a schematic of the experimental setup. During this period, the following parameters were monitored and recorded:

- The ambient temperature average of two sensors.
- The inlet temperature average of four sensors.
- The absorber plate temperature average of six sensors.
- The outlet temperature average of four sensors.
- The temperature of the drying chamber at the inlet and on each tray.
- The orifice plate pressure drops ΔP_{or}.
- The solar radiation intensity.
- The ambient air relative humidity.
- The inlet air relative humidity of the drying chamber.
- The outlet air relative humidity of the drying chamber.
- The relative humidity of each tray.
- The initial, hourly, and final weight of the apple slice.

Fig. 3.31. Photograph of the tested drying system

Fig. 3.32. Schematic view of the solar drying setup

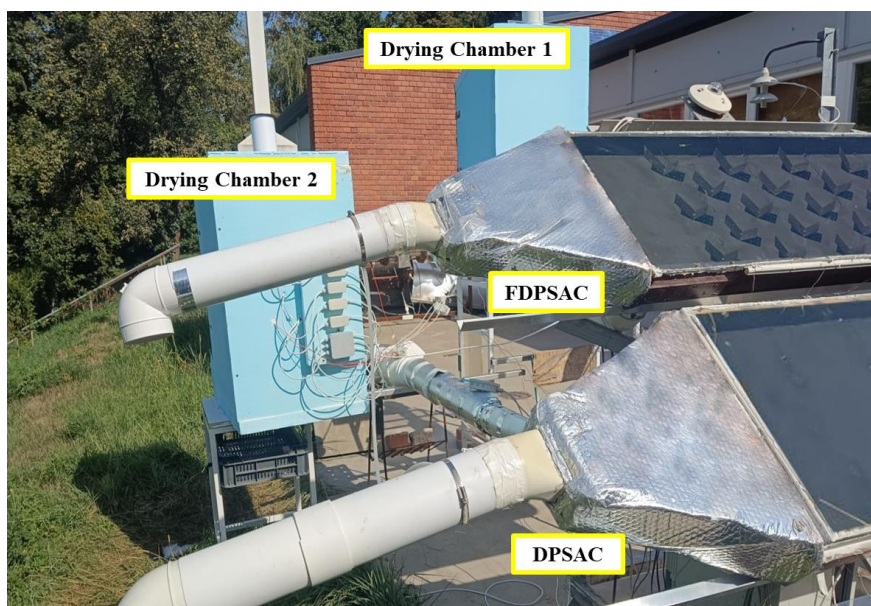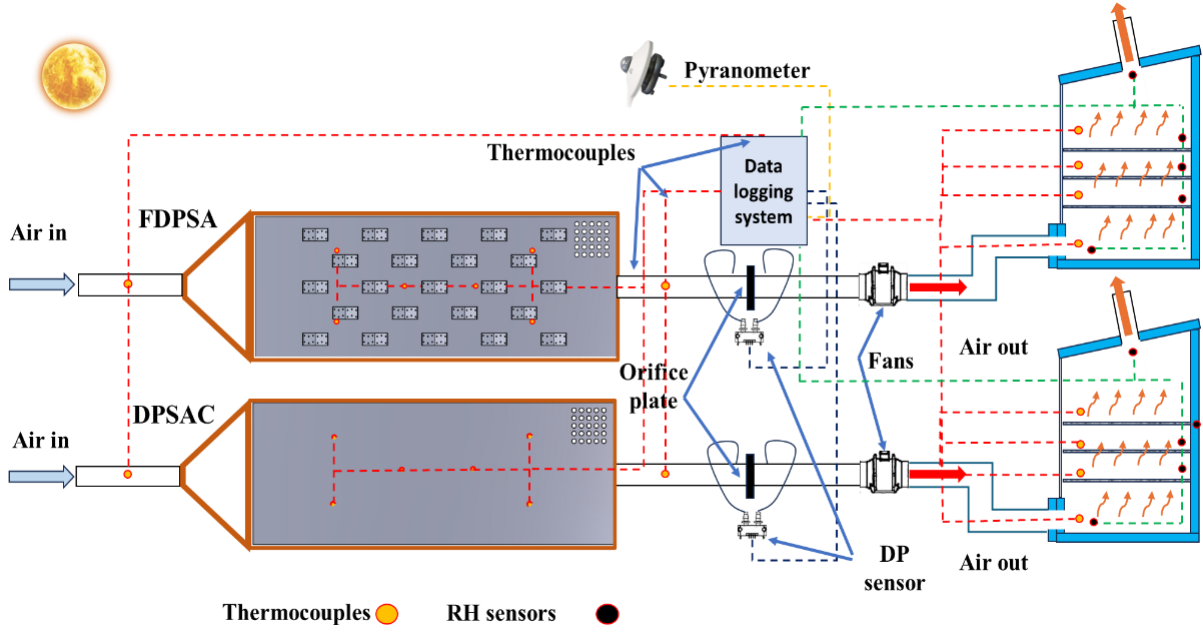## 3.6. Performance assessment of the collectors

The thermal efficiency of the SAC is crucial in assessing how effectively the system transforms solar power into usable thermal energy (Maarof et al., 2023). This efficiency is affected by various critical factors including the air flow rate, its specific heat, the collector's area, as well as the temperatures across the entrance, exit, and the solar intensity. The instantaneous efficiency of SAC can be calculated by the following expression (Kabeel et al., 2016b):

$$\eta_C = \frac{Q_u}{A_p\,I}, \tag{3.58}$$

where A_p denotes the projected area of the collector (m²), I represent the solar radiation incident on the collector (W/m²), and Q_u is the useful heat rate of the air through the collector, which is defined as follows:

$$Qu = \dot{m}\,Cp\,\Delta T. \tag{3.59}$$

Hence $\dot{m}$ denotes the airflow rate (kg/s) calculated using Eq. 3.60 (Alam et al., 2014b; Sukhmeet Singh et al., 2012), C_p represents the air specific heat (J/kg°C), and ΔT is the temperature difference of the air across the collector:

$$\dot{m} = C_d\,A_o \left[\frac{2\rho_o\,\Delta P_{or}}{1-\beta^4}\right]^{1/2} \tag{3.60}$$

C_d is the discharge coefficient of the orifice plate, A_o signifies the orifice plate's area, and ρ_o denotes the air density at the outlet temperature, ΔP_{or} the drop in pressure across the orifice plate, and β is the proportion of the orifice's diameter to that of the duct's diameter.

The heat balance equation that controls a solar air collector functioning under stable conditions is articulated, taking into account the solar radiation that is incident, as presented below (Duffie et al., 2013):

$$Q_u = A_c F_R \left[I(\tau\alpha_p) - U_L(T_i - T_a)\right]. \tag{3.61}$$

The Hottel-Whillier-Bliss equation holds significant importance in the field of solar collector design and analysis. This equation, comprised of several key components, allows researchers

and engineers to comprehensively evaluate the performance of solar collectors. It considers three fundamental aspects: first, the collector's ability to efficiently absorb and transmit incoming sunlight represented by $I(\tau\alpha_p)$; second, its effectiveness in transferring the absorbed heat to the working fluid, captured by a factor named heat removal F_R; and third, the mitigation of overall loss, factored as $U_L(T_i - T_a)$.

In this context, the temperature at the inlet represented by T_i, the surrounding temperature of the air by T_a, and the coefficient for overall heat losses by U_L.

From Eq. 3.58 and Eq. 3.61 we get very important equation to be estimated the performance of solar collectors, as follows:

$$\eta_C = F_R(\tau\alpha_p) - F_R U_L \frac{(T_i - T_a)}{I}. \tag{3.62}$$

As the T_i and T_a are almost the same in outdoor test its beneficial and more reliable to use the $\frac{T_{f,av} - T_a}{I}$, where $T_{f,av}$ stands for the mean temperature measured from the collector's inlet to its outlet. Following this, Eq. 3.62 can be expressed as (Duffie et al., 2013):

$$\eta_C = F_{f,av}(\tau\alpha_p)_n - F_{f,av} U_L \frac{T_{f,av} - T_a}{I} \tag{3.63}$$

The efficiency of the SAC was computed using Eq. 3.58 and plotted against the dimensionless parameter $\frac{T_{f,av} - T_a}{I}$ as scattered data points. Subsequently, a best-fitted line was applied to this data, characterized by two parameters: the intercept, denoted as $F_{f,av}(\tau\alpha_p)_n$, and the slope, represented as $-F_{f,av} U_L$ as determined by Eq. 3.63. These terms derived from the average air temperature, can be transformed to calculate the heat removal factor F_R concerning the inlet temperature using the following equations (Duffie et al., 2013):

$$F_R(\tau\alpha_p)_n = F_{f,av}(\tau\alpha_p)_n \left(1 + \frac{A_c F_{f,av} U_L}{2\dot{m}C_p}\right)^{-1} \tag{3.64}$$

$$F_R U_L = F_{f,av} U_L \left(1 + \frac{A_c F_{f,av} U_L}{2\dot{m}C_p}\right)^{-1} \tag{3.65}$$

The heat removal factor F_R influenced by a range of factors including the collector design, flow rate of the fluid, and overall heat loss coefficient U_L which also effected by the temperature and the wind speed.

3.7. Performance assessment of the dryer

The moisture content of the product on a wet mass basis (m_p) can be calculated using Eq. 3.66 (Umayal Sundari and Veeramanipriya, 2022):

$$m_p = \frac{m_1 - m_2}{m_t}\ 100 \tag{3.66}$$

In this equation, m_1 represents the initial mass, m_2 represents the mass after drying, and m_t is the total mass of the product in kg.

The moisture ratio (MR) can be expressed as:

$$MR = \frac{M}{M_0} \tag{3.67}$$

where, M refers to the moisture content at any given time, and M_0 represents the initial moisture content of the product (Nasri, 2020).

The thermal efficiency of a dryer is defined as the ratio of the energy used for the evaporation of moisture to the total energy supplied to the drying process (Mugi and Chandramohan, 2022):

$$\eta_D = \frac{m_w\, h_{le}}{E_{in}},$$

(3.68)

where m_w is the mass of water evaporated in (kg) which can be found by the difference between the initial and final mass of the product after drying is completed, h_{le} is the latent heat of water vaporization in kJ/kg, and E_{in} is the solar energy supplied to the drying system (Baniasadi et al., 2017).

The m_w can be calculated, as follows:

$$m_w = m_1 - m_2$$

(3.69)

and E_{in} can be found, as:

$$E_{in} = I\, A_p\, t_d$$

(3.70)

where t_d is the total drying time.

The h_{le} can be calculated in the following formula corresponding to the outlet air wet bulb temperature T_{wb} of the dryer in (K) (Rajesh et al., 2024):

$$h_{le} = 2501.8 - 0.002378(\,T_{wb} - 273.15)$$

(3.71)

3.8. Uncertainty analysis

Variations between experimental data and true values can occur due to uncontrolled factors during the experiment, leading to what is known as uncertainty. The methodology applied in this study has been comprehensively detailed in prior research from (Kumar, 2019; Ozgen et al., 2009; Sundari and Veeramanipriya, 2022):

$$\delta_R = \left[\left(\frac{\delta R}{\delta x_1}\delta x_1\right)^2 + \left(\frac{\delta R}{\delta x_2}\delta x_2\right)^2 + \left(\frac{\delta R}{\delta x_3}\delta x_3\right)^2 + \cdots + \left(\frac{\delta R}{\delta x_n}\delta x_n\right)^2\right]^{0.5}$$

(3.72)

The above is a general equation where errors can exist in the variables x_n, with δx_n demonstrating possible error, and δ_R denoting absolute uncertainty. The calculated uncertainties for each variable will be presented in the results section for each experiment. Including these uncertainties will provide a clearer understanding of the reliability of the experimental data. This will ensure that any variations due to uncontrolled factors are accounted for, offering a more accurate interpretation of the results. Presenting uncertainties alongside the data is a common practice in experimental research to ensure the precision and validity of the findings.

4. RESULTS

This chapter presents the detailed results of the experiments conducted to achieve the thesis objectives. The following sections will discuss the outcomes of various experimental and numerical setups, focusing on key factors influencing the performance of solar air collectors. These factors include the effect of entrance flue design, V-angled fins design, selective coatings, channel depth, and the comparison of drying rates for different configurations. Each section will present the findings and their implications for improving the performance of the solar air collectors. Finally, the chapter closes with a summary of the significant scientific findings derived from this thesis.

4.1. Effect of entrance flue design evaluation

This section evaluates the impact of entrance flue design on the thermal performance of solar air collectors. The entrance flue plays a critical role in directing airflow into the collector, which directly affects heat transfer efficiency and overall performance. The experimental procedures, as outlined in the previous chapter, were thoroughly followed to ensure reliability and accuracy in the evaluation process.

The experiments were conducted in August 2023 at the solar laboratory of MATE University in Gödöllő, Hungary, to assess two solar air collectors with identical dimensions but differing inlet port designs. Both collectors were tested simultaneously at three distinct airflow rates to eliminate variability from changing weather conditions across test days. This approach minimized the influence of external factors, such as wind and temperature fluctuations, allowing for a more focused assessment of the impact of inlet design on collector performance. The simultaneous testing further enhanced the reliability and validity of the results.

Fig. 4.1 presents the ambient temperature T_a and solar radiation curves recorded during the experimental period for three airflow rate cases: 0.01118 kg/s (Case A), 0.01231 kg/s (Case B), and 0.01469 kg/s (Case C). The figure highlights the variation of solar radiation intensity and its corresponding impact on ambient temperature throughout the day. The solar radiation increases from the morning, peaks around noon, and declines towards the end of the experiment at 15:30. After this time, despite the presence of sunlight, the decreasing radiation levels, dropping below 500 W/m², along with shading, rendered further measurements ineffective. Maximum solar radiation observed for case A was 998.4 W/m², while cases B and C reached 987.4 W/m² and 933.2 W/m², respectively.

Fig. 4.2 provides a comparative analysis of temperature measurements at the collector's outlet over time. These measurements were recorded under the same airflow rates specified for cases A, B, and C. These airflow rate cases will serve as reference points throughout the subsequent results analysis sections. As shown in the figure, for both collectors, the outlet temperature follows a similar pattern across all cases: it rises steadily in the morning, peaks between 12:30 and 13:30, and then declines gradually as solar intensity decreases in the afternoon. However, the outlet temperatures are consistently higher for FESAC compared to SESAC in all cases. This is attributed to the more efficient air distribution over the absorber plate in FESAC, which eliminates dead zones and enhances heat transfer.
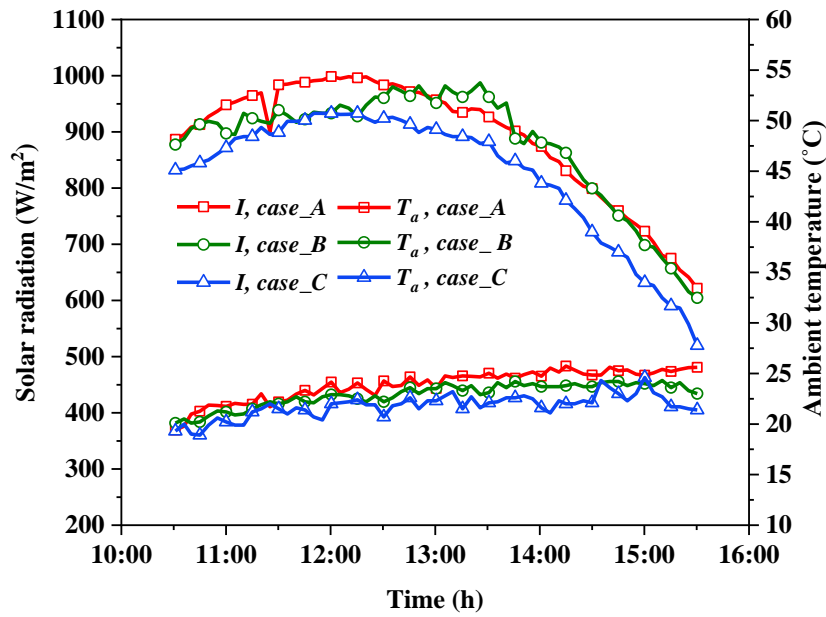
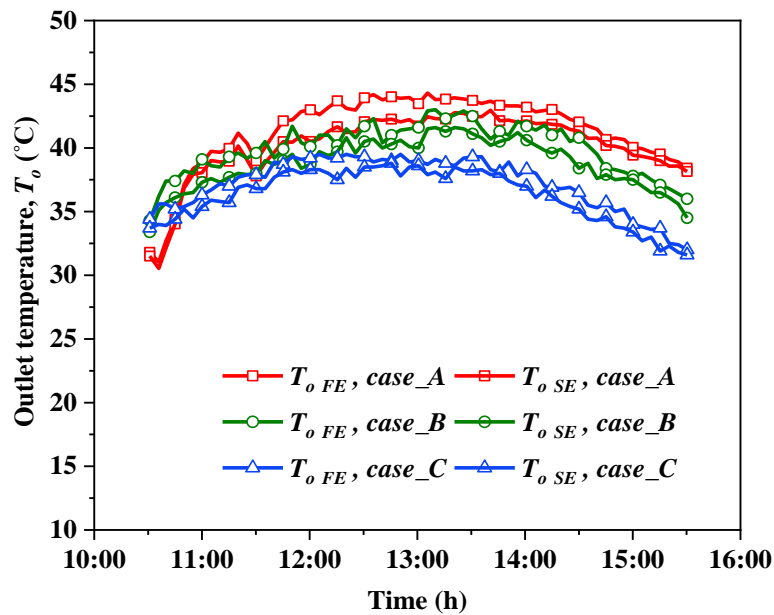Fig. 4.1. The solar radiation and the surrounding temperature versus time

Fig. 4.2. Outlet temperature profiles for the collectors over time

The maximum recorded outlet temperatures for FESAC were 45.2 °C, 42.9 °C, and 39.5 °C for cases *A*, *B*, and *C*, respectively. For SESAC, the corresponding maximum temperatures were slightly lower: 43.1 °C, 41.4 °C, and 37.8 °C. These findings indicate that as airflow increases, the outlet temperature decreases for both collectors, but FESAC consistently demonstrates higher temperature due to its optimized design.

Additionally, it was observed that the inlet temperature and solar radiation intensity play a significant role in influencing the outlet temperature trends. The fluctuations in outlet temperature closely align with the solar radiation curve, as previously illustrated in Fig. 4.1, confirming the strong correlation reported in previous studies (Alomar et al., 2022; Chand et al., 2022; Debnath et al., 2018).

Fig. 4.3 illustrates the variations in the temperature differential, denoted as ΔT, reflecting the difference between inlet and outlet temperatures during the experimental days. This variation is impactful in determining the efficiency of SAC. A greater temperature difference indicates enhanced heat extraction, which is essential for efficient heat transfer and directly impacts the SAC's overall efficiency. As the temperature difference increases, heat extraction becomes more effective, leading to improved thermal performance. Therefore, careful monitoring and optimization of this temperature differential are crucial for advancing SAC efficiency.
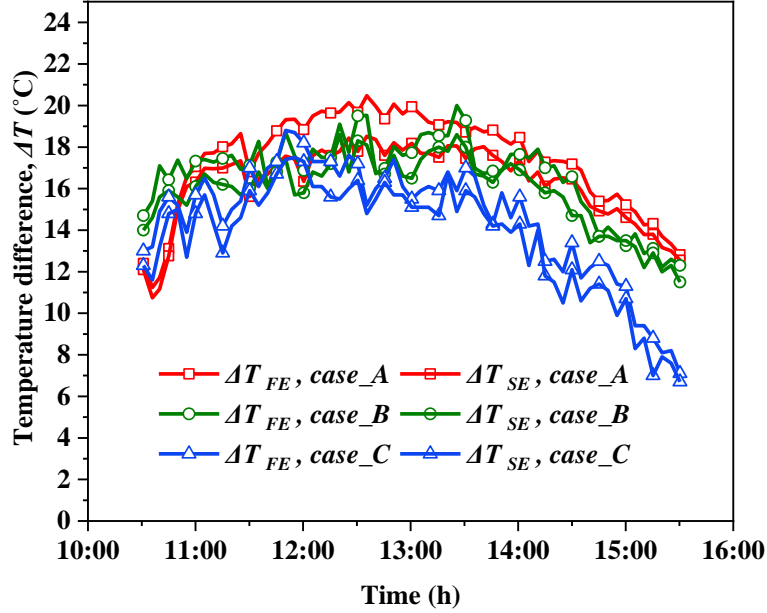

Fig. 4.3. The temperature difference across the collectors versus time

It is evident that the FESAC consistently demonstrates a higher temperature differential compared to the SESAC, regardless of the mass flow rate. The maximum ΔT for FESAC were 20.6 °C, 19.8 °C, and 18.7 °C, for cases A, B, and C, respectively, while for SESAC, the corresponding values were 19.1 °C, 18.3 °C, and 17.5 °C. An important trend revealed in the figure is the inverse relationship between the temperature differential and the mass flow rate. As the airflow rate increases, the temperature difference decreases, indicating that higher mass flow rates lead to reduced heat extraction efficiency. This observation is consistent with findings in previous studies (Abd et al., 2022; Omojaro and Aldabbagh, 2010; Yassien et al., 2020) which also report that higher mass flow rates negatively affect the temperature differential.

Fig. 4.4 describes the average temperature of the absorbing surface, plotted against experimental time for the respective flow rates. According to case A, the absorber temperature rises with time until a maximum value between 12:30 and 13:30, then declines until the end of the experiment. Similar behaviour was observed in cases B and C, with notable decreases in plate temperatures as airflow rates increased. This trend reflects improved heat extraction from the absorbing surface to the circulating air, thereby reducing overall heat loss. The maximum T_p for the FESAC is 86 °C, 82.9 °C, and 76.6 °C for cases A, B, and C, respectively, while for the SESAC, 90.4 °C, 85.9 °C, and 79.1 °C for the same case order. It can be observed from the graphs that the FESAC exhibits considerably higher heat extraction than the SESAC, regardless of flow rate. The better heat extraction from the absorber for the FESAC results from better air distribution on the absorber plate, reducing dead zones and the absorber plate temperature

compared with SESAC. This approach aligns with the findings and methodologies reported in previous studies, specifically those referenced in publications (Alomar et al., 2022; Machi et al., 2022).
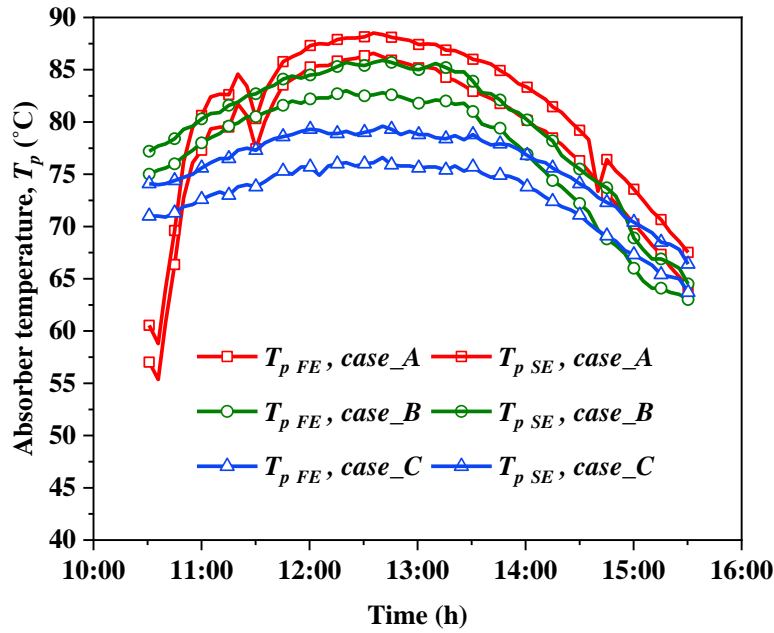
Fig. 4.4. The absorber plate temperature profiles vs time

The heat gain rate of the SAC is illustrated in Fig. 4.5. Primarily, the energy gained depends on the outlet temperature, which is influenced by solar radiation and mass flow rate. The trends in useful heat rate closely follow the solar radiation curve, with airflow rate playing a key role in determining heat gain. The increase in useful heat rate is attributed to both the rise in outlet temperature and the increased airflow rate, with the latter being the primary influence. The maximum heat gain rate recorded for FESAC was 229.4 W, 240 W, and 277.8 W for the three airflow rates. Similarly, the highest energy rate gained by SESAC was 215.7 W, 230.1 W, and 257.8 W under the same airflow conditions.

Fig. 4.5. Energy gain rate by the collectors over time

The efficiency of the SAC is a crucial metric for evaluating its performance. This study focused on efficiency as a primary performance indicator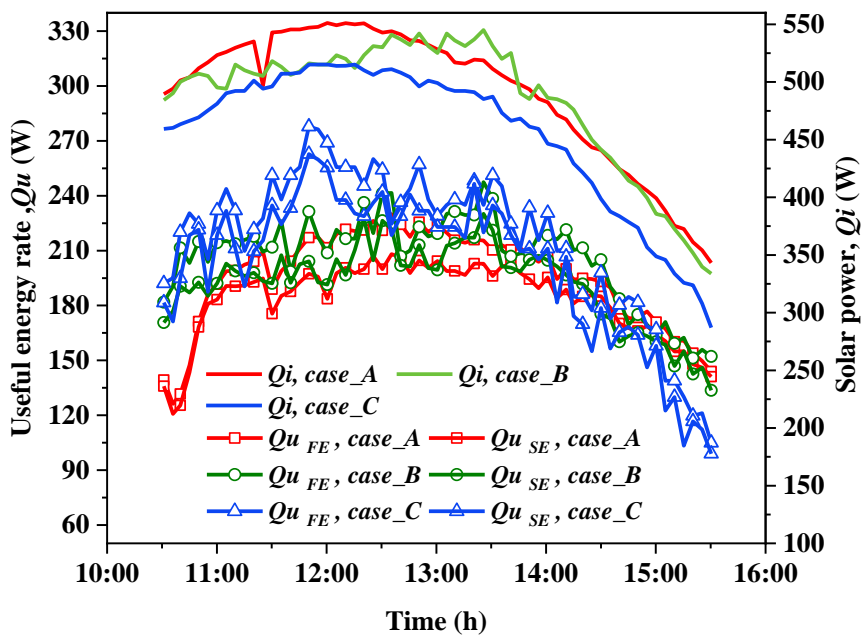. As shown in Fig. 4.6, the instantaneous efficiency curves exhibit trends that are somewhat similar to those observed in the useful heat rate plots displayed in Fig. 4.5. The maximum efficiency achieved by FESAC was 43.8%, 47.3%, and 53.9% for cases *A*, *B*, and *C*, respectively. In comparison, SESAC recorded maximum efficiencies of 41.6%, 44.7%, and 51.1% for the same cases.
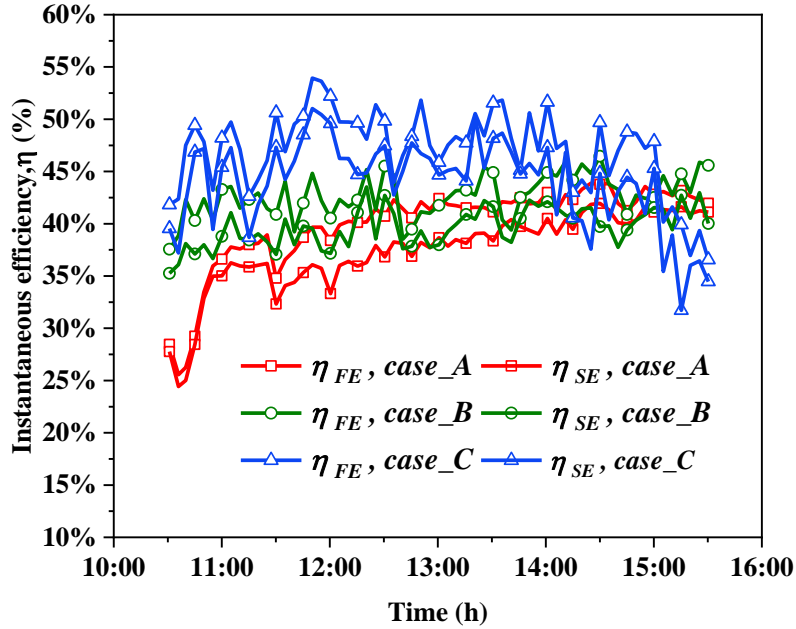

Fig. 4.6. Instantaneous thermal efficiency over time

The same behaviour was reported in literature by Abd et al. (2022); Akpinar et al. (2010) and Chabane et al. (2013) they noted that increased airflow rates enhance the collector's thermal efficiency. Notably, FESAC consistently demonstrated higher efficiency than SESAC, regardless of airflow rate. However, the comparatively high values of instantaneous efficiency may not provide a comprehensive representation of the collector performance. For a more accurate insight into the system's performance, it is crucial to calculate the efficiency on an hourly or daily basis as seen in Fig. 4.7. Instantaneous efficiency measures the heat output of the collector relative to solar radiation input at a given moment. While useful, this metric is sensitive to factors such as airflow rate, weather conditions, and temperature variations, which can cause significant fluctuations. To better understand collector performance, daily efficiency is calculated by integrating instantaneous efficiency values over a specific period, following the approach outlined by Machi et al. (2022). The results showed that FESAC consistently outperformed SESAC in daily efficiency at all tested airflow rates. For FESAC, daily efficiency values were 39.9%, 43.4%, and 47.5% at airflow rates of 0.01118 kg/s, 0.01231 kg/s, and 0.01469 kg/s, respectively. In comparison, SESAC achieved daily efficiencies of 37.2%, 40.4%, and 44.4% at the same airflow rates. FESAC exhibited a relative improvement in daily efficiency of 6.9% to 7.4% over SESAC, which can be attributed to the airflow entrance modification from the side to the front.
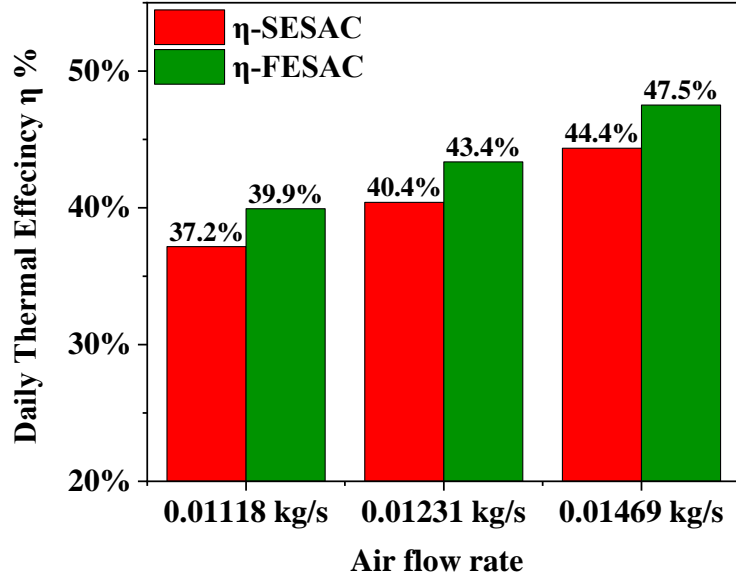
Fig. 4.7. The daily thermal efficiency versus airflow rate

Fig. 4.8 (a) consists of three integrated plots, *A*, *B,* and *C*, each representing different test cases characterized by distinct mass flow rates. These unified plots visually demonstrate the relationship between collector efficiency and the temperature rise factor. The slopes of the curves within these plots correspond to $F_{f\text{-}av}U_L$, and their intercepts represent $F_{f\text{-}av}(\tau\alpha_p)_n$. The $F_R(\tau\alpha_p)_n$ and F_RU_L values were calculated using Eq. (3.64) and Eq. (3.65), respectively. This conversion facilitates the determination of the heat removal factor F_R concerning the air inlet temperature, as detailed in Table 4.1. F_R is crucial for understanding how effectively the collector transfers useful heat compared to the maximum potential heat gain. In Fig. 4.8 (b), depicts the relationship between F_R and the changes in airflow rate. The increase in the F_R value with rising airflow rate suggests that lower airflow rates are associated with less efficient heat extraction from the collector, while higher airflow rates improve the heat transfer from the collector to the air. The enhanced performance in each case, as the data indicates, can be attributed to the optimized air distribution over the absorber surface, which minimizes inactive zones and maximizes thermal transfer efficiency.
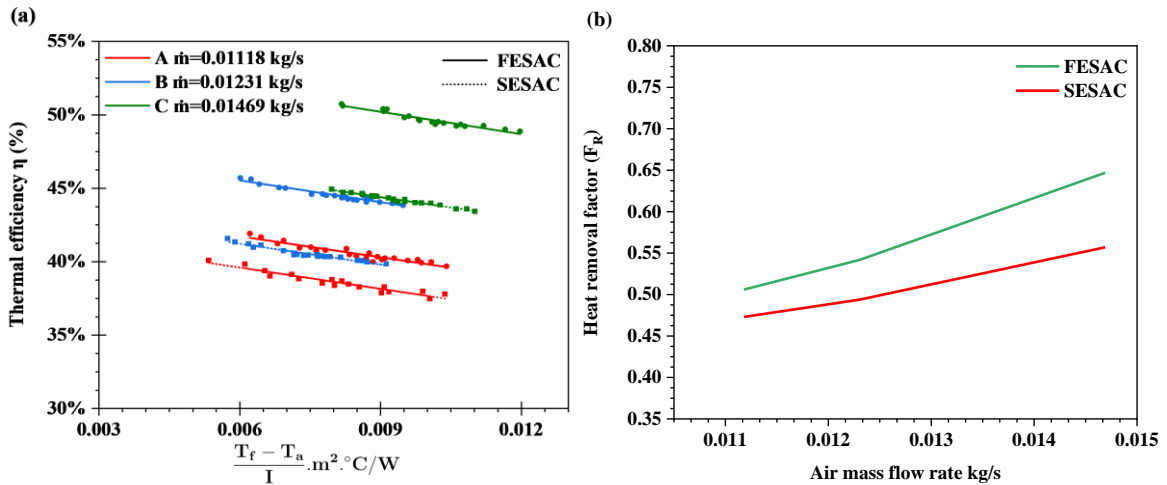

Fig. 4.8. a) collector efficiency versuse temperature rise factor, b) heat removal factor versus mass flow rate

Table 4.1 The F_R values corresponding to air inlet temperature

Case	Collector type	$F_{f-av}(\tau\alpha_p)_n$	$F_{f-av}U_L$	R^2	$F_R(\tau\alpha_p)_n$	$F_R U_L$	F_R
A	FESAC	0.450	5.696	0.910	0.395	4.997	0.506
	SESAC	0.413	4.836	0.932	0.369	4.323	0.473
B	FESAC	0.516	9.888	0.932	0.423	8.101	0.542
	SESAC	0.477	10.743	0.941	0.385	8.666	0.494
C	FESAC	0.601	11.406	0.946	0.505	8.535	0.647
	SESAC	0.527	10.156	0.926	0.434	9.401	0.557

The primary focus of the investigation is the collector's efficiency. Therefore, to ascertain its final relative uncertainty, we first computed the average of all variables individually for every day of experimentation. Subsequently, we calculated the overall mean from the average values obtained across all the experimental days (Omojaro and Aldabbagh, 2010). The mean values of the variables considered are listed in Table 4.2. The resulting relative uncertainty values were found to be 1.508% for airflow rate and 2.48% for thermal efficiency, respectively.

Table 4.2. The mean values of variables considered in the uncertainty

No	Variables	Mean value
1	Inlet temperature (T_i)	24 °C
2	Outlet temperature (T_o)	40 °C
3	Average fluid temperature (T_f)	32.3 °C
4	Pressure drops in the orifice meter (ΔP_{or})	30.7 Pa
5	Solar Radiation (I)	865.2 W/m^2

4.2. Effect of V-angled fins design evaluation

This section focuses on the evaluation of V-angle perforated fins and their impact on the performance of DPSACs. The analysis is divided into two parts: the first section explores the performance of the collector with V-angle perforated fins in a continuous configuration, while the second section examines the effects of discrete V-angle fins. Both configurations will be analysed in terms of their influence on thermal efficiency, airflow distribution, and overall heat transfer performance, providing a comprehensive assessment of how V-angle fins enhance collector performance.

4.2.1. Continuous perforated V-angled fins evaluation

This section presents the results of the performance evaluation of smooth (DPSAC) and continuous perforated V-angled finned (FDPSAC). The experiments were conducted outdoors between August 15th and August 22nd, 2023, under clear conditions to assess the impact of fin configurations on collector performance. The experimental procedures, as described in the methods section, were rigorously followed to ensure accurate and reliable data collection. Both collectors were tested side-by-side at three distinct airflow rates: 0.00864 kg/s (case *I*), 0.01143 kg/s (case *II*), and 0.01317 kg/s (case *III*). This kind of experimental setup minimized external factors, such as variations in ambient temperature and solar radiation, allowing for a focused comparison of the two designs. The collected data, including temperature measurements, pressure drops, and solar radiation, were analysed to evaluate the impact of each collector's design on its thermal efficiency and heat transfer performance.

Fig. 4.9 illustrates the changes in surrounding ambient temperature and relative humidity during the experiments. The ambient air temperatures for cases *II* and *III* were relatively closer, but case *I* exhibited a slight difference. Nonetheless, the ambient temperature for all cases varied between 28.5 °C to 35.5 °C. On the other hand, the relative humidity fluctuated between 46.6% and 61.3% for all cases, with case *III* showing a notably higher percentage. Minor differences between testing days are attributed to the climatic conditions in Gödöllő, which may impact the overall efficiency of the SACs. However, since both collectors were tested simultaneously under identical conditions, these environmental fluctuations do not affect their comparative evaluation. Therefore, the influence of varying weather conditions during the experimental period can be dismissed.
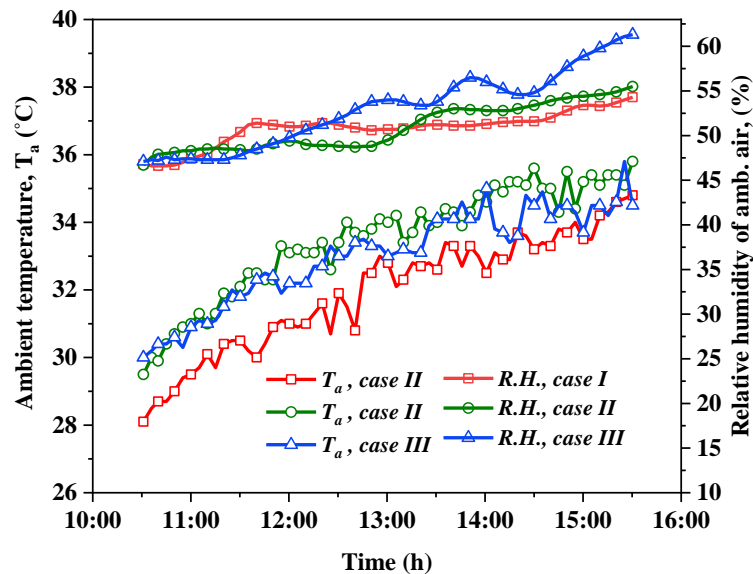

Fig. 4.9. The surrounding ambient temperature and its relative humidity versus time

Fig. 4.10 illustrates the solar intensity recorded during the investigational days. The solar radiation rises from the morning, peaking at noon, and declines towards the experiment's end at 15:30. After this time, despite the availability of sunlight, the declining radiation levels, dropping below 500 W/m², and shading render further measurements ineffective for our purposes. The maximum solar radiation observed for case *I* was 914.8 W/m², with cases *II* and *III* reaching 925.6 W/m² and 934.3 W/m², respectively.

Fig. 4.11 illustrates the absorber plate temperature for both collectors in each test case over time. The efficiency of SAC is greatly impacted by the absorber plate temperature, affecting it positively and negatively. A positive influence occurs when a sufficient temperature difference exists between the plate and the circulating fluid, enhancing the heat transfer rate. Conversely, a negative impact arises when the temperature becomes excessively high, leading to increased heat losses between the collector and the ambient environment, as Rani and Tripathy (2020) noted. As illustrated, absorber plate temperatures rise in the morning with increasing solar radiation intensity, peaking around solar noon for each case. Subsequently, temperatures fall as solar intensity decreases. Additionally, the pattern observed in the absorber plate temperature closely reflects the solar radiation intensity, as demonstrated in Fig. 4.9. This indicates a significant influence of solar power on the absorber temperature. Moreover, plate temperature is inversely related to airflow rate, decreasing as mass flow rate increases, and increasing as mass flow rate decreases. Notably, the plate temperature of the FDPSAC remains lower than

that of the DPSAC, due to the fins' role in enhancing heat transfer, which reduces absorber temperature. This finding aligns with previous research conducted by (Alomar et al., 2022; Hassan and Abo-Elfadl, 2018).
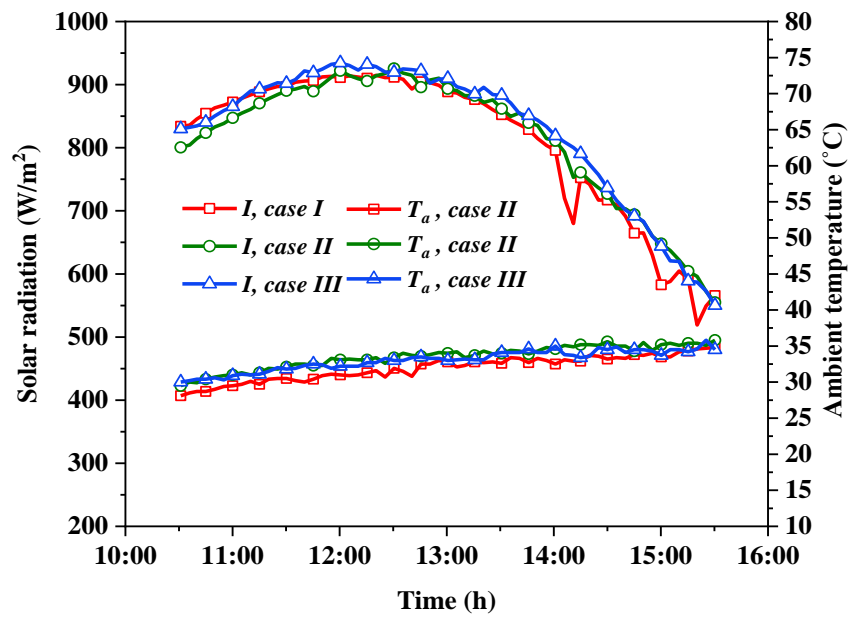
Fig. 4.10. The solar radiation and the surrounding temperature vs time
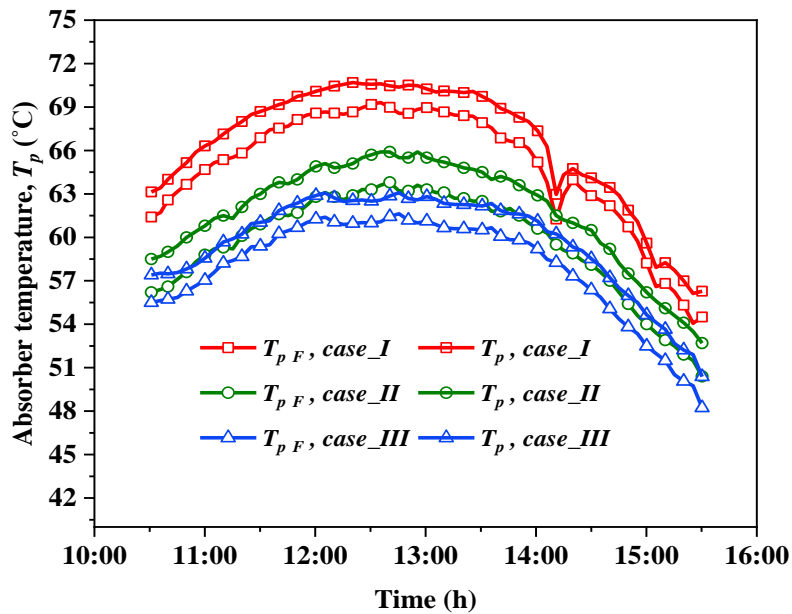
Fig. 4.11. The absorbing plate temperature profiles versus time

Similarly, the connection between solar intensity and plate temperature is reflected in the outlet temperatures of the collectors, demonstrating a comparable pattern as shown in Fig. 4.12. For both collectors, as solar radiation intensity rises throughout the morning, the outlet temperature (T_o) increases until reaching a peak around noon. Subsequently, there is an obvious decline in temperature, observed gradually until the conclusion of the experiment at 15:30. Additionally, the figure shows that T_o is influenced by both the flowrate and the radiation intensity. An inverse relationship is observed, where T_o decreases as the airflow rate increases for both collectors. The maximum recorded outlet temperatures for the FDPSAC collector were 60.6

°C, 57 °C, and 56.2 °C for cases *I*, *II*, and *III*, respectively, between 12:30 and 13:30. Similarly, the DPSAC collector reached highest temperatures of 59 °C, 55 °C, and 53 °C for the similar cases. Notably, T_o of the FDPSAC consistently remains higher than that of the DPSAC under all airflow rate conditions. The improvement in the rate of heat transfer, attributed to the V-angled fins, stems from an expanded surface area and heightened airflow turbulence, disrupting the stagnant layer between the air in motion and the absorbing surface. This observation aligns with the findings reported by (Abd et al., 2022; Alam and Kim, 2017; Vengadesan et al., 2024), underscoring the thermal benefits of such fin configurations.
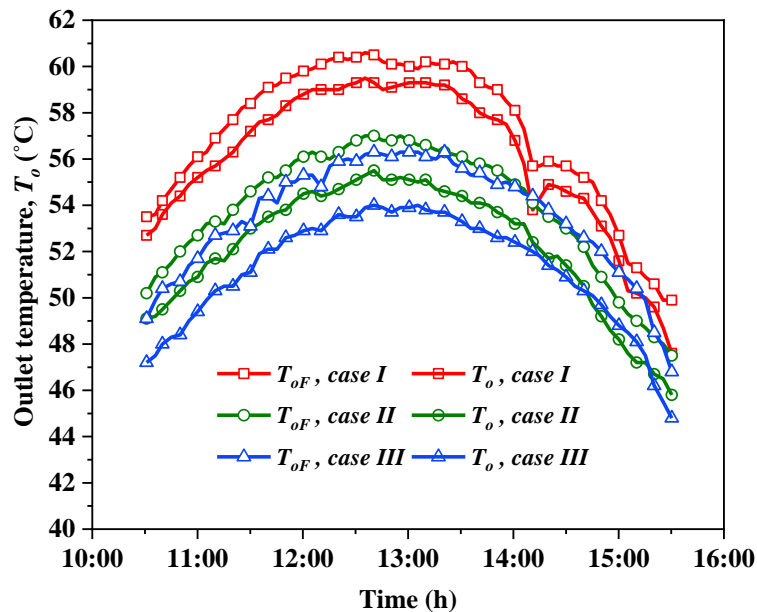

Fig. 4.12. Outlet temperature profiles for the collectors over time

Fig. 4.13 illustrates the variation relating inlet and outlet temperatures ($\Delta T = T_o - T_i$) of the tested collectors over time. The collectors, tested outdoors, experienced inlet air temperatures at or below ambient levels due to forced airflow. The profile of temperature differences aligns with trends observed in Figs. 4.11 and 4.12, highlighting the substantial impact of sun radiation and ambient temperature upon these variations. Additionally, mass flow rate through the collectors directly impacts the temperature difference, with higher airflow rates resulting in lower temperature differentials, so it crucial to be balanced. Moreover, the FDPSAC consistently showed greater temperature differences compared to the DPSAC at all airflow rates. Peak temperature differentials observed for FDPSAC were 30.7 °C, 25.8 °C, and 24.1 °C from 12:30 to 13:30 for cases *I*, *II*, and *III*, respectively, exceeding those recorded of DPSAC, which were 29.0 °C, 23.8 °C, and 21.5 °C. These findings highlight the vital role of fins in improving performance by enhancing heat transfer area as well as optimizing flow behaviour. The results align with earlier research findings reported in (Abd et al., 2022; Abdullah et al., 2018; Omojaro and Aldabbagh, 2010; Yassien et al., 2020).
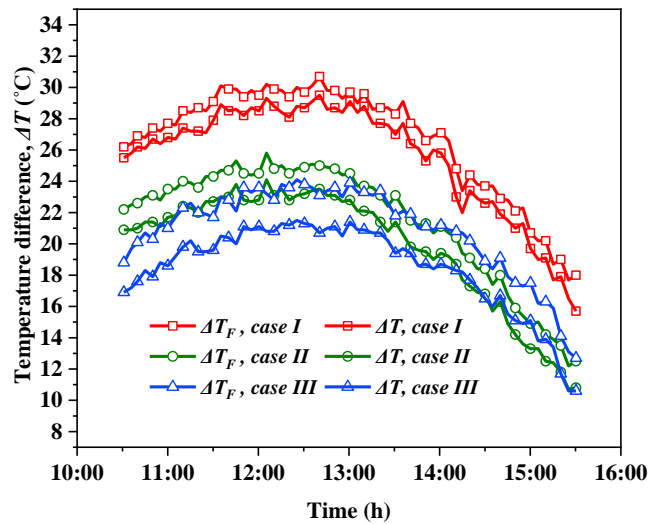
Fig. 4.13. The temperature difference across the collectors versus time

Fig. 4.14 demonstrates the profile of the energy rate gained over time for the collectors. As observed in the figure, the energy rate gain raises with time from middy morning till reaching its maximum around noon and then declining till the end of the experiments, after which the energy is minimal. Moreover, the energy rate profile trend follows the solar power energy curve for all cases, as presented in the figure. This alignment indicates that the useful energy rate is constrained by the flow rate and the temperature difference ΔT. The limitation is due to the fact that temperature variation is governed by the outlet temperature, which, in turn, is impacted by the radiation intensity. Furthermore, temperature difference is a key factor in the process of heat gain, representing the most significant variable in the calculation equation. Additionally, airflow rate directly influences useful energy rate, with higher mass flow rates enhancing heat transfer. The FDPSAC consistently outperforms the DPSAC in energy rate gain across all cases due to improved heat transfer from fins, which expand the heat transfer area and disrupt the boundary layer, enhancing efficiency. The maximum heat energy rate gain for FDPSAC, recorded between 12:00 and 13:00, were 267.1 W, 297.3 W, and 318.3 W corresponding to cases *I*, *II*, and *III*, respectively, while for the DPSAC were 256.5 W, 274.4 W, and 289 W for the same cases. The above results align with findings in literature as reported in (Alomar et al., 2022; Kabeel et al., 2016b; Machi et al., 2024).
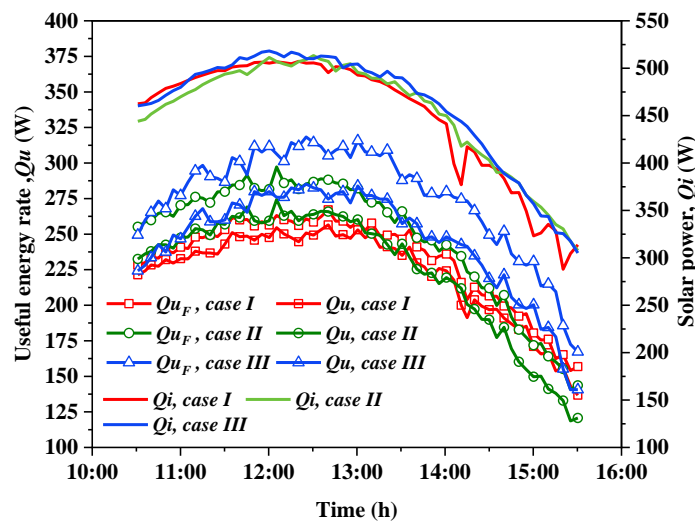

Fig. 4.14. Energy gain rate by the collectors over time

Efficiency curves for solar collectors typically rise and fall from sunrise to sunset through the day, relatively mirroring the solar radiation curve. This pattern is expected when experiments span from early morning to sunset. However, in practice, conducting tests at low radiation levels can be inefficient and costly due to the energy expended on operating the air circulation pump. Therefore, in these experiments, data collection began at 10:30, when solar radiation exceeded 750 W/m^2 and no shading impacted the collector, concluding at 15:30 as radiation levels fell below 500 W/m^2, rendering further testing ineffective. Fig. 4.15 corresponds to these expectations, displaying an initial increase in efficiency, followed by fluctuations until peak values are reached around noon; subsequently, they gradually decline until the end of the test. The collector's instantaneous efficiency directly correlates to airflow rates due to enhanced heat transfer rates, which augment heat gain and optimize efficiency. Despite variations in airflow rates, the FDPSAC consistently demonstrates superior instantaneous efficiency linked to its fin design that improved heat energy transfer and consequently elevating overall efficiency. The maximum calculated efficiency for FDPSAC was 58.2%, 59.4%, and 64.8% corresponding to cases *I*, *II*, and *III*, respectively, while DPSAC achieved 54.7%, 54.8%, and 57% for the same cases. These findings align with previous researches by (Abd et al., 2022; Kabeel et al., 2016b; Ozgen et al., 2009; Salih et al., 2021). Additionally, the instantaneous efficiency is highly sensitive to solar radiation intensity. A drop in radiation intensity caused by a sudden cloud cover or an error in solar radiation data can initially result in higher efficiency. The reason is that the absorber still has stored heat, and the useful energy rate remains constant while the input energy decreases. Consequently, peak instantaneous efficiency may not accurately reflect the collector performance, making the calculation of daily thermal efficiency essential for an accurate evaluation.
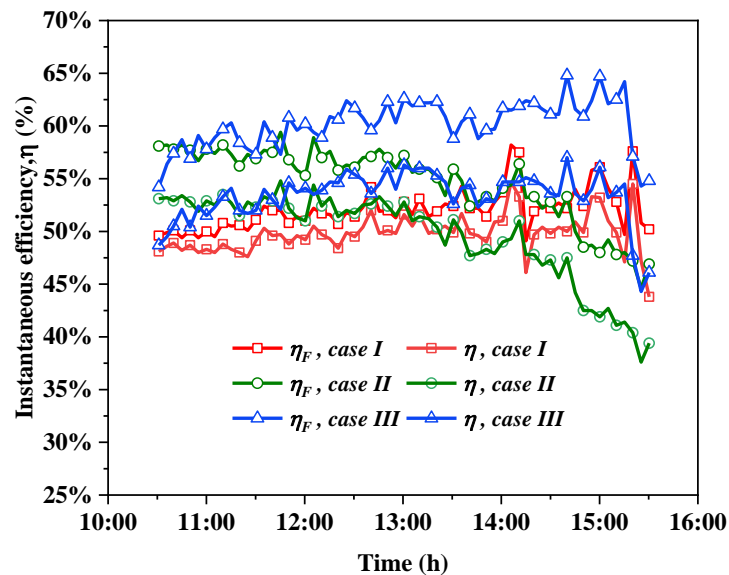
Fig. 4.15. Instantaneous thermal efficiency over time

As outlined, daily efficiencies were calculated utilizing the trapezoidal rule for numerical integration, ensuring precise performance assessment as described in (Machi et al., 2022). The results in Fig. 4.16 shows that the FDPSAC outperforms the DPSAC in terms of daily efficiency across all tested airflow rates. Notably, the FDPSAC achieved daily efficiency values of 51.6%, 54.7%, and 59.2% at mass flow rates of 0.00864 kg/s, 0.01143 kg/s, and 0.01317 kg/s, respectively. In contrast, the DPSAC reported lower efficiencies of 49.4%, 50.5%, and

53.9% for the same airflow rates. The data reveals that the innovative V-angled perforated fin design in the FDPSAC leads to notable relative efficiency improvements of approximately 4.45%, 8.32%, and 9.83% over the DPSAC. These significant efficiency gains validate the effectiveness of the fin design in improving the solar collector's efficiency. The present study found that the newly proposed configuration exhibited superior efficiency, corroborating previous research findings. When considering a 0.01317 kg/s flow rate, the proposed collector showed improved performance compared to those documented in the existing literature.
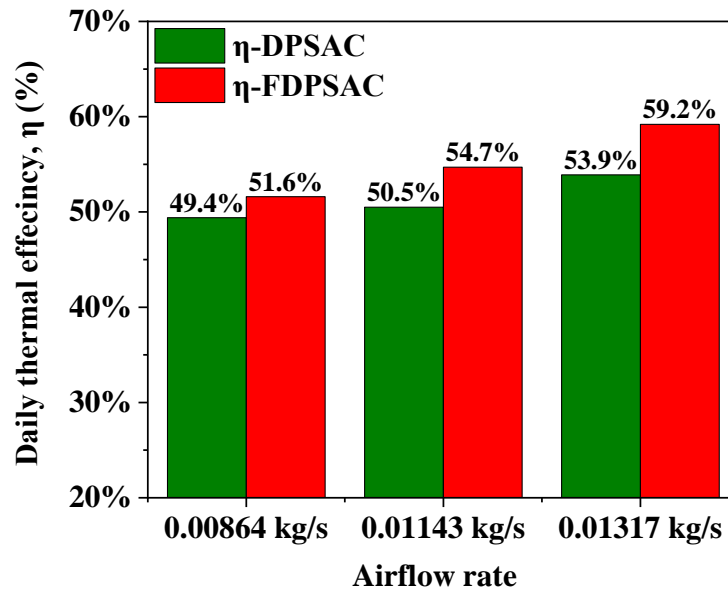
Fig. 4.16. The daily thermal efficiency versus airflow rate

The relative uncertainty of the parameters in this section was determined following the same procedure outlined in the previous section of the thesis. As before, the average values of all variables were computed for each day of experimentation, and the overall mean was calculated from these daily averages. The uncertainty for the investigated parameters is presented in Table 4.3.

Table 4.3. Measurement uncertainties for investigated parameters

Parameter	Relative uncertainty
Airflow rate	1.55%,
Thermal efficiency	2.36%.

4.2.2. Discrete perforated V-angled fins evaluation

This section presents the results of the experiments conducted to evaluate the impact of discrete perforated V-angled fins on the thermal performance DPSACs. As with the continuous perforated V-angled fins, the same experimental setup and methodology were followed. Three distinct fin configurations were tested: *Type I*, with fins oriented parallel to the airflow; *Type II*, with fins inclined at 45° to the airflow; and *Type III*, with fins oriented perpendicular to the airflow. These configurations were compared alongside a smooth DPSAC to assess their effects on thermal efficiency and airflow performance. The experiments were conducted under outdoor conditions at mass flow rates of 0.00932 kg/s, 0.01143 kg/s, and 0.01311 kg/s. Data were collected for several key parameters, including temperatures at various points, pressure

drops, and solar radiation intensity. This section will analyse the collected data to assess how the different fin orientations influence heat transfer and overall collector performance.

Fig. 4.17 illustrate the variations in solar intensity observed across all experimental days for each tested configuration. The extended duration of the experiments allows for observing variations in radiation and ambient air temperature. Typically, these values increase through the morning, peak around midday, and then gradually decline until the conclusion of the experiments at 15:30. After this time, reduced radiation levels, coupled with shading effects, make further measurements unproductive for analysis. In Fig. 4.17 a), the radiation levels recorded during the testing of *Type I* configuration with parallel fins in the SAC were 923.5 W/m², 918.2 W/m², and 921.6 W/m², corresponding to MFRs of 0.00932 kg/s, 0.01143 kg/s, and 0.01311 kg/s, respectively. The highest ambient temperatures for these MFRs were 32.6 °C, 32.2 °C, and 32.8 °C, respectively. For testing *Type II* configuration, featuring fins oriented at a 45° angle, peak radiation levels were 976.7 W/m², 957.1 W/m², and 980.2 W/m², with corresponding ambient temperature peaks of 29.5 °C, 30.7 °C, and 29.9 °C, as shown in Fig. 4.17 b). For testing *Type III* with perpendicular fins configuration, the maximum radiation readings were 946.2 W/m², 928.5 W/m², and 919.5 W/m², alongside ambient temperatures of 31.2 °C, 32.4 °C, and 32.2 °C, respectively, as illustrated in Fig. 4.17 c).
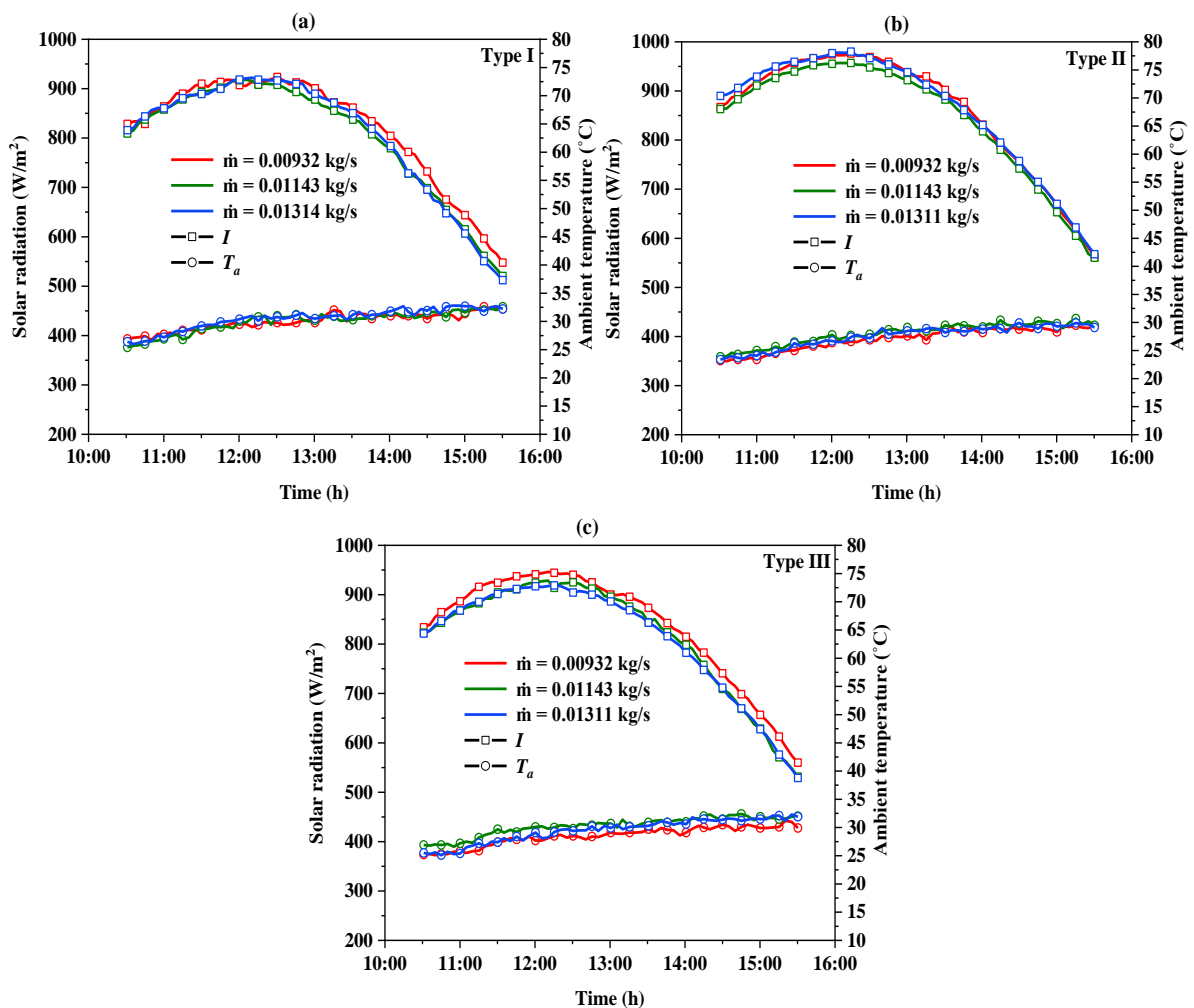

Fig. 4.17. The variations in solar power and ambient temperature during the test

Fig. 4.18 illustrates the absorber surface temperature variations across fin configurations over time, capturing the effects of fin orientation and MFR on thermal performance. The data indicate a rise in temperature in the morning, peaking around noon, and declining afterwards, with measurements concluding at 15:30 as declining solar radiation and shading limit data reliability. This pattern is consistent across all tests, underscoring the active relationship between solar radiation and temperature of the absorber plates.

Fig. 4.18 a) presents data for the *Type I* configuration, with maximum absorber plate temperatures of 66.9 °C, 62.1 °C, and 59.8 °C for MFRs of 0.00932 kg/s, 0.01143 kg/s, and 0.01311 kg/s. In comparison, smooth collector reached slightly higher peak temperatures of 68.7 °C, 64.1 °C, and 63.2 °C under the same rates. These results suggest that *Type I*, despite their parallel arrangement, enhance heat dissipation by mainly increasing heat transfer area and directing airflow, though limited turbulence generation reduces their effectiveness relative to inclined fins.

Fig. 4.18 b) presents data for *Type II* with 45° fins orientation, which consistently yielded the lowest absorber temperatures among all configurations. Maximum absorber temperatures recorded were 67.5 °C, 61.3 °C, and 60.4 °C at the three MFRs, compared to the higher values of 69.1 °C, 63.3 °C, and 62.1 °C in the smooth collector. *Type II* fins generate secondary jet streams through perforations, creating localized air jets that dissipate hot zones on the absorber surface. The V-angle directs cooler air to replace warmer boundary layer air, further enhancing heat dissipation efficiency. Similarly, Fig. 4.18 c) illustrates the temperature behaviour for the *Type III* configuration, which is oriented perpendicularly. The recorded maximum plate temperatures were 66.3 °C, 62.9 °C, and 60.3 °C across the same MFRs sequence, while the smooth collector reached slightly higher temperatures of 67.5 °C, 64.2 °C, and 61.7 °C. *Type III* fins generate moderate turbulence by redirecting airflow around fins, enhancing cooling through perforations localized jet streams but without the extensive boundary layer disruption seen in *Type II* fins.

The results clearly demonstrate the impact of fin presence and orientation on thermal performance through boundary layer disturbance. Previous study by (Darici and Kilic, 2020; Hassan and Abo-Elfadl, 2018; Rajendran et al., 2023), have confirmed that using fins or grooved absorbers effectively enhances SAC performance and lowers plate temperature.
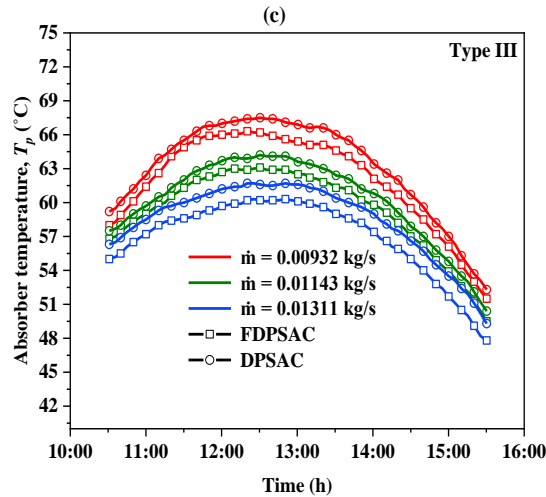

78
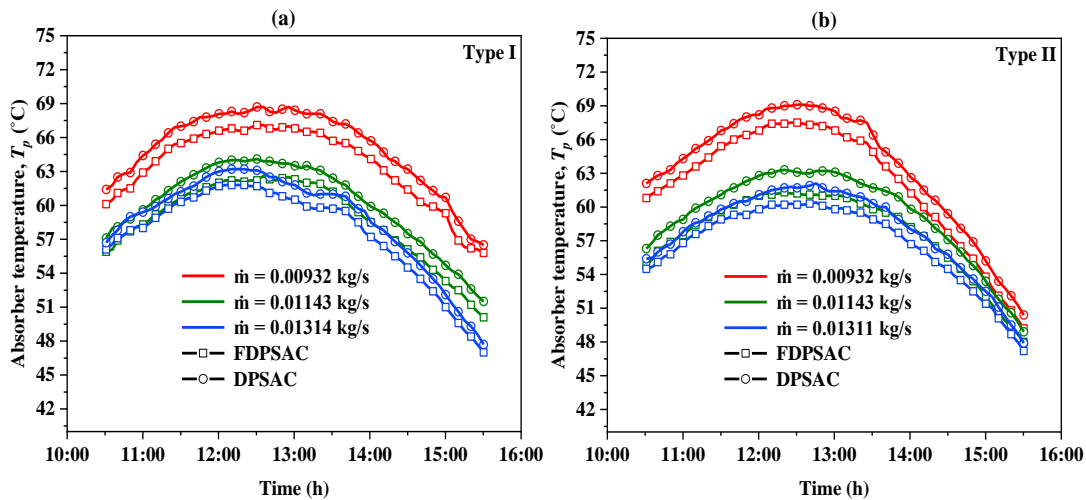
Fig. 4.18. Temperature variations of the absorbing plate over time

Fig. 4.19 illustrates the outlet temperature profiles (T_o) over time for each fin configuration. The outlet temperatures generally increase as solar radiation increases in the morning, peaking between 11:30 and 12:30, and gradually decrease until the experiments end at 15:30. An inverse relationship is observed between T_o and MFR, with higher MFRs resulting in lower outlet temperatures across all configurations. Among the tested setups, *Type II* consistently achieves the highest outlet temperatures, followed by *Type III* and *Type I*, indicating the significant role of fin orientation in enhancing heat transfer efficiency.

As shown in Fig. 4.19 a), the *Type I* configuration reached maximum outlet temperatures of 57 °C, 53.1 °C, and 50.8 °C for MFRs of 0.00932 kg/s, 0.01143 kg/s, and 0.01311 kg/s, respectively. These values were slightly higher than those for the smooth collector, which reached maximum temperatures of 56.1 °C, 52 °C, and 49.6 °C under identical conditions. This increase can be attributed to the expanded heat transfer area offered by the parallel *Type I* fins, which enhances heat dissipation. However, the parallel orientation limits the generation of turbulence and secondary flows, reducing the effectiveness of heat transfer compared to other tested fin orientations.

Fig. 4.19 b), shows that the *Type II* configuration achieved the highest outlet temperatures among all configurations when compared to its smooth counterpart, with maximum values of 56.5 °C, 53 °C, and 51.6 °C for the tested MFRs, while the smooth collector showed lower temperatures of 54.8 °C, 51.2 °C, and 49.3 °C. This superior thermal performance is attributed to the expanded heat transfer area provided by the fins, along with the V-angle's ability to generate secondary flows and vortices that continuously mix cooler air with the warmer boundary layer near the absorber plate. Additionally, the perforations in the *Type II* fins introduce localized jet streams, breaking up stagnant hot zones on the absorber surface and enabling cooler air to contact the plate, further enhancing heat transfer. These perforation-induced jets effectively raise the outlet temperature, highlighting the configuration's optimized capability for heat extraction.

For *Type III* configuration with a perpendicular orientation, maximum outlet temperatures recorded were 56.2 °C, 54.4 °C, and 50.4 °C, whereas the smooth collector reached slightly lower temperatures of 55.1 °C, 53.1 °C, and 48.9 °C (see Fig. 4.19 c). The perpendicular orientation of *Type III* fins enhances heat transfer by expanding the available surface area for

energy exchange and generating moderate turbulence through airflow redirection around the fins. This boundary layer disruption improves heat dissipation, while the perforations further assist in introduce localized jet streams, though less effectively than the angled *Type II* fins. These combined effects result in moderate gains in outlet temperature.

These findings demonstrate that *Type II* fins always yield the highest outlet temperatures, due to their optimized design that links surface area and turbulence generation. This configuration enhances heat transfer through boundary layer disruption and secondary flow formation, grounded in fluid dynamics principles, and outperforms the other configurations in thermal efficiency. The inverse relationship observed between MFR and outlet temperature highlights a critical balance, where optimizing MFR enhances heat extraction without compromising efficiency. These results align with previous findings (Borah et al., 2023; Rajendran et al., 2023; Taha and Farhan, 2021), which emphasize the importance of fin in optimizing solar collector performance.
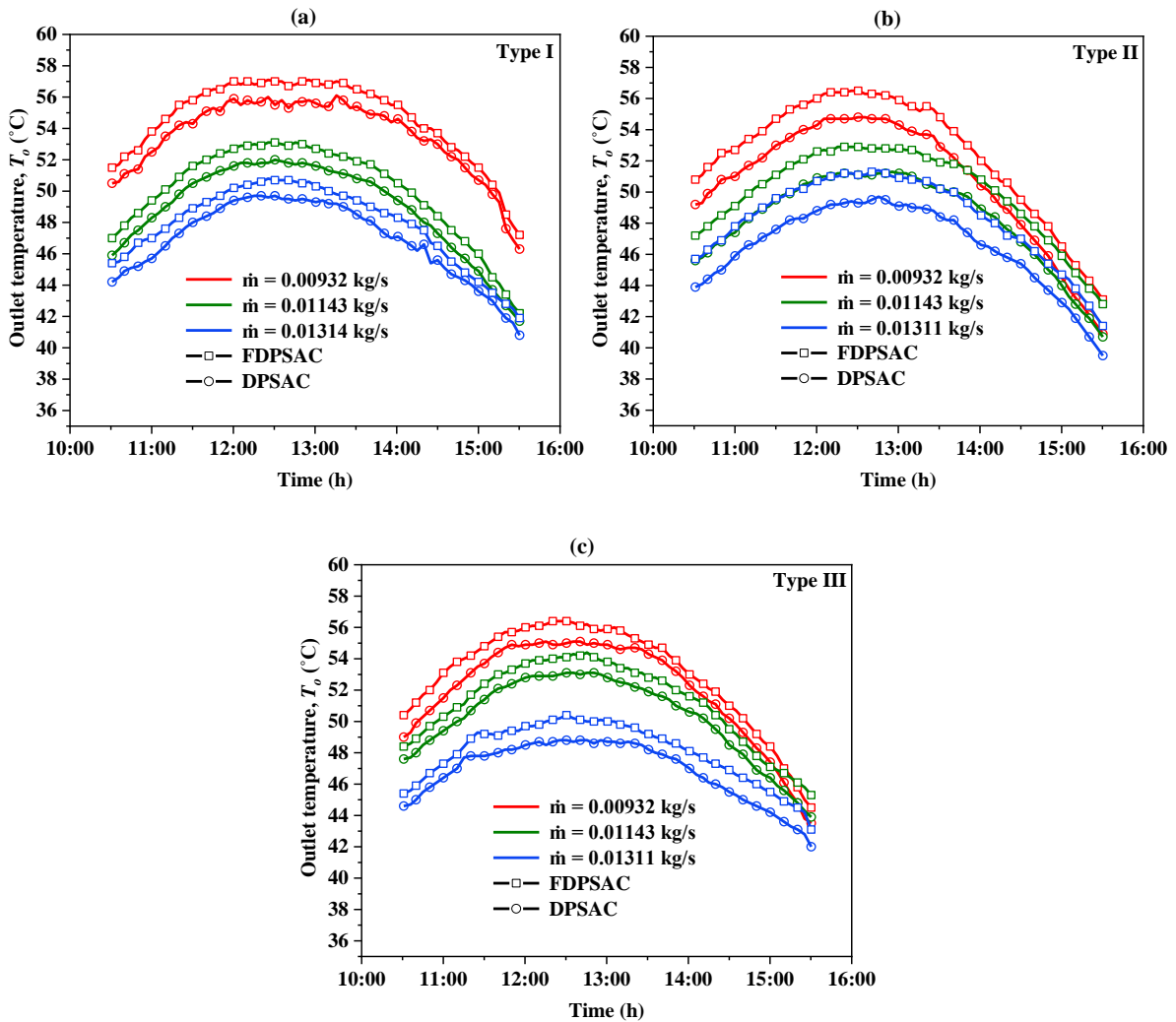
Fig. 4.19. Time-series of outlet temperature profiles for tested rigs

Fig. 4.20 illustrates changes in the temperature difference observed between the inlet and outlet of the tested SACs. These devices operated outdoors, intake inlet air that often measures at or slightly below the ambient temperature due to the mechanism of forced airflow. The observed variations in ΔT correlate with previously noted trends, highlighting the impact of solar

radiation and ambient air temperatures on these differences. In Fig. 4.20 a), for the *Type I* configuration, the FDPSAC achieved maximum ΔT of 28.8 °C, 24.7 °C, and 22.8 °C for MFRs of 0.00932 kg/s, 0.01143 kg/s, and 0.01311 kg/s, respectively. The DPSAC showed lower temperature differences of 27.6 °C, 23.5 °C, and 21.9 °C under the same conditions. These results indicate that the parallel alignment of *Type I* fins supports effective heat transfer by expanding the surface area available for heat exchange.

Fig. 4.20 b) presents that *Type II* configuration consistently yielded the highest ΔT among all configurations compared to its smooth pair. The FDPSAC with *Type II* fins reached ΔT values of 32.1 °C, 26.6 °C, and 25.5 °C, whereas the DPSAC recorded slightly lower differentials of 30.4 °C, 24.9 °C, and 23.6 °C for the respective MFRs. The superior performance of *Type II* fins is due to the expanded heat transfer area provided by the fins. Moreover, the orientation of the fins facilitates the formation of secondary jet streams through their angle of attack and perforations. These jets enhance localized heat transfer that disrupt hot zones on the absorber surface.

Similarly, Fig. 4.20 c) illustrates the ΔT behaviour for the *Type III* configuration. This FDPSAC recorded maximum temperature differentials of 30.2 °C, 25.1 °C, and 23.2 °C, while the DPSAC reached slightly lower values of 29 °C, 24.3 °C, and 22 °C across the MFRs. The perpendicular alignment of *Type III* fins improves heat transfer by increasing the surface area available for energy exchange and inducing moderate turbulence as airflow is redirected around the fins. Additionally, the perforations create localized jet streams that help to extract heat. However, without the extensive boundary layer disruption achieved by *Type II* fins, the ΔT are comparatively lower.

Additionally, the airflow rate is crucial, as higher rates typically result in reduced temperature difference, highlighting the need for accurate management of airflow settings. Similar behaviour has been reported in several studies, including those by (Kabeel et al., 2016b; Machi et al., 2024).
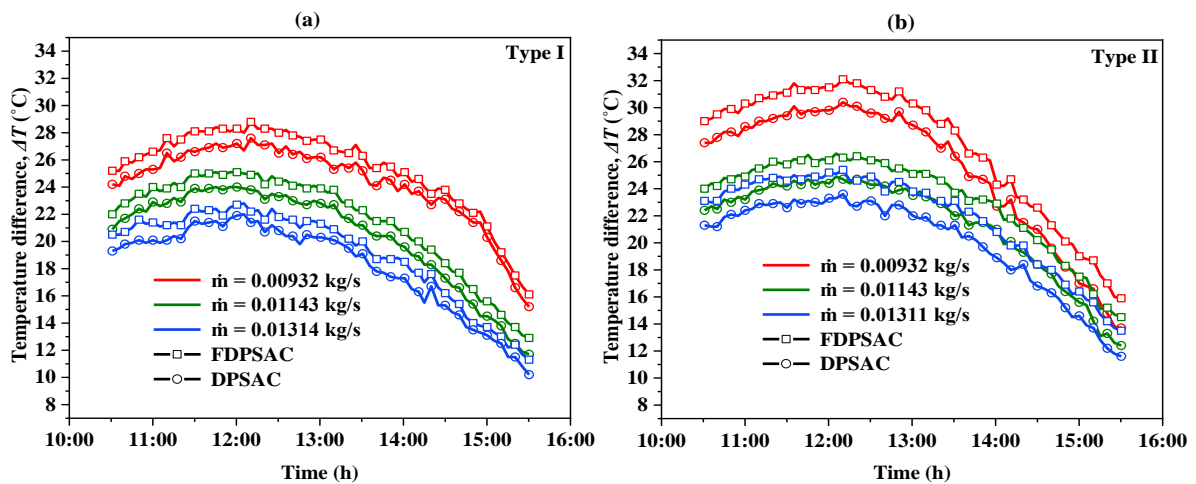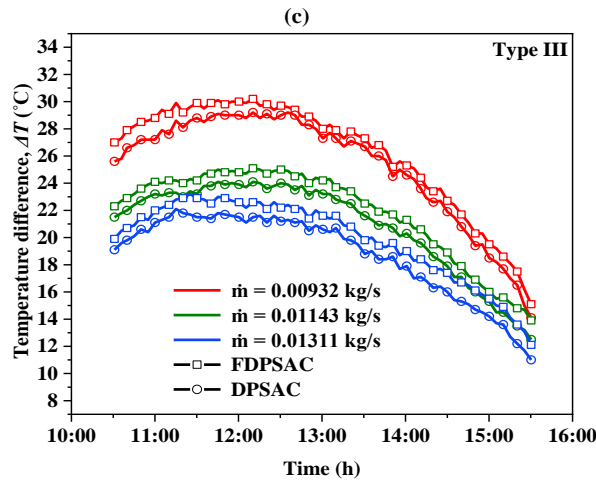
Fig. 4.20. Temperature difference through the SAC with time

Fig. 4.21 display the energy gain rate profiles for each configuration throughout the experiments. The data show that the rate of energy gained increases from mid-morning, peaks around noon, and declines in the afternoon, with minimal energy gain observed toward the end of the day. This pattern aligns with the solar power curve (Qi), indicating that energy gain is closely linked to solar radiation intensity, MFR, and the temperature difference (ΔT). The relationship between ΔT and energy gain is critical, as ΔT reflects the efficiency of heat transfer from the absorber to the air, influenced by both solar intensity and MFR.

Fig. 4.21 a) displays the performance of *Type I* configuration, were the FFDPSAC achieved maximum heat gain rates of 269.7 W, 283.8 W, and 301 W at MFRs of 0.00932 kg/s, 0.01143 kg/s, and 0.01311 kg/s, respectively, while the DPSAC showed slightly lower gains of 272.3 W, 290.4 W, and 285.3 W at the same flow rates. These results suggest that *Type I* collector enhance energy gain by increasing the heat transfer area. However, due to the limited turbulence generated by the parallel orientation, *Type I* fins provide only moderate heat transfer efficiency compared to other orientations.

Fig. 4.21 b) presents data for *Type II* fins orientation, which consistently achieved the highest energy gains under all flow rates. It achieved a maximum heat gain rate of 301.2 W, 305.6 W, and 335.3 W across the tested MFRs, while the smooth collector recorded slightly lower values of 285.3 W, 288.0 W, and 311.7 W under identical conditions. The improved performance of *Type II* fins is attributed to their orientation, which generates secondary flows and vortices that mix cooler air with warmer boundary layer air while increasing the surface area for heat transfer. Additionally, perforations in the fins introduce localized jet streams that actively cool high temperature areas on the absorber surface, further enhancing the overall heat transfer process. This combined mechanism of increased surface area, turbulence generation, boundary layer disruption, and localized heat transfer enhances thermal efficiency, resulting in the highest rate of useful heat gain.

The *Type III* configuration, the FDPSAC achieved energy gain rates of 282.8 W, 288.4 W, and 306.3 W, while the DPSAC showed slightly lower values of 273.4 W, 276.9 W, and 291.7 W at the same MFRs (see Fig. 4.21 c). The perpendicular orientation of *Type III* fins enhances heat transfer by expanding the surface area available for energy exchange and generating moderate turbulence as airflow is redirected around the fins. Additionally, the perforations in

the fins introduce localized jet streams, which actively extract heat by directing cooler air into high-temperature zones, thereby reducing hot spots and promoting more heat extracted.
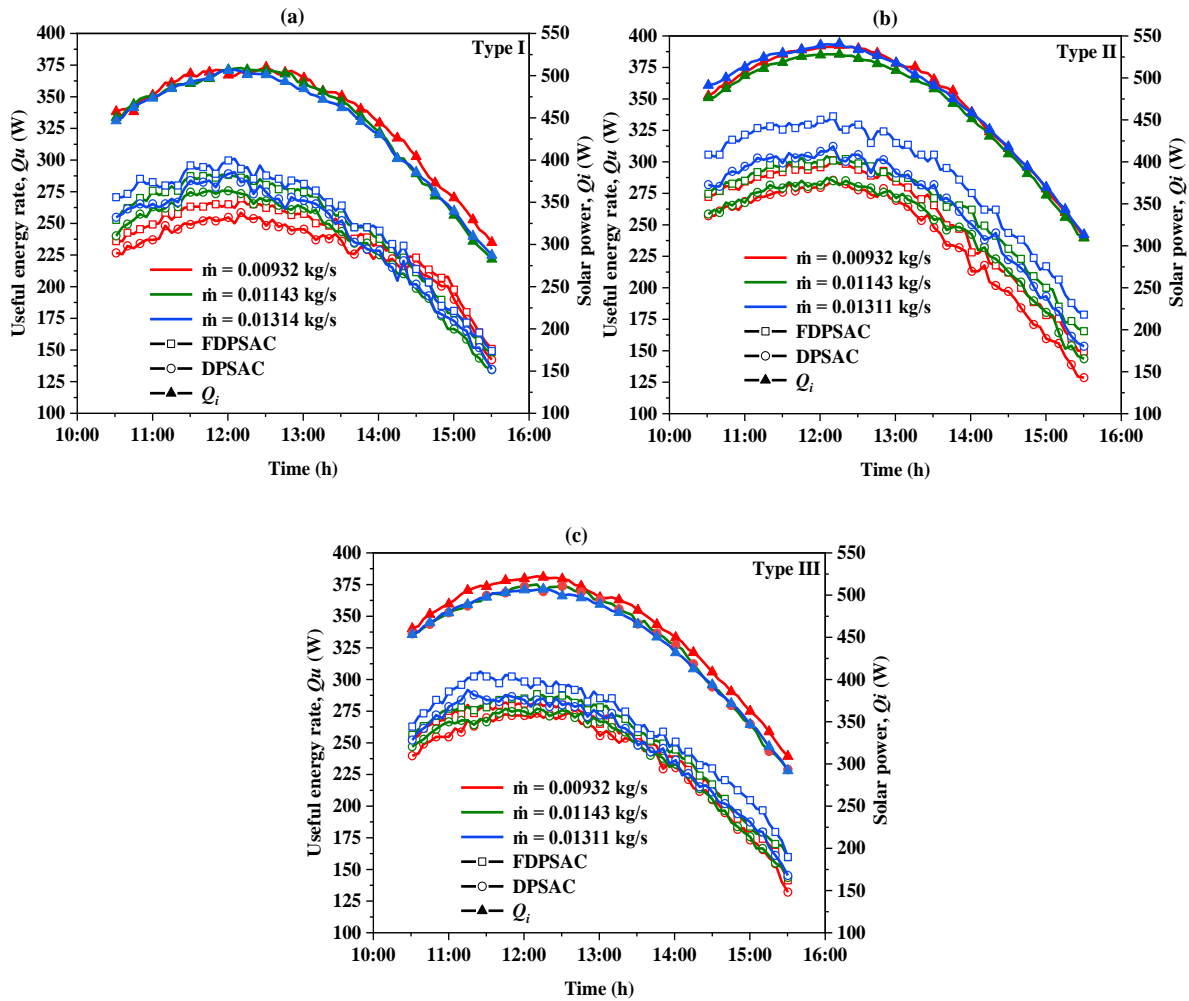
Fig. 4.21. Energy gain rate as a function of time

The efficiency patterns of the tested solar collectors correlate with the sun's daily path, peaking at midday and declining by evening. Fig. 4.22 captures these efficiency trends, showing how the pattern is influenced by solar radiation, which directly affects heat transfer and efficiency. The data reveals that the FDPSAC consistently achieve higher efficiencies than the DPSAC because of the enhanced heat transfer performance of the fins. For *Type I* as shown in Fig. 4.22 a), the FDPSAC achieved instantaneous efficiencies of 57.5%, 57.9%, and 60.3% at the tested MFRs, compared to 55.4%, 55%, and 57.8% for DPSAC. This improved efficiency in *Type I* is primarily due to the fins' increased surface area, which enhances convective heat transfer; however, the parallel orientation results in limited turbulence generation, leading to moderate efficiency gains.

Fig. 4.22 b) shows the performance of *Type II* fins, which achieve the highest efficiency among all configurations. The FDPSAC with *Type II* fins reached efficiencies of 57%, 58.7%, and 62.8%, while the DPSAC recorded lower values of 53.6%, 54.6%, and 58.1% at the same MFRs. The superior performance of *Type II* is attributed to the V-angle orientation, which induces secondary flows and vortices that effectively mix cooler air with warmer boundary layer air. The increased heat transfer area provided by the fins further enhances this process by

expanding the surface available for thermal exchange. Additionally, the perforations also play a significant role, producing localized jet streams that actively cool high-temperature areas on the absorber surface, enhancing the efficiency by maximizing turbulence and boundary layer disruption.

In Fig. 4.22 c), the *Type III* fins achieved instantaneous efficiencies of 55.1%, 55.8%, and 61.1% in the FDPSAC, while the DPSAC shows slightly lower values of 53%, 55.5%, and 59% across the same MFRs. The perpendicular orientation of the *Type III* fins increases the heat transfer area, enhancing thermal exchange and promoting moderate turbulence by redirecting airflow around the fins, which improves convective heat transfer relative to the smooth collector. Additionally, the perforations in the fins introduce localized jet streams that direct cooler air into high-temperature regions, further boosting efficiency by actively extracting heat from the absorber surface. Although *Type III* does not reach the same turbulence intensity as *Type II*, it effectively enhances airflow interaction with the absorber surface, achieving significant efficiency gains.

Fig. 4.22. Instantaneous efficiency changes over time
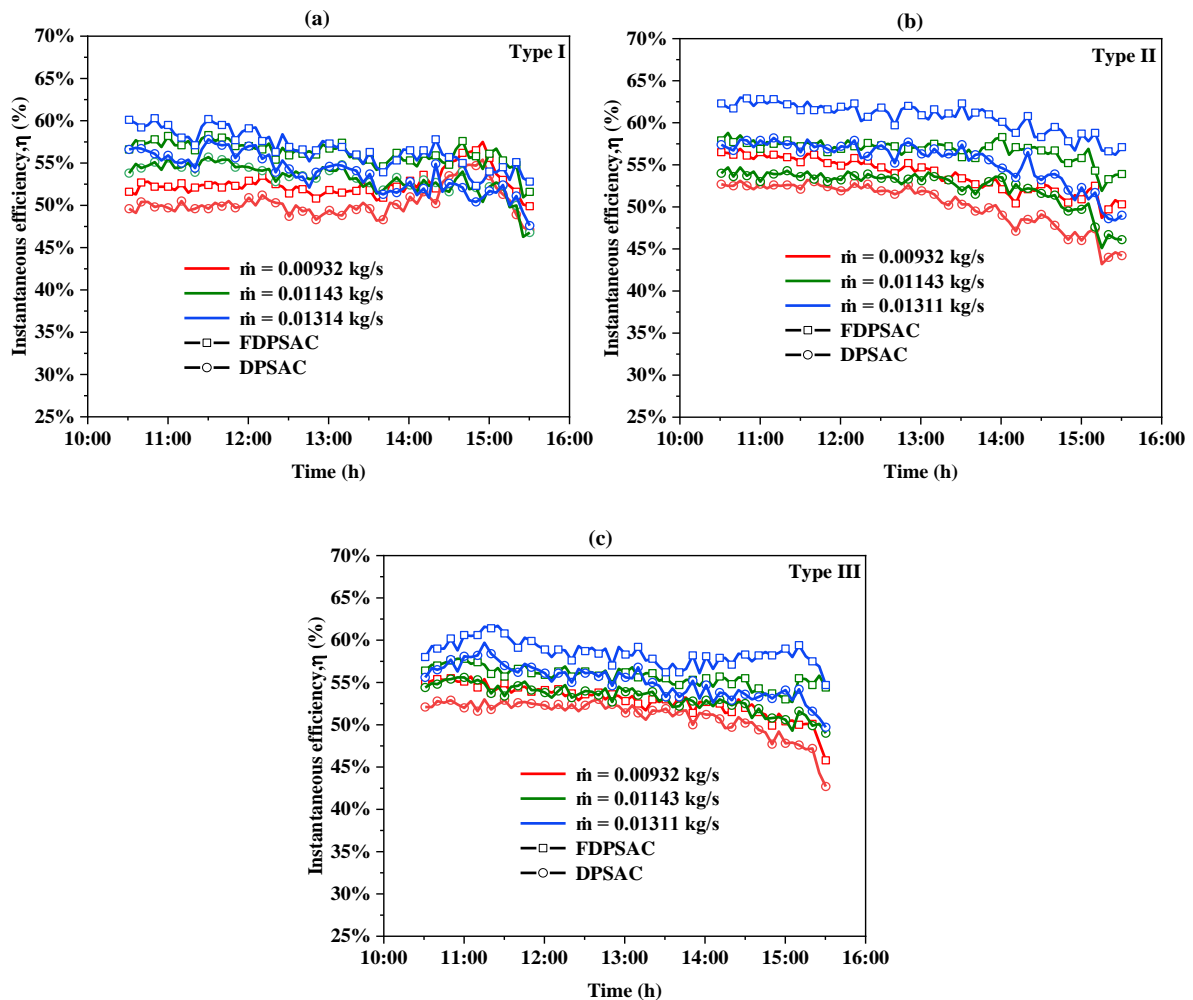
Instantaneous efficiency is sensitive to solar radiation fluctuations; for instance, cloud cover can quickly increase efficiency readings due to retained heat in the absorber. This variability highlights the importance of calculating daily thermal efficiency to assess performance reliably, consistent with prior studies. Fig. 4.23 displays daily efficiency trends across each fin

configuration, demonstrating that finned collectors consistently achieve higher efficiencies than smooth collectors across all MFRs. For instance, the FDPSAC with *Type I* fins reached daily efficiencies of 52.5%, 54.9%, and 56.9% at MFRs of 0.00932 kg/s, 0.01143 kg/s, and 0.01311 kg/s, respectively, compared to 50.4%, 52.3%, and 54.1% for smooth collectors at the same rates (see Fig. 4.23 a). *Type II* fins, shown in Fig. 4.23 b), achieved the highest daily efficiencies overall, with the FDPSAC recording values of 53.6%, 56.9%, and 60.7%, outperforming DPSAC's 50.6%, 52.7%, and 55.6%. For *Type III*, shown in Fig. 4.23 c), the FDPSAC achieved efficiencies of 53.3%, 55.8%, and 58.7%, compared to DPSAC's 51.1%, 53.1%, and 55.3%.

This comparison across fin orientations shows *Type II* fins achieving the highest efficiency, followed by *Type III*, with *Type I* fins showing the lowest. This order underscores the importance of fin design and orientation in maximizing heat transfer and enhancing collector efficiency. Relative daily efficiency improvements were achieved in the range of 4.1% to 9.1% across all fin orientations, with *Type I* showing improvements between 4.1% and 5.1%, *Type II* between 5.9% and 9.1%, and *Type III* between 4.3% and 6.1%. These findings emphasize the effectiveness of the perforated discrete V-angled fin design in FDPSAC, significantly boosting efficiency by enhancing heat transfer and underscoring the critical role of fin design in optimizing solar collector performance
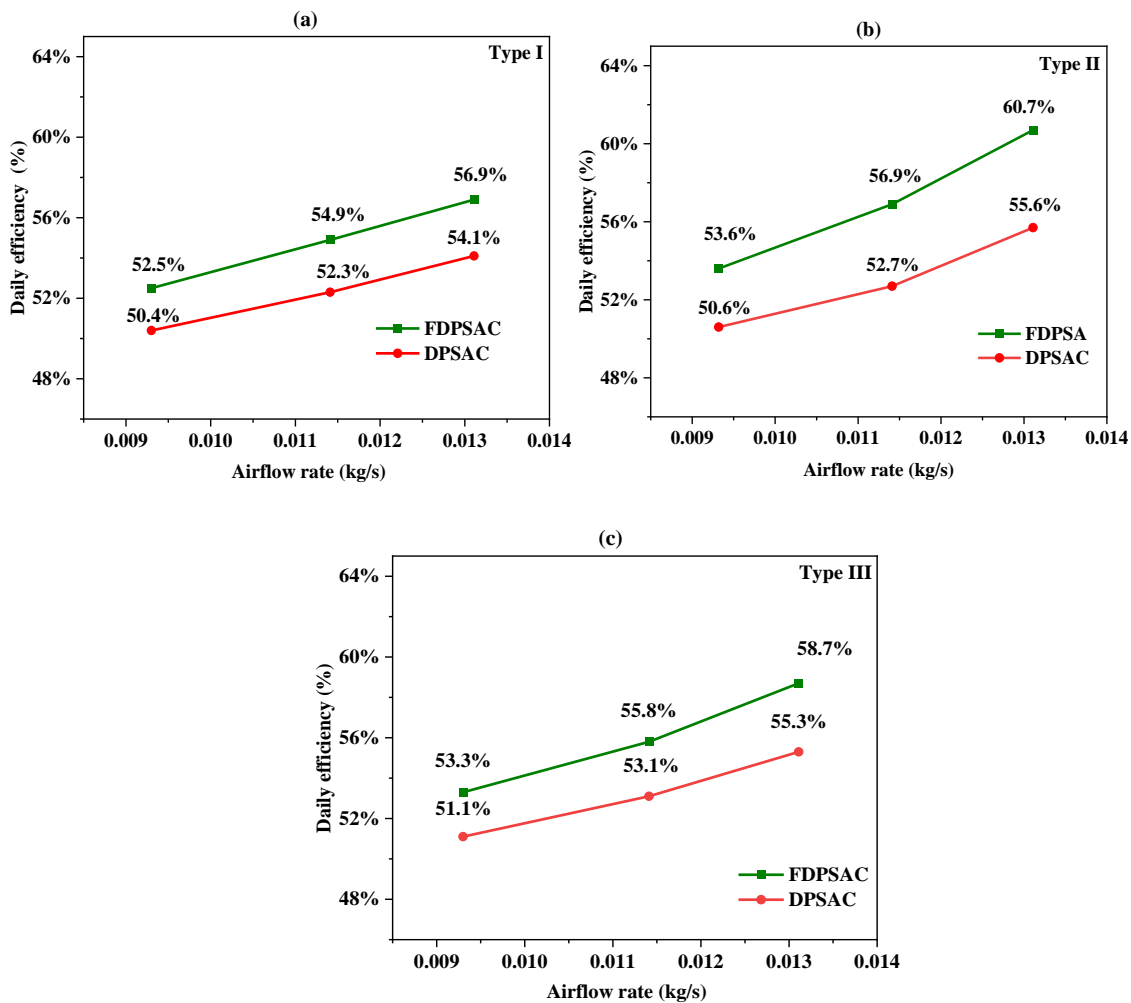

Fig. 4.23. Daily thermal efficiency versus MFRs

4.3. Impact of selective coatings evaluation

This section presents the experimental findings on the impact of selective coatings on the thermal performance of solar air collectors, focusing on efficiency and heat transfer characteristics for both single-pass and double-pass configurations. To evaluate this, two identical collectors were tested under identical outdoor conditions: one with a solar selective coating (SOLKOTE HI/SORB-II) and the other with a standard black matte coating. Performance was assessed across various mass flow rates to capture behaviour under different operational conditions. Key performance metrics include thermal efficiency, temperature differentials, and heat transfer rates.

For SPSAC, the mass flow rates were 0.00946 kg/s, 0.01388 kg/s, 0.02158 kg/s, and 0.02629 kg/s. The DPSAC was evaluated with mass flow rates of 0.00877 kg/s, 0.01059 kg/s, 0.01425 kg/s, and 0.01632 kg/s.

Fig. 4.24 illustrates the variations in solar radiation and ambient temperature throughout the experiment for the four cases tested in both single and double-pass mode. Solar radiation increased gradually from the start of the experiments at 10:30, peaking around midday, and then declined towards the end of the observation period at 15:30. Continuous data on solar intensity and ambient temperatures were recorded for each case, providing key information for assessing the performance of the collectors with and without the selective coating. For the single pass mode (Fig. 4.24 a), at a MFR of 0.00946 kg/s, the maximum solar radiation was 967.8 W/m², while the ambient temperature reached 34.1 °C. At an MFR of 0.01388 kg/s, solar radiation reached a maximum of 981.2 W/m², and the ambient temperature was 29.7 °C. For an MFR of 0.02158 kg/s, the highest solar radiation recorded was 990.6 W/m², but the ambient temperature was the lowest at 28.6 °C. Lastly, at a MFR of 0.02629 kg/s, solar radiation reached 947.3 W/m², while the ambient temperature reached a maximum of 34.8 °C.
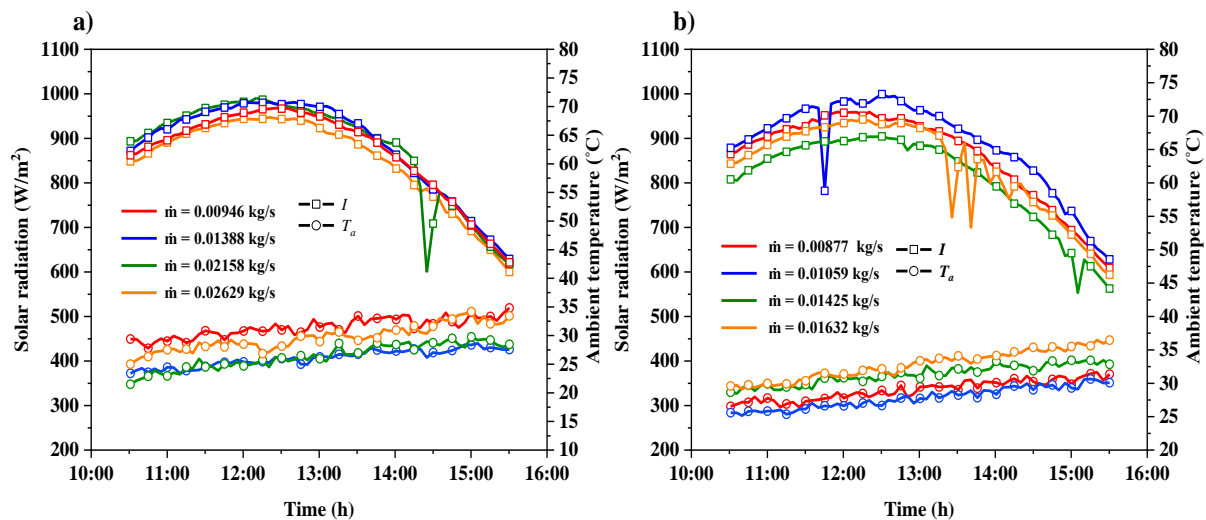
Fig. 4.24. Solar power and ambient temperature variations during tests for (a) SPSAC and (b) DPSAC

In the double-pass mode (Fig. 4.24b), at a MFR of 0.00877 kg/s, the maximum solar radiation was 959.2 W/m², while the ambient temperature reached 31.6 °C. At an MFR of 0.01059 kg/s, solar radiation reached a peak of 999.2 W/m², while the ambient temperature was 30.6 °C. At an MFR of 0.01425 kg/s, the maximum solar radiation recorded was 904.3 W/m², accompanied

by an ambient temperature of 33.4 °C. Finally, at the highest MFR of 0.01632 kg/s, solar radiation reached 942.2 W/m², and the ambient temperature reached 36.4 °C. While solar radiation remained relatively stable across the different configurations, variations in ambient temperature were more pronounced. The MFRs of 0.00877 kg/s and 0.02629 kg/s in their respective configurations exhibited the highest ambient temperatures, while the 0.02158 kg/s and 0.01059 kg/s rates recorded the lowest temperatures of 28.6 °C and 30.6 °C, respectively. Despite these differences, solar radiation levels remained consistently high throughout the testing period, providing reliable conditions to compare the thermal performance of the collectors.

Fig. 4.25 presents the variations in absorber plate temperatures over time for different MFRs in both the single-pass mode and the double-pass mode. The absorber plate temperatures rise throughout the morning as solar radiation increases, reaching their peak around midday, before gradually decreasing as solar intensity declines in the afternoon. This trend is observed across all tested configurations and MFRs, demonstrating the close relationship between solar radiation and the absorber plate's thermal behaviour. For the single pass solar air collector with selective coatings (SPSAC-Se) (Fig.4.25 a), the maximum absorber plate temperatures recorded at MFRs of 0.00946 kg/s, 0.01388 kg/s, 0.02158 kg/s, and 0.02629 kg/s were 90.5 °C, 84.1 °C, 76.4 °C, and 75.3 °C, respectively. In comparison, the collector with a standard black matte coating (SPSAC-Bl) exhibited lower temperatures under the same conditions, with maximum values of 84.6 °C, 78.8 °C, 72.3 °C, and 70.6 °C for the corresponding MFRs.

In the double-pass mode (Fig. 4.25 b), the maximum absorber plate temperatures for the collector with selective coating (DPSAC-Se) were recorded as 66.4 °C, 61.7 °C, 59.1 °C, and 57.1 °C for the MFRs of 0.00877 kg/s, 0.01059 kg/s, 0.01425 kg/s, and 0.01632 kg/s, respectively. In contrast, the black matte-coated collector (DPSAC-Bl) exhibited slightly lower maximum temperatures under identical conditions, with values of 64.9 °C, 60.5 °C, 57.6 °C, and 55.8 °C. These findings underscore the selective coating's effectiveness in enhancing thermal performance through improved energy absorbing and reduced heat loss. The difference in absorber plate temperatures between single-pass and double-pass modes is significant, with the selective coating maintaining higher temperatures than the black matt coating in both configurations. In single-pass collectors, this temperature advantage leads to enhanced heat absorption, directly increasing the outlet temperature and overall heat gained. In double-pass collectors, although the absorber temperatures are lower, the selective coating still promotes higher outlet temperatures and improved thermal performance compared to the black matt coating. Thus, the selective coating effectively enhances the performance of the collector by maximizing energy absorbing and minimizing heat losses, regardless of the collector configuration.

An inverse relationship between MFR and absorber plate temperature is observed in both modes: as the MFR increases, the absorber plate temperature decreases. For instance, at the highest MFR of 0.02629 kg/s in the SPSAC, both collectors recorded their lowest temperatures, whereas at the lowest MFR of 0.00946 kg/s, the highest temperatures were achieved, reflecting the longer time available for heat transfer at lower MFRs.
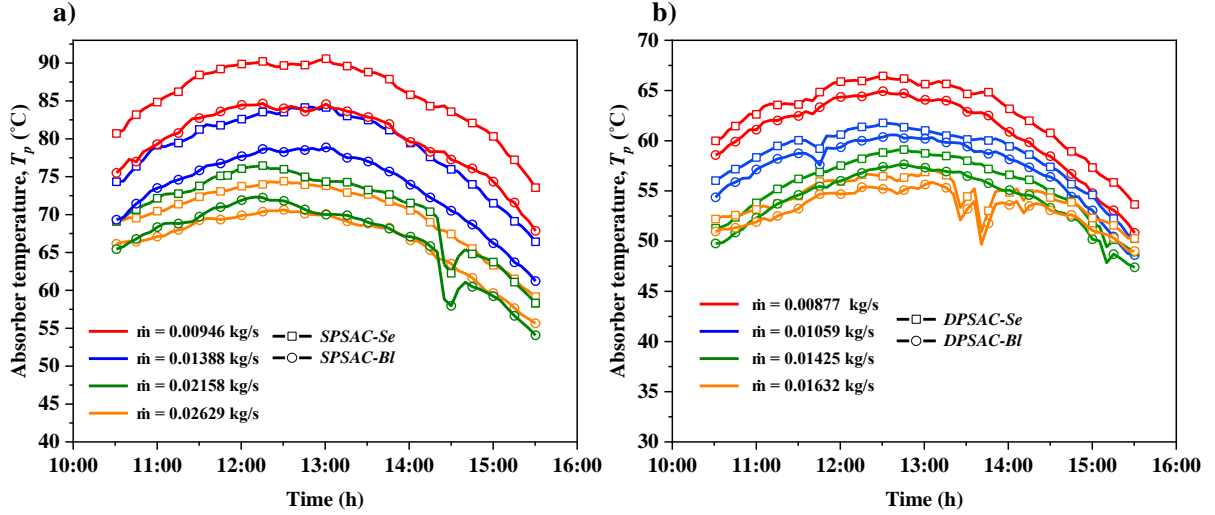
Fig. 4.25. Temperature variations of the absorbing plate over time for (a) SPSAC and (b) DPSAC

Similarly, in the double-pass mode, the highest MFR of 0.01632 kg/s resulted in lower temperatures, while the lowest MFR of 0.00877 kg/s yielded the highest temperatures. To quantify the relationship between solar radiation intensity I (W/m²), MFR (kg/s), and absorber plate temperature T_p (°C), quadratic regression models with interaction terms were applied to both configurations. The general form of the regression equation used to estimate the absorber plate temperature is:

$$\hat{T}_p = a \cdot I + b \cdot \dot{m} + a_2 \cdot I^2 + b_2 \cdot \dot{m}^2 + d \cdot I \cdot \dot{m} + c$$

The coefficients and model accuracy for both selective and non-selective configurations are summarized in Table 4.4. Both models exhibit a high degree of accuracy, as reflected by the R^2 values, indicating that most of the variance in absorber plate temperature is effectively captured by the models.

Table 4.4. Coefficients and R^2 values for selective and non-selective coatings

Coefficient	a	b	a$_2$	b$_2$	d	c	R²
SPSAC-Se	0.0436	-3691.7	5.22×10^{-7}	82244.8	-0.1167	76.22	0.969
SPSAC-Bl	0.0373	-3340.4	4.55×10^{-6}	74108.9	-0.0949	69.96	0.974
DPSAC-Se	0.0794	-6050.2	-1.572×10^{-5}	2.837×10^{5}	-2.4853	56.16	0.941
DPSAC-Bl	0.0938	-4498.1	-1.958×10^{-5}	2.429×10^{5}	-3.0049	38.26	0.946

Figs. 4.26 and 4.27 show the 3D plots of the regression results for both SPSACs and DPSACs. In these plots, the red circles represent the actual experimental data points, while the mesh surfaces represent the predicted absorber plate temperatures from the regression model. The model effectively captures the relationships between solar radiation intensity, mass flow rate, and absorber plate temperature for both types of collectors. The plots clearly indicate that as the mass flow rate decreases, the absorber plate temperature increases, as evidenced by the rising surfaces at lower flow rates. Additionally, an increase in solar radiation intensity correlates with a rise in temperature, as demonstrated by the upward slopes of the surfaces for both single-pass and double-pass modes. It is important to note that the model performs well

within the tested range of MFRs. However, predictions outside this range should be approached with caution, as the model has not been validated beyond these values.
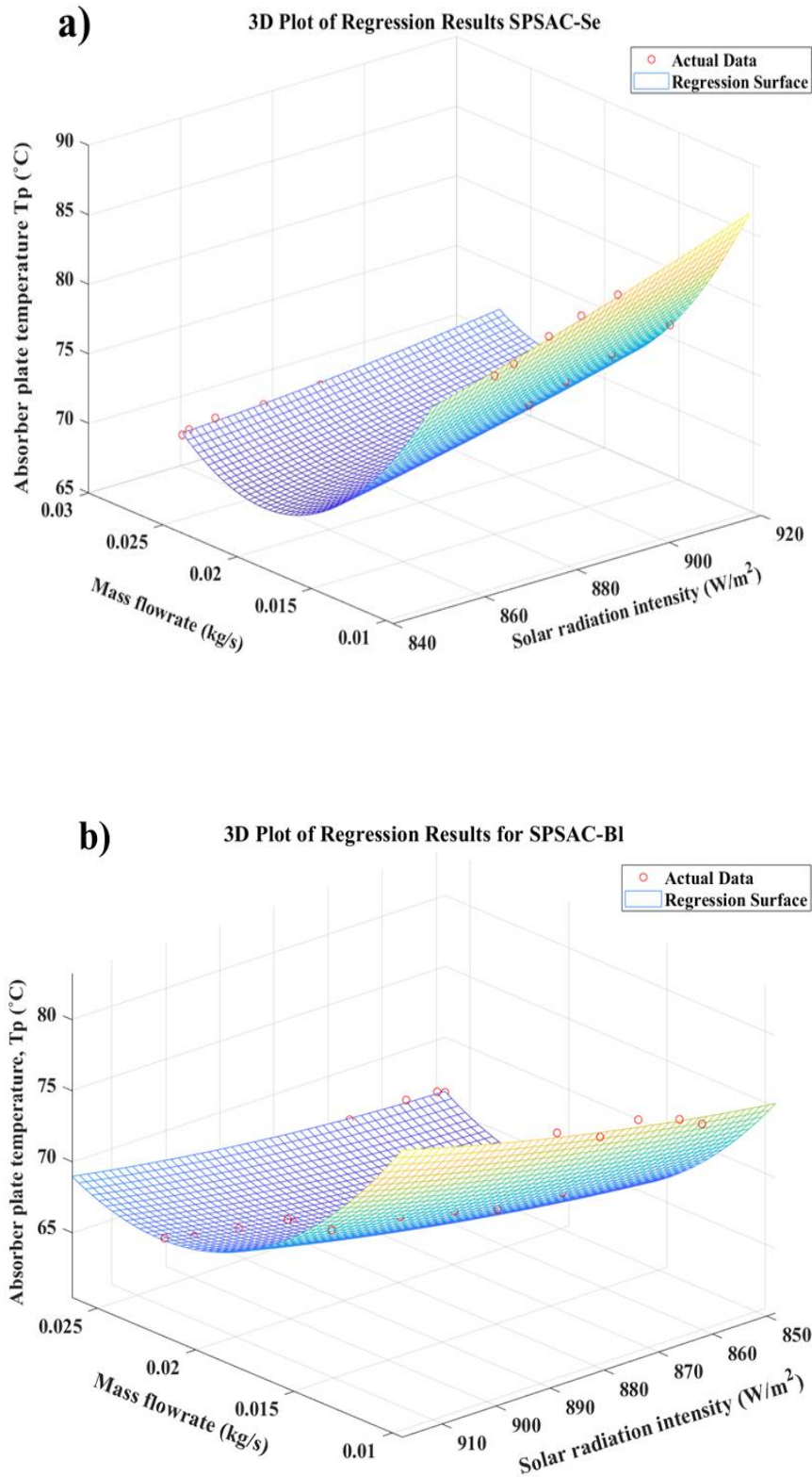
Fig. 4.26. 3D plot of the regression model for a) SPSAC-Se, b) SPSAC-BL, showing absorber plate temperature estimations and actual data points
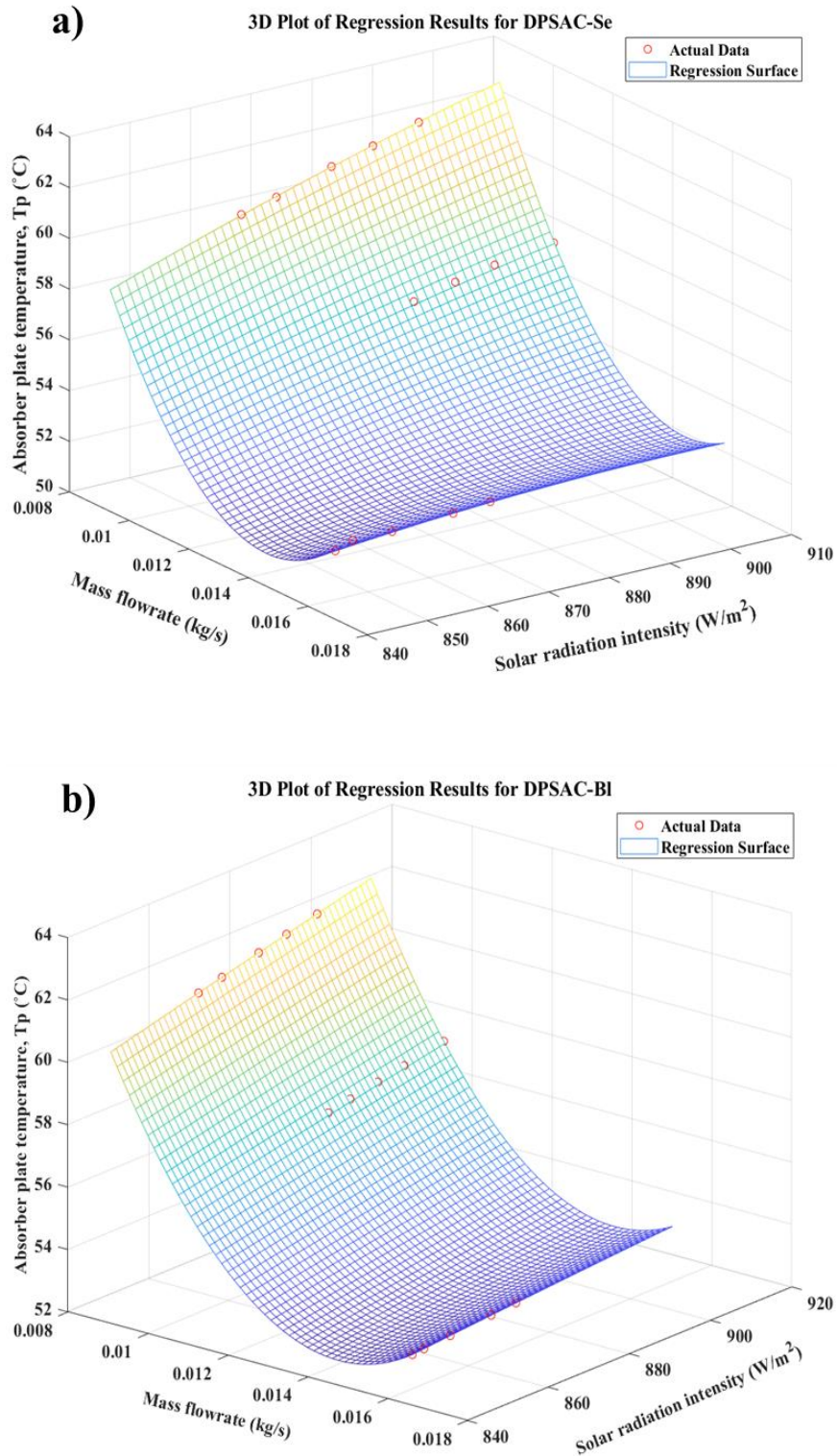
Fig. 4.27. 3D plot of the regression model for, a) DPSAC-Se, b) DPSAC-Bl showing absorber plate temperature estimations and actual data points

Fig. 4.28 shows the outlet temperature (T_o) profiles over time for different mass flow rates in both the single-pass and the double-pass mode. The outlet temperature in both modes increased steadily in the morning as solar radiation intensified, reaching peak values between 11:30 and 12:30, before gradually decreasing as the day progressed. The results indicate that as the mass

flow rate increases, the outlet temperature decreases. For the single-pass mode, at the highest flow rate of 0.02629 kg/s, the SPSAC-Se recorded a maximum outlet temperature of 42.5 °C, slightly higher than the 41.6 °C of the SPSAC-Bl. As the flow rate decreased, the difference in outlet temperatures between the two single-pass modes became more pronounced, with maximum temperatures of 50.4 °C for SPSAC-Se and 49.5 °C for SPSAC-Bl at the lowest flow rate of 0.00946 kg/s.

For the intermediate flow rates, 0.02158 kg/s and 0.01388 kg/s, the SPSAC-Se reached maximum outlet temperatures of 39.2 °C and 45.5 °C, respectively. In contrast, the SPSAC-Bl recorded slightly lower temperatures of 37.9 °C and 43 °C for the same flow rates.

In the double-pass mode, at the highest flow rate of 0.01632 kg/s, the DPSAC-Se achieved a maximum outlet temperature of 50.4 °C, slightly higher than the 49.3 °C of the DPSAC-Bl. At the lowest flow rate of 0.00877 kg/s, the DPSAC-Se recorded a maximum temperature of 58.6 °C, compared to 57.7 °C for DPSAC-Bl. For intermediate flow rates of 0.01425 kg/s and 0.01059 kg/s, the DPSAC-Se reached outlet temperatures of 52 °C and 54.1 °C, respectively, while the DPSAC-Bl recorded lower temperatures of 51.1 °C and 53.2 °C.

These results demonstrate that the selective coating significantly improves thermal performance in both modes, particularly at lower MFRs where heat transfer efficiency is critical. The coating's high absorptivity and reduced radiative losses lead to higher outlet temperatures in both SPSAC-Se and DPSAC-Se, especially when air has more time to absorb heat. This underscores the coating's essential role in enhancing heat retention and overall thermal efficiency in solar air collectors.
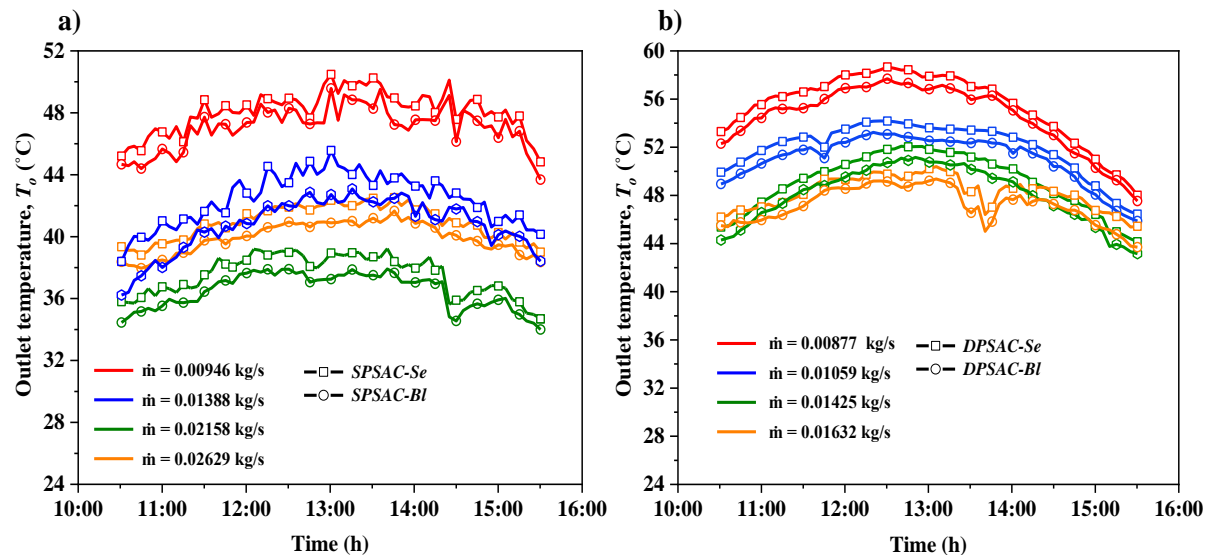
Fig. 4.28. Outlet temperature profiles for the collectors over time for (a) SPSAC and (b) DPSAC

Fig. 4.29 presents the temperature difference (ΔT) between the inlet and outlet air for both the single-pass and the double-pass collectors at different MFRs. The collectors were tested under outdoor conditions, where the inlet air often starts at or slightly below ambient temperature due to the forced airflow mechanism. The temperature differences reflect the impact of solar

radiation and ambient temperatures on heat transfer, with lower MFRs yielding larger ΔT values.

For the single pass mode (Fig. 4.29 a), at the highest MFR of 0.02629 kg/s, the SPSAC-Se recorded a maximum temperature difference of 13.2 °C, while the SPSAC-Bl showed a lower value of 11.9 °C. As the MFR decreased, the temperature difference increased. At 0.02158 kg/s, the SPSAC-Se and SPSAC-Bl reached 14.2 °C and 12.9 °C, respectively. For the MFR of 0.01388 kg/s, the SPSAC-Se achieved a ΔT of 19.9 °C, while the SPSAC-Bl recorded 17.3 °C. Finally, at the lowest MFR of 0.00946 kg/s, the SPSAC-Se reached a maximum ΔT of 22.5 °C, outperforming the SPSAC-Bl, which recorded 21.6 °C.

In the double-pass mode (Fig. 4.29 b), the DPSAC-Se recorded maximum ΔT values of 32.3 °C, 29.3 °C, 21.6 °C and 20.6 °C, at MFRs of 0.00877 kg/s, 0.01059 kg/s, 0.01425 kg/s, and 0.01632 kg/s, respectively. The DPSAC-Bl showed slightly lower values of 31.2 °C, 28.2 °C, 20.4 °C, and 19.8 °C for the same MFRs.

These results demonstrate a clear pattern: in both mode the collectors with selective coating consistently achieve higher ΔT values than their respective counterparts with black matt across all MFRs, particularly at lower flow rates where the air has more time to absorb heat. The selective coating enhances energy absorbing and retention, contributing to the observed higher ΔT in both single-pass and double-pass modes. Overall, the selective coating significantly improves thermal performance, underscoring its role in optimizing the performance of SACs.
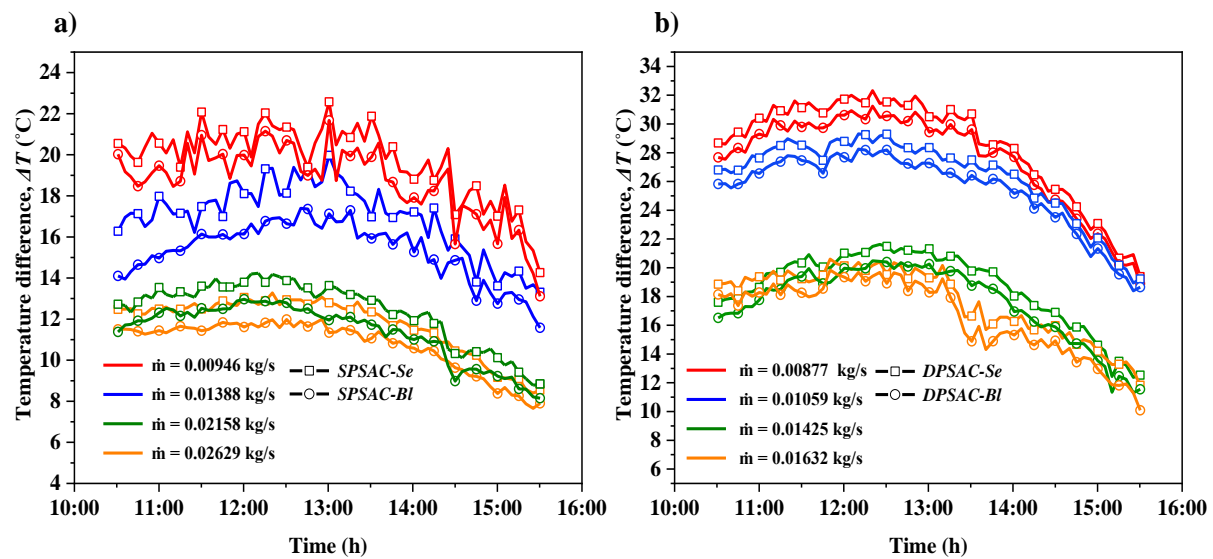
Fig. 4.29. The temperature difference across the collectors versus time for (a) SPSAC and (b) DPSAC

Fig. 4.30 illustrates the variation of the useful energy rate for the tested collector in both operational modes throughout the experiments. As shown in the figure, the energy rate output rises from mid-morning, peaks around midday, and then declines toward the end of the experiment, consistent with the patterns of solar radiation and temperature difference. This behaviour reflects the close relationship between solar radiation intensity, temperature difference, and useful heat generation in the collectors. The trend also highlights the significant influence of MFR on the heat output, with lower MFRs leading to higher heat accumulation

due to the longer residence time of air within the collector, allowing for more efficient heat transfer.

For single pass mode (Fig. 4.30 a), at the highest MFR of 0.02629 kg/s, the SPSAC-Se reached a maximum useful energy rate of 351.4 W, compared to 317.4 W for the SPSAC-Bl. As the MFR decreased, the useful heat rate values also declined. At 0.02158 kg/s, the SPSAC-Se achieved 309.3 W, while the SPSAC-Bl recorded 281.7 W. At 0.01388 kg/s, the SPSAC-Se produced 279.1 W, compared to 243.1 W for the SPSAC-Bl. Finally, at the lowest MFR of 0.00946 kg/s, the SPSAC-Se generated 215 W, outperforming the SPSAC-Bl, which produced 206.4 W.

In the double-pass mode (Fig. 4.30 b), the DPSAC-Se exhibited maximum useful energy rate of 285.4 W, 312.5 W, 310.3 W, and 338.6 W at MFRs of 0.00877 kg/s, 0.01059 kg/s, 0.01425 kg/s, and 0.01632 kg/s, respectively. The DPSAC-Bl displayed slightly lower outputs of 275.8 W, 301.3 W, 293.9 W, and 325.9 W for the same respective MFRs. The DPSAC-Se consistently outperformed the DPSAC-Bl, further confirming the effectiveness of the selective coating in enhancing thermal performance in double-pass configurations.

The results demonstrate that the collectors with selective coatings achieve higher heat rate gained than those with black matte coatings across all MFRs. This highlights the effectiveness of selective coatings in enhancing heat retention and overall thermal performance. Overall, the selective coating significantly enhances the thermal performance across both configurations, emphasizing its importance in maximizing energy output in solar thermal applications.
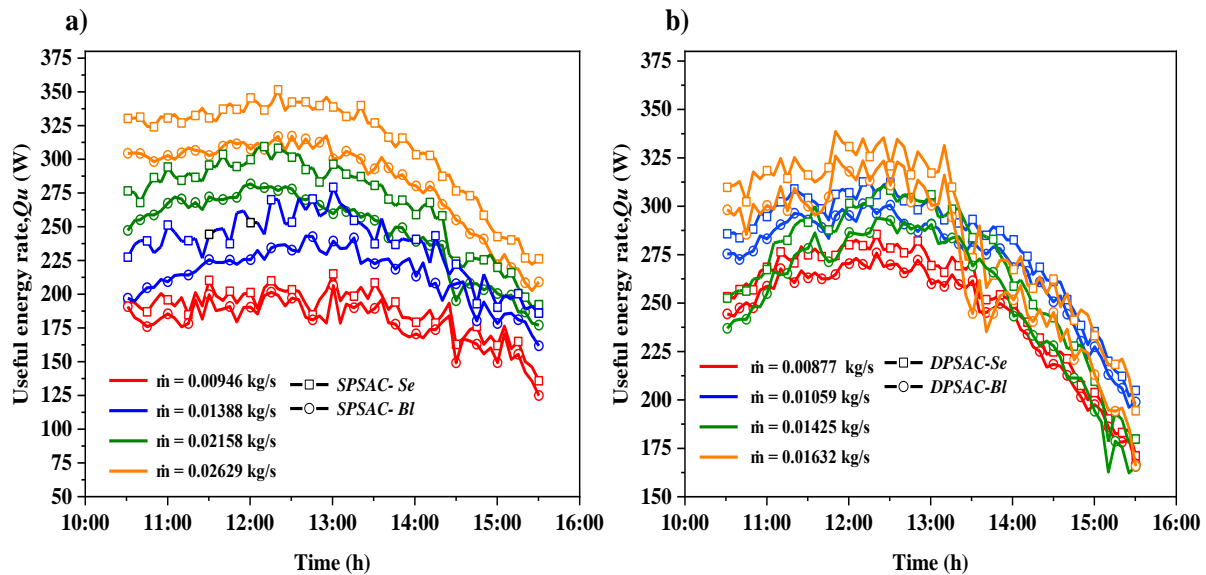
Fig. 4.30. Energy gain rate over time for (a) SPSAC and (b) DPSAC

Fig. 4.31 presents the instantaneous thermal efficiency trends for tested collectors at different MFRs. The instantaneous efficiency directly correlates with the MFR due to the increased heat transfer rates that enhance heat gain and optimize the collector's performance.

For the single pass mode (Fig. 4.31 a), at the highest MFR of 0.02629 kg/s, the SPSAC-Se reached a maximum thermal efficiency of 70.5%, compared to 65% for the SPSAC-Bl. As the MFR decreases, efficiency values drop accordingly. For 0.02158 kg/s, the SPSAC-Se achieved

a maximum efficiency of 69.2%, while the SPSAC-Bl reached 63.9%. At 0.01388 kg/s, the SPSAC-Se recorded 53.9%, compared to 49.3% for the SPSAC-Bl. Finally, at the lowest MFR of 0.00946 kg/s, the SPSAC-Se exhibited a maximum efficiency of 46.1%, slightly higher than the 44.6% recorded for the SPSAC-Bl.

In addition, for the double pass mode (Fig. 4.30 b), the maximum thermal efficiencies for the DPSAC-Se were recorded as 54.9%, 67.8%, 66.7%, and 68.3% at MFRs of 0.00877 kg/s, 0.01059 kg/s, 0.01425 kg/s, and 0.01632 kg/s, respectively. In comparison, the DPSAC-Bl exhibited thermal efficiencies of 53.1%, 65.6%, 61.6%, and 64.0% for the same MFRs.

The collectors with selective coatings consistently demonstrated superior efficiency compared to the black matt coated ones across all MFRs. This can be attributed to the ability of selective coatings to reduce radiative heat loss and enhance heat absorption.
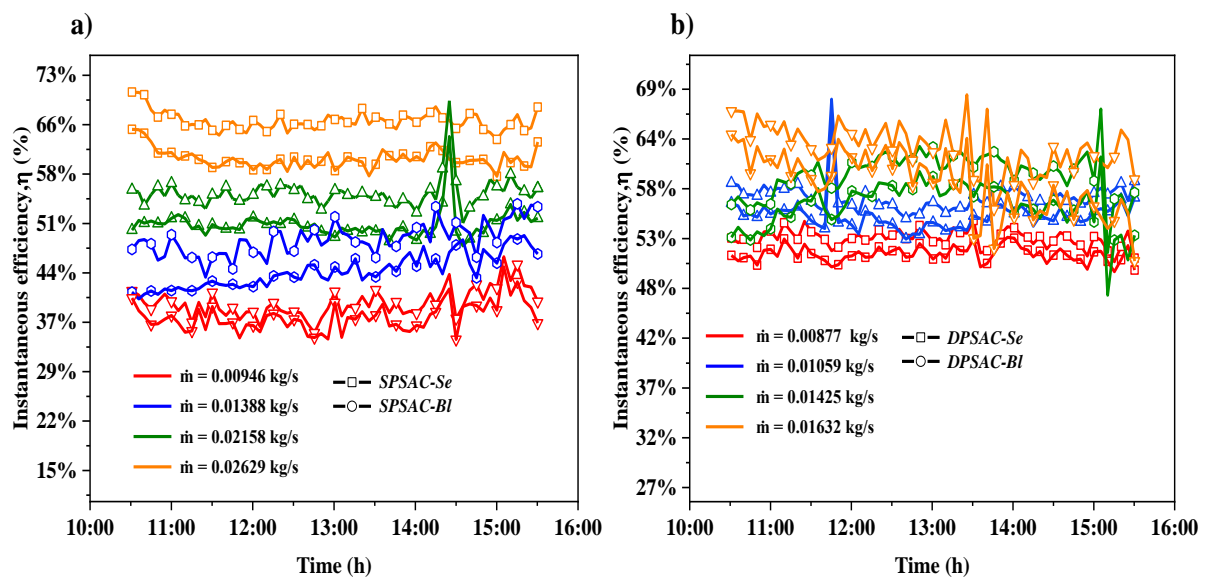
Fig. 4.31. Instantaneous thermal efficiency over time for (a) SPSAC and (b) DPSAC

Fig. 4.32 a) demonstrates a clear distinction in the daily efficiencies between the SPSAC-Bl and SPSAC-Se configurations across different MFRs. As the MFR increases, both collectors show an improvement in efficiency, but the SPSAC-Se consistently outperforms the SPSAC-Bl across all rates. Specifically, at a MFR of 0.00946 kg/s, SPSAC-Se achieves a daily efficiency of 39.2%, compared to 37.1% for SPSAC-Bl, marking a relative enhancement of 5.6%. At 0.01388 kg/s, SPSAC-Se records an efficiency of 48.6%, surpassing the 43.8% efficiency of SPSAC-Bl with a notable improvement of 10.9%. Similarly, at a MFR of 0.02158 kg/s, SPSAC-Se achieves 55.5%, exceeding the 50.8% efficiency of SPSAC-Bl, with relative enhancement of 9.0%. Finally, at 0.02629 kg/s, the efficiencies are 66.2% for SPSAC-Se and 60.6% for SPSAC-Bl, resulting in a 9.2% increase in performance.

The results for the double-pass mode also highlight the impact of selective coatings (Fig.4.32 b). For the DPSAC-Se, the maximum thermal efficiencies reached 53.1%, 57.3%, 60.1%, and 63.0% at MFRs of 0.00877 kg/s, 0.01059 kg/s, 0.01425 kg/s, and 0.01632 kg/s, respectively. In contrast, the DPSAC-Bl exhibited efficiencies of 51.4%, 55.3%, 56.7%, and 59.3% for the same MFRs, resulting in relative enhancements of 3.3%, 3.6%, 5.9%, and 6.2%.

These results across all mass flow rates underscore the superior thermal performance of selective-coated collectors in both single-pass and double-pass mode. The observed relative efficiency enhancement from 5.6% to 10.9% in single-pass mode and from 3.3% to 6.2% in double-pass mode highlight the effectiveness of selective coatings in minimizing radiative heat losses and enhancing energy absorption. While selective coatings reduce radiative heat losses in both configurations, the impact is more pronounced in the single-pass mode due to the higher absorber temperatures achieved, which amplify radiative losses. The low emittance of the selective coating is particularly beneficial under these conditions. In contrast, the typically lower absorber temperatures and potential temperature gradients in double-pass collectors may slightly offset the selective coating's ability to further reduce radiative losses.

The relative uncertainties of the parameters in this section were calculated using the same methodology described in the preceding section of the thesis. Consistent with this approach, daily average values for all variables were computed for each day of experimentation, followed by an overall mean derived from these daily averages. In the SPSAC configuration, the relative uncertainties for airflow rates and collector efficiency were found to be 1.58% and 2.62%, respectively. For the DPSAC configuration, these uncertainties were slightly different, with values of 1.62% for airflow rates and 2.60% for efficiency.
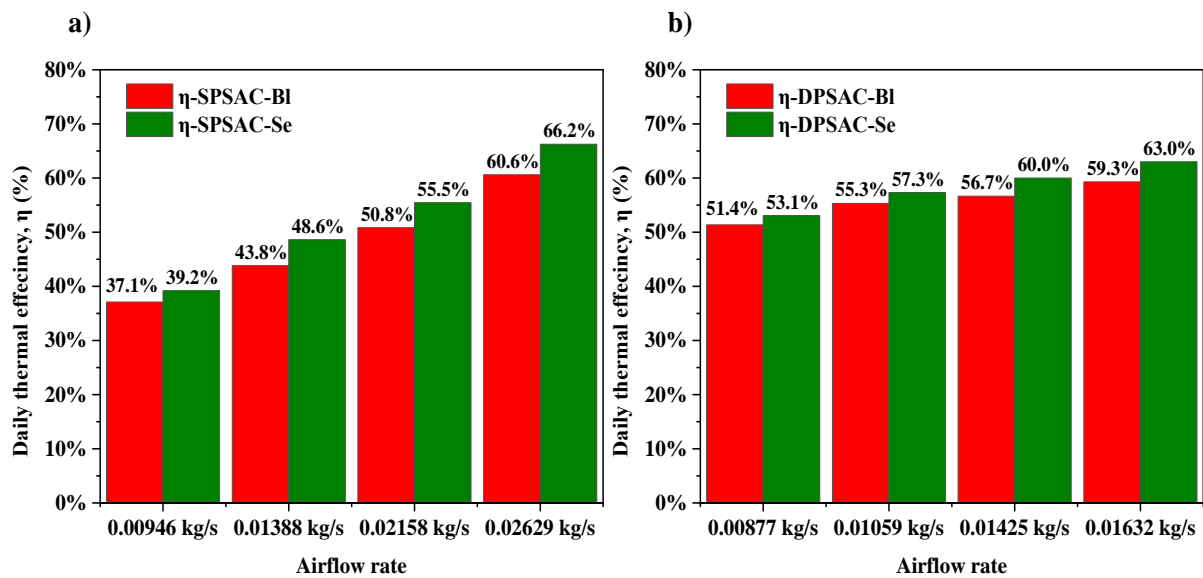
Fig. 4.32. The daily thermal efficiency versus airflow rate for (a) SPSAC and (b) DPSAC

4.4. Influence of channel depth evaluation

This section examines the effect of varying channel depths on the thermal performance of SACs. The depth of the air channel is a crucial design parameter that influences airflow patterns within the collector, thereby affecting heat transfer efficiency and overall system performance.

4.4.1. Effect on single pass mode

To ensure accuracy and consistency in the evaluation, the experimental procedures detailed in the previous chapter were accurately followed.

The experiments, conducted in August 2024, examined the performance of single-pass collectors with varying channel depths. In each experiment, two collectors were tested simultaneously: the reference collector, SPSAC-5.5 cm with a standard channel depth of 5.5 cm, and a modified collector with a different channel depth. One set of tests involved SPSAC-7.5 cm with an increased depth of 7.5 cm, while another set used SPSAC-3.5 cm with a reduced depth of 3.5 cm. Each configuration was tested at two flow rates, low and high, under consistent environmental conditions. This setup ensured that both collectors were exposed to the same ambient temperature and solar radiation, minimizing the impact of external variables and allowing for a focused assessment of how variations in channel depth influence collector performance.

Fig. 4.33 shows the variations in solar radiation intensity and ambient temperature across different mass flow rates during the experiments. Solar radiation generally increases in the morning, reaches its peak around midday, and decreases toward the end of the experiment at 15:30. The highest recorded solar radiation values for MFRs of 0.00892, 0.01813, 0.00901, and 0.01527 kg/s were 959.6 W/m², 935.7 W/m², 906.1 W/m², and 952.3 W/m², respectively. Similarly, the maximum ambient temperatures recorded were 35.5 °C, 37 °C, 28.8 °C, and 36.1 °C for the same MFRs. These values reflect the conditions under which the collectors were tested, with radiation and ambient temperature that influences the thermal performance of the solar air collectors.
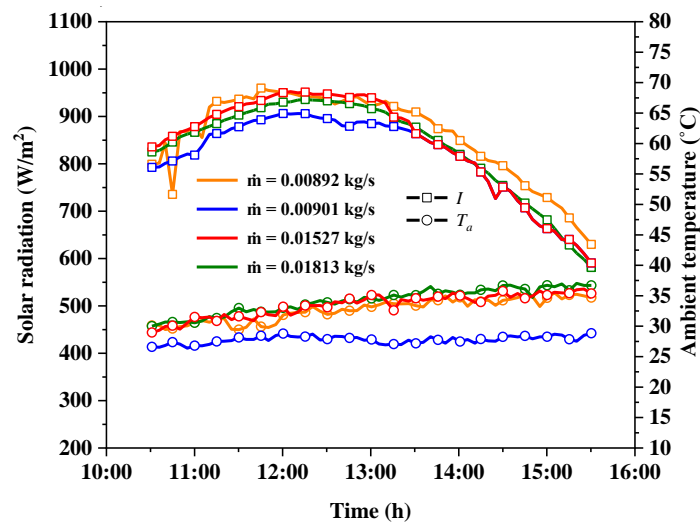
Fig. 4.33. The variations in solar power and ambient temperature during the test

Fig. 4.34 illustrates the variations in absorber plate temperatures over time for each tested channel depth configuration: SPSAC-7.5 cm, SPSAC-5.5 cm, and SPSAC-3.5 cm. The absorber plate temperatures generally follow the trend of rising solar radiation, peaking around midday, and decreasing as solar intensity reduces. This pattern is observed across all MFRs, highlighting the direct impact of solar radiation on absorber plate temperature.

For the SPSAC-5.5 cm and SPSAC-3.5 cm combination, the maximum recorded absorber plate temperatures were 89.1 °C and 87.1 °C, respectively, at a flow rate of 0.00892 kg/s, while at 0.01813 kg/s, the maximum temperatures were 83.4 °C and 80.9 °C. In the SPSAC-5.5 cm and SPSAC-7.5 cm combination, maximum absorber plate temperatures of 84.9 °C and 86.6 °C were recorded at 0.00901 kg/s, and 81.8 °C and 84 °C at 0.01527 kg/s.

These results demonstrate that the SPSAC with a 7.5 cm channel depth, the deepest among the configurations, retains heat more efficiently, resulting in higher absorber plate temperatures, especially at lower MFRs. The increased channel depth reduces air velocity at a given MFR due to the larger cross-sectional area, resulting in a lower convective heat transfer coefficient. Consequently, less heat is transferred to the air, leading to elevated absorber plate temperatures and increased heat losses to the surroundings. For example, at a low MFR of 0.00901 kg/s, the absorber plate temperature of the SPSAC-7.5 cm is 2.0% higher than that of the SPSAC-5.5 cm. At a higher MFR of 0.01527 kg/s, this difference increases to 2.6%. This behavior highlights that higher flow rates enhance convective cooling, reducing absorber plate temperatures more significantly in shallower configurations, while lower flow rates limit heat transfer, allowing the absorber plate to maintain higher temperatures in deeper configurations.

In contrast, SPSAC-3.5 cm, with the shallowest channel, promotes faster air velocity, enhancing convective heat transfer and cooling the absorber plate more effectively. This results in lower absorber plate temperatures, evidenced by a 2.2% temperature difference at the lower flow rate of 0.00892 kg/s and 3.0% at 0.01813 kg/s, demonstrating that increased air velocity at higher flow rates enhances the cooling effect. The SPSAC-5.5 cm provides a balanced performance, maintaining relatively stable absorber temperatures and efficiently managing heat transfer across various flow rates. This configuration achieves a compromise between heat retention and convective heat transfer, making it adaptable for consistent thermal performance regardless of flow rate. The moderate channel depth allows for sufficient air velocity to enhance convective cooling without causing excessive pressure drops or requiring additional pumping power.
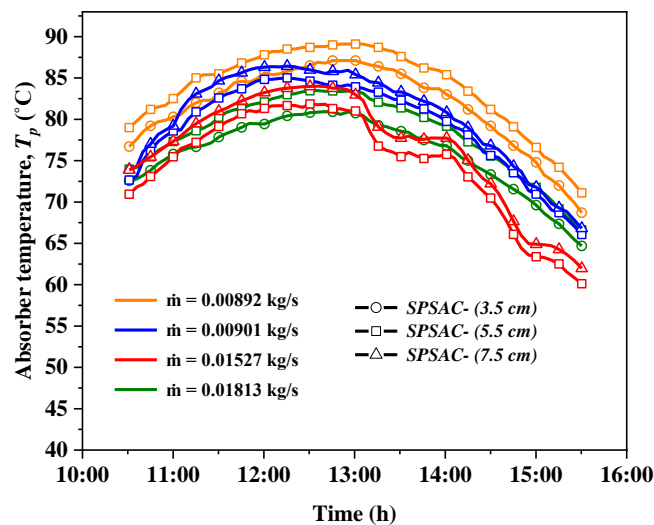
Fig. 4.34. Temperature variations of the absorber plate over time

Fig. 4.35 presents the outlet temperature profiles over time, illustrating the variation across different mass flow rates for each tested channel depth. The outlet temperatures across all configurations increase steadily in the morning as solar radiation increases, peaking between 11:30 and 12:30, and then gradually decline as solar intensity decreases in the afternoon. The data indicate that increasing the mass flow rate generally results in lower outlet temperatures across all channel depths.

At the lowest flow rate of 0.00892 kg/s, SPSAC-5.5 cm collector recorded a maximum outlet temperature of 52.9 °C, while SPSAC-3.5 cm achieved a slightly higher temperature of 54.2 °C. This suggests that at low flow rates, the shallower channel of SPSAC-3.5 cm allows for more effective heat transfer to the air. The reduced channel depth leads to higher air velocity within the collector for a given MFR, enhancing the convective heat transfer coefficient and resulting in a greater temperature rise of the outlet air. At the higher flow rate of 0.01813 kg/s, SPSAC-5.5 cm reached an outlet temperature of 47.7 °C, with SPSAC-3.5 cm reaching a temperature of 48.6 °C. This smaller difference suggests that the influence of channel depth on heat transfer efficiency is reduced as air velocity increases, with forced convection effects becoming more dominant and mitigating the performance advantage of the shallower channel.

For SPSAC-5.5 cm and SPSAC-7.5 cm combination, the maximum recorded outlet temperatures were 49.1 °C and 48.3 °C at a flow rate of 0.00901 kg/s, with SPSAC-5.5 cm slightly outperforming SPSAC-7.5 cm. At a higher flow rate of 0.01527 kg/s, however, SPSAC-5.5 cm reached a maximum outlet temperature of 50.2 °C, which was higher than SPSAC-7.5 cm at 48.9 °C. This consistent advantage for SPSAC-5.5 cm in maintaining higher outlet temperatures suggests that the moderate channel depth provides a balance between air velocity and convective heat transfer, enhancing thermal performance across different flow rates. The findings emphasize the impact of channel depth on thermal performance, particularly at lower flow rates where longer residence times facilitate greater heat transfer. The SPSAC-3.5 cm benefits from its shallow channel depth, promoting higher outlet temperatures at low flow rates due to rapid heat transfer. The SPSAC-5.5 cm demonstrates stable and balanced performance across flow rates, while the SPSAC-7.5 cm's deeper channel enhances heat retention but limits outlet temperatures, especially at higher flow rates where reduced residence time diminishes heat transfer efficiency. These trends correspond with the absorber plate temperature patterns discussed earlier, reinforcing the critical role of channel depth and flow rate in optimizing collector performance.
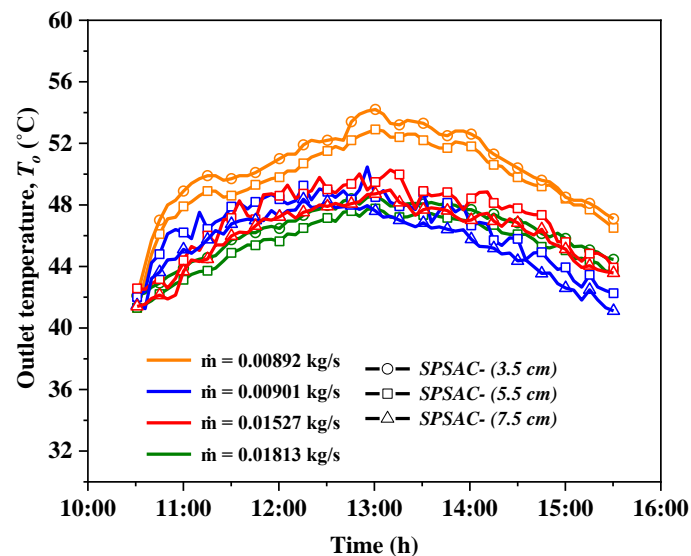

Fig. 4.35. Outlet temperature profiles for the collectors over time

Fig. 4.36 illustrates the variations in the temperature differential ΔT between the inlet and outlet temperatures throughout the experimental period. This differential is a key indicator of heat

extraction efficiency in SACs. A higher ΔT signifies enhanced heat transfer from the absorber plate to the airflow, directly influencing the SAC's overall thermal performance. Therefore, monitoring and optimizing ΔT is essential for improved efficiency.
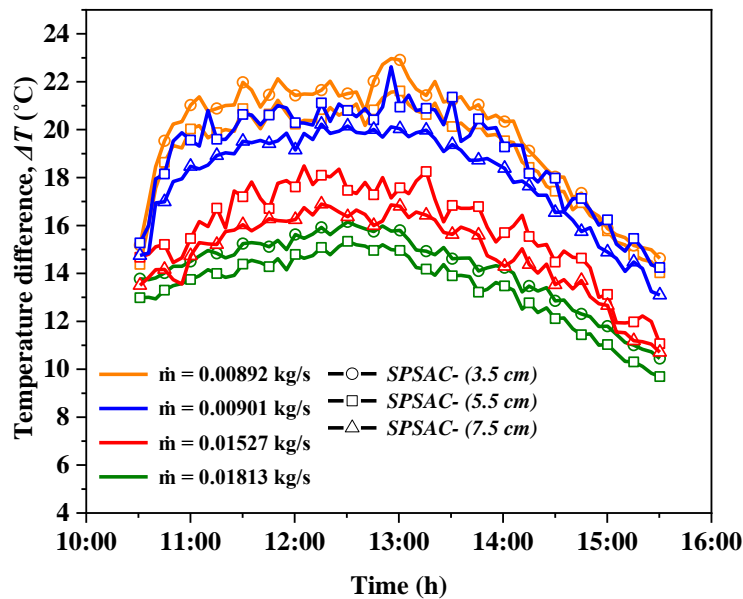

Fig. 4.36. The temperature difference across the collectors versus time

At the lowest flow rate of 0.00892 kg/s, SPSAC-3.5 cm achieved a maximum ΔT of 23 °C, while SPSAC-5.5 cm recorded a slightly lower ΔT of 21.6 °C. This demonstrates the advantage of the shallower channel in promoting heat transfer by increasing air velocity and the convective heat transfer coefficient. At the higher flow rate of 0.01813 kg/s, SPSAC-3.5 cm maintained a ΔT of 16.1 °C, with SPSAC-5.5 cm reaching a closer ΔT of 15.3 °C. The smaller difference in ΔT suggests that the influence of channel depth on heat transfer efficiency diminishes with increased air velocity.

For the 5.5 cm and 7.5 cm combination, at a flow rate of 0.00901 kg/s, SPSAC-5.5 cm recorded a maximum ΔT of 22.6 °C, while SPSAC-7.5 cm achieved a slightly lower ΔT of 20.2 °C. This indicates that at low flow rates, the shallower 5.5 cm channel provides better heat transfer efficiency due to the higher air velocity. At a higher flow rate of 0.01527 kg/s, SPSAC-5.5 cm achieved a ΔT of 18.5 °C, compared to 16.9 °C for SPSAC-7.5 cm. The consistent advantage of the SPSAC-5.5 cm highlights that excessive channel depth reduces heat transfer efficiency, particularly at higher flow rates where air velocity becomes more dominant.

These results highlight the importance of both MFR and channel depth on ΔT. The shallow channel in SPSAC-3.5 cm enhances heat extraction by increasing the convective heat transfer coefficient, while the deeper channel in SPSAC-7.5 cm limits it due to reduced air velocity and convective efficiency. Optimizing the balance between these factors is essential for maximizing thermal performance in SACs.

Fig. 4.37 illustrates the useful energy rate of the tested collectors over the experimental period. The useful heat rate increases from mid-morning, peaks around midday, and then declines in the afternoon, reflecting the influence of solar radiation and temperature difference. The mass flow rate significantly influences the heat output: higher flow rates enhance convective heat

transfer by increasing air velocity, whereas lower flow rates allow greater heat accumulation but may result in reduced overall heat extraction due to slower air movement.
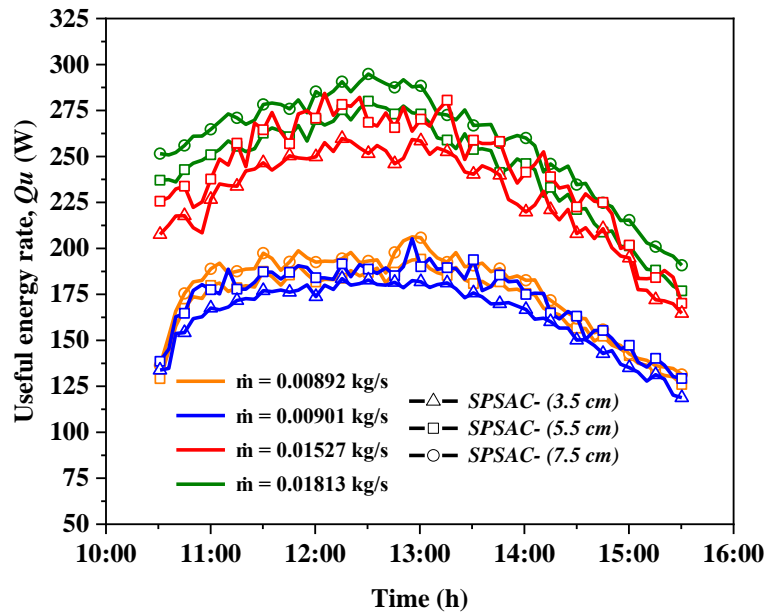

Fig. 4.37. Energy gain rate of the collectors over time

At a flow rate of 0.00892 kg/s, the SPSAC-3.5 cm collector demonstrated a maximum useful energy rate of 206.2 W, whereas the SPSAC-5.5 cm collector produced 194.1 W, representing a 6.2% reduction in output. This indicates that at low flow rates, the shallower 3.5 cm channel improves heat transfer by bringing air closer to the heated surface, raising the convective heat transfer coefficient and the outlet temperature. At a higher flow rate of 0.01813 kg/s, the SPSAC-3.5 cm collector achieved an energy rate of 292 W, which is only 4.2% greater than the 280 W produced by the SPSAC-5.5 cm collector. The smaller gap at higher flow rates shows the reducing influence of channel depth as air velocity increases. Nonetheless, raising the flow rate can reduce outlet temperature, which may be disadvantageous for applications requiring higher temperatures.

For the 5.5 cm and 7.5 cm channel depths, at 0.00901 kg/s, the SPSAC-5.5 cm achieved 205.2 W, which is 11% greater than the SPSAC-7.5 cm output of 183.5 W. This improvement is attributed to the moderate channel depth, which reduces the distance between the air and the absorber, thereby enhancing convective heat transfer. At 0.01527 kg/s, the SPSAC-5.5 cm recorded 284.3 W, which is 9.4% above the 259.7 W of SPSAC-7.5 cm. Although the difference narrowed at higher flow rates, channel depth continued to affect performance.

These findings underscore the importance of both mass flow rate and channel depth on useful energy rate and outlet air temperature. The deeper channel shows lower performance than the moderate and shallower channels, as evidenced by the relative enhancement of useful heat rate from 6.2% to 4.2% in the first combination and from 11% to 9.4% in the second combination. The shallower 3.5 cm and moderate 5.5 cm channels enhance heat extraction by increasing convective heat transfer, particularly at lower flow rates. In contrast, the deeper 7.5 cm channel lowers efficiency at low flow rates due to reduced air velocity and lower convective heat transfer.

Fig. 4.38 shows the instantaneous thermal efficiency of the tested collectors during the experiments. The trend highlights the significant influence of MFR on thermal efficiency, with higher MFRs generally enhancing efficiency due to increased convective heat transfer. Conversely, lower MFRs can lead to higher outlet temperatures but may reduce overall efficiency because of decreased useful heat rate gained resulting from lower air velocities.

For the SPSAC-5.5 cm and SPSAC-3.5 cm combination, the SPSAC-3.5 cm collector consistently outperformed the SPSAC-5.5 cm at both mass flow rates of 0.00892 kg/s and 0.01813 kg/s. At the lower flow rate of 0.00892 kg/s, the SPSAC-3.5 cm achieved a maximum instantaneous thermal efficiency of 43.2%, compared to 41.2% for the SPSAC-5.5 cm. This difference is attributed to the shallower channel of SPSAC-3.5 cm, which increases air velocity within the collector due to the reduced cross-sectional area. The higher air velocity enhances the convective heat transfer coefficient, improving the rate of heat transfer from the absorber plate to the air. At 0.01813 kg/s, SPSAC-3.5 cm collector reached a thermal efficiency of 59.4%, surpassing the 55.1% efficiency of SPSAC-5.5 cm, further illustrating the benefits of a higher MFR combined with a shallower channel for improved heat transfer.

In the comparison between SPSAC-5.5 cm and SPSAC-7.5 cm collectors, SPSAC-5.5 cm consistently outperformed SPSAC-7.5 cm at both MFRs. At 0.00901 kg/s, it achieved 41.8% maximum instantaneous efficiency compared to 39%, and at 0.01527 kg/s, it reached 58.3% versus 55.1%. The lower efficiency of SPSAC-7.5 cm is due to its deeper channel, which reduces air velocity and the convective heat transfer coefficient, leading to less effective heat transfer.

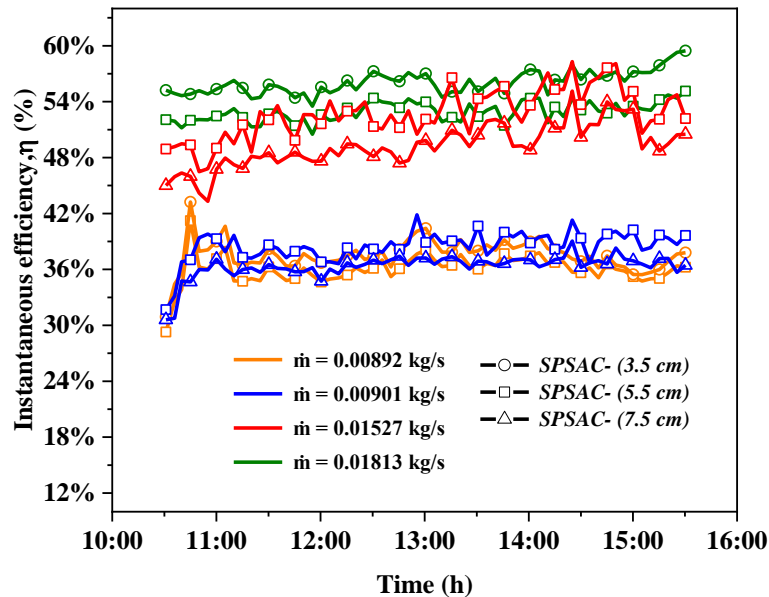Fig. 4.38. Instantaneous thermal efficiency over time

The daily efficiency of SAC configurations provides a comprehensive measure of heat output relative to solar radiation input over the day, offering a more stable metric compared to instantaneous efficiency. Fig. 4.39 presents the daily efficiencies for SPSAC-3.5 cm, SPSAC-5.5 cm, and SPSAC-7.5 cm at the relevant MFRs for each configuration.

The comparison between SPSAC-3.5 cm and SPSAC-5.5 cm collectors at MFRs of 0.00892 kg/s and 0.01813 kg/s highlights the superior daily efficiencies achieved by the shallower channel configuration. At 0.00892 kg/s, SPSAC-3.5 cm attains a daily efficiency of 37.6%, marking a 4.4% relative improvement over SPSAC-5.5 cm, which was 36%. Similarly, at the higher flow rate of 0.01813 kg/s, SPSAC-3.5 cm reaches an efficiency of 56%, outperforming SPSAC-5.5 cm of 52.9%, with a relative enhancement of 5.8%. This higher efficiency in SPSAC-3.5 cm is attributed to its reduced channel depth, which facilitates faster airflow by decreasing the cross-sectional area. The resulting increase in air velocity enhances the convective heat transfer coefficient, enabling more efficient heat transfer from the absorber plate to the passing air.

The comparison between SPSAC-5.5 cm and SPSAC-7.5 cm at MFRs of 0.00901 kg/s and 0.01527 kg/s highlights the consistent performance advantage of the moderate channel depth. At 0.00901 kg/s, SPSAC-5.5 cm reaches a daily efficiency of 38.5%, compared to 36.4% for SPSAC-7.5 cm, reflecting a 4.9% enhancement. Similarly, at 0.01527 kg/s, SPSAC-5.5 cm achieves 52.6%, while SPSAC-7.5 cm records 49.1%, resulting in a 7.1% improvement. The deeper channel in SPSAC-7.5 cm slows the airflow due to its larger cross-sectional area, reducing the convective heat transfer coefficient and overall thermal efficiency compared to SPSAC-5.5 cm.
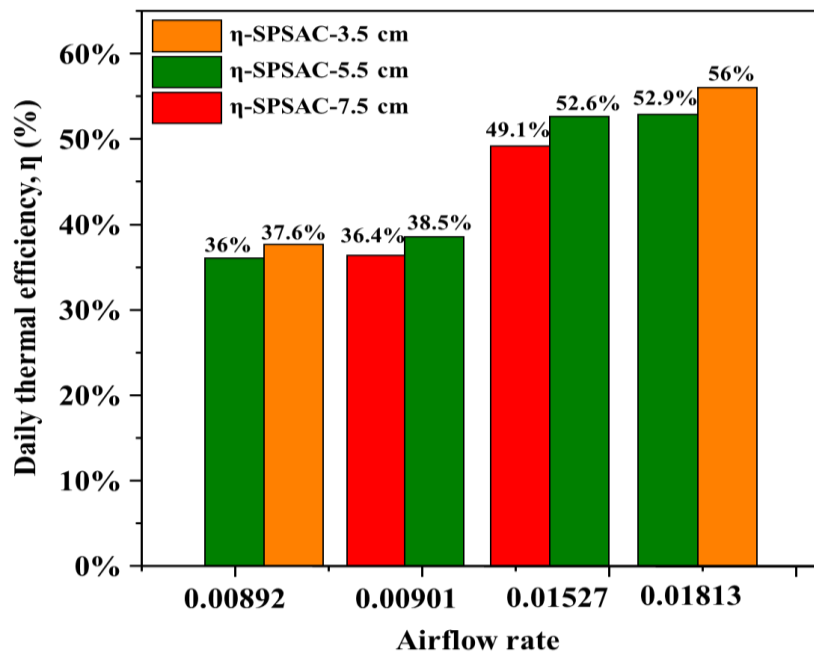
Fig. 4.39. The daily thermal efficiency versus airflow rate

Optimizing channel depth is essential for maximizing thermal performance in SACs. While shallower channels like SPSAC-3.5 cm offer higher efficiencies due to enhanced convective heat transfer, they also lead to increased pressure drops and energy consumption for air movement. For instance, the pressure drop for the 3.5 cm channel was measured at 17 Pa, compared to 14 Pa for the 5.5 cm channel at a flow rate of 0.00892 kg/s. This highlights the compromise between improved thermal performance and higher operational costs associated with shallower channels. The SPSAC-5.5 cm, with its moderate depth, strikes a practical balance, delivering high thermal efficiency while keeping pressure drops and energy

consumption relatively lower. In contrast, deeper channels, such as the SPSAC-7.5 cm, may reduce energy requirements for air movement but sacrifice thermal efficiency. By carefully selecting the channel depth and adjusting MFRs, designers can develop SACs tailored for a variety of applications, balancing performance and energy consumption.

4.4.2. Effect on double pass mode

The effect of channel depth on the performance of DPSAC was examined through mathematical modelling. Initially, experiments were conducted at a fixed upper channel depth of 5.5 cm to validate the model, using data collected at a mass flow rate of 0.0103 kg/s. The strong agreement between the experimental data and the mathematical model confirmed the model's accuracy. Following validation, the model was used to numerically analyse the impact of varying upper channel depths on DPSAC performance. This numerical analysis provided further insights into how channel depth adjustments affect thermal efficiency, complementing the experimental findings for single-pass collectors.

Fig. 4.40 compares the predicted and experimental results for the outlet temperature. The model exhibits excellent agreement with the experimental data, yielding R^2 values of 0.989. These high R^2 values indicate that the model accounts for 98.9% of the variability in outlet temperature, underscoring the model's accuracy and reliability in predicting DPSAC performance under the tested conditions.

Equation	y = a + b*x
Plot	To_ pr
Weight	No Weighting
Intercept	5.10583 ± 1.135
Slope	0.89757 ± 0.021
Residual Sum of Squares	1.00399
Pearson's r	0.99501
R-Square (COD)	0.98903
Adj. R-Square	0.98766
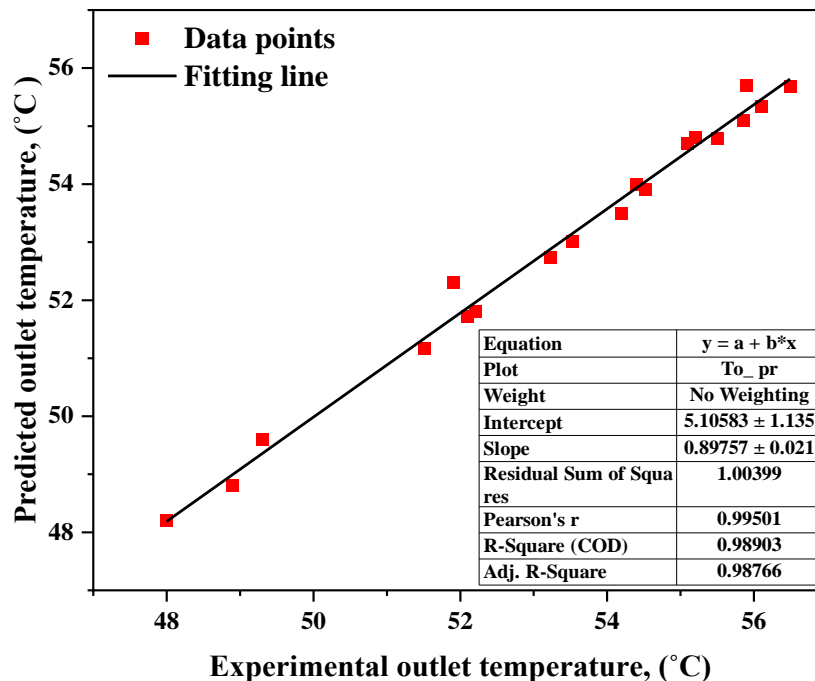
Fig. 4.40. Comparison of predicted and experimental data for outlet temperature

The derived equation was applied to the entire experimental dataset, effectively capturing all significant variations, as illustrated in Fig. 4.41. Furthermore, the model was tested against additional experimental data collected at mass flow rates of 0.0088, 0.0137, and 0.0143 kg/s. The results indicate that the R^2 values for the predicted outlet temperature ranged from 0.932

to 0.989, demonstrating a strong correlation and confirming that the model explains the majority of the variance in the experimental data.
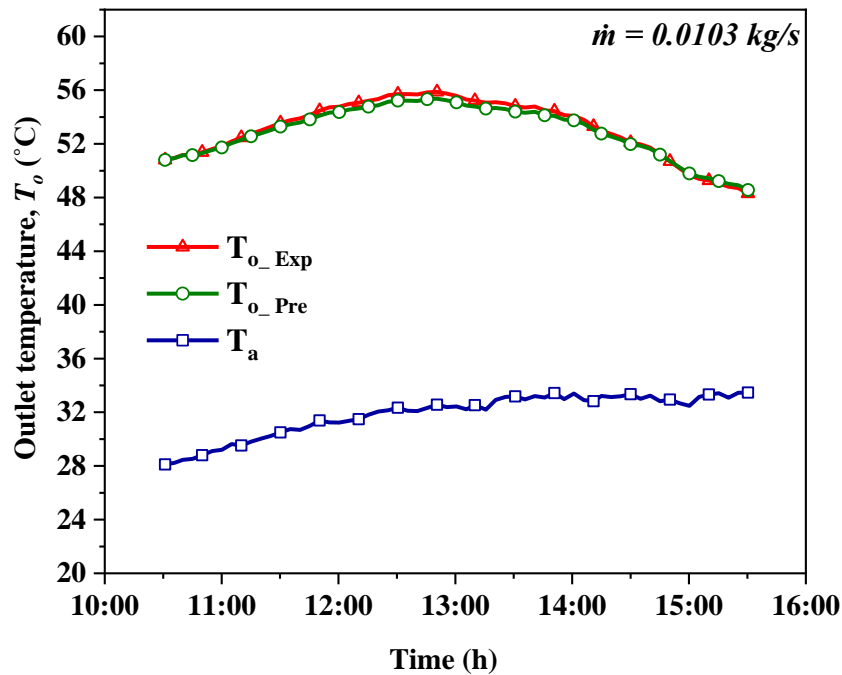

Fig. 4.41. Hourly variation of predicted and experimental data at MFR of 0.0103 kg/s

The model was employed to simulate the impact of channel depth on the performance of the DPSAC across various channel depths (2.5 cm, 3.5 cm, 5.5 cm, 7.5 cm, 9.5 cm, and 11.5 cm) and mass flow rates (0.0088 kg/s, 0.0103 kg/s, 0.0137 kg/s, 0.0151 kg/s, 0.0181 kg/s, and 0.021 kg/s). Fig. 4.42 illustrates the predicted outlet temperature for these configurations, while Fig. 4.43 presents the corresponding instantaneous thermal efficiency. Both sets of figures provide insight into how varying channel depths and flow rates influence the thermal performance of the collector, with distinct patterns emerging for each parameter.

At lower flow rates, such as 0.0088 kg/s in Fig. 4.42(a), the outlet temperature is highest for the shallowest channel (2.5 cm) and decreases as the channel depth increases. This trend is mirrored in Fig. 4.43(a), where the thermal efficiency follows a similar pattern, with the shallowest channels achieving the highest efficiency. These results indicate that at low flow rates, the trapped air in shallow channels has more contact with the absorber plate, enhancing heat transfer and leading to higher outlet temperatures and thermal efficiencies. Deeper channels, by contrast, allow air to move more freely, resulting in less effective heat transfer.

As the flow rate increases to 0.0103 kg/s and 0.0137 kg/s, shown in Fig. 4.42 (b, c) and Fig. 4.43 (b, c), the effect of channel depth on both outlet temperature and thermal efficiency begins to reduce. While shallower channels (2.5 cm and 3.5 cm) continue to outperform deeper ones, the differences between the two become less pronounced. This observation suggests that at moderate flow rates, the heat transfer process is increasingly driven by airflow velocity rather than channel depth. Nevertheless, shallower channels still provide slightly better performance, indicating their advantage under these conditions.
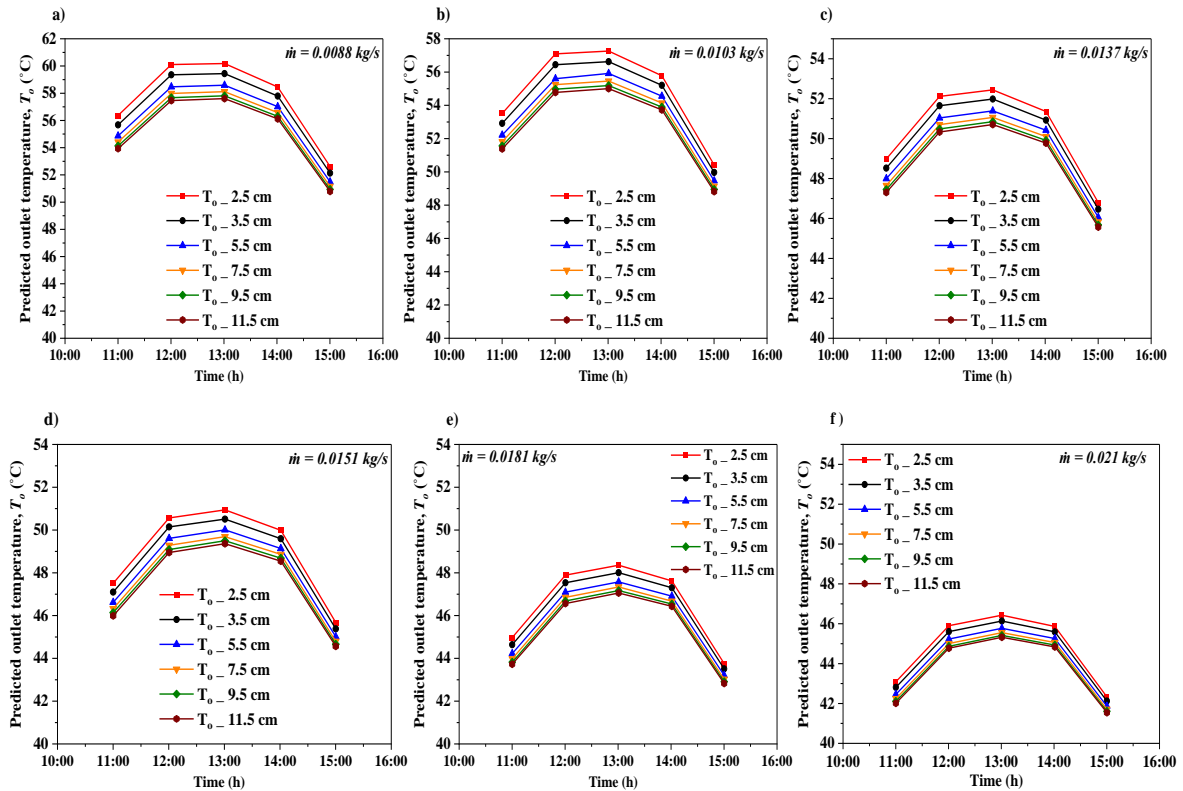
Fig. 4.42. Predicted outlet temperature over time for various channel depths and flow rates

At intermediate flow rates, such as 0.0151 kg/s in Fig. 4.42(d) and Fig. 4.43(d), the differences in performance among various channel depths become increasingly small. The outlet temperature and thermal efficiency begin to converge, indicating that the effect of channel depth is waning. At this stage, the mass flow rate plays a more significant role in determining overall thermal behaviour, which minimizes variations attributable to depth. As the flow rate increases further to 0.0181 kg/s and 0.021 kg/s in Fig. 4.42(e, f) and Fig. 4.43(e, f), the influence of channel depth is further diminished. The outlet temperature profiles across the different channel depths become nearly identical, and their thermal efficiencies also exhibit similar trends.

In conclusion, the combined analysis of outlet temperature and thermal efficiency reveals a distinct relationship between channel depth and mass flow rate in determining the DPSAC's performance. At lower flow rates, shallow channels significantly enhance thermal performance, resulting in higher outlet temperatures and efficiencies due to the improved heat transfer between the air and absorber plate. However, as the flow rate increases, the influence of channel depth progressively weakens. Beyond a certain point, particularly at higher flow rates, the airflow becomes the dominant factor, rendering the channel depth less impactful on both outlet temperature and efficiency. This behaviour underscores the importance of carefully balancing channel depth and flow rate to optimize the system's performance. By tailoring these parameters to the specific operational conditions, maximum efficiency and thermal output can be achieved across a wide range of flow rates. The results emphasize that while channel depth plays a critical role in the design of SACs, its effect is closely tied to the airflow conditions within the system. These simulation results corroborate the experimental observations and

reinforce the understanding of how channel depth and mass flow rate interact to affect thermal performance in SACs.
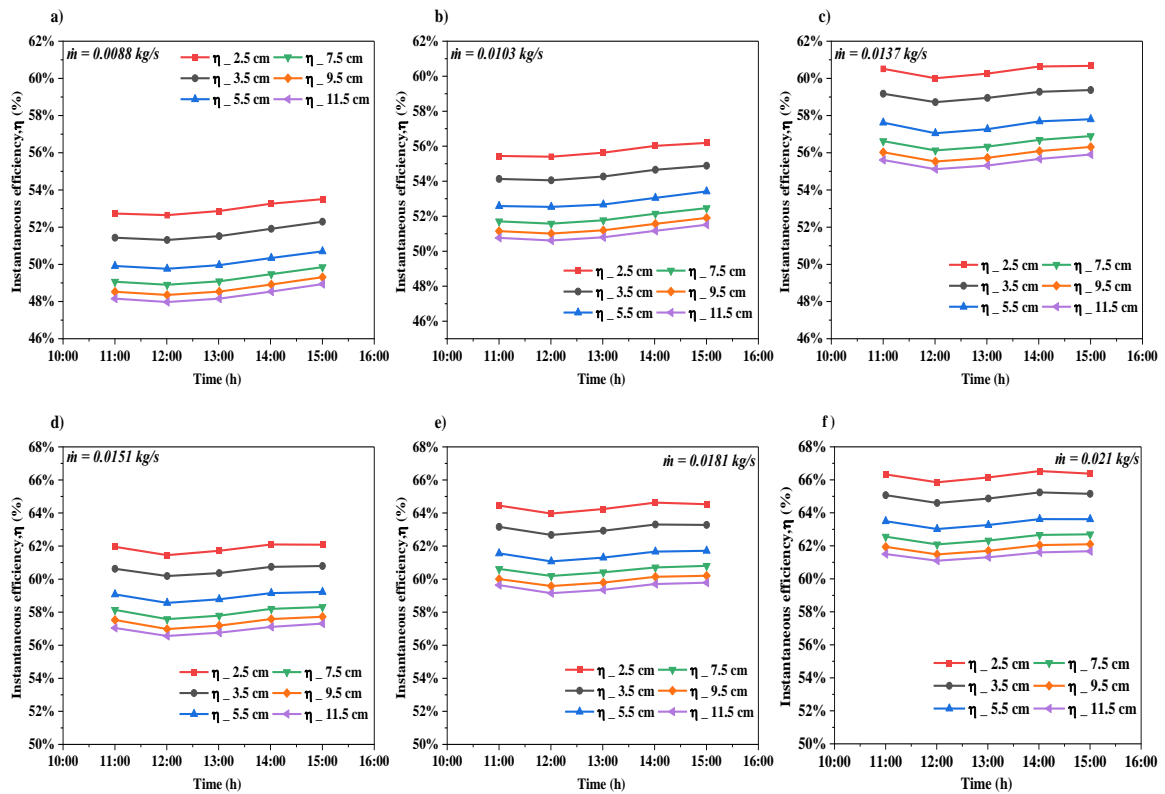
Fig. 4.43. Predicted instantaneous thermal efficiency over time for various channel depths and flow rates

4.5. Effect of different fins configuration on drying process

This section presents the experimental results on the effect of different fin shapes and orientations on the drying efficiency within SACs. The study aims to determine how variations in fin configuration influence the thermal efficiency and drying rates during the drying process of apple slices. To achieve this, four distinct absorber configurations were tested under identical conditions: *Type I*, with fins oriented parallel to the airflow; *Type II*, with fins inclined at a 45° angle to the airflow; *Type III*, with fins perpendicular to the airflow; and *Type IV*, incorporating continuous V-angled fins placed perpendicular to the airflow. Each configuration was evaluated based on its impact on drying performance across a five-hour test period, considering key parameters such as outlet temperature, absorber plate temperature, airflow rates, humidity levels, and temperature variations inside the drying chamber.

For each experiment, two DPSACs were connected to separate drying chambers: one chamber contained the test configuration with the finned absorber plate, while the other chamber housed the smooth absorber plate as a control. Each chamber held 1200 grams of uniformly cut apple slices, ensuring comparable initial conditions. All experiments were conducted under a single airflow rate and repeated on multiple days to ensure data reliability. This parallel testing approach allowed for a direct assessment of drying rates, thermal efficiency, and temperature profiles, providing insights into the effectiveness of fin orientation and shape in enhancing drying performance.

106

Fig. 4.44 (a–d) illustrates the profiles of ambient, outlet, and absorber plate temperatures over time during the experiments. As discussed in previous sections, the absorber plate temperature increases gradually with rising solar intensity, reaching its peak around noon, after which it begins to decline until the end of the experiment. This trend is mirrored in the outlet temperature as well. For all experimental configurations, the absorber plate temperature in the finned collector is consistently lower than that of the smooth plate collector. For *Type I*, the maximum recorded temperature for the FDPSAC absorber plate was 64.9 °C, compared to 66.5 °C for the smooth DPSAC. Similarly, for *Type II*, the maximum temperature was 62.3 °C compared to 63.8 °C for the DPSAC. For *Type III*, the highest outlet temperature recorded was 61.3 °C, compared to 62.6 °C for the smooth collector. Finally, for *Type IV*, the maximum temperature recorded was 61.3 °C for the FDPSAC compared to 62.7 °C for the smooth DPSAC. This consistent reduction in absorber plate temperature is attributed to enhanced heat transfer facilitated by the fins, which dissipate heat more effectively from the absorber plate.
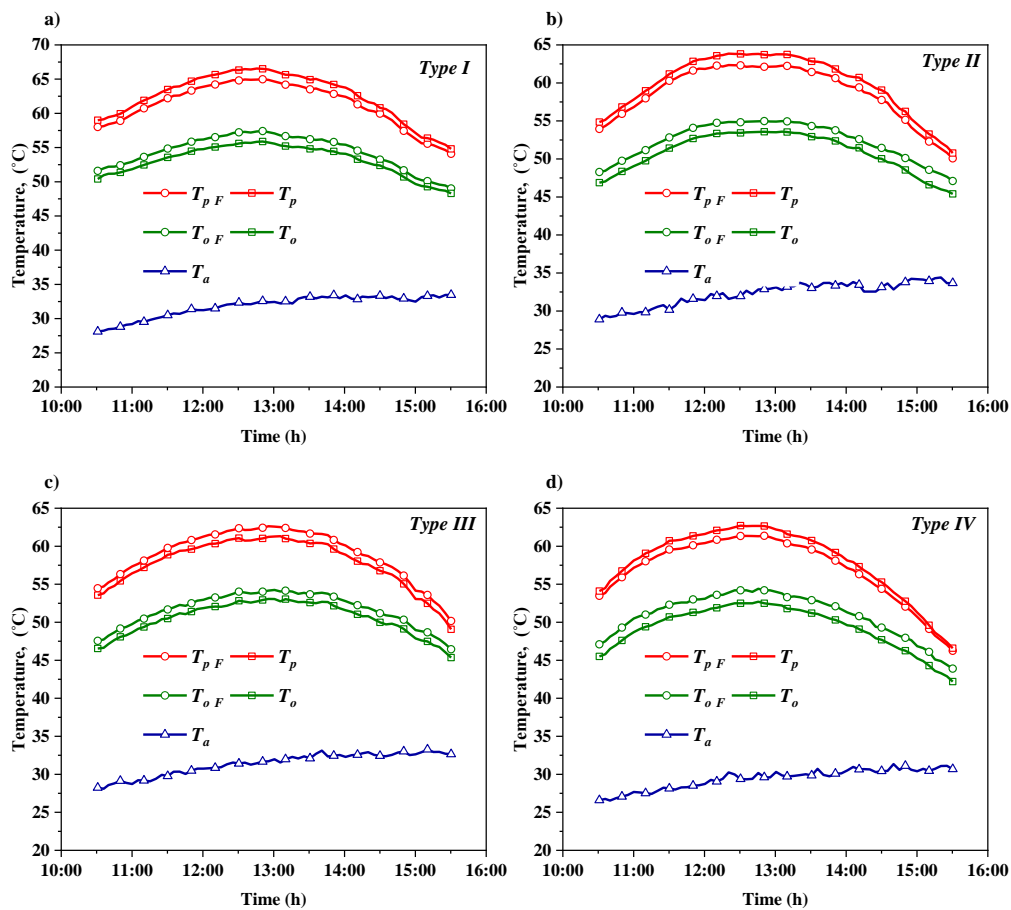
Fig. 4.44. The profiles of ambient, outlet, and absorber plate temperatures

Conversely, the outlet temperature for all configurations is higher in the FDPSAC compared to the smooth collector, underscoring the fins' ability to improve the heat transfer rate. This enhanced transfer allows better airflow circulation and reduces the formation of dead zones. For *Type I*, the maximum recorded outlet temperature for the FDPSAC was 57.4 °C, compared to 55.8 °C for the smooth DPSAC. Similarly, for *Type II*, the maximum outlet temperature was 55.2 °C, compared to 53.5 °C for the DPSAC. For *Type III*, the highest outlet temperature recorded was 54.2 °C compared to 53 °C for the smooth collector. Finally, for *Type IV*, the

maximum outlet temperature recorded was 54.4 °C for the FDPSAC compared to 52.3 °C for the smooth DPSAC. These observations further confirm the effectiveness of fins in facilitating improved heat transfer to the airflow, resulting in higher outlet temperatures.

Fig. 4.45 (a-d) illustrates the useful energy rate profile versus time for all experiments. The graph shows that energy gained begins to increase from mid-morning, reaches a peak around noon, and then gradually declines until the experiment concludes, with minimal energy rate gained afterward. This pattern aligns with the solar power curve (Qi), also shown in the figure for all experimental cases. Among the configurations, the FDPSAC consistently achieved the highest heat rate gains, particularly for *Type II* and *Type IV*, when compared to the smooth DPSAC counterparts. As shown in the figure, the maximum heat rate gain recorded for the FDPSAC in *Type II* was 283 W and in *Type IV* was 276.4 W, compared to 267.4 W and 258.6 W for their smooth DPSAC counterparts respectively. In comparison, *Type III* demonstrated a moderate effect on heat rate gain, with the FDPSAC reaching 258.9 W, compared to 245.8 W for the smooth collector. Meanwhile, *Type I* consistently exhibited lower heat rate gains than the other configurations, with a maximum recorded value of 272.5 W for the FDPSAC versus 257.2 W for the smooth DPSAC. These results emphasize the critical role of fin orientation in enhancing heat rate gain, with certain designs, particularly those used in *Types II* and *IV*, showing superior performance. This underscores the importance of fin design and orientation as key factors in optimizing the thermal efficiency of SACs.
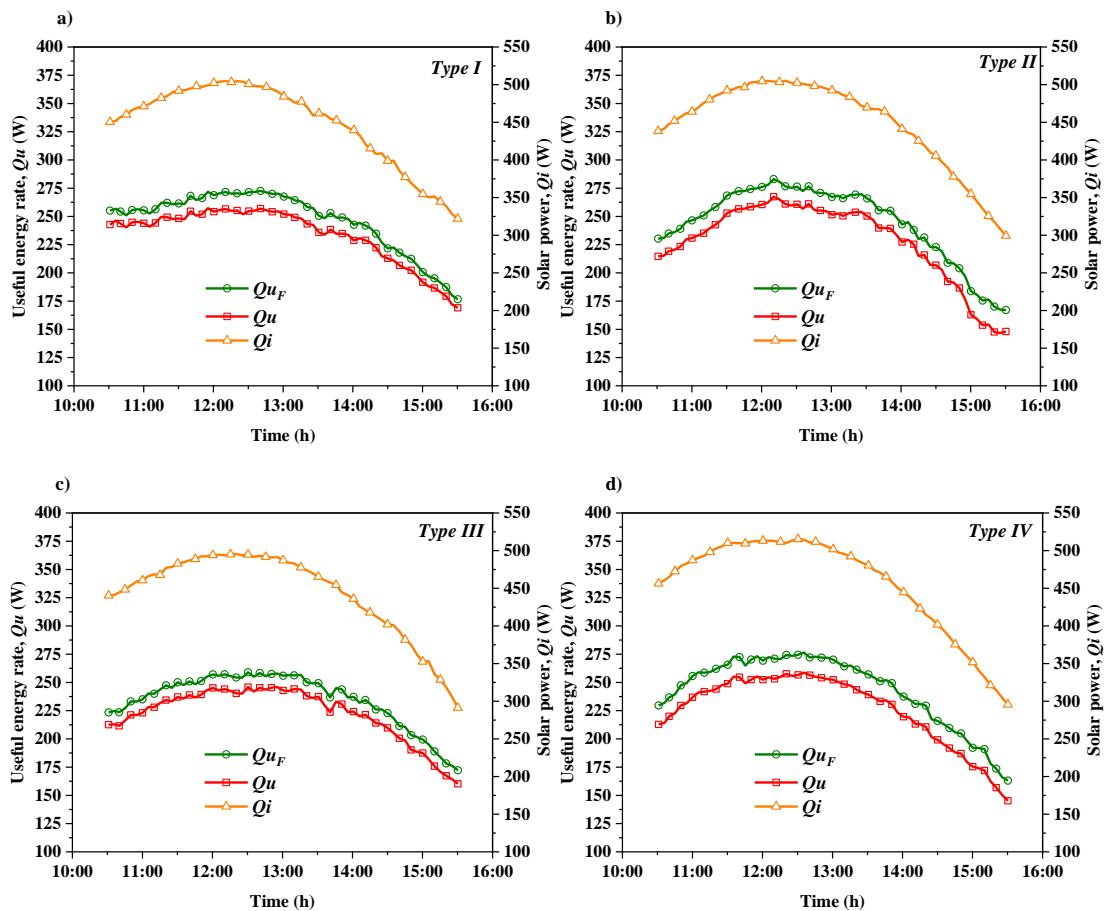

Fig. 4.45. The energy rate gained over time

Fig. 4.46 (a–d) presents the instantaneous and daily efficiency profiles of the collectors. Similar to the useful heat outcomes, the data indicate that the FDPSAC consistently achieves higher efficiencies than the smooth DPSAC due to the enhanced heat transfer properties provided by the fins. Among the configurations, *Type II* and *Type IV* exhibited the highest efficiencies, followed by *Type III,* with *Type I* being the least efficient. Specifically, the maximum instantaneous efficiency for Type I FDPSAC was 57.7%, surpassing the smooth DPSAC, which achieved 54.7%. For *Type II* FDPSAC, the maximum instantaneous efficiency was 57.1%, compared to 53.8% for the smooth DPSAC. Similarly, for *Type III*, the maximum instantaneous efficiency reached 59.1%, compared to 55% for the smooth DPSAC. Finally, for *Type IV*, the maximum instantaneous efficiency achieved was 57.4%, surpassing the smooth DPSAC, which achieved 51.7%.

As discussed in the previous section, instantaneous thermal efficiency is highly sensitive to fluctuations in solar intensity and ambient temperature; thus, peak instantaneous efficiency may not fully represent collector performance. Therefore, calculating daily thermal efficiency is essential for a comprehensive evaluation. The data further reveal that finned collectors consistently achieve higher daily efficiencies than smooth collectors across all configurations tested. For instance, *Type I* FDPSAC recorded a daily efficiency of 54.9%, surpassing the DPSAC's corresponding efficiency of 52.1%. *Type II* configurations showed daily efficiencies of 54.5% for FDPSAC and 50.8% for DPSAC. For *Type III*, the FDPSAC achieved an efficiency of 52.9%, compared to the DPSAC's 50.1%. Similarly, *Type IV* FDPSAC recorded an efficiency of 53.3%, exceeding the DPSAC's 49.5%.

In the case of discrete V-angled fins, the orientation of the fins plays a crucial role in efficiency improvements, with *Type II* showing the highest performance, followed by *Type III*, and *Type I* being the least effective. Meanwhile, the continuous V-angled fin configuration (*Type IV*) demonstrated the highest performance of all configurations when compared to the smooth collector. This hierarchy of performance underscores that specific fin designs and orientations are pivotal in maximizing heat transfer and optimizing the solar collector's thermal efficiency. The relative improvements in daily efficiency for FDPSAC over smooth DPSAC were 5.3% for *Type I*, 7.2% for *Type II*, 5.5% for *Type III*, and 7.6% for *Type IV*.
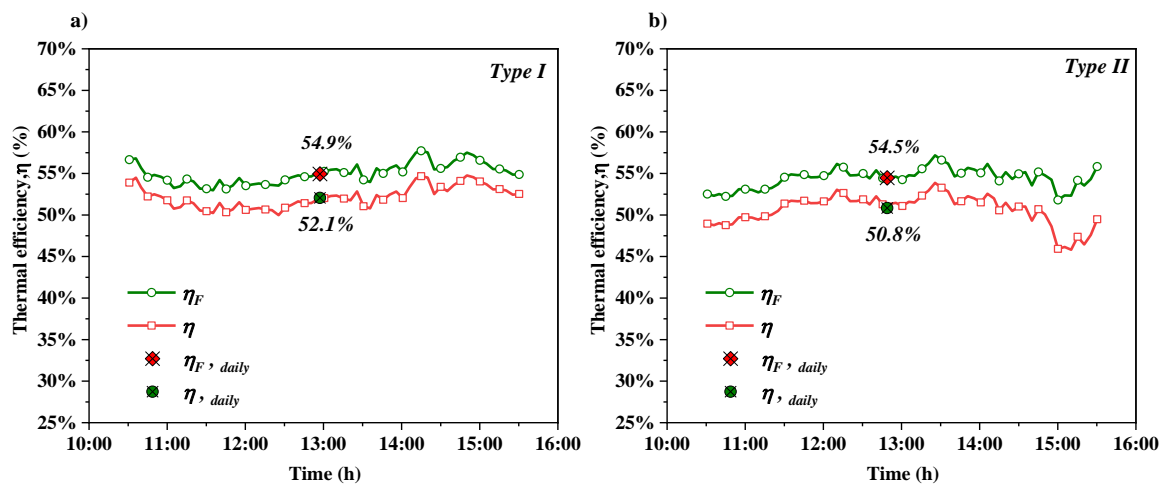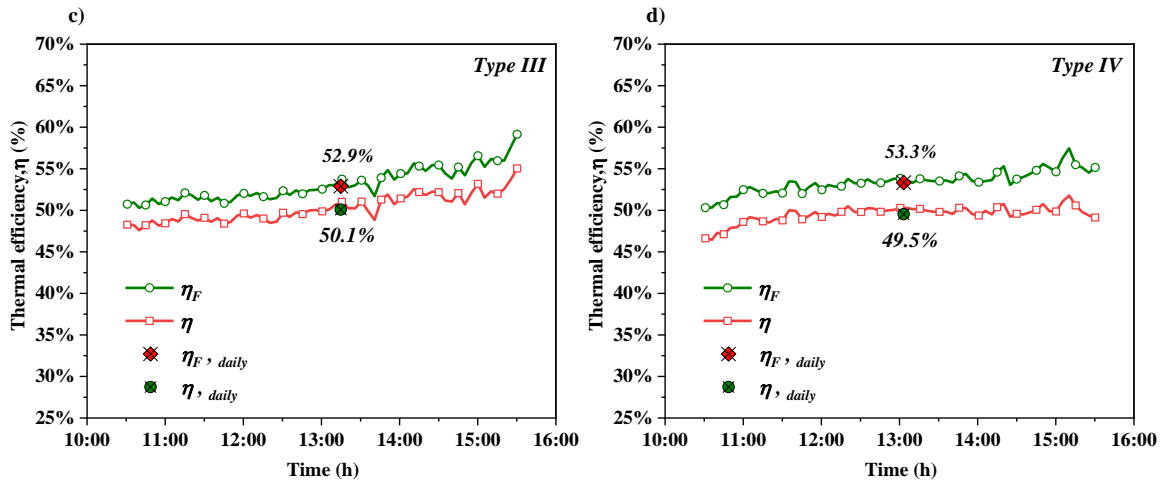
Fig. 4.46. The instantaneous and daily efficiency of the collectors

Figs. 4.47– 4.50 display the temperature variations within the drying chambers for each tested configuration. In each figure, subplot (a) represents the drying chamber temperatures achieved with the finned collector, while subplot (b) shows the corresponding temperatures using the smooth plate collector. The inlet temperature follows a similar trend to the outlet temperature of the collector, with minor differences attributed to heat losses occurring along the piping.

Additionally, the drying chamber of the finned collector consistently exhibits higher temperatures compared to the smooth collector's chamber, indicating that the addition of fins enhances heat transfer. This improvement is due to the fins' ability to increase the surface area, thereby enhancing the convective heat transfer rate to the air passing through the collector.

A clear temperature gradient is observed across the trays, with the temperature difference from the inlet decreasing progressively from Tray 1 to Tray 3. This gradient indicates that as warm air flows through the drying chamber, each tray absorbs a portion of the thermal energy, resulting in a gradual reduction in temperature along the flow path. The fluctuations seen in the graphs correspond to the hourly intervals for measuring the weight of the apple slices, during which chamber temperatures are briefly impacted by the opening of the chamber.
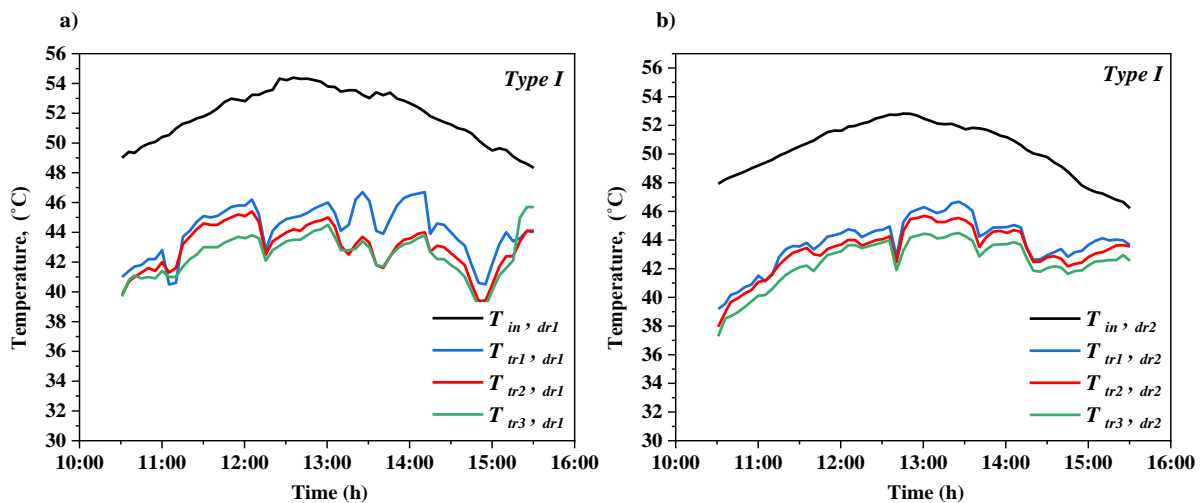
Fig. 4.47. Temperature variation of the drying chambers: a) using *Type I* FDPSAC, b) smooth DPSAC

110
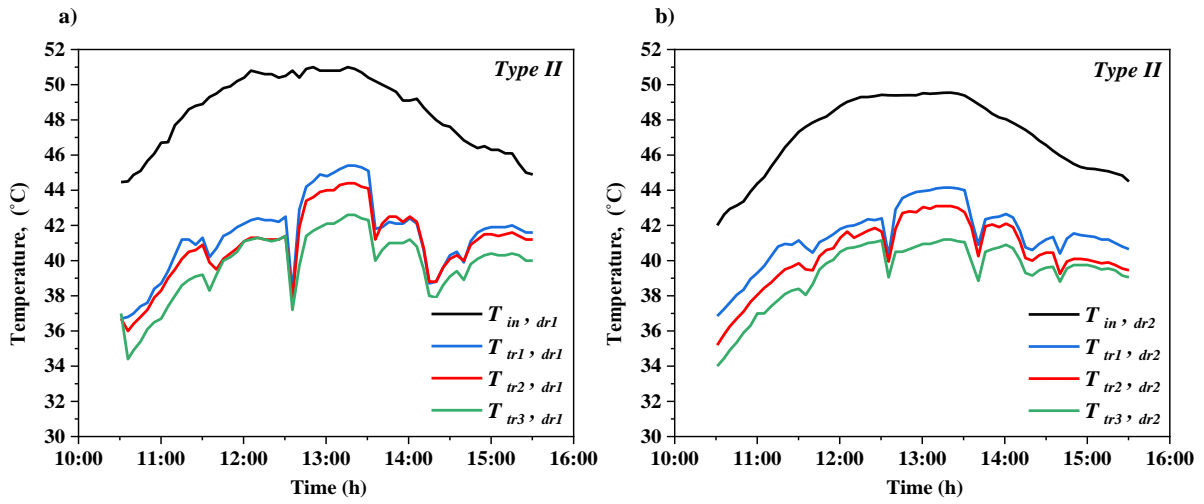
Fig. 4.48. Temperature variation of the drying chambers using: a) *Type II* FDPSAC,
b) smooth DPSAC

Fig. 4.49. Temperature variation of the drying chambers using: a) *Type III* FDPSAC,
b) smooth DPSAC
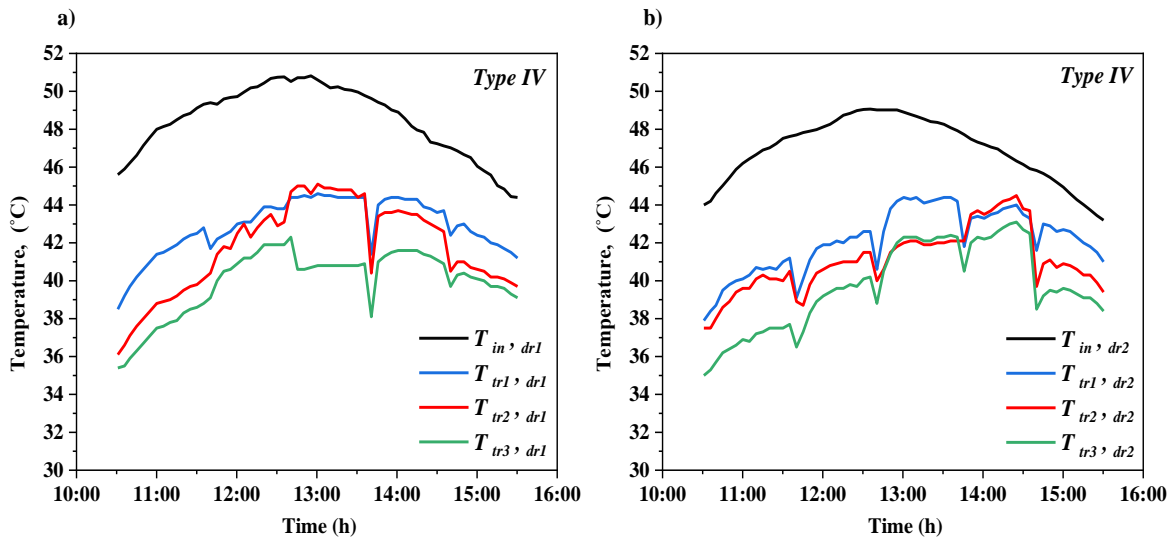
Fig. 4.50. Temperature variation of the drying chambers using: a) *Type IV* FDPSAC,
b) smooth DPSAC

Figs. 4.51–4.54 display the relative humidity (RH%) variations within the drying chambers for each tested configuration. In each figure, subplot (a) represents the relative humidity levels in the chamber connected to the finned collector, while subplot (b) shows the corresponding relative humidity levels in the chamber with the smooth plate collector.

The data reveal that the drying chamber connected to the finned collector consistently maintains lower relative humidity levels than the smooth collector's chamber. This reduction in RH% can be attributed to the enhanced heat transfer rate provided by the fins, which effectively reduces moisture content in the air as it passes over the heated absorber surface and circulates through the trays.

A noticeable gradient in relative humidity is observed from the inlet to each tray position within the drying chamber, with RH% levels progressively increasing from Tray 1 (nearest to the inlet) to Tray 3 (farthest from the inlet). This gradient reflects the cumulative moisture release from the apple slices as air moves across each tray, absorbing more moisture as it proceeds, and hence elevating the relative humidity in downstream trays.

The fluctuations in relative humidity observed across the different zones can also be linked to the periodic opening of the drying chamber for hourly weight measurements, which briefly impacts the internal humidity conditions. Additionally, the ambient RH% serves as a reference, showing variations in environmental humidity that slightly influence the drying chamber conditions, albeit to a lesser extent than the airflow and heat transfer dynamics within the collector. These observations highlight the effectiveness of finned configurations in maintaining lower relative humidity levels within the drying chamber, suggesting a more efficient drying environment that accelerates moisture removal from the product, particularly during periods of high solar radiation. This comparative analysis underscores the critical role of fin design in optimizing humidity reduction, airflow management, and overall drying efficiency.
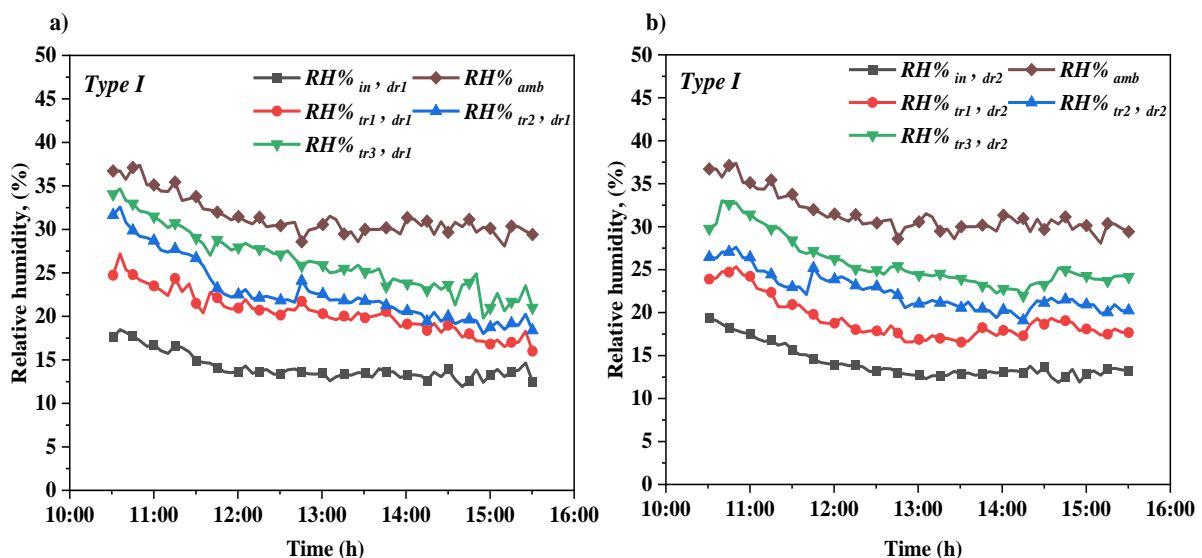
Fig. 4.51. The relative humidity variation of the drying chambers using: a) *Type I* FDPSAC, b) smooth DPSAC
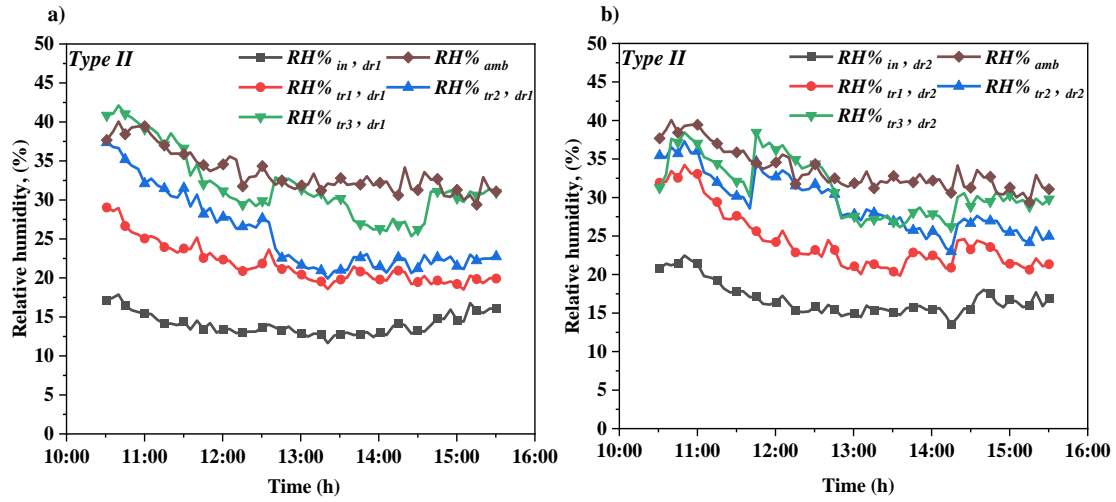
Fig. 4.52. The relative humidity variation of the drying chambers using: a) *Type II* FDPSAC, b) smooth DPSAC
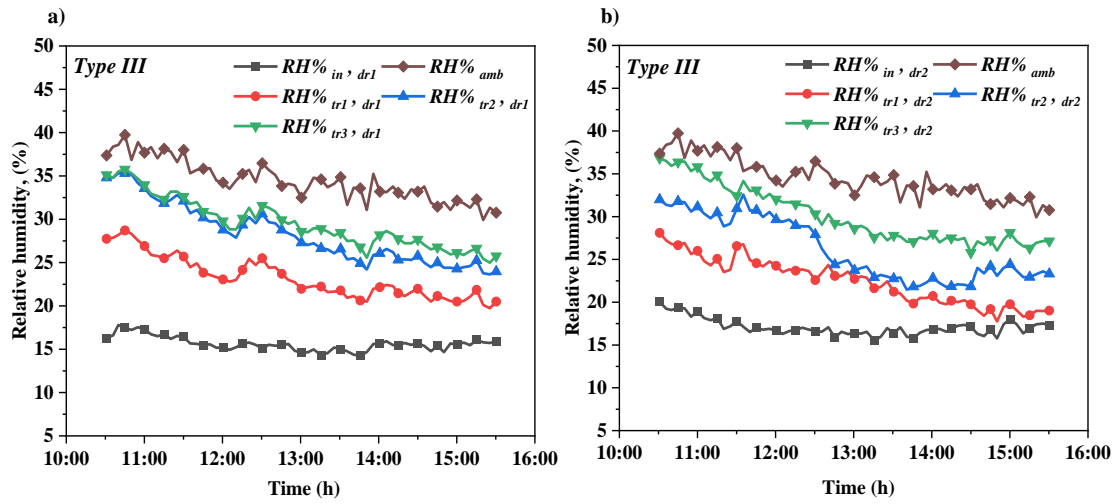
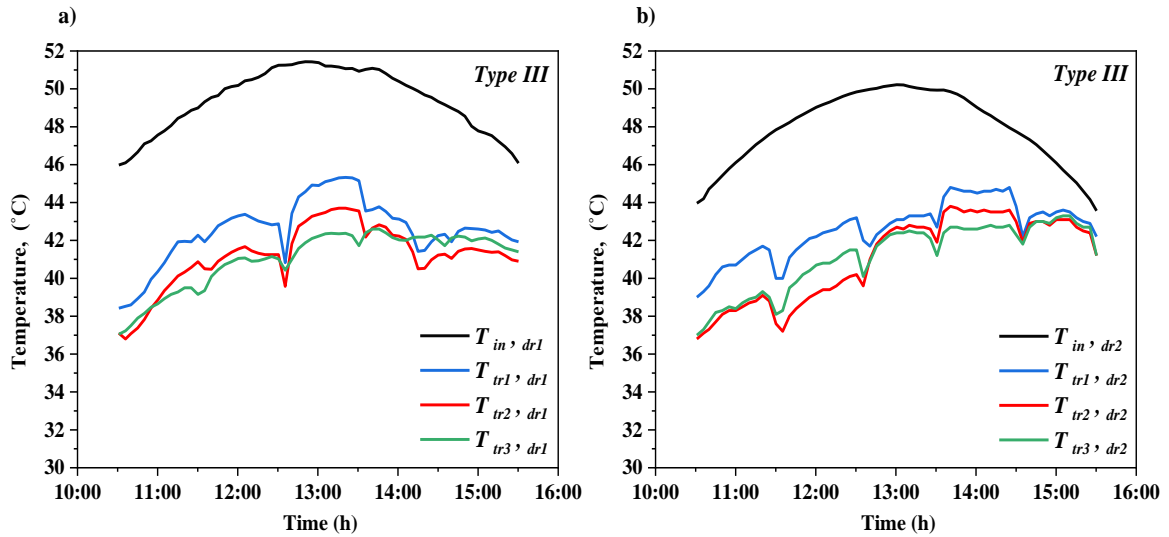Fig. 4.53. The relative humidity variation of the drying chambers using: a) *Type III* FDPSAC, b) smooth DPSAC
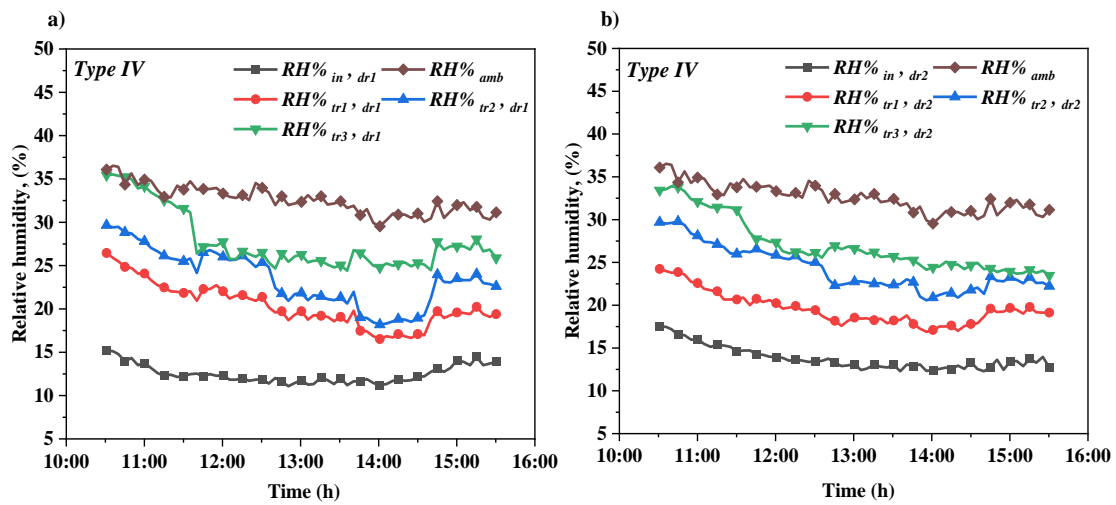
Fig. 4.54. The relative humidity variation of the drying chambers using: a) *Type IV* FDPSAC, b) smooth DPSAC

Fig. 4.55 (a–d) illustrates the moisture ratio (MR) of apple slices over time for each tested configuration. Across all subplots, the FDPSAC demonstrates a more reduction in moisture content compared to the DPSAC, highlighting the effectiveness of fins in enhancing the drying process.

The improved heat transfer capabilities of the finned collector, resulting from the increased surface area and optimized airflow dynamics, contribute to higher air temperatures within the drying chamber. This temperature elevation enhances the driving force for mass transfer, facilitating faster moisture evaporation from the apple slices. Consequently, the FDPSAC dryer achieves a lower moisture ratio at each time point compared to DPSAC dryer, supporting its superior drying performance. The effect of fin shape and orientation on drying performance is also evident across the different configurations. For instance, configurations of *Types II* and *IV* exhibit a more substantial improvement in drying rate. These configurations introduce additional turbulence and enhance the interaction between airflow and the heated absorber plate, further promoting heat transfer. In contrast, parallel and perpendicular fin orientations (*Types I* and *III*) provide moderate improvements but do not achieve the same level of effectiveness as other tested configurations.
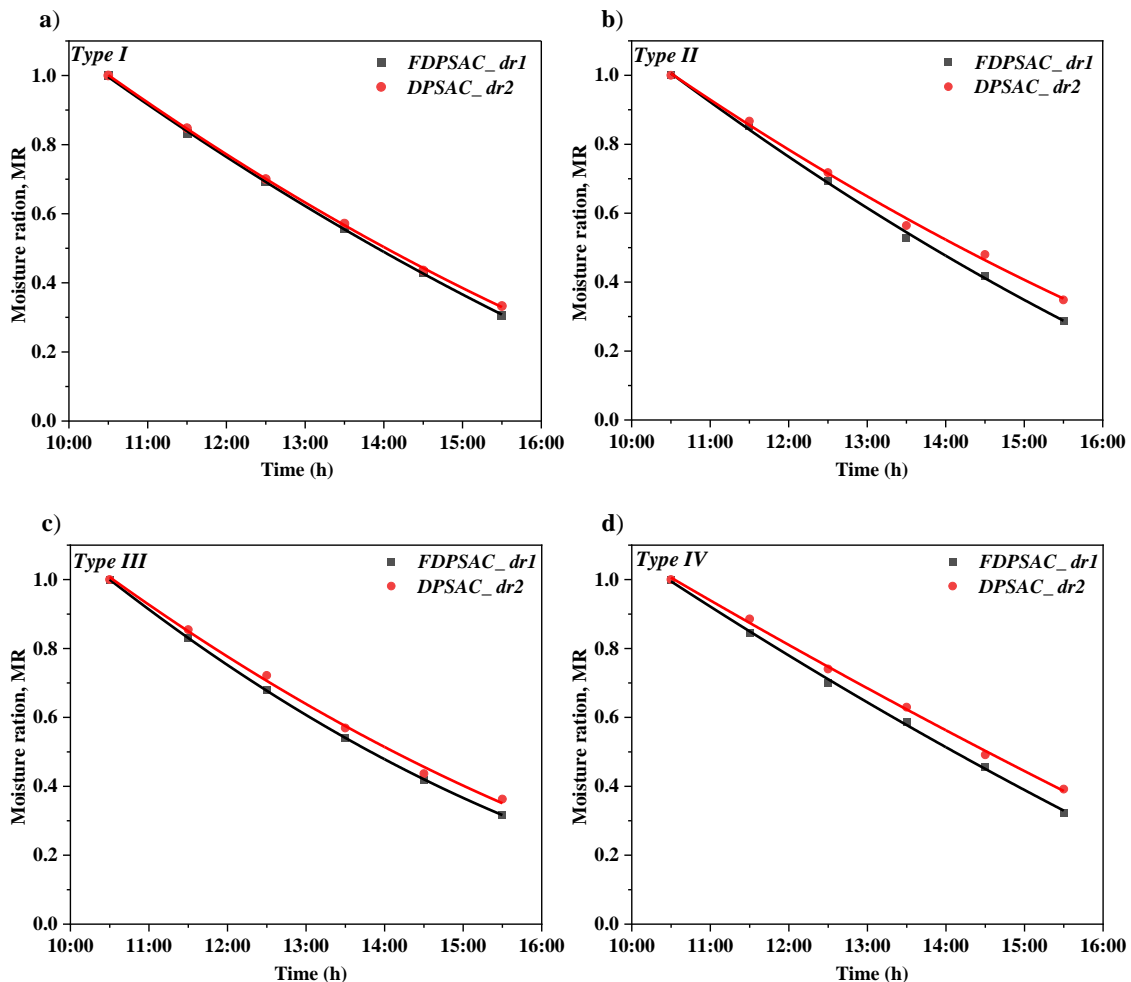
Fig. 4.55. The moisture ratio (MR) of apple slices over time

Fig. 4.56 presents the drying efficiency of the tested configurations. The results indicate that the drying efficiency of the dryer connected to the FDPSAC is consistently higher than that of

the dryer connected to the smooth collector. This enhancement is attributed to the increased amount of useful heat supplied by the finned collector, which effectively raises the temperature within the drying chamber, promoting faster moisture evaporation.

In terms of specific configurations, *Type I* demonstrates a drying efficiency of 20.7%, compared to 19.9% for the smooth collector, reflecting a relative improvement of 4%. *Type II* exhibits an even greater efficiency advantage, with 21.3% compared to 19.4% for the smooth collector, yielding a relative increase of 9.7%. Similarly, *Type III* achieves a drying efficiency of 20.5%, outperforming the smooth collector's 19.2% and showing an enhancement of 6.7%. *Type IV*, sharing the highest efficiency with *Type II*, reaches 20.9% versus 18.9% for the smooth collector, resulting in a relative improvement of 10.8%.

These findings emphasize that the addition of V-angled fins not only enhances collector performance by increasing the heat transfer rate through an expanded heat transfer area but also improves airflow distribution and turbulence generation within the collector. This enhancement in thermal performance directly translates into higher drying efficiency, as the improved heat transfer leads to more effective energy utilization and moisture removal in the drying chamber. Configurations with different V-angled fin orientations, such as *Types II* and *IV*, exhibited the most significant improvements, as they effectively promote uniform heat distribution and convective heat transfer. However, further increases in drying efficiency may be achievable by increasing the airflow rate, which could strengthen convective heat transfer and accelerate the drying process. Since the current experiments were conducted at a relatively low flow rate of 0.0103 kg/s, future investigations at higher flow rates are warranted to explore this potential for further efficiency gains.
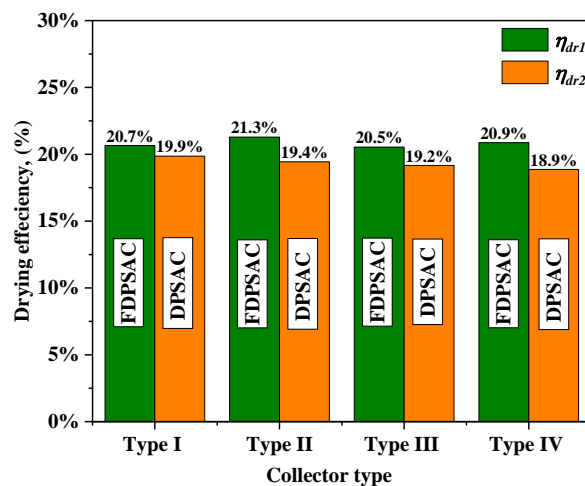
Fig. 4.56. The drying efficiency using proposed configurations

Fig. 4.57 illustrates the initial and final weights of the dried apple slices for each tested configuration. The initial weight for all experiments was approximately equal, at 1200 g. The results indicate that the final weight of the product in the dryer connected to the FDPSAC is consistently lower than that in the dryer connected to the smooth collector. This improvement is due to the increased amount of useful heat supplied by the finned collector, which elevates the drying chamber temperature and promotes more effective moisture evaporation.

For the *Type I* configuration, the FDPSAC reduced the apple weight from 1200 g to 531 g after 5 hours, retaining 55.7% of its initial weight, while the smooth collector retained 557 g, showing a relative improvement of 4.7%. In the *Type II* configuration, the final weight of the apples in the FDPSAC was 514 g (57.1% of the initial weight), compared to 572 g for the smooth collector, reflecting a 10.1% improvement. For the *Type III* configuration, the FDPSAC achieved a final weight of 542 g (54.8% of the initial weight), outperforming the smooth collector's 585 g with a 7.4% improvement. Lastly, in the *Type IV* configuration, the FDPSAC reduced the final weight to 548 g (54.3% of the initial weight), surpassing the smooth collector's 614 g with a 10.7% improvement.
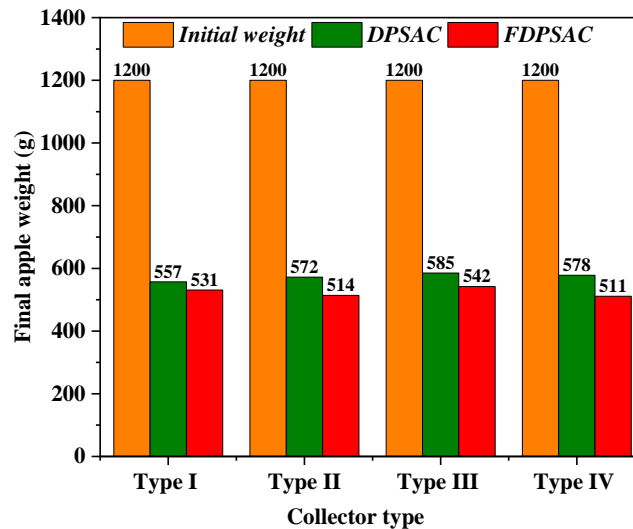
Fig. 4.57. The final weight of the dried apple using proposed configurations

These results underscore the enhanced drying capability of the FDPSAC across all configurations, with particularly notable improvements in the *Type II* and *Type IV* setups. Fig. 4.58 provides a visual comparison of the initial and final appearance of the apple slices before and after drying in the FDPSAC and DPSAC setups. The images illustrate changes in size and color, further emphasizing the impact of each drying configuration on product quality.

The relative uncertainties of the parameters in this section were determined using the same methodology as described in the previous section of the thesis. Consistent with this approach, daily average values for each variable were calculated for all experimental days, and an overall mean was derived from these daily averages. For the DPSAC configuration, the relative uncertainties for airflow rates and collector efficiency were found to be 1.66% and 2.56%, respectively, while the uncertainty in drying efficiency was estimated at 0.4%.
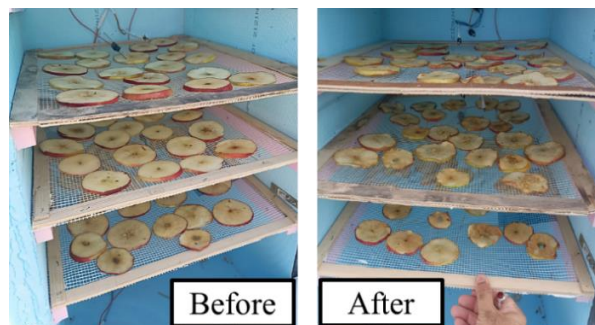
Fig. 4.58. Visual comparison of the initial and final appearance of dried apple

5. NEW SCIENTIFIC RESULTS

This section presents the new scientific findings from this research work as follows:

1. Modification of entrance flue design

Based on experimental results, I evaluated and demonstrated the significant impact of entrance flue design on the thermal performance of solar air collectors. The entrance flue plays a crucial role in directing airflow into the collector, which directly influences heat transfer efficiency and overall performance. Additionally, the proposed entrance flue design enhances heat extraction by enhancing air distribution across the absorber plate, reducing dead zones, and resulting in lower absorber plate temperatures compared to the side entrance solar air collector (SAC).

Through the proposed entrance design, a relative improvement in daily thermal efficiency, ranging between 6.9% and 7.4%, achieved solely by changing the air entrance from a side to a front configuration in the SPSAC.

Furthermore, I developed a linear model for the thermal efficiency of the front entrance single pass solar air collector, expressed as a function of the average fluid to ambient temperature difference and solar intensity:

$$\eta = a - b \frac{T_{f,av} - T_a}{I}$$

The model's coefficients of correlation for various flow rates are as follows:

$$\dot{m} = 0.01118 \text{ kg/s } [a = 0.450, b = 5.696, R^2 = 0.910]$$

$$\dot{m} = 0.01231 \text{ kg/s } [a = 0.516, b = 9.888, R^2 = 0.932]$$

$$\dot{m} = 0.01469 \text{ kg/s } [a = 0.601, b = 11.406, R^2 = 0.946]$$

2. Effect of the V- angled perforated fins

I have developed and evaluated novel V-angled perforated fins in both continuous and discrete configurations to enhance the thermal performance of double-pass solar air collectors (DPSAC). The proposed fins were tested in various orientations, with attachments on the upper absorber surface of the collector. The discrete V-angled perforated fins were arranged in three configurations: parallel to the flow (Type I), inclined at 45° to the flow (Type II), and perpendicular to the flow (Type III). In contrast, the continuous V-angled perforated fins were positioned perpendicular to the flow direction.

I have demonstrated that the daily thermal efficiency of the continuous V-angled fins achieved a relative improvement ranging from 4.5% to 9.8%, depending on the tested mass flow rate. This enhancement is attributed to the increased heat transfer area and the turbulence-generating effect of the fins, which significantly improve heat transfer performance. Similarly, the discrete V-angled fins displayed efficiency improvements between 4.1% and 9.1%, with variation based on fin orientation and airflow rate.

Moreover, I have proved that fin orientation significantly influences the overall efficiency of DPSACs. *Type I* demonstrated the least enhancement, with relative improvements ranging

117

from 4.1% to 5.1%. In contrast, *Type II* provided the most substantial enhancement, ranging from 5.9% to 9.1%. *Type III* followed with relative efficiency gains between 4.3% and 5.9%. The finned collector surpasses the smooth collector in all configurations, regardless of the flow rates. These findings highlight the critical role of fin design and orientation in optimizing the thermal performance of SACs, making the V-angled fins a versatile solution applicable to various DPSAC designs.

3. Impact of selective coatings on collector performance

Based on experimental results, I have demonstrated that selective coatings significantly enhance the thermal performance of SACs by increasing energy absorption and reducing radiative heat losses. This enhancement is reflected in higher absorber plate temperatures and improved outlet temperatures compared to standard black matte coatings. The application of selective coatings also leads to notable improvements in thermal efficiency across different collector configurations and mass flow rates. A relative improvement in thermal efficiency has been observed, with increases ranging from 5.6% to 10.9% in SPSACs and from 3.3% to 6.2% in DPSACs, depending on the tested mass flow rate. These efficiency gains underscore the coating's role in improving energy absorbing and retention. Moreover, the experimental findings, revealed that selective coating has a considerably stronger effect on the SPSAC compared to the DPSAC, this due to differences in airflow dynamics and heat transfer mechanisms between the two collectors.

To further interpret these findings, I have developed a quadratic regression model to predict the absorber plate temperature as a function of solar radiation intensity, mass flow rate. This model is applicable within a solar radiation range of 600–1000 W/m² and mass flow rates from 0.00877 to 0.02629 kg/s for both selective and non-selective coatings. It provides a reliable method for predicting the absorber plate temperature in various solar collector designs under varying conditions. The general form of the model is:

$$\hat{T}_p = a \cdot I + b \cdot \dot{m} + a_2 \cdot I^2 + b_2 \cdot \dot{m}^2 + d \cdot I \cdot \dot{m} + c$$

SPSAC-Se [a= 0.0436, b= -3691.7, a_2 = 5.22×10^{-7}, b_2= 82244.8, d = -0.1167, c=76.22 R²=0.969]

SPSAC-Bl [a= 0.0373, b= -3340.4, a_2 = 4.55×10^{-6}, b_2= 74108.9, d = -0.0949, c=69.96, R²=0.974]

DPSAC-Se [a= 0.0794, b= -6050.2, a_2 = -1.572×10^{-5}, b_2= 2.837×10^5, d =-2.4853, c=56.16, R²=0.941]

DPSAC-Bl [a= 0.0938, b= -4498.1, a_2 = -1.958×10^{-5}, b_2= 2.429×10^5, d = -3.0049, c=38.26 R²=0.946]

4. Influence of channel depth on collector performance

Based on experimental and modelling results, I evaluated how channel depth affects the thermal performance of both single-pass and double-pass solar air collectors. Channel depth significantly influences airflow patterns and heat transfer efficiency within the collector. Shallow channels enhance heat transfer but increase flow resistance, demanding more power to maintain airflow, whereas deeper channels reduce resistance but sacrifice thermal performance.

For single-pass collectors, I have demonstrated that shallow channel depth improved daily efficiency by 4.4% at a low flow rate and by 5.8% at a higher flow rate compared to the

moderate depth. In comparison, the moderate depth outperformed the deepest channel at both low and higher flow rates, showing efficiency gains improvements of 4.9% and 7.1%, respectively. These results underscore that a shallower channel enhances efficiency at low flow rates, while a moderate depth provides balanced performance across conditions, optimizing efficiency.

In double-pass collectors, I have developed a MATLAB-based mathematical model to predict the outlet temperature with high accuracy, achieving an R^2 value of 0.989. This model was validated through experiments and used for simulating the effect of varying upper channel depths on collector performance. Based on simulation results, I have demonstrated that at low flow rates, shallow upper channels substantially improve thermal efficiency due to enhanced heat transfer. Moreover, at high flow rates, the impact of channel depth decreases as air velocity becomes the dominant factor in heat transfer, resulting in stable efficiency across different channel depths.

Furthermore, selecting a moderate channel depth minimizes pressure drop and reduces the need for additional pumping power, enhancing system performance in both single-pass and double-pass collectors. This balanced approach ensures optimal thermal efficiency while maintaining energy-efficient operation, making it applicable to various solar air collector design.

5. Comparison of different fin configurations on drying performance

I have proved that the configuration of fins significantly influences drying performance within the DPSAC, as shown by variations in drying efficiency and final product weight across different fin arrangements. The experiments revealed that continuous V-angled fins *Type IV*, oriented perpendicular to the airflow, deliver the highest enhancement in performance, with a 10.8% improvement in drying efficiency compared to the smooth collector. Additionally, the discrete V-angled *Type II* fins demonstrated strong performance, increasing drying efficiency by 9.7% relative to the smooth collector.

I found that fin orientation significantly affects the drying efficiency of solar air collectors. Fins oriented parallel to the airflow (*Type I*) and those positioned perpendicular to the airflow (*Type III*) demonstrated moderate improvements in drying efficiency and final product weight compared to the smooth collector. In contrast, *Type II* fins, inclined at 45°, achieved a drying efficiency of 21.3%, surpassing the 19.4% efficiency of the smooth collector, thus reflecting a relative increase of 9.7%.

6. CONCLUSION AND SUGGESTIONS

In conclusion, an experimental analysis of design enhancements conducted to improve the thermal performance of solar air collectors (SACs). Testing of front versus side entrance designs in single-pass collectors demonstrated that the front entrance configuration significantly improves airflow distribution and heat transfer, leading to an efficiency gain of approximately 6.9% to 7.4%. For double-pass SACs, both continuous and discrete V-angled fin configurations were evaluated. Continuous V-angled fins, oriented perpendicular to the airflow, enhanced thermal performance with efficiency gains ranging from 4.4% to 9.8%, depending on the mass flow rate. Discrete V-angled fins, tested in orientations parallel, inclined at 45°, and perpendicular to airflow, showed the highest improvement when inclined at 45°, with efficiency gains from 4.1% to 9.1% based on flow rate and configuration.

The use of selective coatings on the absorber plates in both single-pass and double-pass SACs led to significant improvements, particularly in single-pass collectors where efficiency gains ranged from 5.6% to 10.9%, while double-pass collectors showed increases between 3.3% and 6.2%. This enhancement is attributed to higher energy absorbing and reduced radiative losses, resulting in elevated absorber plate temperatures and more consistent outlet air temperatures, especially beneficial under variable solar conditions. Channel depth analysis revealed that shallower channels effectively boosted thermal performance at low flow rates by enhancing the heat transfer between the absorber and airflow. Moderate channel depths, however, provided a balanced approach, achieving stable efficiency while reducing pressure drops, which is advantageous for applications requiring a range of operating conditions.

In drying applications, the impact of different fin orientations on drying efficiency was examined using apple slices as the test material. Continuous V-angled fins oriented perpendicular to the airflow achieved a drying efficiency relative improvement of 10.8% compared to a smooth absorber. The optimized fin design allowed for more uniform airflow and enhanced heat distribution within the drying chamber, accelerating the moisture removal process. Among the discrete configurations, fins inclined at a 45° angle achieved a 9.7% relative increase in drying efficiency over smooth collectors, reflecting the effect of airflow direction on drying rates. The presence of fins maintained higher drying temperatures and reduced drying times, which is advantageous for drying applications.

Future research should examine the effects of friction and pressure drop within collectors, as these impact system efficiency. Further optimization of fin configurations, including angles, perforation patterns, and spacing, would maximize thermal performance and airflow in double-pass SACs. Additionally, investigating environmental factors like solar radiation, ambient temperature, and humidity would provide insights into the performance of finned double-pass SACs under varying conditions.

Combining selective coatings with phase change materials (PCMs) could enhance SAC energy storage, as selective coatings improve solar absorption and reduce PCM charging time. This integration, alongside optimized designs, may lead to highly efficient and adaptable solar collectors suited for thermal energy capture and agricultural drying.

7. SUMMARY

EFFICIENCY IMPROVEMENT OF SOLAR AIR COLLECTORS USED IN DRYING PROCESSES

A comprehensive experimental analysis was conducted to enhance the efficiency of solar air collectors (SACs) for drying applications, under the climatic conditions of Gödöllő, Hungary (47° 35' 39" N, 19° 21' 59" E). The study focused on improving the thermal performance of SACs through the design and testing of entrance flue configurations, novel fin structures, selective coatings, and optimized channel depths in both single-pass (SPSAC) and double-pass (DPSAC) collectors. These enhancements were developed and tested in the Solar Energy Laboratory at the Hungarian University of Agriculture and Life Sciences (MATE).

To achieve the research objectives, experiments were conducted using various collector configurations to evaluate thermal efficiency, energy gain, and drying efficiency. The entrance flue design was modified for the SPSAC, comparing a front entrance with a side entrance configuration. Results showed that the front entrance flue improved thermal efficiency by 6.9% to 7.4% over the side entrance, attributed to enhanced airflow distribution across the absorber plate, resulting in more effective heat transfer.

In DPSACs, discrete V-angled fins were tested in three orientations: Type I (parallel to the airflow), Type II (inclined at 45°), and Type III (perpendicular to the airflow). Among these, Type II fins, inclined at 45° to the airflow, achieved the highest efficiency improvements, with gains of 5.9% to 9.1% depending on the flow rate. Type III fins, oriented perpendicular to the airflow, provided moderate gains between 4.3% and 5.9%, while Type I fins, aligned parallel to the airflow, showed the lowest relative improvement, ranging from 4.1% to 5.1%. The continuous V-angled fins, oriented perpendicular the airflow, also achieved efficiency gains of 4.5% to 9.8%, demonstrating the effectiveness of this design in enhancing thermal performance across varying flow rates.

The use of selective coatings on absorber plates showed significant improvements in thermal efficiency, with increases of 5.6% to 10.9% in SPSACs and 3.3% to 6.2% in DPSACs. This enhancement is attributed to higher energy absorbing and reduced radiative losses provided by the selective coating. Channel depth variations were also tested, with results indicating that shallower channels enhance efficiency at low flow rates by improving heat transfer. However, moderate channel depths were found to offer balanced performance across a range of operating conditions reducing pressure drop and minimizing the need for additional pumping power.

In drying applications, apple slices were used as a model product to evaluate drying efficiency across different fin configurations. Continuous V-angled fins, oriented perpendicular to the airflow, yielded the highest improvement in drying efficiency, with a relative gain of 10.8% compared to smooth absorbers. Among the discrete fins, Type II (45° inclined) showed a 9.7% relative increase in drying efficiency, reflecting the effectiveness of airflow disruption in enhancing drying rates. Fins positioned parallel or perpendicular to the airflow also improved drying efficiency, though to a lesser extent than the 45° inclined orientation.

8. ÖSSZEFOGLALÁS (SUMMARY IN HUNGARIAN)

A SZÁRÍTÁSI FOLYAMATOKBAN ALKALMAZOTT LEVEGŐS NAPKOLLEKTOROK HATÉKONYSÁGÁNAK JAVÍTÁSA

Átfogó kísérleti elemzés készült a levegős napkollektorok (SAC) hatékonyságának növelésére szárítási alkalmazásokhoz, a magyarországi Gödöllő éghajlati viszonyai között (47° 35' 39" É, 19° 21' 59" K). A kutatómunka célja a SAC-ok termikus teljesítményének javítása volt a belépő levegőelosztó csatornák konfigurációinak, az új légterelő szerkezetek, a szelektív bevonat és az optimalizált csatornamagasságok kialakítása és tesztelése révén, egy- és kettő levegő átvezető járattal kialakított kollektorokban egyaránt. Ezek a megoldások a Magyar Agrár- és Élettudományi Egyetem (MATE) Napenergia Laboratóriumában kerültek tesztelésre.

A kutatási célok elérése érdekében különböző kollektor konfigurációkkal kísérletek kerültek elvégzésre a termikus és szárítási hatékonyságok és az energianyereség értékelésére. Az egy levegő átvezető járattal kialakított napkollektor esetén a belépő légelosztó csatorna módosításra került, összehasonlítva az elülső és oldalsó konfigurációval. Az eredmények azt mutatták, hogy az elülső kialakítású csatorna 6,9-7,4%-kal javította a termikus hatékonyságot az oldalsó belépéshez képest, amit a napsugárzáselnyelő abszorberlemez mentén történő légáramlás jobb eloszlása eredményezett, ezáltal hatékonyabb hőátvitelt biztosítva.

A kettő levegő átvezető járattal kialakított napkollektorokban a levegő áramlási irányához képest három felszerelési irányban tesztelték a V-alakú, 90°-ban meghajlított légterelő lemezezek hatását: I. típus (párhuzamos a légáramlással), II. típus (45°-os légáramlással), és III. típus (merőleges a légáramlásra). Ezek közül a II. típusú légterelők érték el a legmagasabb hatékonyságnövekedést 5,9-9,1% közötti értékekkel a légáramlás sebességétől függően. A légáramlásra merőlegesen elhelyezett III. típusú bordák mérsékelt növekedést eredményeztek 4,3-5,9% között, míg az I. típusú bordák, amelyek párhuzamosan helyezkedtek el a légáramlással, a legalacsonyabb relatív javulást mutatták, 4,1-5,1% tartományban. A légáramlás irányára merőlegesen, az abszorber lemezen keresztben elhelyezett perforált légterelőkkel 4,5-9,8% közötti hatékonyságnövekedés érhető el, ami azt mutatja, hogy ez a kialakítás különböző áramlási sebességeken is javítja a termikus teljesítményt.

A szelektív bevonat használata az elnyelő lemezeken jelentős javulást mutatott a termikus hatékonyság terén, 5,6-10,9%-os növekedést eredményezve az egy levegő átvezető járatú és 3,3-6,2%-os növekedést a kétjáratú napkollektorok esetében. Ez a javulás a szelektív bevonat által a napsugárzás hullámhossztartományában biztosított nagyobb elnyelésnek és az infravörös tartományban az abszorber csökkent hősugárzási veszteségének tulajdonítható. A levegő átvezető csatornamagasság változatokat vizsgálva, az eredmények azt mutatták, hogy az alacsonyabb csatornák kis áramlási sebességnél növelik a hatékonyságot a jobb hőátvitel révén. A közepes csatornamagasság kiegyensúlyozott teljesítményt mutatott különböző üzemeltetési feltételek mellett, csökkentve a nyomásesést és minimalizálva a további ventilációs teljesítményigényt.

A szárítási kísérleteknél almakarikákat használtak modelltermékként a hatékonyság értékelésére a különböző légterelő konfigurációk esetén. A légáramlásra merőlegesen, az abszorber lemezen keresztben elhelyezett perforált légterelők eredményezték a legnagyobb javulást a szárítási hatékonyságban, 10,8%-os relatív növekedéssel a sima (légterelők nélküli) elnyelő lemezekhez képest. A légáramlás irányával 45°-os szögben elhelyezett II. típusú légterelő 9,7%-os növekedést mutatott, ami a légáramlás zavarásának hatékonyságát tükrözi a szárítási sebesség növelésében. A légáramlással párhuzamosan vagy merőlegesen elhelyezett bordák szintén javították a hatékonyságot, bár kevésbé, mint a 45°-os dőlésszögű orientáció.

9. APPENDICES

A1: Bibliography

1. Abd, H. M., Alomar, O. R., and Salih, M. M. M. (2022): Improving the performance of solar air heater using a new model of V-corrugated absorber plate having perforations jets, International Journal of Energy Research, 46(6), 8130–8144. https://doi.org/10.1002/er.7715

2. Abdelkader, T. K., Zhang, Y., Gaballah, E. S., Wang, S., Wan, Q., and Fan, Q. (2020): Energy and exergy analysis of a flat-plate solar air heater coated with carbon nanotubes and cupric oxide nanoparticles embedded in black paint, Journal of Cleaner Production, 250, 119501. https://doi.org/10.1016/j.jclepro.2019.119501

3. Abdullah, A. S., Abou Al-sood, M. M., Omara, Z. M., Bek, M. A., and Kabeel, A. E. (2018): Performance evaluation of a new counter flow double pass solar air heater with turbulators, Solar Energy, 173(July), 398–406. https://doi.org/10.1016/j.solener.2018.07.073

4. Abed, A. F., Dahham, R. B., Hashim, N. A. W., and Hamad, R. F. (2023): Performance Enhancement of a Solar Air Collector Using a V-Corrugated Absorber, Journal of Aerospace Technology and Management, 15, 1–13. https://doi.org/10.1590/jatm.v15.1304

5. Abubakar, S., Umaru, S., Kaisan, M. U., Umar, U. A., Ashok, B., and Nanthagopal, K. (2018): Development and performance comparison of mixed-mode solar crop dryers with and without thermal storage, Renewable Energy, 128, 285–298. https://doi.org/10.1016/j.renene.2018.05.049

6. Abushanab, W. S., Zayed, M. E., Sathyamurthy, R., Moustafa, E. B., and Elshiekh, A. H. (2023): Performance evaluation of a solar air heater with staggered/longitudinal finned absorber plate integrated with aluminium sponge porous medium, Journal of Building Engineering, 73(May), 106841. https://doi.org/10.1016/j.jobe.2023.106841

7. Acar, C., Dincer, I., and Mujumdar, A. (2020): A comprehensive review of recent advances in renewable-based drying technologies for a sustainable future, Drying Technology, 40(6), 1029–1050. https://doi.org/10.1080/07373937.2020.1848858

8. Ahmadkhani, A., Sadeghi, G., and Safarzadeh, H. (2021): An in depth evaluation of matrix, external upstream and downstream recycles on a double pass flat plate solar air heater efficacy, Thermal Science and Engineering Progress, 21(May 2020), 100789. https://doi.org/10.1016/j.tsep.2020.100789

9. Akamphon, S., Sukkasi, S., and Sedchaicharn, K. (2018): An integrated heat-transfer-fluid-dynamics-mass-transfer model for evaluating solar-dryer designs, Journal of Food Processing and Preservation, 42(7), 1–9. https://doi.org/10.1111/jfpp.13649

10. Akpinar, E. K., Koçyiğit, F., and Koçyiğit, F. (2010): Experimental investigation of thermal performance of solar air heater having different obstacles on absorber plates, International Communications in Heat and Mass Transfer, 37(4), 416–421. https://doi.org/10.1016/j.icheatmasstransfer.2009.11.007

11. Al-Damook, M., Obaid, Z. A. H., Al Qubeissi, M., Dixon-Hardy, D., Cottom, J., and Heggs, P. J. (2019): CFD modeling and performance evaluation of multipass solar air heaters, Numerical Heat Transfer; Part A: Applications, 76(6), 438–464. https://doi.org/10.1080/10407782.2019.1637228

12. Alam, T., and Kim, M.-H. H. (2017): Performance improvement of double-pass solar air heater – A state of art of review, Renewable and Sustainable Energy Reviews, 79(May), 779–793. https://doi.org/10.1016/j.rser.2017.05.087

13. Alam, T., Saini, R. P., and Saini, J. S. (2014a): Effect of circularity of perforation holes in V-shaped blockages on heat transfer and friction characteristics of rectangular solar air heater duct, Energy Conversion and Management, 86, 952–963. https://doi.org/10.1016/j.enconman.2014.06.050

14. Alam, T., Saini, R. P., and Saini, J. S. (2014b): Experimental investigation on heat transfer enhancement due to V-shaped perforated blocks in a rectangular duct of solar air heater, Energy Conversion and Management, 81, 374–383. https://doi.org/10.1016/j.enconman.2014.02.044

15. Alnakeeb, M. A., Hassan, M. A., and Teamah, M. A. (2024): Thermal performance analysis of corrugated plate solar air heater integrated with vortex generator, Alexandria Engineering Journal, 97(November 2023), 241–255. https://doi.org/10.1016/j.aej.2024.04.019

16. Alok, P., Javvadi, S.C.T., Konchada, P.K., and Dheep, G. R. (2021): Numerical Simulation of a Single-Pass Parallel Flow Solar Air Heater with Circular Fins Using S2S Radiation Model, Lecture Notes in Mechanical Engineering, Springer Singapore, 111–121. https://doi.org/10.1007/ 978-981-15-7831-1_10

17. Alomar, O. R., Abd, H. M., and Mohamed Salih, M. M. (2022): Efficiency enhancement of solar air heater collector by modifying jet impingement with v-corrugated absorber plate, Journal of Energy Storage, 55(PB), 105535. https://doi.org/10.1016/j.est.2022.105535

18. Alomar, O. R., Salih, M. M. M., and Abd, H. M. (2023): Performance analysis of single-pass solar air heater thermal collector with adding porous media and finned plate, Energy Storage, 5(5), 1–12. https://doi.org/10.1002/est2.447

19. Alrashidi, A., Altohamy, A. A., and Abdelrahman, M. A. (2024): Case Studies in Thermal Engineering Energy and exergy experimental analysis for innovative finned plate solar air heater, Case Studies in Thermal Engineering, 59(March), 104570. https://doi.org/10.1016/j.csite.2024.104570

20. Antony, A. L., Shetty, S. P., Madhwesh, N., Yagnesh Sharma, N., and Vasudeva Karanth, K. (2020): Influence of stepped cylindrical turbulence generators on the thermal enhancement factor of a flat plate solar air heater, Solar Energy, 198(September 2019), 295–310. https://doi.org/10.1016/j.solener.2020.01.065

21. Araújo, A. (2020): Thermo-hydraulic performance of solar air collectors with artificially roughened absorbers: A comparative review of semi-empirical models, Energies, 13(14). https://doi.org/10.3390/en13143536

22. Arfaoui, N., Bouadila, S., and Guizani, A. (2017): A highly efficient solution of off-sunshine solar air heating using two packed beds of latent storage energy, Solar Energy, 155, 1243–1253. https://doi.org/10.1016/j.solener.2017.07.075

23. Arunkumar, H. S., Vasudeva Karanth, K., and Kumar, S. (2020): Review on the design modifications of a solar air heater for improvement in the thermal performance, Sustainable Energy Technologies and Assessments, 39(January), 100685. https://doi.org/10.1016/j.seta.2020.100685

24. Assadeg, J., Al-Waeli, A. H. A., Fudholi, A., and Sopian, K. (2021): Energetic and exergetic analysis of a new double pass solar air collector with fins and phase change material, Solar Energy, 226(March), 260–271. https://doi.org/10.1016/j.solener.2021.08.056

25. Atsu, D., Seres, I., and Farkas, I. (2021): The state of solar PV and performance analysis of different PV technologies grid-connected installations in Hungary, Renewable and Sustainable Energy Reviews, 141, 110808. https://doi.org/10.1016/j.rser.2021.110808

26. Bangura, A. B. M., Hantoro, R., Fudholi, A., and Uwitije, P. D. (2022): Mathematical Model of the Thermal Performance of Double-Pass Solar Collector for Solar Energy Application in Sierra Leone, International Journal of Renewable Energy Development, 11(2), 347–355. https://doi.org/10.14710/IJRED.2022.41349

27. Baniasadi, E., Ranjbar, S., and Boostanipour, O. (2017): Experimental investigation of the performance of a mixed-mode solar dryer with thermal energy storage, Renewable Energy, 112, 143–150. https://doi.org/10.1016/j.renene.2017.05.043

28. Belessiotis, V., and Delyannis, E. (2011): Solar drying, Solar Energy, 85(8), 1665–1691. https://doi.org/10.1016/J.SOLENER.2009.10.001

29. Bensaci, C. E., Moummi, A., Sanchez de la Flor, F. J., Rodriguez Jara, E. A., Rincon-Casado, A., and Ruiz-Pardo, A. (2020): Numerical and experimental study of the heat transfer and hydraulic performance of solar air heaters with different baffle positions, Renewable Energy, 155, 1231–1244. https://doi.org/10.1016/j.renene.2020.04.017

30. Borah, P. P., Pathak, K. K., Gupta, A., Roy, S., and Das, B. (2023): Experimental study of a solar air heater with modified absorber plate through square obstacles with threaded pin fins, Applied Thermal Engineering, 228(March), 120544. https://doi.org/10.1016/j.applthermaleng.2023.120544

31. Can, A. (2000): Drying kinetics of pumpkinseeds, International Journal of Energy Research, 24(11), 965–975. https://doi.org/10.1002/1099-114X(200009)24:11<965::AID-ER635>3.0.CO;2-W

32. Chabane, F., and Aouissi, Z. (2024): Experimental investigations on the thermal efficiency of a solar air collector with transverse rectangular baffles incline by an angle of 135°, Energy and Built Environment, 5(4), 544–555. https://doi.org/10.1016/j.enbenv.2023.04.004

33. Chabane, F., Kherroubi, D., Arif, A., Moummi, N., and Brima, A. (2020): Influence of the rectangular baffle on heat transfer and pressure drop in the solar collector, Energy Sources, Part A: Recovery, Utilization, and Environmental Effects, 46(1), 8547–8563. https://doi.org/10.1080/15567036.2020.1767727

34. Chabane, F., Moummi, N., Brima, A., and Benramache, S. (2013): Thermal efficiency analysis of a single-flow solar air heater with different mass flow rates in a smooth plate, Frontiers in Heat and Mass Transfer, 4(1). https://doi.org/10.5098/hmt.v4.1.3006

35. Chand, S., Chand, P., and Kumar Ghritlahre, H. (2022): Thermal performance enhancement of solar air heater using louvered fins collector, Solar Energy, 239(May), 10–24. https://doi.org/10.1016/j.solener.2022.04.046

36. Chand, S., Ghritlahre, H. K., and Singh, A. P. (2024): Exergetic performance evaluation of louvered finned solar air heater: an experimental investigation, Journal of Engineering and Applied Science, 1–22. https://doi.org/10.1186/s44147-024-00478-8

37. Chang, Y., Xue, Y., and Geng, G. (2024): Effect of the baffle's type on thermal performance of solar air heaters, Case Studies in Thermal Engineering, 59(March), 104580. https://doi.org/10.1016/j.csite.2024.104580

38. Chauhan, Y. B., and Rathod, P. P. (2020): A comprehensive review of the solar dryer, International Journal of Ambient Energy, 41(3), 348–367. https://doi.org/10.1080/01430750.2018.1456960

39. Chen, C. Q., Diao, Y. H., Zhao, Y. H., Wang, Z. Y., Liang, L., Wang, T. Y., Zhu, T. T., and Ma, C. (2020): Thermal performance of a closed collector–storage solar air heating system with latent thermal storage: An experimental study, Energy, 202. https://doi.org/10.1016/j.energy.2020.117764

40. Chhaparwal, G. K., Goyal, R., Srivastava, A., Goyal, A., Oza, A. D., Haque Siddiqui, M. I., Natrayan, L., Kumar, L., and Chandrakant, S. (2024): Numerical and experimental investigation of a solar air heater duct with circular detached ribs to improve its efficiency, Case Studies in Thermal Engineering, 60(March), 104780. https://doi.org/10.1016/j.csite.2024.104780

41. Chouksey, V. K., and Sharma, S. P. (2016): Investigations on thermal performance characteristics of wire screen packed bed solar air heater, Solar Energy, 132, 591–605. https://doi.org/10.1016/j.solener.2016.03.040

42. Darici, S., and Kilic, A. (2020): Comparative study on the performances of solar air collectors with trapezoidal corrugated and flat absorber plates, Heat and Mass Transfer/Waerme- Und Stoffuebertragung, 56(6), 1833–1843. https://doi.org/10.1007/s00231-020-02815-y

43. Debnath, S., Das, B., Randive, P. R., and Pandey, K. M. (2018): Performance analysis of solar air collector in the climatic condition of North Eastern India, Energy, 165, 281–298. https://doi.org/10.1016/j.energy.2018.09.038

44. Deo, N. S., Chander, S., and Saini, J. S. (2016): Performance analysis of solar air heater duct roughened with multigap V-down ribs combined with staggered ribs, Renewable Energy, 91, 484–500. https://doi.org/10.1016/j.renene.2016.01.067

45. Dhiman, P., and Singh, S. (2015): Recyclic double pass packed bed solar air heaters, International Journal of Thermal Sciences, 87, 215–227. https://doi.org/10.1016/j.ijthermalsci.2014.08.017

46. Duffie, J. A., Beckman, W. A., and Worek, W. M. (2013): Solar Engineering of Thermal Processes (4th ed.), John Wiley & Sons, Inc., Hoboken, New Jersey Published. https://doi.org/10.1115/1.2930068

47. El-khawajah, M. F., Aldabbagh, L. B. Y., and Egelioglu, F. (2011): The effect of using transverse fins on a double pass flow solar air heater using wire mesh as an absorber, Solar Energy, 85(7), 1479–1487. https://doi.org/10.1016/j.solener.2011.04.004

48. El-mesery, H. S., El-seesy, A. I., Hu, Z., and Li, Y. (2022): Recent developments in solar drying technology of food and agricultural products: A review, Renewable and Sustainable Energy Reviews, 157(January), 112070. https://doi.org/10.1016/j.rser.2021.112070

49. El-Sebaii, A. A., Aboul-Enein, S., Ramadan, M. R. I., Shalaby, S. M., and Moharram, B. M. (2011): Investigation of thermal performance of-double pass-flat and v-corrugated plate solar air heaters, Energy, 36(2), 1076–1086. https://doi.org/10.1016/j.energy.2010.11.042

50. El-Sebaii, A. A., and Al-Snani, H. (2010): Effect of selective coating on thermal performance of flat plate solar air heaters, Energy, 35(4), 1820–1828. https://doi.org/10.1016/j.energy.2009.12.037

51. El Hage, H., Herez, A., Ramadan, M., Bazzi, H., and Khaled, M. (2018): An investigation on solar drying: A review with economic and environmental assessment, Energy, 157, 815–829. https://doi.org/10.1016/j.energy.2018.05.197

52. El Khadraoui, A., Bouadila, S., Kooli, S., Farhat, A., and Guizani, A. (2017): Thermal behavior of indirect solar dryer: Nocturnal usage of solar air collector with PCM, Journal of Cleaner Production, 148, 37–48. https://doi.org/10.1016/j.jclepro.2017.01.149

53. Esam, A., Abdulmejeed, A., Khanlari, A., and Gungor, A. (2024): Investigation of combined parallel and triple-pass v-corrugated solar air heater: A numerical and experimental study, 185(March), 1385–1398. https://doi.org/10.1016/j.psep.2024.03.107

54. Esper, A., and Mühlbauer, W. (1998): Solar drying - An effective means of food preservation, Renewable Energy, 15(1–4), 95–100. https://doi.org/10.1016/s0960-1481(98)00143-8

55. Farhan, A. A., Issam M.Ali, A., and Ahmed, H. E. (2021): Energetic and exergetic efficiency analysis of a v-corrugated solar air heater integrated with twisted tape inserts, Renewable Energy, 169, 1373–1385. https://doi.org/10.1016/j.renene.2021.01.109

56. Farzan, H., and Zaim, E. H. (2023): Thermal analysis of a new double-pass solar air heater using perforated absorber and porous materials: An experimental study, Thermal Science and Engineering Progress, 38(January), 101680. https://doi.org/10.1016/j.tsep.2023.101680

57. Fudholi, A., Sopian, K., Ruslan, M. H., and Othman, M. Y. (2013): Performance and cost benefits analysis of double-pass solar collector with and without fins, Energy Conversion and Management, 76, 8–19. https://doi.org/10.1016/j.enconman.2013.07.015

58. Fudholi, A., Sopian, K., Ruslan, M. H., Othman, M. Y., and Yahya, M. (2011): Thermal efficiency of double pass solar collector with longitudinal fins absorbers, American Journal of Applied Sciences, 8(3), 254–260. https://doi.org/10.3844/ajassp.2011.254.260

59. Gabhane, M. G., and Kanase-Patil, A. B. (2017): Experimental analysis of double flow solar air heater with multiple C shape roughness, Solar Energy, 155, 1411–1416. https://doi.org/10.1016/j.solener.2017.07.038

60. Ganesh Kumar, P., Vigneswaran, V. S., Balaji, K., Vinothkumar, S., Prabakaran, R., Sakthivadivel, D., Meikandan, M., and Kim, S. C. (2022): Augmented v-corrugated absorber plate using shot-blasting for solar air heater – Energy, Exergy, Economic, and Environmental (4E) analysis, Process Safety and Environmental Protection, 165(July), 514–531. https://doi.org/10.1016/j.psep.2022.07.036

61. Garg, H. P. (1987): Advances in Solar Energy Technology. Volume 1: Collection and Storage Systems, 1, 666.

62. Ghiami, A., and Ghiami, S. (2018): Comparative study based on energy and exergy analyses of a baffled solar air heater with latent storage collector, Applied Thermal Engineering, 133, 797–808. https://doi.org/10.1016/j.applthermaleng.2017.11.111

63. Goel, V., Hans, V. S., Singh, S., Kumar, R., Pathak, S. K., Singla, M., Bhattacharyya, S., Almatrafi, E., Gill, R. S., and Saini, R. P. (2021): A comprehensive study on the progressive development and applications of solar air heaters, Solar Energy, 229(February), 112–147. https://doi.org/10.1016/j.solener.2021.07.040

64. Gupta, V., Sunil, L., Sharma, A., and Sharma, N. (2012): Construction and performance analysis of an indirect solar dryer integrated with solar air heater, Procedia Engineering, 38, 3260–3269. https://doi.org/10.1016/j.proeng.2012.06.377

65. Hamad, R. F., Alshukri, M. J., Eidan, A. A., and Alsabery, A. I. (2023): Numerical investigation of heat transfer augmentation of solar air heater with attached and detached trapezoidal ribs, Energy Reports, 10, 123–134. https://doi.org/10.1016/j.egyr.2023.06.031

66. Hans, V. S., Saini, R. P., and Saini, J. S. (2010): Heat transfer and friction factor correlations for a solar air heater duct roughened artificially with multiple v-ribs, Solar Energy, 84(6), 898–911. https://doi.org/10.1016/j.solener.2010.02.004

67. Hassan, H., and Abo-Elfadl, S. (2018): Experimental study on the performance of double pass and two inlet ports solar air heater (SAH) at different configurations of the absorber plate, Renewable Energy, 116, 728–740. https://doi.org/10.1016/j.renene.2017.09.047

68. Hedau, A., and Singal, S. K. (2023): Development of Nusselt number and friction factor correlations for double-pass solar air heater duct, Applied Thermal Engineering, 234(July), 121227. https://doi.org/10.1016/j.applthermaleng.2023.121227

69. Hedayatizadeh, M., and Chaji, H. (2016): A review on plum drying, Renewable and Sustainable Energy Reviews, 56, 362–367. https://doi.org/10.1016/j.rser.2015.11.087

70. Hedayatizadeh, M., Sarhaddi, F., Safavinejad, A., Ranjbar, F., and Chaji, H. (2016): Exergy loss-based efficiency optimization of a double-pass/glazed v-corrugated plate solar air heater, Energy, 94, 799–810. https://doi.org/10.1016/j.energy.2015.11.046

71. Hegde, A. K., Raghuvir Pai, and Karanth, K. V. (2023): Performance augmentation of solar air heaters: A comprehensive analysis, Solar Energy, 253(September 2022), 527–553. https://doi.org/10.1016/j.solener.2023.01.031

72. Hosseini, S. S., Ramiar, A., and Ranjbar, A. A. (2018): Numerical investigation of natural convection solar air heater with different fins shape, Renewable Energy, 117, 488–500. https://doi.org/10.1016/j.renene.2017.10.052

73. Hussein, N. F., Ahmed, S. T., and Ekaid, A. L. (2023): Thermal Performance of Double Pass Solar Air Heater With Tubular Solar Absorber, International Journal of Renewable Energy Development, 12(1), 11–21. https://doi.org/10.14710/ijred.2023.46328

74. Ismail, A. F., Abd Hamid, A. S., Ibrahim, A., Jarimi, H., and Sopian, K. (2022): Performance Analysis of a Double Pass Solar Air Thermal Collector with Porous Media Using Lava Rock, Energies, 15(3), 905. https://doi.org/10.3390/en15030905

75. Jain, P. K., and Lanjewar, A. (2019): Overview of V-RIB geometries in solar air heater and performance evaluation of a new V-RIB geometry, Renewable Energy, 133, 77–90. https://doi.org/10.1016/j.renene.2018.10.001

76. Jain, S. K., Agrawal, G. Das, and Misra, R. (2019): A detailed review on various V-shaped ribs roughened solar air heater, Heat and Mass Transfer/Waerme- Und Stoffuebertragung, 55(12), 3369–3412. https://doi.org/10.1007/s00231-019-02656-4

77. Jin, D., Quan, S., Zuo, J., and Xu, S. (2019): Numerical investigation of heat transfer enhancement in a solar air heater roughened by multiple V-shaped ribs, Renewable Energy, 134, 78–88. https://doi.org/10.1016/j.renene.2018.11.016

78. Jin, D., Zhang, M., Wang, P., and Xu, S. (2015): Numerical investigation of heat transfer and fluid flow in a solar air heater duct with multi V-shaped ribs on the absorber plate, Energy, 89, 178–190. https://doi.org/10.1016/j.energy.2015.07.069

79. Jin, D., Zuo, J., Quan, S., Xu, S., and Gao, H. (2017): Thermohydraulic performance of solar air heater with staggered multiple V-shaped ribs on the absorber plate, Energy, 127, 68–77. https://doi.org/10.1016/j.energy.2017.03.101

80. Kabeel, A. E., Hamed, M. H., Omara, Z. M., and Kandeal, A. W. (2018a): Influence of fin height on the performance of a glazed and bladed entrance single-pass solar air heater, Solar Energy, 162(September 2017), 410–419. https://doi.org/10.1016/j.solener.2018.01.037

81. Kabeel, A. E., Hamed, M. H., Omara, Z. M., and Kandel, A. W. (2018b): On the performance of a baffled glazed-bladed entrance solar air heater, Applied Thermal Engineering, 139(April), 367–375. https://doi.org/10.1016/j.applthermaleng.2018.04.141

82. Kabeel, A. E., Khalil, A., Shalaby, S. M., and Zayed, M. E. (2016a): Experimental investigation of thermal performance of flat and v-corrugated plate solar air heaters with and without PCM as thermal energy storage, Energy Conversion and Management, 113, 264–272. https://doi.org/10.1016/j.enconman.2016.01.068

83. Kabeel, A. E., Khalil, A., Shalaby, S. M., and Zayed, M. E. (2016b): Investigation of the Thermal Performances of Flat, Finned, and v-Corrugated Plate Solar Air Heaters, Journal of Solar Energy Engineering, Transactions of the ASME, 138(5), 1–7. https://doi.org/10.1115/1.4034027

84. Kabeel, A. E., Khalil, A., Shalaby, S. M., and Zayed, M. E. (2017): Improvement of thermal performance of the finned plate solar air heater by using latent heat thermal storage, Applied Thermal Engineering, 123, 546–553. https://doi.org/10.1016/j.applthermaleng.2017.05.126

85. Kapadiya, S., and Desai, M. A. A. (2014): Solar Drying of Natural and Food Products: A Review, International Journal of Agriculture and Food Science Technology, 5(6), 565–576. https://www.academia.edu/9031085/Solar_drying_of_natural_and_food_products_a_review

86. Karim, M. A., Perez, E., and Amin, Z. M. (2014): Mathematical modelling of counter flow v-grove solar air collector, Renewable Energy, 67, 192–201. https://doi.org/10.1016/j.renene.2013.11.027

87. Karwa, R. (2024): Performance of Finned Absorber Plate Solar Air Heater Having Multiple Triangular Air Flow Passages in Parallel Under Transition to Turbulent Flow Condition, Journal of Solar Energy Engineering, 146(2), 1–46. https://doi.org/10.1115/1.4063494

88. Karwa, R., and Chitoshiya, G. (2013): Performance study of solar air heater having v-down discrete ribs on absorber plate, Energy, 55, 939–955. https://doi.org/10.1016/j.energy.2013.03.068

89. Karwa, R., and Srivastava, V. (2012): Thermal Performance of Solar Air Heater Having Absorber Plate with V-Down Discrete Rib Roughness for Space-Heating Applications, Journal of Renewable Energy, 2013, 1–13. https://doi.org/10.1155/2013/151578

90. Khanlari, A., Sözen, A., Afshari, F., Ceylin, Ş., Do, A., and Gungor, A. (2020): Science of the Total Environment Drying municipal sewage sludge with v-groove triple-pass and quadruple-pass solar air heaters along with testing of a solar absorber drying chamber, 709. https://doi.org/10.1016/j.scitotenv.2019.136198

91. Khanlari, A., Tuncer, A. D., Sözen, A., Aytaç, İ., Çiftçi, E., and Variyenli, H. İ. (2022): Energy and exergy analysis of a vertical solar air heater with nano-enhanced absorber coating and perforated baffles, Renewable Energy, 187, 586–602. https://doi.org/10.1016/j.renene.2022.01.074

92. Kumar, Anil, Priyanka, Kumar, S., Maithani, R., Sharma, S., Alam, T., Siddiqui, M. I. H., Dobrotă, D., and Rotaru, I. M. (2024): Influence of 45º V-type with collective ring turbulence promoters parameters of thermal performance of flat plate heat collector, Case Studies in Thermal Engineering, 55(October 2023), 104113. https://doi.org/10.1016/j.csite.2024.104113

93. Kumar, Anup, and Layek, A. (2018): Thermo-hydraulic performance of solar air heater having twisted rib over the absorber plate, International Journal of Thermal Sciences, 133(April), 181–195. https://doi.org/10.1016/j.ijthermalsci.2018.07.026

94. Kumar, Anup, and Layek, A. (2019): Energetic and exergetic performance evaluation of solar air heater with twisted rib roughness on absorber plate, Journal of Cleaner Production, 232, 617–628. https://doi.org/10.1016/j.jclepro.2019.05.363

95. Kumar, Anup, Sen, A. P., Kumar, R. R., and Layek, A. (2023): The enhancement of energetic and exergetic performance of embedded twisted rib turbulator over absorber plate of solar air heater, E-Prime - Advances in Electrical Engineering, Electronics and Energy, 5(July), 100212. https://doi.org/10.1016/j.prime.2023.100212

96. Kumar, H., Purvi, G., and Ashfaque, C. (2021): A Comprehensive Review on Performance Prediction of Solar Air Heaters Using Artificial Neural Network, Annals of Data Science, Springer Berlin Heidelberg, 8, 405–449. https://doi.org/10.1007/s40745-019-00236-1

97. Kumar, P., and Singh, D. (2020): Advanced technologies and performance investigations of solar dryers: A review, Renewable Energy Focus, 35(December), 148–158. https://doi.org/10.1016/j.ref.2020.10.003

98. Kumar, Raj, Kumar, A., Chauhan, R., and Sethi, M. (2016): Heat transfer enhancement in solar air channel with broken multiple V-type baffle, Case Studies in Thermal Engineering, 8, 187–197. https://doi.org/10.1016/j.csite.2016.07.001

99. Kumar, Raj, Kumar, A., Sharma, A., Chauhan, R., and Sethi, M. (2017): Experimental study of heat transfer enhancement in a rectangular duct distributed by multi V-perforated baffle of different relative baffle width, Heat and Mass Transfer/Waerme-Und Stoffuebertragung, 53(4), 1289–1304. https://doi.org/10.1007/s00231-016-1901-7

100. Kumar, Raj, Kumar, R., Kumar, S., Thapa, S., Sethi, M., Fekete, G., and Singh, T. (2022): Impact of artificial roughness variation on heat transfer and friction characteristics of solar air heating system, Alexandria Engineering Journal, 61(1), 481–491. https://doi.org/10.1016/j.aej.2021.06.031

101. Kumar, Rajesh, and Chand, P. (2017): Performance enhancement of solar air heater using herringbone corrugated fins, Energy, 127, 271–279. https://doi.org/10.1016/j.energy.2017.03.128

102. Kumar, S., Das, R. K., Kulkarni, K., Alam, T., and Eldin, S. M. (2023): Designing of low cost solar air heater equipped with roughness of streamlined cross-section, Case Studies in Thermal Engineering, 45(March), 102915. https://doi.org/10.1016/j.csite.2023.102915

103. Kumar, V. (2019): Thermal and thermohydraulic performance analysis of three sides artificially roughened solar collectors, Solar Energy, 190(August), 212–227. https://doi.org/10.1016/j.solener.2019.08.018

104. Kumar, V., and Murmu, R. (2023): Performance based investigation of inclined spherical ball roughened solar air heater, Applied Thermal Engineering, 224(December 2022), 120033. https://doi.org/10.1016/j.applthermaleng.2023.120033

105. Lamidi, R. O., Jiang, L., Pathare, P. B., Wang, Y. D., and Roskilly, A. P. (2019): Recent advances in sustainable drying of agricultural produce: A review, Applied Energy, 233–234(September 2018), 367–385. https://doi.org/10.1016/j.apenergy.2018.10.044

106. Lingayat, A. B., Chandramohan, V. P., Raju, V. R. K., and Meda, V. (2020): A review on indirect type solar dryers for agricultural crops – Dryer setup, its performance, energy storage and important highlights, Applied Energy, 258(May 2019), 114005. https://doi.org/10.1016/j.apenergy.2019.114005

107. Lingayat, A., Chandramohan, V. P., and Raju, V. R. K. (2017): Design, Development and Performance of Indirect Type Solar Dryer for Banana Drying, Energy Procedia, 109, 409–416. https://doi.org/10.1016/j.egypro.2017.03.041

108. Maarof, H. A., Shamsi, M., Younas, M., and Rezakazemi, M. (2023): Hybrid thermal and optical modeling of a solar air heater with a non-flat plate absorber, Energy Reports, 9, 6102–6113. https://doi.org/10.1016/j.egyr.2023.05.227

109. Machi, M. H., Al-Neama, M. A., Buzás, J., and Farkas, I. (2022): Energy-based performance analysis of a double pass solar air collector integrated to triangular shaped fins, International Journal of Energy and Environmental Engineering, 13(1), 219–229. https://doi.org/10.1007/s40095-021-00422-z

110. Machi, M. H., Farkas, I., and Buzas, J. (2024): Enhancing solar air collector performance through optimized entrance flue design: A comparative study, International Journal of Thermofluids, 21(January), 100561. https://doi.org/10.1016/j.ijft.2024.100561

111. Mahboub, C., Moummi, N., Brima, A., and Moummi, A. (2016): Experimental study of new solar air heater design, International Journal of Green Energy, 13(5), 521–529. https://doi.org/10.1080/15435075.2014.968922

112. Mahfoud, O., Danane, F., Moummi, A., and Moummi, N. (2024): Enhancing thermo-hydraulic performance of solar air collectors through three-dimensional airflow using novel artificial roughness designs, Journal of the Taiwan Institute of Chemical Engineers, 157(February), 105403. https://doi.org/10.1016/j.jtice.2024.105403

113. Mohamad, A. A. (1997): High efficiency solar air heater, Solar Energy, 60(2), 71–76. https://doi.org/10.1016/S0038-092X(96)00163-6

114. Mohammed, S. A., Alawee, W. H., Chaichan, M. T., Abdul-Zahra, A. S., Fayad, M. A., and Aljuwaya, T. M. (2024): Optimized solar food dryer with varied air heater designs, Case Studies in Thermal Engineering, 53(October 2023), 103961. https://doi.org/10.1016/j.csite.2023.103961

115. Mohana, Y., Mohanapriya, R., Anukiruthika, T., Yoha, K. S., Moses, J. A., and Anandharamakrishnan, C. (2020): Solar dryers for food applications: Concepts, designs, and recent advances, Solar Energy, 208(February), 321–344. https://doi.org/10.1016/j.solener.2020.07.098

116. Moriarty, P., and Honnery, D. (2018): Global renewable energy resources and use in 2050, Managing Global Warming: An Interface of Technology and Human Issues, Elsevier Inc., 221–235. https://doi.org/10.1016/B978-0-12-814104-5.00006-5

117. Mugi, V. R., and Chandramohan, V. P. (2022): Energy, exergy, economic and environmental (4E) analysis of passive and active-modes indirect type solar dryers while drying guava slices, Sustainable Energy Technologies and Assessments, 52(January), 102250. https://doi.org/10.1016/j.seta.2022.102250

118. Mund, C., Rathore, S. K., and Sahoo, R. K. (2021): A review of solar air collectors about various modifications for performance enhancement, Solar Energy, 228(January), 140–167. https://doi.org/10.1016/j.solener.2021.08.040

119. Mund, C., Rathore, S. K., and Sahoo, R. K. (2024): Experimental investigation of heat transfer augmentation of impinging jet solar air heater with stepped transverse ribs, Thermal Science and Engineering Progress, 56(June), 103020. https://doi.org/10.1016/j.tsep.2024.103020

120. Murthy, M. V. R. (2009): A review of new technologies, models and experimental investigations of solar driers, Renewable and Sustainable Energy Reviews, 13(4), 835–844. https://doi.org/10.1016/j.rser.2008.02.010

121. Naphon, P. (2005): On the performance and entropy generation of the double-pass solar air heater with longitudinal fins, Renewable Energy, 30(9), 1345–1357. https://doi.org/10.1016/j.renene.2004.10.014

122. Nasri, F. (2020): Solar thermal drying performance analysis of banana and peach in the region of Gafsa (Tunisia), Case Studies in Thermal Engineering, 22(December 2019), 100771. https://doi.org/10.1016/j.csite.2020.100771

123. Obaid, Z. A. H., Azzawi, I. D. J., and Azeez, K. (2022): The experimental study of energy features for solar air heaters with different turbulator configurations, Heat Transfer, (January 2022), 1380–1394. https://doi.org/10.1002/htj.22745

124. Obaideen, K., Olabi, A. G., Swailmeen, Y. Al, Shehata, N., Abdelkareem, M. A., Alami, A. H., Rodriguez, C., and Sayed, E. T. (2023): Solar Energy: Applications, Trends Analysis, Bibliometric Analysis and Research Contribution to Sustainable Development Goals (SDGs), Sustainability, 15, 1418. https://doi.org/10.3390/su15021418

125. Omojaro, A. P., and Aldabbagh, L. B. Y. (2010): Experimental performance of single and double pass solar air heater with fins and steel wire mesh as absorber, Applied Energy, 87(12), 3759–3765. https://doi.org/10.1016/j.apenergy.2010.06.020

126. Omotosho, E., and Hackney, P. (2024): Performance prediction of single-pass and multi-pass low-cost solar air heater, Thermal Science and Engineering Progress, 47(June 2023), 102322. https://doi.org/10.1016/j.tsep.2023.102322

127. Ong, K. S. (1995): Thermal performance of solar air heaters: Mathematical model and solution procedure, Solar Energy, 55(2), 93–109. https://doi.org/10.1016/0038-092X(95)00021-I

128. Ozgen, F., Esen, M., and Esen, H. (2009): Experimental investigation of thermal performance of a double-flow solar air heater having aluminium cans, Renewable Energy, 34(11), 2391–2398. https://doi.org/10.1016/j.renene.2009.03.029

129. Oztop, H. F., Bayrak, F., and Hepbasli, A. (2013): Energetic and exergetic aspects of solar air heating (solar collector) systems, Renewable and Sustainable Energy Reviews, 21, 59–83. https://doi.org/10.1016/j.rser.2012.12.019

130. Pachori, H., Choudhary, T., Sheorey, T., and Kumar, A. (2024): A novel energy, exergy and sustainability analysis of a decentralized solar air heater integrated with V-shaped artificial roughness for solar thermal application, Sustainable Energy Technologies and Assessments, 66(May), 103816. https://doi.org/10.1016/j.seta.2024.103816

131. Panda, S., and Kumar, R. (2024): Investigation of the effect of dimensional and non-dimensional parameters on the performance of pitch-varied staggered arranged dimple solar air heaters, Solar Energy, 276(May), 112663. https://doi.org/10.1016/j.solener.2024.112663

132. Parag Jyoti Bezbaruah, Rajat Subhra Das, and Sarkar, B. K. (2020): Solar Air Heater with Finned Absorber Plate and Helical Flow Path: A CFD Analysis, Applied Solar Energy, 56(1), 35–41. https://doi.org/10.3103/S0003701X20010041

133. Patel, S. S., and Lanjewar, A. (2018): Experimental analysis for augmentation of heat transfer in multiple discrete V-patterns combined with staggered ribs solar air heater, Reinforced Plastics, 25(June), 31–39. https://doi.org/10.1016/j.ref.2018.03.003

134. Patel, S. S., and Lanjewar, A. (2019): Performance study of solar air heater duct with gap in V-rib with symmetrical gap and staggered ribs, Heat and Mass Transfer, 55(9), 2517–2532. https://doi.org/10.1007/s00231-019-02592-3

135. Patel, Y. M., Jain, S. V., and Lakhera, V. J. (2021): Thermo-hydraulic performance analysis of a solar air heater roughened with discrete reverse NACA profile ribs, International Journal of Thermal Sciences, 167(March), 107026. https://doi.org/10.1016/j.ijthermalsci.2021.107026

136. Priyam, A., and Chand, P. (2016): Thermal and thermohydraulic performance of wavy finned absorber solar air heater, Solar Energy, 130, 250–259. https://doi.org/10.1016/j.solener.2016.02.030

137. Promvonge, P., Promthaisong, P., and Skullong, S. (2021): Numerical heat transfer in a solar air heater duct with punched delta-winglet vortex generators, Case Studies in Thermal Engineering, 26(May), 101088. https://doi.org/10.1016/j.csite.2021.101088

138. Promvonge, P., Promthaisong, P., and Skullong, S. (2022): Experimental and numerical thermal performance in solar receiver heat exchanger with trapezoidal louvered winglet and wavy groove, Solar Energy, 236(October 2021), 153–174. https://doi.org/10.1016/j.solener.2022.02.052

139. Promvonge, P., Tongyote, P., and Skullong, S. (2019): Thermal behaviors in heat exchanger channel with V-shaped ribs and grooves, Chemical Engineering Research and Design, 150, 263–273. https://doi.org/10.1016/j.cherd.2019.07.025

140. Qader, B. S., Supeni, E. E., Ariffin, M. K. A., and Talib, A. R. A. (2019): Numerical investigation of flow through inclined fins under the absorber plate of solar air heater, Renewable Energy, 141, 468–481. https://doi.org/10.1016/j.renene.2019.04.024

141. Qamar, Z., Munir, A., Langrish, T., Ghafoor, A., and Tahir, M. (2023): Experimental and Numerical Simulations of a Solar Air Heater for Maximal Value Addition to Agricultural Products, Agriculture (Switzerland), 13(2). https://doi.org/10.3390/agriculture13020387

142. Raj, A. K., Kunal, G., Srinivas, M., and Jayaraj, S. (2019): Performance analysis of a double-pass solar air heater system with asymmetric channel flow passages, Journal of Thermal Analysis and Calorimetry, 136(1), 21–38. https://doi.org/10.1007/s10973-018-7762-1

143. Rajendran, V., Singaraj, K., and Rajarathinam, J. (2023): Environmental, economic, and performance assessment of solar air heater with inclined and winglet baffle, Environmental Science and Pollution Research, 30(6), 14337–14352. https://doi.org/10.1007/s11356-022-23213-3

144. Rajesh, S., Sekar, S., and Madhankumar, S. (2024): Energy and environmental analysis in an indirect solar dryer with flat coil inserted phase change material, Sustainable Energy Technologies and Assessments, 66(April), 103805. https://doi.org/10.1016/j.seta.2024.103805

145. Ramani, B. M., Gupta, A., and Kumar, R. (2010): Performance of a double pass solar air collector, Solar Energy, 84(11), 1929–1937. https://doi.org/10.1016/j.solener.2010.07.007

146. Rani, P., and Tripathy, P. P. (2020): Thermal characteristics of a flat plate solar collector: Influence of air mass flow rate and correlation analysis among process parameters, Solar Energy, 211(August), 464–477. https://doi.org/10.1016/j.solener.2020.08.057

147. Ravi, R. K., and Saini, R. P. (2016): Experimental investigation on performance of a double pass artificial roughened solar air heater duct having roughness elements of the combination of discrete multi V shaped and staggered ribs, Energy, 116, 507–516. https://doi.org/10.1016/j.energy.2016.09.138

148. Ravi, R. K., and Saini, R. P. (2018): Nusselt number and friction factor correlations for forced convective type counter flow solar air heater having discrete multi V shaped and staggered rib roughness on both sides of the absorber plate, Applied Thermal Engineering, 129, 735–746. https://doi.org/10.1016/j.applthermaleng.2017.10.080

149. Ray, A., Bhonsle, A. K., Singh, J., Trivedi, J., and Atray, N. (2025): Examining alternative carbon resources for sustainable energy generation: A comprehensive review, Next Energy, 6(August 2024), 100194. https://doi.org/10.1016/j.nxener.2024.100194

150. Razak, A. A., Majid, Z. A. A., Azmi, W. H., Ruslan, M. H., Choobchian, S., Najafi, G., and Sopian, K. (2016): Review on matrix thermal absorber designs for solar air collector, Renewable and Sustainable Energy Reviews, 64, 682–693. https://doi.org/10.1016/j.rser.2016.06.015

151. Romano, G., Kocsis, L., and Farkas, I. (2009): Analysis of energy and environmental parameters during solar cabinet drying of apple and carrot, Drying Technology, 27(4), 574–579. https://doi.org/10.1080/00304940802716233

152. Sahel, D., and Benzeguir, R. (2017): Thermal characteristic in solar air heater fitted with plate baffles and heating corrugated surface, Energy Procedia, 139, 307–314. https://doi.org/10.1016/j.egypro.2017.11.213

153. Salih, M. M. M., Alomar, O. R., Ali, F. A., and Abd, H. M. (2019): An experimental investigation of a double pass solar air heater performance: A comparison between natural and forced air circulation processes, Solar Energy, 193(June), 184–194. https://doi.org/10.1016/j.solener.2019.09.060

154. Salih, M. M. M., Alomar, O. R., and Yassien, H. N. S. (2021): Impacts of adding porous media on performance of double-pass solar air heater under natural and forced air circulation processes, International Journal of Mechanical Sciences, 210(July), 106738. https://doi.org/10.1016/j.ijmecsci.2021.106738

155. Saravanakumar, P. T., Somasundaram, D., and Matheswaran, M. M. (2019): Thermal and thermo-hydraulic analysis of arc shaped rib roughened solar air heater integrated with fins and baffles, Solar Energy, 180(January), 360–371. https://doi.org/10.1016/j.solener.2019.01.036

156. Saravanan, A., Murugan, M., Reddy, M. S., Ranjit, P. S., Elumalai, P. V., Kumar, P., and Sree, S. R. (2021): Thermo-hydraulic performance of a solar air heater with staggered C-shape finned absorber plate, International Journal of Thermal Sciences, 168(February), 107068. https://doi.org/10.1016/j.ijthermalsci.2021.107068

157. Saxena, A., Agarwal, N., and Cuce, E. (2020a): Thermal performance evaluation of a solar air heater integrated with helical tubes carrying phase change material, Journal of Energy Storage, 30(April), 101406. https://doi.org/10.1016/j.est.2020.101406

158. Saxena, A., Agarwal, N., and Srivastava, G. (2013): Design and performance of a solar air heater with long term heat storage, International Journal of Heat and Mass Transfer, 60(1), 8–16. https://doi.org/10.1016/j.ijheatmasstransfer.2012.12.044

159. Saxena, A., Srivastava, G., and Tirth, V. (2015): Design and thermal performance evaluation of a novel solar air heater, Renewable Energy, 77, 501–511. https://doi.org/10.1016/j.renene.2014.12.041

160. Saxena, A., Verma, P., Srivastava, G., and Kishore, N. (2020b): Design and thermal performance evaluation of an air heater with low cost thermal energy storage, Applied Thermal Engineering, 167(September 2019), 114768. https://doi.org/10.1016/j.applthermaleng.2019.114768

161. Sharma, A., Bharadwaj, G., and Varun (2017): Heat transfer and friction factor correlation development for double-pass solar air heater having V-shaped ribs as roughness elements, Experimental Heat Transfer, 30(1), 77–90. https://doi.org/10.1080/08916152.2016.1161676

162. Sharma, S. K., and Kalamkar, V. R. (2017): Experimental and numerical investigation of forced convective heat transfer in solar air heater with thin ribs, Solar Energy, 147, 277–291. https://doi.org/10.1016/j.solener.2017.03.042

163. Sharma, S. L., and Debbarma, A. (2024): Experimental Study of Reverse Flow Solar Air Heater Having Perforation and Delta Wing on Absorber Plate, Energy Technology, 2301246, 1–15. https://doi.org/10.1002/ente.202301246

164. Singh, A. K., Agarwal, N., and Saxena, A. (2021): Effect of extended geometry filled with and without phase change material on the thermal performance of solar air heater, Journal of Energy Storage, 39(June 2020), 102627. https://doi.org/10.1016/j.est.2021.102627

165. Singh, D., and Kumar, V. (2023): Thermal performance investigation of frustum roughened solar air heater, Solar Energy, 255(October 2022), 339–354. https://doi.org/10.1016/j.solener.2023.03.036

166. Singh Patel, S., and Lanjewar, A. (2019): Experimental and numerical investigation of solar air heater with novel V-rib geometry, Journal of Energy Storage, 21(December 2018), 750–764. https://doi.org/10.1016/j.est.2019.01.016

167. Singh, Satyender (2020): Thermohydraulic performance of double pass solar thermal collector with inline, staggered and hybrid fin configurations, Journal of Energy Storage, 27(August 2019), 101080. https://doi.org/10.1016/j.est.2019.101080

168. Singh, Satyender, and Dhiman, P. (2016): Exergoeconomic analysis of recyclic packed bed solar air heater- sustained air heating system for buildings, Journal of Energy Storage, 5, 33–47. https://doi.org/10.1016/j.est.2015.11.008

169. Singh, Satyender, and Dhiman, P. (2018): Analytical and experimental investigations of packed bed solar air heaters under the collective effect of recycle ratio and fractional mass flow rate, Journal of Energy Storage, 16, 167–186. https://doi.org/10.1016/j.est.2018.01.003

170. Singh, Satyender, and Negi, B. S. (2020): Numerical thermal performance investigation of phase change material integrated wavy finned single pass solar air heater, Journal of Energy Storage, 32(September), 102002. https://doi.org/10.1016/j.est.2020.102002

171. Singh, Simarpreet (2017): Performance evaluation of a novel solar air heater with arched absorber plate, Renewable Energy, 114, 879–886. https://doi.org/10.1016/j.renene.2017.07.109

172. Singh, Sukhmeet, Chander, S., and Saini, J. S. (2012): Investigations on thermo-hydraulic performance due to flow-attack-angle in V-down rib with gap in a rectangular duct of solar air heater, Applied Energy, 97, 907–912. https://doi.org/10.1016/j.apenergy.2011.11.090

173. Singh, V. P., Jain, S., and Gupta, J. M. L. (2022a): Performance assessment of double-pass parallel flow solar air heater with perforated multi-V ribs roughness — Part B, Experimental Heat Transfer, 35(7), 1059–1076. https://doi.org/10.1080/08916152.2021.2019147

174. Singh, V. P., Jain, S., Karn, A., Kumar, A., Dwivedi, G., Meena, C. S., Dutt, N., and Ghosh, A. (2022b): Recent Developments and Advancements in Solar Air Heaters: A Detailed Review, Sustainability, 14(19), 12149. https://doi.org/10.3390/su141912149

175. Singh Yadav, A., and Bhagoria, J. L. (2015): Numerical investigation of flow through an artificially roughened solar air heater, International Journal of Ambient Energy, 36(2), 87–100. https://doi.org/10.1080/01430750.2013.823107

176. Sivarathinamoorthy, H., and Sureshkannan, G. (2021): The influence of internal heat storage material and longitudinal fins on a double-pass solar air heater performance, Journal of Solar Energy Engineering, Transactions of the ASME, 143(1). https://doi.org/10.1115/1.4047454

177. Sopian, K., Alghoul, M. A., Alfegi, E. M., Sulaiman, M. Y., and Musa, E. A. (2009): Evaluation of thermal efficiency of double-pass solar collector with porous-nonporous media, Renewable Energy, 34(3), 640–645. https://doi.org/10.1016/j.renene.2008.05.027

178. Soteris Kalogirou (2009): Solar energy engineering: processes and systems (1st ed.), Solar Energy Engineering, Elsevier, California, 756. https://doi.org/10.1016/b978-0-12-374501-9.00014-5

179. Srivastav, A., Maithani, R., and Sharma, S. (2024): Influence of submerged impingement jet designs on solar air collector performance, Renewable Energy, 237(PB), 121699. https://doi.org/10.1016/j.renene.2024.121699

180. Sudhakar, P., and Cheralathan, M. (2019): Encapsulated PCM based double pass solar air heater: A comparative experimental study, Chemical Engineering Communications, 208(6), 788–800. https://doi.org/10.1080/00986445.2019.1641701

181. Sudhakar, P., and Cheralathan, M. (2020): Thermal performance enhancement of solar air collector using a novel V-groove absorber plate with pin-fins for drying agricultural products: an experimental study, Journal of Thermal Analysis and Calorimetry, 140(5), 2397–2408. https://doi.org/10.1007/s10973-019-08952-9

182. Suherman, S., Asy-Syaqiq, M. A., Hadiyanto, H., Djaeni, M., and Prasetiyono, B. W. H. E. (2024): Advancements and 4E + Q performance analyses in solar drying for maize kernels preservation: A comprehensive review, Journal of Food Process Engineering, 47(6), 1–29. https://doi.org/10.1111/jfpe.14659

183. Suresh Bhuvad, S., Husain Rizvi, I., and Azad, R. (2023): Apex-up discrete-arc rib roughened solar air heater- energy and exergy based experimental study, Solar Energy, 258(March), 361–371. https://doi.org/10.1016/j.solener.2023.04.007

184. Taha, S. Y., and Farhan, A. A. (2021): Performance augmentation of a solar air heater using herringbone metal foam fins: An experimental work, International Journal of Energy Research, 45(2), 2321–2333. https://doi.org/10.1002/er.5927

185. Thakur, D. S., Khan, M. K., and Pathak, M. (2017): Performance evaluation of solar air heater with novel hyperbolic rib geometry, Renewable Energy, 105, 786–797. https://doi.org/10.1016/j.renene.2016.12.092

186. Thapa, S., Kumar, R., and Lee, D. (2024): Energetic and exergetic analysis of jet impingement solar thermal collector featuring discrete multi-arc shaped ribs absorber surface, Energy, 306(June), 132392. https://doi.org/10.1016/j.energy.2024.132392

187. Toshniwal, U., and Karale, S. R. (2013): A review paper on Solar Dryer, International Journal of Engineering Research and Applications (IJERA), 3(2), 896–902. https://www.ijera.com/papers/Vol3_issue2/ER32896902.pdf

188. Tyagi, V. V., Panwar, N. L., Rahim, N. A., and Kothari, R. (2012): Review on solar air heating system with and without thermal energy storage system, Renewable and Sustainable Energy Reviews, 16(4), 2289–2303. https://doi.org/10.1016/j.rser.2011.12.005

189. Umayal Sundari, A. R., and Veeramanipriya, E. (2022): Performance evaluation, morphological properties and drying kinetics of untreated Carica Papaya using solar hybrid dryer integrated with heat storage material, Journal of Energy Storage, 55(PC), 105679. https://doi.org/10.1016/j.est.2022.105679

190. Vengadesan, E., Arunkumar, T., Krishnamoorthi, T., and Senthil, S. (2024): Thermal performance improvement in solar air heating: An absorber with continuous and discrete tubular and v-corrugated fins, Thermal Science and Engineering Progress, 48(January), 102416. https://doi.org/10.1016/j.tsep.2024.102416

191. Vijayan, S., Arjunan, T. V., and Kumar, A. (2016): Mathematical modeling and performance analysis of thin layer drying of bitter gourd in sensible storage based indirect solar dryer, Innovative Food Science and Emerging Technologies, 36, 59–67. https://doi.org/10.1016/j.ifset.2016.05.014

192. Yadav, A. S., and Bhagoria, J. L. (2013): A CFD (computational fluid dynamics) based heat transfer and fluid flow analysis of a solar air heater provided with circular transverse wire rib roughness on the absorber plate, Energy, 55, 1127–1142. https://doi.org/10.1016/j.energy.2013.03.066

193. Yadav, A. S., and Bhagoria, J. L. (2014a): A CFD based thermo-hydraulic performance analysis of an artificially roughened solar air heater having equilateral triangular sectioned rib roughness on the absorber plate, International Journal of Heat and Mass Transfer, 70, 1016–1039. https://doi.org/10.1016/j.ijheatmasstransfer.2013.11.074

194. Yadav, A. S., and Bhagoria, J. L. (2014b): A numerical investigation of turbulent flows through an artificially roughened solar air heater, Numerical Heat Transfer; Part A: Applications, 65(7), 679–698. https://doi.org/10.1080/10407782.2013.846187

195. Yadav, A. S., and Sharma, A. (2022): Experimental Investigation on Heat Transfer Enhancement of Artificially Roughened Solar Air Heater, Heat Transfer Engineering, 44(7), 624–637. https://doi.org/10.1080/01457632.2022.2079048

196. Yang, M., Wang, P., Yang, X., and Shan, M. (2012): Experimental analysis on thermal performance of a solar air collector with a single pass, Building and Environment, 56, 361–369. https://doi.org/10.1016/j.buildenv.2012.04.009

197. Yang, M., Yang, X., Li, X., Wang, Z., and Wang, P. (2014): Design and optimization of a solar air heater with offset strip fin absorber plate, Applied Energy, 113, 1349–1362. https://doi.org/10.1016/j.apenergy.2013.08.091

198. Yassien, H. N. S., Alomar, O. R., and Salih, M. M. M. (2020): Performance analysis of triple-pass solar air heater system: Effects of adding a net of tubes below absorber surface, Solar Energy, 207(July), 813–824. https://doi.org/10.1016/j.solener.2020.07.041

199. Yusaidi, N. J., Fauzan, M. F., Abdullah, A. F., Ibrahim, A., and Ishak, A. A. (2024): Theoretical and experimental investigations on the effect of double pass solar air heater with staggered-diamond shaped fins arrangement, Case Studies in Thermal Engineering, 60(April), 104619. https://doi.org/10.1016/j.csite.2024.104619

200. Zhang, J., and Zhu, T. (2022): Systematic review of solar air collector technologies: Performance evaluation, structure design and application analysis, Sustainable Energy Technologies and Assessments, 54(409), 102885. https://doi.org/10.1016/j.seta.2022.102885

201. Zhang, T., Lu, G., Zhai, X., and Li, B. (2021): Structure optimization of a phase change material integrated solar air collector/storage unit based upon phase change analysis, Energy Reports, 7, 1828–1836. https://doi.org/10.1016/j.egyr.2021.03.040

A2: Publications related to the dissertation

Refereed papers in foreign languages:

1. **Machi, M.H**, Buzas, J., Farkas I. (2020): Potential of solar energy utilization in Iraq, Mechanical Engineering Letters, Vol. 20, 80–88. https://www.gek.szie.hu/english/sites/default/files/MEL_2020_20.pdf

2. **Machi, M.H.**, Al-Neama, M.A., Buzás, J., Farkas, I. (2022): Energy-based performance analysis of a double pass solar air collector integrated to triangular shaped fins, International Journal of Energy and Environmental Engineering, 13(1), pp. 219–229. https://doi.org/10.1007/s40095-021-00422-z. (Scopus: Q2, IF = 1.9)

3. **Machi, M.H**., Farkas, I., Buzas, J. (2024): Enhancing solar air collector performance through optimized entrance flue design: A comparative study, International Journal of Thermofluids, 21(January), Paper No. 100561. https://doi.org/10.1016/j.ijft.2024.100561 (Scopus: D1)

4. **Machi, M.H.**, Farkas, I., Buzas, J. (2024): Enhancing thermal efficiency of double-pass solar air collectors: A comparative study on the role of V-angled perforated fins, Energy Reports, 12(December), pp. 481–494. https://doi.org/10.1016/j.egyr.2024.06.048. (Scopus: Q2 IF = 4.7)

5. **Machi, M.H.**, Farkas, I., Buzas, J. (2025): Modelling the performance of double pass solar air collectors, European Journal of Energy Research. Vol. 5, No. 1, pp. 1-9. https://doi.org/10.24018/ejenergy.2025.5.1.159

6. **Machi, M.H.**, Farkas, I., Buzas, J. (2025): Optimizing double-pass solar air collector efficiency: Impact of a perforated discrete V-angled fins, Energy Reports, Vol. 13, pp. 2021–2034. https://doi.org/10.1016/j.egyr.2025.01.057. (Scopus: Q2 IF = 4.7)

7. **Machi, M.H.**, Zhu, Q.K., Farkas, I., Buzas, J. (2025): Impact of Fin shape and orientation on drying performance in solar air collectors. Acta Technologica Agriculturae, 24(4), pp. xx-xx. *https://doi.org/xxxxxxxxxxxx.* (IF = 1.3*)* (in progress)

8. **Machi, M.H.**, Farkas, I., Buzas, J. (2025): Investigating the role of air channel depth on solar air collector performance. International Journal of Thermofluids, xx(xx), pp. xxx. https://doi.org/xxxxx/xxxxxx (Scopus: D1) (in progress)

9. **Machi, M.H**., Farkas, I., Buzas, J. (2025): Impact of selective coatings on efficiency of solar air collectors: An experimental investigation. Results in Engineering, xx(xx), pp. xxx. https://doi.org/xxxxx/xxxxxx (Scopus: Q1, IF = 6) (in progress)

International conference abstracts

10. **Machi, M. H.**, Buzas J., Farkas I. (2020): Thermal performance of solar air collectors used in modular solar dryer, Book of Abstracts, 26th Workshop on Energy and Environment, Gödöllő, Hungary, December 10-11, 2020, p. 19. ISBN 978-963-269-928-8.

11. **Machi, M. H.**, Buzas J., Farkas, I. (2021): Enhancement techniques of solar air collector performance, Book of abstracts, BioPhys Spring 2021, Lublin, Poland, May 18, 2021, p. 71. ISBN 978-83-89969-68-6.

12. **Machi, M. H.**, Buzas J., Farkas I. (2021): Modelling the flue conditions in a single pass solar air collector, Book of Abstracts, 27th Workshop on Energy and Environment, Gödöllő, Hungary, December 9-10, 2021, p. 25. ISBN 978-963-269-972-1.

13. **Machi**, M. H., Buzas J., Farkas, I. (2022): Thermal performance modelling of a single pass solar air collector, Book of abstracts, 21th International Workshop for Young Scientists BioPhys Spring 2022, Nyitra, Slovakia, May 30-31, 2022, p. 120. ISBN 978-83- 89969-74-3

14. **Machi, M. H.**, Buzas J., Farkas I. (2022): The effect of channel height on the performance of a single pass solar air collector, Book of Abstracts, 28th Workshop on Energy and Environment, Gödöllő, Hungary, December 8-9, 2022, pp. 45-46. ISBN 978-963- 623-016-6.

15. **Machi**, M. H., Buzas J., Farkas, I. (2023): CFD modelling of channel depth effect on the solar air collector efficiency, Book of abstracts, BioPhys Spring 2023, Gödöllő, Hungary, June 15-16, 2023, p. 45. ISBN 978-963-623-054-8

16. **Machi**, M. H., Farkas I, Buzas J. (2023): Comparative analysis of single pass and double pass solar air collectors: an efficiency assessment, Book of Abstracts, 29th Workshop on Energy and Environment, Gödöllő, Hungary, December 7-8, 2023, pp. 45-46. ISBN 978-963-623-079-1

17. **Machi**, M. H., Farkas I, Buzas J. (2024): Mathematical modelling and experimental validation of double-pass solar air collectors, Book of Abstracts, 30th Workshop on Energy and Environment, Gödöllő, Hungary, December 12-13, pp. 41-42. ISBN 978-963-623-108-8

10. ACKNOWLEDGEMENT

First and foremost, I praise and acknowledge Allah, the Most Beneficent and the Most Merciful, whose compassion and mercy enabled me to complete my thesis.

I deeply acknowledge the Stipendium Hungaricum Scholarship Program and the Mechanical Engineering Doctoral School at the Hungarian University of Agriculture and Life Sciences (MATE), Gödöllő, Hungary, for financially supporting this work.

I wish to convey my deepest appreciation to my supervisors, Prof. István Farkas and Dr. János Buzás, for their invaluable guidance, constant encouragement, and unwavering support. Their insightful suggestions and ideas were essential to the structure and success of this research. Collaborating with them over the years has been an immensely rewarding experience, and without their mentorship, this thesis would not have been possible.

I owe my deepest gratitude to my parents for their endless support and prayers throughout my life; their love and sacrifices have brought me to where I am today. I pray that Allah protects and blesses them always.

I am more than appreciative and grateful to my beloved wife (Noorulhuda) and kids (Fadel and Ahmed), for their patience, understanding, encouragement, sacrifice, and ongoing support. Thank you from the bottom of my heart.

My thanks are also extended to my brothers, sister, and their families for their great support during my graduate studies.

I want to thank all my relatives and friends in Iraq and Hungary for supporting me during my studies.

I would like to give a special thank to Dr. István Seres for his valuable support. Special thanks and gratitude also go to my university coordinators (Ms. Zsuzsanna Tassy, Mrs. Judit Czingli Tallárom, Mrs Edit Dolányi Sima and Mrs. Katalin Fekete Sivatagi) for there valuable support during my study.

Finally, I deeply acknowledge the Ministry of Higher Education of Iraq and my home university, the University of Kufa, for nominating and supporting me during my studies.

Gödöllő, February 2025

Maytham Hasan Mahdi Machi